

Universidade de São Paulo
Instituto de Astronomia, Geofísica e Ciências Atmosféricas
Departamento de Astronomia

CARLOS EDUARDO BARBOSA

**Kinematics and stellar populations of
galaxies in the local universe**

**Cinemática e populações estelares de
galáxias no universo local**

São Paulo

2016

CARLOS EDUARDO BARBOSA

**Kinematics and stellar populations of
galaxies in the local universe**

**Cinemática e populações estelares de
galáxias no universo local**

A dissertation submitted to the Institute of Astronomy, Geophysics and Atmospheric Sciences of the University of São Paulo in partial fulfillment of the requirements for the degree of DOCTOR OF PHILOSOPHY in the Department of Astronomy.

Field: Astronomy

Advisor: Dr. Cláudia Mendes de Oliveira

São Paulo

2016

To Lilian and Ulisses.

Acknowledgements

I would like to express my sincere gratitude to my advisor Prof. Dr. Cláudia Mendes de Oliveira, who has immensely supported me throughout my academic life. I am truly indebted for the respectful and enthusiastic attitude towards my scientific work, and for the dedication to the completion of this dissertation.

I am much indebted to all my collaborators for their incredible scientific teachings, hard work and support: Dr. Magda Arnaboldi, Dr. Michael Hilker, Dr. Lodovico Coccatto and Dr. Tom Richtler in the Hydra I project, Dr. Fabrício Ferrari, Dr. Philippe Amram and the GHASP collaboration, and Dr. Robert Proctor for the work on galaxy groups.

I would like to thank the IAG staff, colleagues, officemates, and professors, for proving me a great place to do science and, in particular, thanks to the people that accompanied, discussed and/or contributed to my work here in numerous opportunities: Juan, Jonatan, Alberto, Arianna, Marcus, Paula Coelho and Laura.

My sincere thanks to all the people that helped me during my stay in Munich, the ESO staff, students and fellows, and to Dr. Eric Emsellem in particular for accepting me there as a student. I am also thankful to Dr. Ortwin Gerhard and the dynamics group at the MPE for the stimulating meetings.

I acknowledge the funding of this Ph.D. project by FAPESP (processes 2011/21325-0 and 2012/22676-3).

Last but not the least, I would like to thank my family for all support and encouragement in my life choices. Most of all, I am deeply grateful to my dear wife and friend Lilian for supporting me all these years, and to my son Ulisses for illuminating my life.

“Enlightenment is man’s release from his self-incurred tutelage. [...] Sapere aude! [Dare to know!] ‘Have courage to use your own reason!’ – that is the motto of enlightenment.”

Immanuel Kant, “What is Enlightenment?” (1784)

Resumo

Galáxias são os principais blocos de construção do universo, mas ainda estamos aprendendo sobre aspectos fundamentais da sua formação. Em particular, gostaríamos de entender como as galáxias adquirem suas estrelas, e onde e quando essas estrelas nasceram. Nesta tese, investigamos estas questões pelo estudo da dinâmica e das abundâncias químicas de galáxias no universo local. Estendendo trabalhos anteriores na área, desenvolvemos um método Bayesiano para a obtenção de idades, metalicidades e abundância de elementos alfa ponderados pela luminosidade. Em nosso estudo inicial, pesquisamos seis grupos de galáxias para compreender como esse ambiente em particular pode estar relacionado às transformações morfológicas. Obtivemos uma amostra de 59 membros de grupos com uma vasta gama de massas dinâmicas, que foram utilizados para demonstrar que a relação massa-metalicidade se estende para galáxias de baixa massa. Então, procedemos ao estudo de NGC 3311, uma galáxia cD no centro do aglomerado Hydra I. Confirmamos as observações anteriores do perfil de dispersão das velocidades do sistema, que indicam a presença de uma grande subestrutura fotométrica que ilustra a acreção atual de estrelas no halo estelar difuso. Foi realizado um estudo das populações estelares do sistema, que indica que as estrelas no halo estelar difuso foram obtidas em eventos passados de fusão de grandes galáxias elípticas, enquanto que a região central da galáxia é provavelmente o remanescente de um rápido colapso dissipativo. Além disso, a metalicidade das estrelas na subestrutura fotométrica sugere a ruptura atual de galáxias anãs relacionadas com a presença de um grupo se movimentando em direção ao centro do aglomerado. Estes resultados são consistentes com o modelo de duas fases para a acumulação da massa de galáxias, no qual galáxias elípticas gigantes são formadas por processos dissipativos em altos redshifts, mas continuam a acrescentar estrelas em seus halos pelo deposição de sistemas satélite.

Abstract

Galaxies are the major building blocks of the universe, but we are still learning about fundamental aspects of their formation. In particular, we would like to understand how galaxies acquire their stars, and where and when these stars were born. In this thesis, we investigate these questions by the study of the dynamical and chemical abundances of galaxies in the local universe. Extending previous works in the field, we have developed a Bayesian framework to obtain luminosity-weighted ages, metallicities and alpha-element abundances. In our initial study, we have surveyed six galaxy groups to understand how this particular environment may be related to morphological transformations. We have obtained a sample of 59 group members with a wide range of dynamical masses, which have been used to demonstrate that the mass-metallicity relation extends to low-mass galaxies. We then proceeded to the study of NGC 3311, a cD galaxy at the center of the Hydra I cluster. We have confirmed previous observations of the velocity dispersion profile of the system, which indicates the presence of a large photometric substructure which illustrates the ongoing accretion of the diffuse stellar halo. We performed a study of the stellar populations of the system, which indicated that stars in the diffuse stellar halo have been accreted from past merger events of large elliptical galaxies, whereas the central region of the galaxy is most probably the remnant of a rapid dissipative collapse. Moreover, the metallicity of the stars in the photometric substructure suggest an ongoing disruption of dwarf galaxies possibly related to the presence of an infalling group. These results are consistent with the two-phase model for the mass assembly of galaxies, in which massive ellipticals are formed by dissipative processes at high-redshifts, but continue to build-up their halos by the continuous accretion of satellite systems.

Contents

1. <i>Introduction</i>	25
1.1 Historical overview	26
1.2 Cosmological background	27
1.3 Galaxy formation and evolution	29
1.3.1 Pre-galactic collapse and star formation	29
1.3.2 Galaxy evolution in a hierarchical universe	30
1.3.3 Physical processes involved in galaxy evolution	31
1.4 Recovering the history of galaxy formation with stellar populations	32
1.5 Outline of this thesis	34
2. <i>Methods</i>	37
2.1 Stellar kinematics	38
2.2 Lick indices	41
2.3 Stellar Populations	45
3. <i>Study of nearby galaxy groups</i>	51
3.1 Introduction	51
3.2 Observations and data reduction	52
3.3 Determination of Hydra-CTIO spectral resolution	56
3.4 Group membership and kinematics	58
3.5 Dynamical analysis	61
3.5.1 Formulae	61
3.5.2 Validation of calculations and results	68

3.6	Lick indices	69
3.7	Stellar Populations	73
4.	<i>Kinematic evidence of substructure in the stellar halo of the Hydra I cluster core</i>	79
4.1	Introduction	79
4.2	Observations and data reduction	82
4.3	Data analysis	84
4.4	Discussion	87
4.4.1	Systemic velocity	87
4.4.2	Velocity dispersion	88
4.4.3	Skewness and kurtosis	91
4.5	Summary and conclusion	92
5.	<i>The Hydra I cluster core. I Stellar populations in the cD galaxy NGC 3311 (article)</i>	99
6.	<i>A MUSE view of NGC 3311</i>	117
6.1	Introduction	117
6.2	Observations and data reduction	118
6.3	Data analysis	120
6.4	Stellar kinematics	122
6.5	Emission line analysis	125
6.6	Lick indices	127
6.7	Stellar populations	129
6.8	Summary and future perspectives	130
7.	<i>Conclusion and perspectives</i>	133
	<i>Bibliography</i>	135
A.	<i>GHASP: an Hα survey of spiral galaxies - X. Surface photometry, decompositions and the Tully-Fisher relation in the R$_c$ band (article)</i>	151

List of Figures

1.1	Large-scale distribution of galaxies observed by the 2MASS survey	29
1.2	Merging-tree of a BCG galaxy in the semi-analytic models of De Lucia and Blaizot (2007)	31
1.3	The morphological box, created by Zwicky (1957) to illustrate the interplay of processes involved in galaxy formation.	32
2.1	Effect of high order moments of the Gauss-Hermite expansion, h_3 and h_4 , in the line-of-sight velocity distribution (LOSVD).	40
2.2	Example of the LOSVD fitting process with PPXF for two galaxies in the sample of galaxy groups.	41
2.3	Validation of the routine PYLECTOR against LECTOR for SSP templates in the MILES stellar library.	43
2.4	Comparison of the ages, $[Z/H]$ and $[\alpha/Fe]$ obtained with models of Thomas et al. (2011) and Vazdekis et al. (2015) using the data from Barbosa et al. (2016)	46
2.5	Example of MCMC modeling for the stellar populations based on Lick indices.	49
3.1	Observational masks of the six galaxy groups.	55
3.2	Wavelength-dependent spectral resolution of the Hydra-CTIO spectrograph.	59
3.3	Comparison of the velocities and velocity dispersion for galaxies with multiple spectra.	61
3.4	Stamp of the member galaxy in the group HCG 22 produced with red band DSS imaging.	62
3.5	Same as Figure 3.4 for galaxies in group HCG 42.	63

3.6	Same as Figure 3.4 for galaxies in group HCG 62.	64
3.7	Same as Figure 3.4 for galaxies in group HCG 90.	65
3.8	Same as Figure 3.4 for galaxies in group NGC 193.	65
3.9	Same as Figure 3.4 for galaxies in group NGC 7619.	66
3.10	Validation of the dynamical properties of galaxy groups using data from ZM98.	69
3.11	Scaling relations between the Lick indices and the central velocity dispersion for galaxies in groups.	71
3.12	Luminosity weighted stellar populations abundances as a function of the velocity dispersion and age.	74
4.1	V-band and X-ray imaging of the central region of the Hydra I cluster core.	82
4.2	Observational strategy for the observation of the stellar halo of NGC 3311.	84
4.3	Positioning of the slits for the study of the stellar halo of NGC 3311	85
4.4	Distribution of the S/N in the spectra of the stellar halo of the Hydra I cluster core observed with FORS2.	86
4.5	Distribution of the systemic velocities of the stellar halo around NGC 3311.	88
4.6	Comparison of the systemic velocities in our work with the literature, in- cluding Ventimiglia et al. (2010) and Richtler et al. (2011).	89
4.7	Same as Figure 4.5 for the velocity dispersion of NGC 3311.	89
4.8	Same as Figure 4.6 for the velocity dispersion of NGC 3311.	90
4.9	Same as Figure 4.5 for the skewness parameter h_3 of NGC 3311.	91
4.10	Same as Figure 4.6 for the kurtosis parameter h_4 of NGC 3311.	91
6.1	Scheme of the strategy for the observations of NGC 3311 at the Hydra I cluster using MUSE.	119
6.2	Binning scheme and resulting S/N distribution of the stellar halo of Hydra I cluster core with MUSE observations.	121
6.3	Example of the fitting process with PPXF for the MUSE observations of the Hydra I cluster core.	121
6.4	Maps for the four moments of the LOSVD: systemic velocity (V), velocity dispersion (σ), skewness (h_3) and kurtosis (h_4).	123

6.5	Comparison of the kinematics of the Hydra I cluster core obtained with MUSE and FORS2 data.	124
6.6	Velocity as a function of the position angle for various radial sections. . . .	125
6.7	Analysis of the velocity field of NGC 3311 using KINEMETRY.	126
6.8	Emission line fluxes corrected for the interstellar extinction using Balmer decrement and reddening curves given by Cardelli et al. (1989)	127
6.9	The BPT diagram for the galaxy NGC 3311 restricted to emission lines with amplitude-to-noise larger than one.	128
6.10	Distribution of the Lick indices in the Hydra I cluster core for the MUSE data set.	129
6.11	Radial profile of the Lick indices in the Hydra I cluster core including the MUSE and FORS2 data sets.	130
6.12	Distribution of the stellar population properties in the Hydra I cluster core for the MUSE data set.	131

List of Tables

3.1	Observational properties of studied galaxy groups obtained in the NED database.	53
3.2	Observational setup used in the study of galaxy groups at the Blanco 4m telescope using the Hydra-CTIO Spectrograph.	54
3.3	Summary of the observations of six galaxy groups with the Blanco 4m telescope.	56
3.4	Dynamical properties for five galaxy groups.	70
3.5	Identification, coordinates and kinematics of galaxies that are members of groups.	75
4.1	Moments of the line-of-sight velocity distribution in the stellar halo of NGC 3311 calculated with PPXF.	93
4.1	continued.	94
4.1	continued.	95
4.1	continued.	96
4.1	continued.	97

List of Acronyms

AGN active galactic nucleus

BCG brightest cluster galaxy

BPT Baldwin-Phillips-Terlevich

CDM cold dark matter

CMB cosmic microwave background

CTIO Cerro Tololo inter-American observatory

DM dark matter

DSS digitalized sky survey

EHB extreme horizontal branch

ESO European southern observatory

ETG early-type galaxy

FORS2 focal reducer/ low dispersion spectrograph 2

FOV field of view

FWHM full width at half maximum

GHASP Gassendi H-alpha survey of spirals

GEV generalized extreme value

HCG Hickson compact group

IDS image dissector scanner

IFS integral field spectrograph

IMF initial mass function

ISM interstellar medium

IRAF image reduction and analysis facility

J-PAS Javalambre physics of the accelerating universe astrophysical survey

KDC kinematically decoupled core

Λ **CDM** Lambda cold dark matter

LOESS locally weighted scatterplot smoothing

LOS line-of-sight

LOSVD line-of-sight velocity distribution

LSF line spread function

LTG late-type galaxy

MCMC Monte Carlo Markov chain

MUSE multi unit spectroscopic explorer

MXU mask exchange unit

NFW Navarro-Frenk-White

NED NASA/IPAC extragalactic database

RMS root mean square

SF star formation

SFR star formation rate

SED spectral energy distribution

S/N signal-to-noise ratio

SF star formation

SFR star formation rate

S-PLUS Southern photometric local universe survey

SPS stellar population synthesis

SSP simple stellar population

SDSS Sloan digital sky survey

TP-AGB thermally pulsing asymptotic giant branch

VLT Very Large Telescope

Chapter 1

Introduction

The vastness of the universe is outlined by the light of countless galaxies. Galaxies, systems gravitationally bound containing billions of stars, have been used to unveil fundamental aspects of nature since the confirmation of their extragalactic nature, indicating that we live in an “island universe” among a myriad of others. This paved the way for the establishment of the current cosmological paradigm, the Lambda cold dark matter (Λ CDM), in which the universe is 14 gigayears old, contains much more dark matter than ordinary matter, and is expanding at an accelerated rate owing to dark energy¹.

The large-scale structure of the universe is well described in the current cosmological paradigm, but many aspects of the study of galaxies themselves are still largely unexplained. Important questions, such as what is the origin of the Hubble sequence, and which are the mechanisms involved in the evolution of galaxies, are difficult to answer not only because of the still undetected dark components of the universe, but largely owing to the still fragmentary understanding of the physics involving the baryonic matter that forms stars and regulates the gas. Moreover, the degree of complexity to describe even the known physics involved in a galaxy, including both micro and macro scales, are impossible to be included in models, either analytical or numerical. As a consequence, the study of galaxies is grounded in the phenomenology, and thus the theory requires systematic observations to advance.

Galaxy formation has been historically driven by observations, as we are still in the stage of trying to detect new features rather than testing precise predictions from the

¹ Throughout this work, we explicitly assume Λ CDM cosmological model. The most prominent alternative, MOND, is reviewed in detail by [Famaey and McGaugh \(2012\)](#).

theoretical models. This is even more accentuated today because the testing of models requires high levels of precision and accuracy even for the most advanced observational setups.

Inserted in this context, the goal of this work is to contribute to the current building-up of the knowledge on galaxy formation through the study of the stellar population of galaxies, both by developing some tools for a robust assessment of stellar population properties of galaxies, and by the application of these methods to understand the assembly of the baryonic mass in galaxies. In the remaining of this chapter, we overview the key concepts involved in this work. In Section 1.1, we perform a brief historical overview of the study of galaxies. In Section 1.2, we describe the cosmological background that sets the framework for the study of galaxies. In Section 1.3, we review the basic concepts involved in the formation and evolution of galaxies. In Section 1.4, we describe the concept of stellar populations, the main tool that we have to adopt to understand the physics of the formation of galaxies. Finally, in Section 1.5, we outline the remaining of this thesis.

1.1 *Historical overview*

Astronomy is among the most ancient sciences, with archaeological evidence indicating its usage ten thousand years ago as a time reckoner (Gaffney et al., 2013). However, the first account of observations of galaxies other than the Milky Way comes from the Persian astronomer Abd al-Rahman al-Sufi, which identified the Large Magellanic Cloud (LMC) and the Andromeda galaxy (M31) in his “Book of Fixed Stars” around 964 AD. Even more recent is the concept of galaxies as distant entities similar to our galaxy, which can be traced back to the early eighteenth century in the works of Emanuel Swedenborg, Thomas Wright, and, more prominently, Immanuel Kant (Gordon, 1969). In his 1755 work, “The Universal Natural History and Theories of the Heavens”, Kant suggested that some of the nebulae patches in the sky are other worlds like the Milky Way, in what is known as the “island universe” model (Paneth, 1941). Other contributions to the modern concept of galaxies have been suggested since Kant by other scientists of importance, such as Johann Heinrich Lambert and Pierre-Simon Laplace, but the question about the extragalactic nature of some nebulae was still speculative until the 1910s.

The change of paradigm came with the first measurement of the radial velocity of the

Andromeda galaxy by Vesto Slipher, in a short bulletin note of the Lowell Observatory (Slipher, 1913). Slipher determined a radial velocity of $V = -300 \text{ km s}^{-1}$ for the Andromeda galaxy, which is much much larger than the velocity of stars known at the time, which ranged from 6 km s^{-1} in B stars to 15 km s^{-1} in K stars and to 27 km s^{-1} in planetary nebulae (Smith, 2008).

These results were embraced as proof that some nebulae were extragalactic for part of the astronomers, such as Ejnar Hertzsprung (Freeman, 2013), and by Slipher's himself (Slipher, 1917). However, the skepticism about the subject remained for more than a decade, as illustrated by the Shapley-Curtis debate about the nature of the nebulae in 1920, in which Harlow Shapley argued that the Milk Way consisted of the whole universe, while Heber Curtis advocated that Andromeda was another island-universe (see Shapley and Curtis, 1921). Curtis was correct about the extragalactic nature of the nebulae, but Shapley was considered victorious at the debate due to wrong observational evidence.

The end of the dispute came with the discovery of the relation between the radial velocity of galaxies (V) and their distance (D) observed by Hubble (1929), given by

$$V = H_0 D, \quad (1.1)$$

where H_0 is the so-called Hubble constant which, in modern cosmology, has the value of $H_0 = 67.8 \pm 0.9 \text{ km/s/Mpc}$ (Planck Collaboration et al., 2015). This relation, applied by Hubble to dozens of galaxies, has shown that the farther a galaxy is from the Milky Way, the higher is its relative systemic velocity. A natural consequence is that, if we assume that our view of the cosmos is not privileged, then the whole universe is expanding. More than changing our perspective of the universe similarly to the Copernican revolution, this discovery paved the way for modern cosmology.

1.2 Cosmological background

Modern cosmology is based on the cosmological principle, in which it is assumed that the universe is homogeneous and isotropic on large scales ($\gtrsim 100 \text{ Mpc}$). Under this assumption, the geodesic element of the universe (ds), i.e., the smaller distance between two points, is given by the Friedmann–Lemaître–Robertson–Walker metric,

$$ds^2 = a(t)^2 dr^2 - c^2 dt^2 \quad (1.2)$$

where dr is the Euclidean three-dimensional distance element, dt is the time interval element, c is the speed of light and $a(t)$ is the scale factor of the universe as a function of the time, which measures the size of the universe and it is parametrized such that $a = 1$ for the universe today ($t = t_0$). Using the cosmological principle and the field equations of general relativity (Einstein, 1916), Friedmann (1922) derived the equations that govern the expansion of the universe. The most accepted model in cosmology currently is the spatially-flat Λ CDM cosmology, developed in the 1980s to explain the large structure of the universe, in which the expansion of the universe is related to its content according to the equation

$$H^2(t) \equiv \left[\frac{\dot{a}(t)}{a(t)} \right]^2 = H_0^2 \left(\frac{\Omega_R}{a^4(t)} + \frac{\Omega_M}{a^3(t)} + \frac{\Omega_k}{a^2(t)} + \Omega_\Lambda \right), \quad (1.3)$$

where $\dot{a}(t)$ denotes the time derivative of the scale factor $a(t)$, Ω_R is the radiation density, Ω_M is the total matter density including both dark and baryonic types, Ω_Λ is the cosmological constant (dark energy), and $\Omega_k = 1 - \Omega_m - \Omega_\Lambda - \Omega_R$ is the spatial curvature density of the universe.

According to the most recent cosmological studies including the cosmic microwave background (CMB), the cosmological constant dominates the current expansion of the universe with $\Omega_\Lambda \approx 0.72$, followed by matter with $\Omega_M \approx 0.28$ in terms of fractional energy density (Hinshaw et al., 2013; Planck Collaboration et al., 2015). In the cosmology described by this model, the universe is ≈ 13.5 billion years old. The cold dark matter (CDM) that accounts for most of the matter ($\approx 85\%$) of the universe was proposed by three different teams (Peebles, 1982; Bond et al., 1982; Blumenthal et al., 1982, 1984) to explain the large-scale structure of the universe. Although the details of the physics of dark matter are still only speculative, the idea is that it consists of elementary particles with masses of $\sim 1\text{keV}$ which do not interact with electromagnetic radiation and whose effects are only gravitational.

The cosmological principle is a good approximation at large scales, but the formation of structures occurs owing to perturbations in much smaller scales formed in the first seconds of the universe. We now turn to the question of how galaxies form and evolve according to the current cosmological paradigm.



Figure 1.1: Large-scale distribution of galaxies observed by the 2MASS survey. The color of the galaxies indicates their distance in relation to the Milky Way, with blue (red) indicating close (distant) objects. Courtesy: 2MASS/T. H. Jarrett, J. Carpenter, & R. Hurt, via Wikimedia Commons.

1.3 Galaxy formation and evolution

1.3.1 Pre-galactic collapse and star formation

The seeds for galaxy formation are small fluctuations observed in the CMB, whose origins are believed to be quantum fluctuations amplified in the period of the inflation of the universe (Guth, 1981; Linde, 1982). The dark matter has no pressure and undergoes gravitational collapse, which eventually leads to the formation of dark matter halos, structures approximately stable and in near-equilibrium supported by their own self-gravity (Benson, 2010), with masses following to the Press-Schechter distribution (Press and Schechter, 1974). The use of N-body simulations (Klypin and Shandarin, 1983; Springel et al., 2005) shows that the evolution of these fluctuations results in a complex network of walls, filaments, and nodes, in agreement with the distribution of galaxies at large-scales observed in all-sky surveys such as the 2MASS (Skrutskie et al., 2006) displayed in Figure 1.1.

After the period of recombination of the universe, the baryons are free to collapse towards the minimum of the potential well of the dark matter halos. The process of cooling kinetic energy of pre-galactic clouds is thermalized by shocks, and the result of the process depends on the timescales of cooling and collapse of the gas. Clouds of masses between 10^{10} - $10^{12} M_{\odot}$ cool efficiently enough to collapse at the free-fall rate (Rees and Ostriker,

1977; Kereš et al., 2005), which is the characteristic stellar mass range of galaxies (Benson, 2010). Further fragmentation lead to star-forming regions with filamentary, fractal-like structure (Scalo, 1990) permeated by supersonic turbulence (Elmegreen and Scalo, 2004; Girichidis et al., 2011). The stars born in this process are distributed in mass according to the initial mass function (IMF), which was firstly empirically determined by Salpeter (1955) as a power law given by the equation

$$\xi(M)dm \propto M^{-\alpha}, \quad (1.4)$$

where M is the mass of the star and $\alpha \approx -2.35$. The origin of the IMF is still unclear, but may be related to the turbulence of the star-forming regions (Padoan and Nordlund, 2002). Other common formulations for the IMF are the broken power law (Kroupa, 2001) and the log-normal model (Chabrier, 2001), which essentially change the contribution of the low-mass stars which are over-abundant in Salpeter's law.

1.3.2 Galaxy evolution in a hierarchical universe

The above picture of pre-galactic collapse and star formation gives a simplified overview of the processes that happen in a single galaxy. However, the growth of structures in the Λ CDM occurs hierarchically, i.e., by the coalescence of the halos dominated by dark matter (Searle and Zinn, 1978; White and Rees, 1978). The complexity of this process is illustrated in Figure 1.2, where the merging tree of a brightest cluster galaxy (BCG) is obtained using N-body simulations combined with semi-analytic models by De Lucia and Blaizot (2007). The evolution of the galaxy spans most of the age of the universe, starting from a large number of major merger events and the accretion of galaxies not originally in the same sub-halo. Most of the mass of the galaxy is already in place around 6 Gyr ago, but the continuous infall of smaller galaxies continues up to date. The color evolution of the galaxies that end up in the BCG indicates that galaxies are globally passive by the time of the accretion. This picture is largely supported by observations, such as the population of compact and clumpy galaxies at high redshift (Moustakas et al., 2004; Daddi et al., 2005) and the mass growth of massive elliptical galaxies by a factor of about four since $z = 2$ (van Dokkum et al., 2010).

A consequence of the hierarchical growth of structures is that galaxies live in regions with varied density. For example, considering massive galaxies such as the Milky Way, most

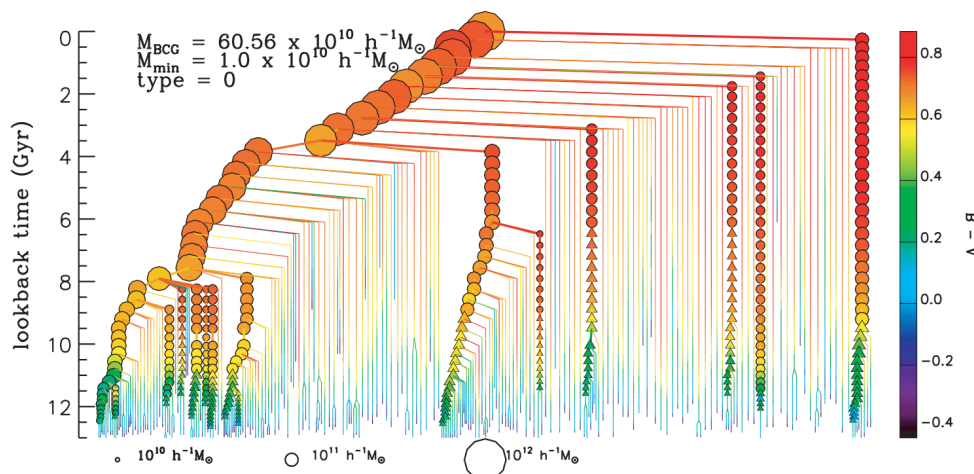


Figure 1.2: Merging-tree of a BCG galaxy in the semi-analytic models of De Lucia and Blaizot (2007). Symbols are colored according to the B-V color of the objects indicated in the right size color bar and the sizes of the symbols indicate the stellar mass of the halo according to the symbols on the bottom. Circles indicate the galaxies that are part of the main branch while triangles indicate galaxies from other branches. Courtesy: MNRAS/ G. de Lucia, reproduced by permission of the author.

systems are found in low-density regions such as the filaments of the cosmic structure, and interact only with a few other galaxies, in the environments of the field and groups. On the other hand, the nodes of the cosmic web contain hundreds of galaxies which interact with each other in completely different physical conditions in the clusters of galaxies.

1.3.3 Physical processes involved in galaxy evolution

The existence of the variety of morphologies in galaxies is explained as the result of a series of physical processes that may shape the morphologies and the star formation (SF) history of galaxies. For instance, spiral galaxies are formed by the collapse of the gas into a disk with conservation of angular momentum, and later interactions of the disk with satellite galaxies may induce the formation of bars (Steinmetz and Navarro, 2002) and spiral arms (Toomre, 1977b). Major mergers of spiral galaxies result in the formation of spheroidal structures such as bulges and elliptical galaxies (Toomre, 1977a). Secular processes in the galaxy induce changes in longer timescales, such as the formation of pseudobulges (Kormendy and Kennicutt, 2004). These and other important processes are shown in Figure 1.3, which displays the “morphological box”, developed by Zwicky (1957) and recently updated by Kormendy and Kennicutt (2004), that indicate these various

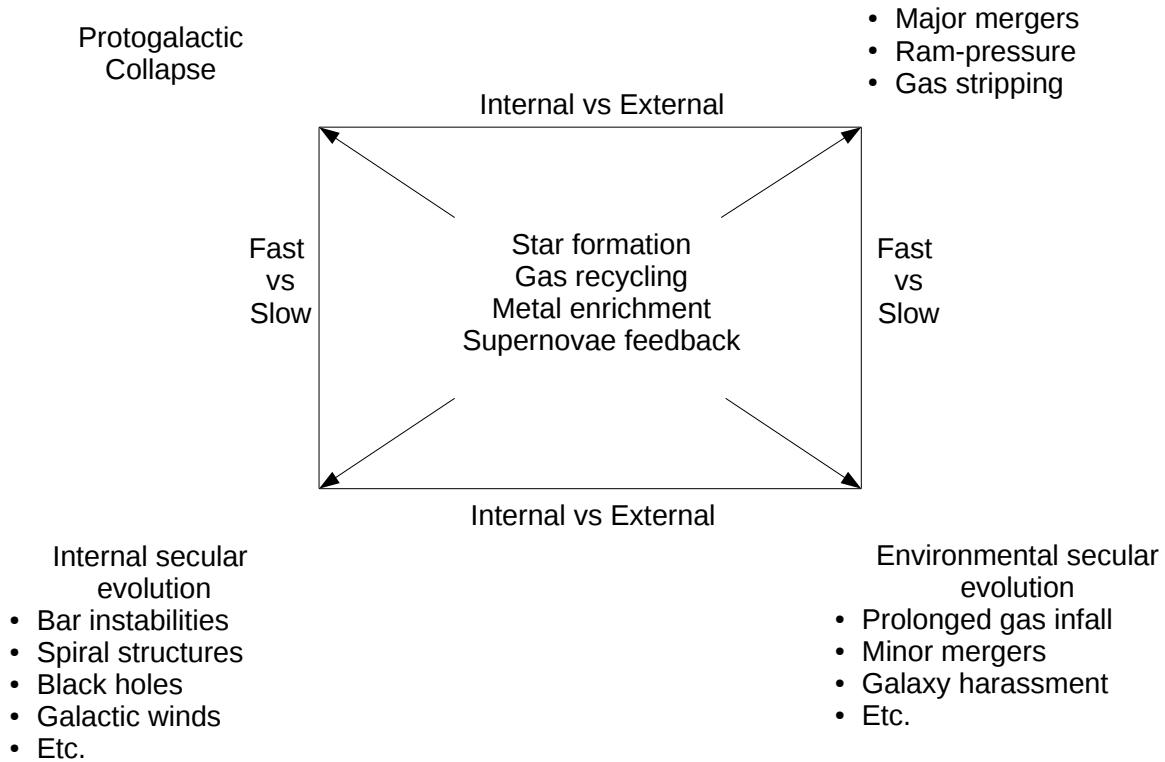


Figure 1.3: The morphological box, created by Zwicky (1957) to illustrate the interplay of processes involved in galaxy formation. On the left side, physical processes that occur internally compete with the processes on the right, which depend on the environment where the galaxy lives. The upper processes occur in short dynamical scales, while the bottom processes occur in timescales much larger than that. The processes inside the central box are involved in all other aspects of galaxy formation.

physical process involved in the evolution of a galaxy.

Although much has been progressed in the last decades, the understand the processes involved in galaxy formation is still far from complete. Current models of galaxy formation have difficulties to reproduce simultaneously all the properties of observed galaxies, mostly because of the unknown physics of the baryonic matter and its related processes, and many aspects of galaxy evolution modeling are based on simple recipes that are tuned to reproduce observations. A powerful tool to advance the understanding of the formation of galaxies is to understand their stellar content, which allows the study of the dynamical properties of the galaxies and contain information about the past events of star formation and chemical enrichment.

1.4 Recovering the history of galaxy formation with stellar populations

The observation of galaxies is only possible owing to the electromagnetic radiation emitted by a population of 10^5 to 10^{12} stars (Binney and Tremaine, 2008) continuously irradiating their energy to the remaining of the universe. The light emitted by most stars keep information about the chemical information of the clouds in which they have formed, and, despite all the dynamical evolution of the galaxies, it is possible to access their history of star formation and chemical enrichment.

With the exception of galaxies in the vicinity of the Milky Way, we are unable to resolve individual stars in a galaxy, and the observations are restricted to the study of ensembles of stars. Baade (1944) have noticed, however, that the color of the stellar light in galaxies varies as a function of the position of the object, indicating that stars are not randomly distributed in the system, but are divided into two stellar populations, ensembles of stars with common properties. In the original formulation by Baade, there are two discrete types of populations: population I, composed of stars such as the Sun, and population II, composed of metal-poor stars.

The concept of stellar populations was generalized by Tinsley (1972) and Searle et al. (1973), who developed the method of stellar population synthesis (SPS), which consists of using all the available knowledge about stellar evolution to produce the spectrum of a simple stellar population (SSP), an ensemble of stars born at the same time and sharing the same chemical abundances. The luminosity of a SSP with age t and metallicity Z is given by

$$L_\nu(t, Z) = \int_M \phi(M)_{t,Z} L_\nu(M, t, Z), \quad (1.5)$$

where $L_\nu(M, t, Z)$ is the spectrum of a star of a given mass, age and element abundance, and $\phi(M)$ is the IMF. The SSPs are the elementary building blocks to describe the spectrum of real galaxies. Equation (1.5) implies a luminosity-weighted sum of the stars, and thus the most massive stars dominate the spectrum in practice. As a consequence, the choice of the IMF has a minor role, because the main differences between different parameterizations usually only differ at low mass stars. According to (Walcher et al., 2011), the most challenging aspect of equation (1.5) are 1) the construction of a stellar library covering the large space parameter necessary for the calculations and 2) the proper

calculation of the stellar evolutionary tracks in the color-magnitude diagram to build the stellar isochrones.

There is a large number of stellar libraries available currently, divided in empirical and theoretical. Empirical stellar libraries, such as the STELIB (Le Borgne et al., 2003) and MILES (Sánchez-Blázquez et al., 2006), are constructed from high-resolution observations of large collections of stars, but which are not able to cover the space parameter, that is, to observe stars with a large variety of effective temperature, gravity, and metallicities. Moreover, observations are restricted to stars in the vicinity of the sun, which are relatively rich in metals. The alternative are theoretical stellar libraries, e.g., Coelho et al. (2005) and Lançon et al. (2007), which are produced with detailed modeling of stellar atmospheres that overcomes the problem of space parameter coverage. However, there are still difficulties in the modeling of all kinds of stars with theoretical models. Therefore, independently of the choice of the models to compute SSP models, there are still many uncertainties that are carried over the process.

The second difficulty in calculating the SSP is the calculation of the isochrones. The main problem here is the determination of the evolutionary path of short-lived but bright stars, such as the thermally pulsing asymptotic giant branch (TP-AGB) stars, extreme horizontal branch (EHB) stars, and blue stragglers. TP-AGB stars are cool evolved stars prominent at low metallicities, whose pulsations are hard to model, but have an important role in the determination of the mass-to-light ratio of galaxies. The origin of EHB stars, evolved core helium-burning stars that dominate the ultraviolet light of old stellar populations, and blue stragglers, stars more luminous and bluer than the main-sequence turn-off of a cluster, have origins still unclear.

Despite these issues, the use of SSP has been advanced considerably in the last decade. One important example is the validation of the models in comparison with observations of a large number of galaxies displayed in Walcher et al. (2011): the comparison of 274613 galaxies observed with Sloan digital sky survey (SDSS) have demonstrated that large deviations between models and observation are small, with reduced χ^2 around 1 ± 0.1 .

1.5 *Outline of this thesis*

The general goal of this thesis is the study of the kinematics and stellar populations of galaxies in the local universe, based on spectroscopic observations, to unveil the physical mechanisms involved in the formation and evolution of galaxies and the role of the environment in morphological transformations. In Chapter 2, we develop the methodology that we have developed to study the spectra of unresolved stellar populations in general, including the extraction of kinematics, the measurement of Lick indices and the modeling of stellar populations. In Chapter 3, we proceed to the study of the dynamics and stellar populations in galaxy groups. The remaining chapters are devoted to our ongoing study of NGC 3311, a cD galaxy in the Hydra I cluster. In Chapter 4, we study the large-scale kinematics of the core of the cluster. In Chapter 5, we reproduce our first article on the study of stellar populations using NGC 3311. In Chapter 6, we present new insights on the kinematics and stellar populations based on our most recent observations with a integral field spectrograph (IFS). Finally, in Chapter 7, we summarize this thesis and discuss our future prospects of research.

Chapter 2

Methods

The hierarchical paradigm implies that galaxies are continuously evolving systems. The morphology of galaxies provide much information about the distribution of the stars and the presence of structures, but it shows only a snapshot of the current state of the system. To gain more insight into the temporal aspects of the process involved in the history of the assembly of galaxies, it is also necessary to comprehend the kinematics of the stars, which provides information about the dynamical aspects of galaxy evolution, and the stellar content, which retains the information of the history of chemical enrichment and star formation episodes. In both cases, this information is encoded in the absorption line features of the optical spectrum of galaxies.

Absorption-line features, such as the 4000 Å break and the Mg band, are the most noticeable patterns in the optical spectrum of galaxies and contain important information about the chemical abundances of the stars in unresolved stellar populations. The Lick-index system ([Faber et al., 1977, 1985](#); [Davies et al., 1987](#); [Gorgas et al., 1990](#)) was developed to quantify the information of these features by comparing the amount of absorption in relation to the surrounding continuum. Initially developed for the characterization of the old stellar populations in early-type galaxies, this approach has been extended to deal also with galaxies with ongoing star formation and late-type galaxies (e.g., [Worthey and Ottaviani, 1997](#)).

We have adopted the use of Lick indices throughout this work, and therefore it is necessary to understand the context in which we have made this decision in face of the increasing popularity of full spectral fitting methods which, ideally, can use all the spectral information instead of selected features. Recent developments in the instrumentation and

methods have allowed a finer detailing of spectral features, and surveys with resolving power $R \gtrsim 2000$, such as the Sloan digital sky survey (SDSS, [Abazajian et al., 2009](#)), allow the investigation of millions of galaxies. However, the internal dynamics of galaxies limit the effective resolving power in elliptical galaxies to $R \lesssim 1000$ ([Buzzoni, 2015](#)), imposing a hard constraint for any method. Furthermore, there are several advantages in the use of Lick indices which have contributed to its success. The first important point is that the absorption features provide a direct and model-independent proxy for the stellar populations. Besides, many recent theoretical models have been working to provide accurate predictions of the Lick indices as a function of the detailed chemical abundances (e.g., [Thomas et al., 2003, 2011](#); [Schiavon, 2007](#)), while stellar libraries with non-solar alpha-element abundances necessary to model elliptical galaxies properly have been released only recently (e.g., [Vazdekis et al., 2015](#)). Also, the use of Lick indices does not require precise flux calibration because the absorption is measured relative to the continuum. Finally, in the few cases where both the use of Lick indices and the full spectral fitting were directly compared, the results are quantitatively similar for the total metallicity ($[Z/H]$) of galaxies and qualitatively similar for ages and alpha-element abundances, in the sense that, despite some offsets, the gradients are similar, even considering completely different models (see [Proctor et al., 2014](#)).

In this chapter, we detail the methodological and technical aspects of extracting kinematics and stellar population properties from spectroscopic observations. In Section [2.1](#), we describe the extraction of the kinematics of stars (and possibly gas) using the PPXF. In Section [2.2](#) we describe the use of Lick indices to obtain information about the absorption line features. Finally, in Section [2.3](#), we describe our approach to the calculation of stellar population properties based on the Lick indices.

2.1 Stellar kinematics

The line-of-sight velocity distribution (LOSVD) contains the information about the kinematics of the galaxies, including the systemic velocity V and the velocity dispersion σ . We have used the penalized pixel-fitting software (PPXF, [Cappellari and Emsellem, 2004](#); [Cappellari, 2012](#)) to calculate a parametric LOSVD for each galaxy spectrum $G(x)$, where $x = \ln \lambda$ is the wavelength (λ) rebinned to a logarithm scale. This program uses a

set of N templates $T_k(x)$, where $k = 1, \dots, N$, to calculate a model given by

$$G_{\text{model}}(x) = \sum_{k=1}^N w_k [\mathcal{L}(V) * T_k(x)] + \sum_{l=0}^L b_l \mathcal{P}_l(x), \quad (2.1)$$

where $w_k \geq 0$ are weights for the templates, $\mathcal{L}(V)$ is a broadening function that describes the LOSVD, the symbol $*$ indicates convolution, and $\mathcal{P}_l(x)$ is a set of Legendre polynomials with arbitrary order L and b_l weights. Additive polynomials have the purpose of matching the continuum of the model with that of the spectrum of the galaxy. The best fit model is determined by a penalized χ^2 minimization which favors solutions with small deviations from a Gaussian profile. Cappellari and Emsellem (2004) adopt a parametrization of the LOSVD as a Gauss-Hermite expansion proposed by van der Marel and Franx (1993) and Gerhard (1993), defined by the equation

$$\mathcal{L}(V) = \frac{e^{-\frac{1}{2}y^2}}{\sigma\sqrt{2\pi}} \left[1 + \sum_{m=3}^M h_m H_m(y) \right], \quad (2.2)$$

where $y = (V - \langle V \rangle)/\sigma$, h_m are the high order moments of the distribution and H_m are Gauss-Hermite polynomials of order m . In practice, the first two terms of the expansion (h_3 and h_4) are of interest for dynamical modeling of galaxies and can be properly constrained for intermediate signal-to-noise ratio (S/N) of ~ 30 , and thus it is customary to truncate the above expansion at $M = 4$. The parameter h_3 measures the skewness of the distribution, which indicates the asymmetry of the LOSVD, while the parameter h_4 measures the kurtosis of the distribution, which indicates how much the LOSVD deviates from a Gaussian distribution and indicates the degree of radial or tangential anisotropy (Gerhard, 1993). In Figure 2.1 we illustrate the effects of the use of high order moments, h_3 and h_4 , departing from a normalized Gaussian profile in the center of the image.

Equation (2.1) illustrate the basic premise of PPXF, which is to model a spectrum as a linear combination of templates, but the implementation of the program includes a number of other features, such as the use of multiplicative polynomials, inclusion of an arbitrary number of kinematic components and sky subtraction among others. Uncertainties calculated by PPXF are based on the deviations from the minimum χ^2 , resulting in precise errors given that the noise level of the input spectrum is realistic, as checked by Monte Carlo simulations. In Figure 2.2, we show the fitting of two galaxies to illustrate typical results of the fitting (more details in Chapter 3). In both cases, we use simple

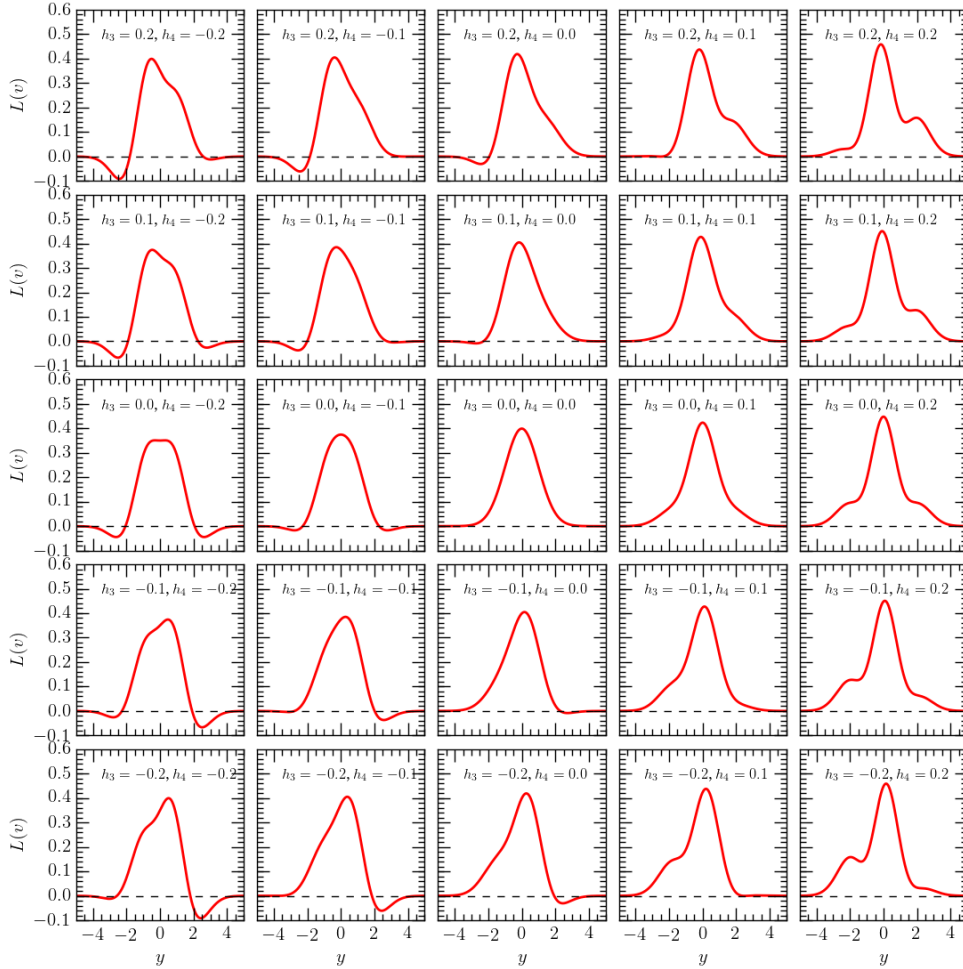


Figure 2.1: Effect of high order moments of the Gauss-Hermite expansion, h_3 and h_4 , in the LOSVD. The profiles are obtained using equation (2.2) as a function of the parameter y , which ensures that the profile is centered at zero, and that the x-axis is scaled in units of standard deviations. The x-axis (y-axis) indicates departures in the h_4 (h_3) between -0.2 and 0.2 . The central panel displays a Gaussian function ($h_3 = 0$ and $h_4 = 0$).

stellar population (SSP) templates with additive polynomials to perform the calculations, one with a single kinematic component and another with two kinematic components (stars plus gas).

The program PPXF is very general, and we have adopted it throughout our work. To handle the output of the program, we have written a custom Python class, i.e., an extensible program that creates an object, which is able not only for the extraction of the kinematics of the spectra, but also to other tasks in the data analysis, such as the decomposition of the spectrum into components based on the weights of the fit and the creation of unbroadened best fit templates, which is used for the decontamination of the

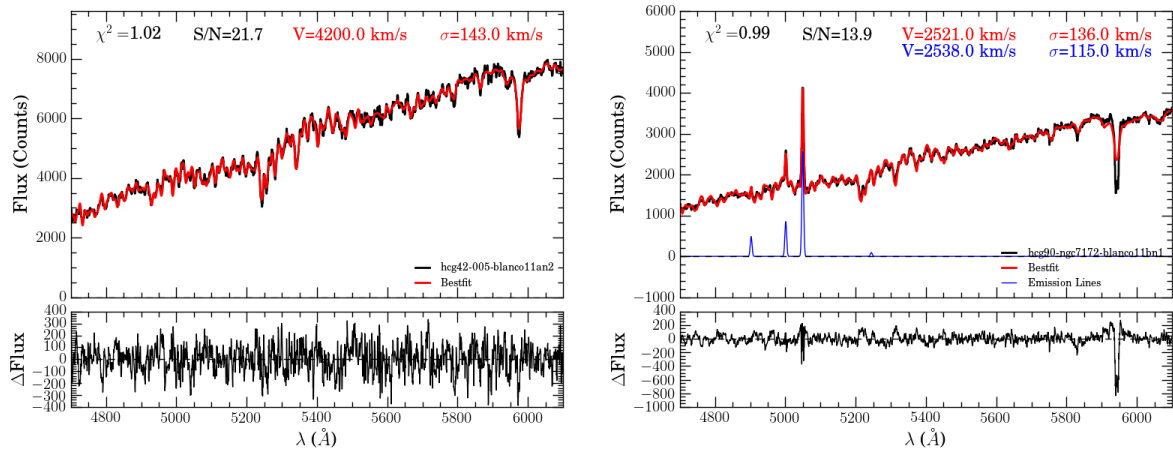


Figure 2.2: Example of the LOSVD fitting process with pPXF for two galaxies in the sample of galaxy groups. HCG42_004 (left) and HCG90_NGC7172 (right) show fittings including one and two kinematic components respectively. In the upper panels, the black red lines indicate the observed spectra, the red the best fit results and the blue line indicate the emission lines. Each bottom panel indicates the residual of the fitting.

stellar light from the emission lines. Although the fitting process is usually very similar, we leave the discussion of the details of the fitting procedure to the next chapters, in context with the specific data sets.

2.2 Lick indices

In the optical wavelength range, the stellar content of galaxies is probed by the analysis of absorption features of the integrated spectra. The set of 25 indices defined by the Lick observatory group (Worthey et al., 1994; Worthey and Ottaviani, 1997) and measured with the image dissector scanner (IDS), contains the most prominent absorption features in the range from 4000 to 6000 Å. Each one of the Lick indices is defined by three wavelength intervals, including a central band, where the absorption feature is located, and two side bands, defined at the sides of the central band for the evaluation of the pseudo-continuum level. In a given band, two limiting wavelengths are defined, λ_1 and λ_2 , with a central wavelength given by $\lambda_c = \frac{1}{2}(\lambda_2 - \lambda_1)$. For the side bands, the average pseudo-continuum flux is calculated according to Worthey et al. (1994) as

$$F_{\text{band}} = \int_{\lambda_1}^{\lambda_2} \frac{F(\lambda)}{\lambda_2 - \lambda_1} d\lambda, \quad (2.3)$$

where $F(\lambda)$ is the flux measured as a function of the wavelength. The pseudo-continuum as a function of the wavelength is then defined as

$$F_P(\lambda) = F_{\text{blue}} + \frac{F_{\text{red}} - F_{\text{blue}}}{\lambda_{\text{red}} - \lambda_{\text{blue}}} \times (\lambda - \lambda_c), \quad (2.4)$$

where $\lambda_c = \frac{1}{2}(\lambda_2 - \lambda_1)$ is the average wavelength measured in the central band. The strength of the absorption line is then measured in the central band either as an equivalent width, for atomic features or as magnitudes, for molecular bands. In the first case, the strength of the absorption feature is defined as

$$\text{EW} = \int_{\lambda_1}^{\lambda_2} \left(1 - \frac{F(\lambda)}{F_P(\lambda)} \right) d\lambda, \quad (2.5)$$

while an index measured in magnitudes is given by

$$\text{Mag} = -2.5 \log \left[\left(\frac{1}{\lambda_2 - \lambda_1} \right) \int_{\lambda_1}^{\lambda_2} \frac{F(\lambda)}{F_P(\lambda)} d\lambda \right]. \quad (2.6)$$

There are a few programs dedicated to the calculation of absorption-line strengths, such as INDEXF (Cardiel, 2010), written in C++, and LECTOR (Vazdekis, 2011), written in FORTRAN. However, most of the routines and pipelines used in the analysis of this thesis are written in the programming language Python and, therefore, we have developed a routine for that purpose that is easily integrated to our other programs. Our routine, which we call PYLECTOR, was tested by the comparison of the Lick indices measured on 304 SSP spectra produced with stars in the MILES library (Sánchez-Blázquez et al., 2006). These spectra were built considering stellar populations of a large range of ages (0.1 to 15 Gyr) and metallicities ($-2.27 \leq [Z/H] \leq 0.4$), synthesized with a Salpeter initial mass function (IMF) to test all realistic scenarios.

The indices measured with our program are compared with the indices measured with LECTOR, and the results are shown in Figure 2.3. The result of this validation of PYLECTOR indicates that our program indeed performs the measurements as expected, with deviations that are at least one order of magnitude smaller than any of the typical uncertainties of the Lick indices in the observed spectra.

In practice, the measurement of the Lick indices in observations requires also a calibration process, which consists in 1) a correction for the instrumental differences and 2) the

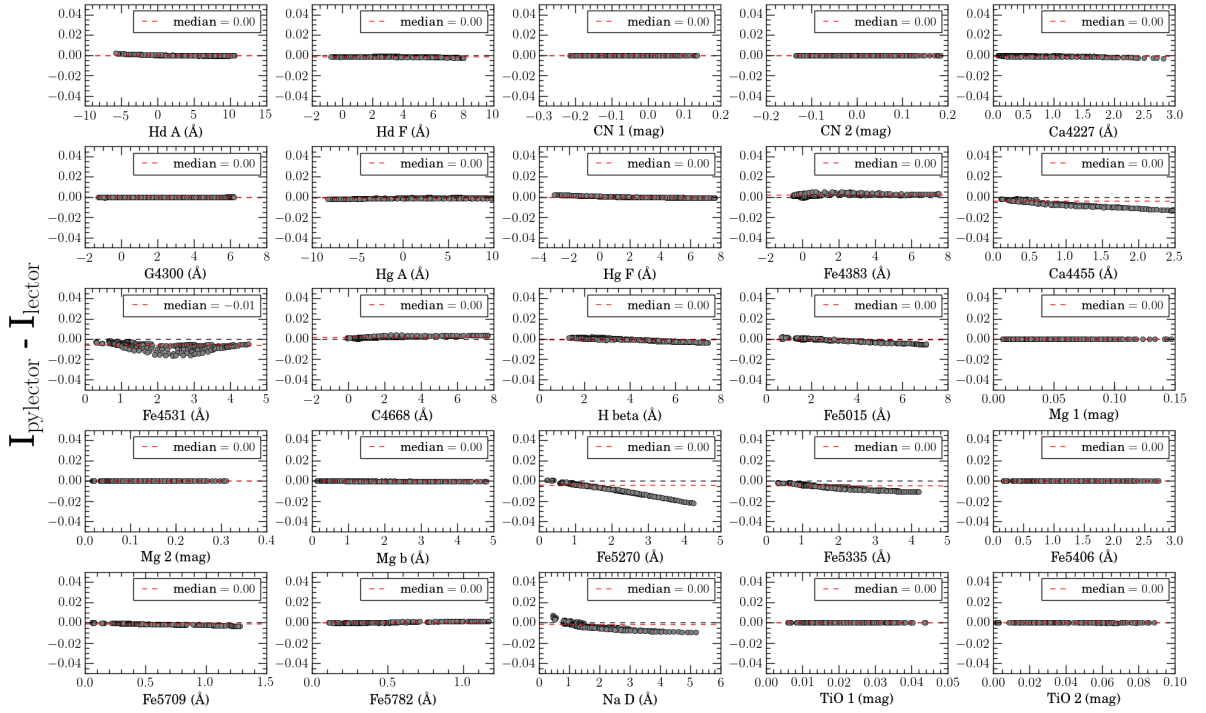


Figure 2.3: Validation of the routine PYLECTOR against LECTOR for 304 SSP templates in the MILES stellar library. The horizontal axis indicate the value of the indices according to the expected value using the LECTOR program while the vertical axis indicate the difference between the two programs. The red dashed line indicates the median differences, which are quoted in the upper right boxes.

correction for the effect of the kinematic broadening which causes a loss in the flux from the central bands of the indices to the surrounding spectra.

The correction for the instrumental difference requires two steps, which are the matching of the spectral resolution and the calculation of offsets. In all data sets used in this work, we have used instruments with better spectral resolution than that of the IDS, which varies as a function of the wavelength but is not lower than 8 Å (Worthey and Ottaviani, 1997). Therefore, the first correction required only the convolution of the data with Gaussian profiles of width given by the difference in resolution. The second part, the calculation of offsets, is usually performed by the comparison of Lick indices observed in standard stars, which are observed in parallel to the observations.

For the correction of the kinematic broadening, we produce a spectrum with the same weights and continuum obtained with pPXF but suppressing the convolution with the LOSVD. The corrected indices are given by the expression

$$I_k = \frac{I'_{k,0}}{I'_{k,\text{LOSVD}}} \cdot I_{k,\text{meas}} \quad \text{for } k = \{\text{H}\delta_{\text{A}}, \dots, \text{TiO}_2\}, \quad (2.7)$$

where I' and I'_{LOSVD} are the indices measured in the unbroadened and broadened best-fit spectra calculated with pPXF respectively, $I_{k,\text{meas}}$ is the actual measurement on the observed galaxy. This method for the correction is very general, automatically considers all the non-Gaussian terms of the LOSVD, and is valid for all kinds of stellar populations. We have validated our method comparing our broadening corrections with Kuntschner (2004), who calculated corrections for non-Gaussian LOSVD, but included only 17 indices and old stellar populations. The comparison indicated good agreement without systematic differences.

The uncertainties in the Lick indices are an important ingredient in the determination of the stellar population properties. Our method for the calculation of uncertainties in Lick indices is based on Monte Carlo simulations, which allows the use of the uncertainties from the kinematics analysis and also considerations from the S/N. The comparison of the uncertainties of our simulations with the analytical values according to the equations derived by Cardiel et al. (1998) indicates that our method incurs in uncertainties $\sim 50\%$ larger, indicating that the uncertainties related to the process of correcting for the broadening have an important contribution to the uncertainties of the Lick indices.

The use of Lick indices is a powerful tool to obtain information about the stellar con-

tent of galaxies, but an inherent difficulty is the interpretation of the indices in physical terms. The sizes of the pass bands of the Lick indices were designed for large elliptical galaxies with significant line broadening owing to the LOSVD, but a consequence of this choice is that all indices are agglomeration of a large number of absorption lines of different chemical elements and, as a consequence, each index is sensitive to various chemical elements (Tripicco and Bell, 1995). Also, it is important to notice that the names of the indices are not necessarily related to the abundance of the species, e.g., the index Fe5782, in fact, measures the chromium abundance, while the index Na D is indeed very sensitive to sodium (Korn et al., 2005). In order to interpret the results of the observations in physical terms, we recur to the modeling of the observations, as discussed in the next section.

2.3 Stellar Populations

Efforts to model Lick indices have started with Tripicco and Bell (1995), who have indicated that the line strengths depend on the total metallicity, $[Z/H]$, but also on the elemental abundances. However, the stellar library of Worthey (1994), used for the computation of metallicities by Tripicco and Bell (1995), included few galaxies with super-solar abundances, which resulted in problems for the modeling of elliptical galaxies. The most noticeable problem was the strong Mg features observed in early-type galaxies, which present stronger indices than those predicted by SSP models at any given $[Fe/H]$. Maraston et al. (2003) have shown that the solution for the problem requires the use of SSP models including alpha-element abundances, $[\alpha/Fe]$.

Proctor and Sansom (2002) have extended previous models with solar abundances (e.g., Worthey, 1994; Vazdekis, 1999) with the sensitivity of the Lick indices from Tripicco and Bell (1995) to obtain accurate estimates of ages, metallicities and alpha-element abundances for a variety of early-type galaxies. Starting with Thomas et al. (2003), the use of $[\alpha/Fe]$ has been incorporated to theoretical models, including Sánchez-Blázquez et al. (2006), Schiavon (2007), Vazdekis et al. (2010, 2015) and Prugniel and Koleva (2012). Most have benefited from improved observations, new sensibility determinations (Korn et al., 2005) and are based on stellar libraries covering larger ranges of parameters, such as the MILES library (Sánchez-Blázquez et al., 2006). However, the impact of the choice of the model in stellar populations of different ages and abundances is not yet understood in

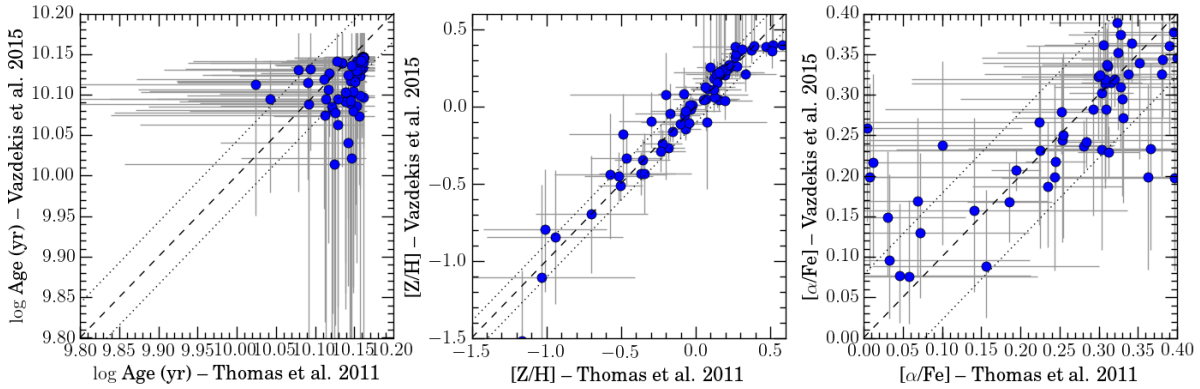


Figure 2.4: Comparison of the ages, $[Z/H]$ and $[\alpha/Fe]$ obtained with models of [Thomas et al. \(2011\)](#) and [Vazdekis et al. \(2015\)](#) using the data from [Barbosa et al. \(2016\)](#).

all situations. As mentioned in the introductory text, [Proctor et al. \(2014\)](#) indicate that there is a good agreement in metallicities and in the gradients of ages and alpha-element abundances in the brightest cluster galaxy (BCG)s of fossil groups. We have tested the effect of the choice of models in our work on the stellar populations of the Hydra I cluster core (Chapter 5) by comparing models of [Thomas et al. \(2011\)](#) and [Vazdekis et al. \(2015\)](#), as illustrated in Figure 2.4. The root mean square (RMS) deviation between the parameters from different models in the same data set is of 0.04, 0.10 and 0.08 dex for the ages, $[Z/H]$ and $[\alpha/Fe]$ respectively, which are smaller than the errors in the determination of individual parameters in our data. Given that data the models of [Thomas et al. \(2011\)](#) cover the largest space parameter, we adopt it throughout this work.

A general method for obtaining stellar population parameters, introduced by [Proctor et al. \(2004\)](#), is the use of a χ^2 minimization using a subset of the N indices, i.e., by the search of a model which minimizes the quantity

$$\chi^2 = \sum_{i=1}^N \left(\frac{I_i - I_{i,\text{model}}(t, [Z/H], [\alpha/Fe])}{\sigma_{I_i}} \right)^2, \quad (2.8)$$

where t is the age of the stellar population, I_k are the observed indices, $I_{i,\text{model}}(t, [Z/H], [\alpha/Fe])$ is a function that predicts the Lick indices of the models considering a SSP, and σ_{I_i} are the uncertainties in the measurements. [Proctor et al. \(2004\)](#) have also shown that a number of indices are improperly modeled for different reasons. The index NaD is severely affected by interstellar absorption. The indices CN₁, CN₂ and Ca4227 are sensitive to the nitrogen abundance, which is not directly treated in any of the models. Finally, the indices Fe5015, TiO₁ and TiO₂ are inconsistently determined in different studies of globular clusters ([Puzia](#)

et al., 2002; Cohen et al., 1998), and thus are not reliable for modeling. Despite these seven indices, however, the modeling of all the remaining indices provided a robust estimation of stellar population parameters.

As we have mentioned, the Lick indices are agglomerations of several absorption lines, which is a problem for the interpretation of their physical meaning. However, the introduction of models with variable element abundances allows the use of Lick indices for more detailed chemical studies, because all indices respond to changes in ages, $[Z/H]$, and $[\alpha/Fe]$ at some level. Based on the results from Proctor et al. (2004), we have introduced the idea of modeling Lick indices using a Bayesian inference (Barbosa et al., 2016, see Chapter 5). Bayesian inference consists of fitting a probability model to a set of data such that the results are given as probability distributions of the parameters (Gelman et al., 2003). The main motivation for the adoption of this method is that it is flexible, and it allows the fitting of a large number of parameters for complex and layered models. In our case, the goal is to obtain probability distributions for the parameters $\theta = (t, [Z/H], [\alpha/Fe])$ given a subset of n Lick indices $D = (I_1, \dots, I_n)$. The calculation of these probability distributions is based on the Bayes' theorem, given by the equation

$$p(\theta|D) = \frac{p(\theta)p(D|\theta)}{p(D)}, \quad (2.9)$$

where $p(X)$ indicates the probability distribution of a random variable X , and $p(X|Y)$ indicates the conditional probability distribution of a random variable X given that Y is known. In the above equation, the probabilities are interpreted as follows:

- $p(\theta)$ is the prior probability distribution, that is, the initial belief in the data D .
- $p(\theta|D)$ represents the joint posterior distribution, which is the belief in the parameters θ when accounted for the data D .
- $p(D|\theta)$ is the likelihood distribution, which informs the support that the fixed data D provides for the model with parameters θ .
- $p(D)$ is the marginal likelihood, which works as a normalization because it does not depend on the parameters θ .

The inference of the parameters calculated with the Bayes' theorem is obtained by the marginalization of the joint probability distribution, which consists in integrating the prob-

ability distribution over all parameters except the one which we want to infer properties of. For instance, given a set of parameters $\theta = (\theta_1, \dots, \theta_n)$ for which we want to estimate the probability distribution of θ_k , the marginalized distribution is given by

$$p(\theta_k|D) = \int p(\theta|D)d\theta_1d\theta_2\dots d\theta_{k-1}d\theta_{k+1}\dots d\theta_n. \quad (2.10)$$

In most cases, it is not possible to calculate the posterior distribution analytically, especially due to the difficulties for the calculation of $p(D)$. However, it is possible to estimate the posterior distribution using a Monte Carlo Markov chain (MCMC) process, that is, by simulating a random process that undergoes transitions in the state space whose stationary distribution approaches to the posterior distribution in the limit of infinite simulations. The Metropolis-Hastings algorithm (Metropolis et al., 1953; Hastings, 1970) is suitable for this purpose because it only requires a function that is proportional to the posterior distribution, dropping the need for calculating the normalization.

To perform our calculations, we have used the package PYMC (Patil et al., 2010) assuming uniform priors within the ranges given by the models of Thomas et al. (2011), i.e., $0.1 \leq t(\text{Gyr}) \leq 15$, $-2.25 \leq [\text{Z}/\text{H}] \leq 0.9$ and $-0.3 \leq [\alpha/\text{Fe}] \leq 0.5$, and considering that the likelihood is described by $p(D|\theta) \propto \exp(-\chi^2)$. This particular modeling results in a posterior likelihood given by a χ^2 distribution and, thus, it is equivalent to the method used by Proctor and Sansom (2002).

To illustrate the process, Figure 2.5 shows the joint probability sample obtained for the set of Lick indices of a spectrum of NGC 3311. The posterior distribution is three-dimensional in our modeling, but a useful visualization of the joint probability distribution is the verification of the correlation between pairs of parameters, which may indicate if degeneracies, e.g., the age-metallicity degeneracy (Renzini and Buzzoni, 1986; Worthey, 1994), are affecting the posterior distributions. The estimation of the parameters is computed with the marginalized distributions, represented by the histograms in the figure. In cases where posterior distributions are symmetric, such as the case of the use of $[\text{Z}/\text{H}]$ in this example, a simple Gaussian fit is able to provide good estimations. However, the truncations in the prior distributions may result in more complex posterior distributions, such as observed in the age and $[\alpha/\text{Fe}]$. To obtain the representative values and uncertainties, we have adjusted the marginalized distributions using a generalized extreme value (GEV) function, defined as

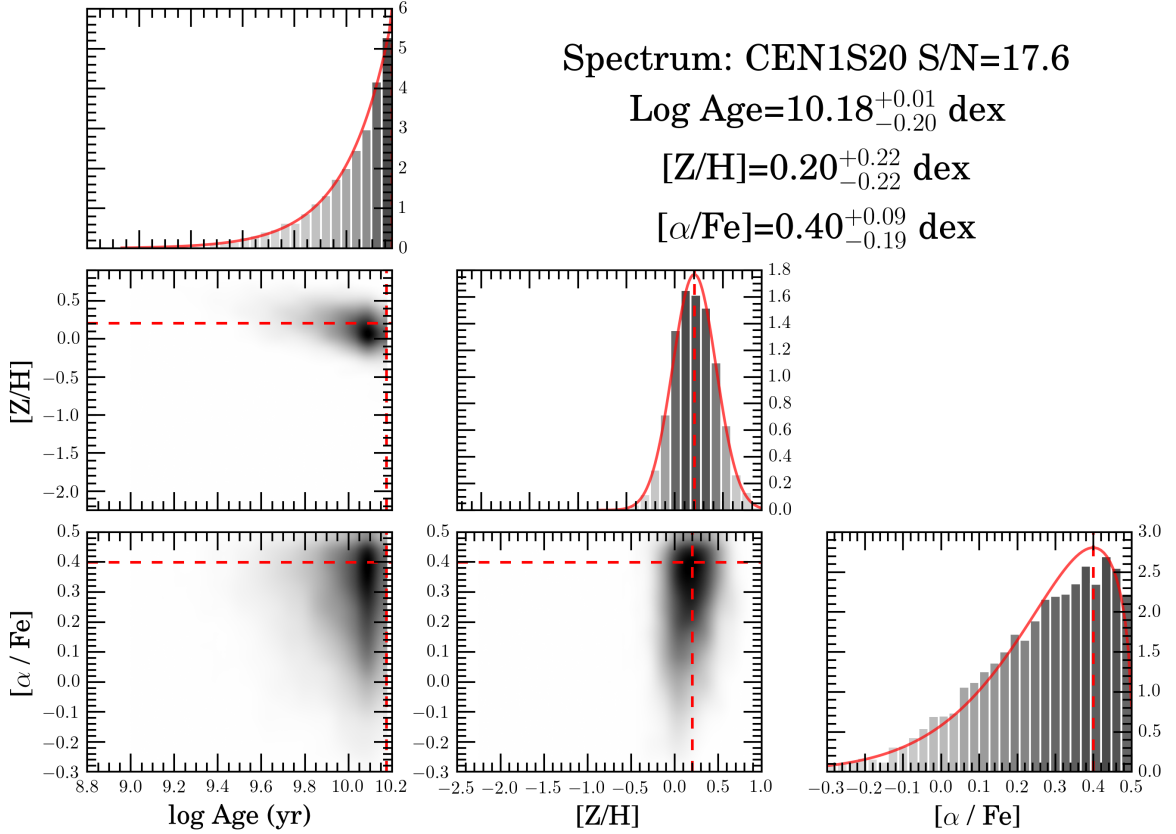


Figure 2.5: Example of MCMC modeling for the stellar populations based on Lick indices. The histograms in the diagonal of the figure indicate the marginalized posterior distributions, which are used for the estimation of parameters, and the red solid lines indicate the best fit obtained with Gaussian or GEV functions. The dashed red line indicates the mean value determined by the fitting. The panels under the diagonal indicate the dependence between pairs of parameters in the posterior distribution. A summary of the fitted model is displayed above the diagonal.

$$\text{GEV}(x|k, \mu, \sigma) = \frac{1}{\sigma} \left[1 + k \left(\frac{x - \mu}{\sigma} \right) \right]^{-(1+1/k)} \exp \left\{ - \left[1 + k \left(\frac{x - \mu}{\sigma} \right) \right]^{-1/k} \right\}, \quad (2.11)$$

where x represents the age, metallicity or alpha-element abundance, and μ , σ and k are the location, scale and shape parameters respectively. To calculate the uncertainties, we have used the highest probability density region containing 68% of the probability, which is the total probability of a normal distribution integrated in the interval $\pm 1\sigma$, where σ is the standard deviation of the distribution.

Although the general results for the stellar population in the context of our modeling are similar to the simple χ^2 minimization, the MCMC method provides much more information about the parameters, because they are described by probability densities.

The marginalization provides uncertainties which contain all the information of the dependencies with other parameters, which is especially important to check if the modeling is able to break the known age-metallicity degeneracy. The example provided in Figure 2.5 indicates that, in this particular modeling, there is some degree of degeneracy between age and metallicity as indicated by the correlation between the two parameters, but the marginal distribution is concentrated into a peaked distribution whose broadening already takes into consideration the degeneracy.

Chapter 3

Study of nearby galaxy groups

3.1 Introduction

The observation of millions of galaxies (e.g. [Blanton et al., 2003](#)) have shown that galaxies are divided into two main categories in the color-magnitude diagram: the red sequence, consisting of early-type galaxies with quiescent star formation, and the blue sequence, composed of late-type galaxies with active star formation. The evolution of the luminosity function since $z \sim 1$ indicates that the stellar mass in blue galaxies is approximately constant over time, while the stellar mass in galaxies in the red sequence has increased by a factor between two and four, indicating that galaxies have their star formation quenched over time ([Bell et al., 2004](#); [Faber et al., 2007](#)). Recent works have shown that the environment of groups and clusters may be responsible for the quenching of galaxies, as opposed to feedback mechanisms such as outflowing galaxy winds driven by AGNs ([Coil et al., 2011](#); [Cooper et al., 2012](#)), but there is still need for a better characterization of the physical properties involved in this process.

The use of galaxy clusters, high density associations containing thousands of galaxies residing in a relatively small volume, has been used to establish that the environments in which galaxies live correlate with galaxy morphologies ([Dressler, 1980](#)): the fraction of red and blue galaxies in galaxy clusters varies as a function of the distance to the center of the system, with early-type galaxies dominating the central regions and late-type galaxies being more numerous in the outskirts. Also, the star formation rates (SFR) in clusters is lower than those from regions of lower densities ([Balogh et al., 1997](#)), indicating that the cluster-specific processes such as galaxy harassment ([Moore et al., 1996](#)), ram-

pressure stripping (Gunn and Gott, 1972) and/or interactions with the cluster gravitational potential (Byrd and Valtonen, 1990) may play an important role in the transformation from the blue to the red sequence. However, most of the morphological transformations happen in environments with different conditions from those found in galaxy clusters we see today (Dressler, 2004), indicating that less dense environments such as galaxy groups may have an important contribution for star formation quenching. Galaxy groups are not only abundant in nature, but also have physical conditions which favor interactions that may either trigger or quench star formation and major mergers that can transform disc galaxies into spheroids (Toomre and Toomre, 1972).

Groups may have an important role in the understanding of the impact of the environment in morphological transformations, but are still rarely studied in detail in the literature, with a few notable exceptions (e.g., de la Rosa et al., 2007; Mendel et al., 2008, 2009). In this chapter, we present the study of kinematics and stellar populations of six nearby loose and compact groups. The initial intention of this data set was the detailed study of each of the six systems in our sample, but incomplete observations and the retirement of the instrument used for the observations determined the changing of the focus to another scientific problem, the study of the Hydra I cluster core, which is presented in the next chapters. Nevertheless, we opt to show the main results we were able to obtain, considering that it is possible to use our sample of galaxies to study scaling relations of the stellar populations, more specifically the mass-metallicity relation which has important consequences in cosmology.

This chapter is structured as follows. In Section 3.2, we present our sample and the data reduction process. In Section 3.3, we detail the process to obtain the instrumental spectral resolution. In section 3.4, we proceed to the extract the information about the kinematics of the galaxies to determine their membership to groups. In Section 3.5, we perform a dynamical analysis of the groups and compare our results with the literature. In Section 3.6, we describe the calculation of the Lick indices and we analyze the scaling relations related to the mass of the galaxies. Finally, in Section 3.7, we calculate ages and abundances using our Bayesian approach and determine scaling relations among stellar population properties. Throughout this chapter, we adopt $H_0 = 67.7$ according to the cosmological parameters given by the Planck Collaboration et al. (2015).

Table 3.1 - Observational properties of studied galaxy groups obtained in the NED database.

Object	RA J2000	DEC J2000	Distance (Mpc)	Velocity (km/s)
(1)	(2)	(3)	(4)	(5)
HCG 22	03h03m31.3s	-15d40m32s	37.5 ± 0.7	2698
HCG 42	10h00m21.8s	-19d38m57s	53.7 ± 1.0	4413
HCG 62	12h53m05.5s	-09d12m01s	61.1 ± 1.3	2638
HCG 90	22h02m05.6s	-31d58m00s	37.9 ± 0.7	3987
NGC 193	00h39m16.4s	+03d17m04s	63.8 ± 1.2	4400
NGC 7619	23h19m42.9s	+08d09m45s	50.9 ± 0.9	3439

3.2 Observations and data reduction

The sample of galaxy groups consists of six systems in the local universe, HCG 22, HCG 42, HCG 62, HCG 90, NGC 193 and NGC 7619, detailed in Table 3.1. Other works in the literature have characterized the systems and obtained their velocity dispersions, but none have done a stellar population analysis. Three of the Hickson compact group (HCG) systems (Hickson, 1982), HCG 42, HCG 62 and HCG 90, are part of the sample studied by Zabludoff and Mulchaey (1998, hereafter ZM98), who characterized the dynamical properties of the poor groups with $L_X \gtrsim 10^{40} h^{-2} \text{ erg s}^{-1}$. HCG 22 was observed with the goal of finding dwarf galaxies and to extend the work of Proctor et al. (2004). Concerning the two loose groups in the sample, NGC 7619 is part of the Garcia (1993) catalog and NGC 193 was observed by Crook et al. (2007).

Observations were carried out at the Blanco 4 m telescope at Cerro Tololo, Chile, using the Hydra-CTIO Optical Spectrograph. This is a multi-object instrument that was mounted at the Cassegrain focus of Blanco to obtain moderate and high resolution spectra ($R < 50000$) using up to 138 fibers with diameters of $300 \mu\text{m}$ ($2''$). The various gratings of the instrument allowed the observation of spectra in the wavelength range $3300 < \lambda(\text{\AA}) < 11000$. An important characteristic of the instrument is that it allowed the survey of several objects simultaneously in a large field of view (FOV), providing a good observational setup for the survey of galaxy groups (see details in Table 3.2), and was available to Brazilian astronomers through the exchange of time with the SOAR telescope. Unfortunately, the commissioning of new facilities at the Blanco telescope forced the retirement of the instrument in 2012, in the middle of our group survey, aborting the

Table 3.2 - Observational setup used in the study of galaxy groups at the Blanco 4m telescope using the Hydra-CTIO Spectrograph.

CCD.....	SiTe $2 \times 4k$
FOV.....	$40'$
Gain Setting.....	2
1 / Gain.....	$0.84 e^- / ADU$
Read Noise.....	$3 e^-$
Grating.....	KPGL3
Lines / mm.....	527
Blaze.....	5500 \AA
Dispersion.....	$0.7 \text{ \AA} / \text{pixel}$
Coverage.....	$\sim 3800 \text{ \AA}$

data collection before the end of the project.

Our observations occurred just before the retirement of the instrument, as detailed in Table 3.3. Each observation required a list of galaxies to be pointed at for the production of an observational mask, with the restriction of enough sky separation to avoid fiber collision. To produce our masks, we have used the SExtractor program (Bertin and Arnouts, 1996) into archival images from the digitalized sky survey (DSS) to produce a catalog of targets. The brightest objects classified as galaxies in the program were selected based on the star-galaxy separation, always including galaxies from previous works in order to maximize the number of members. Figure 3.1 shows all the objects surveyed in our observations. The observations also included a set of standard stars which were used for calibrations of the Lick indices.

The data reduction was carried out using the image reduction and analysis facility (IRAF) system (Tody, 1986, 1993) according to the guidelines from Cigan (2004), summarized in the following. The task CCDPROC was used for the initial preparation of the images, including overscan subtraction, trimming and zero exposure correction. Cosmic rays were detected and cleaned from all images, except arc lamps, with the program L.A. COSMIC (van Dokkum, 2001). The identification and tracing of spectra of the different fibers in the frames was obtained with the tasks APFIND and APEDIT. The dedicated task DOHYDRA was used for the flat field correction, dispersion calibration and spectra extraction of both science and sky targets. Finally, images from the multiple exposures taken in the same night were combined using the task IMCOMBINE. The flux calibration

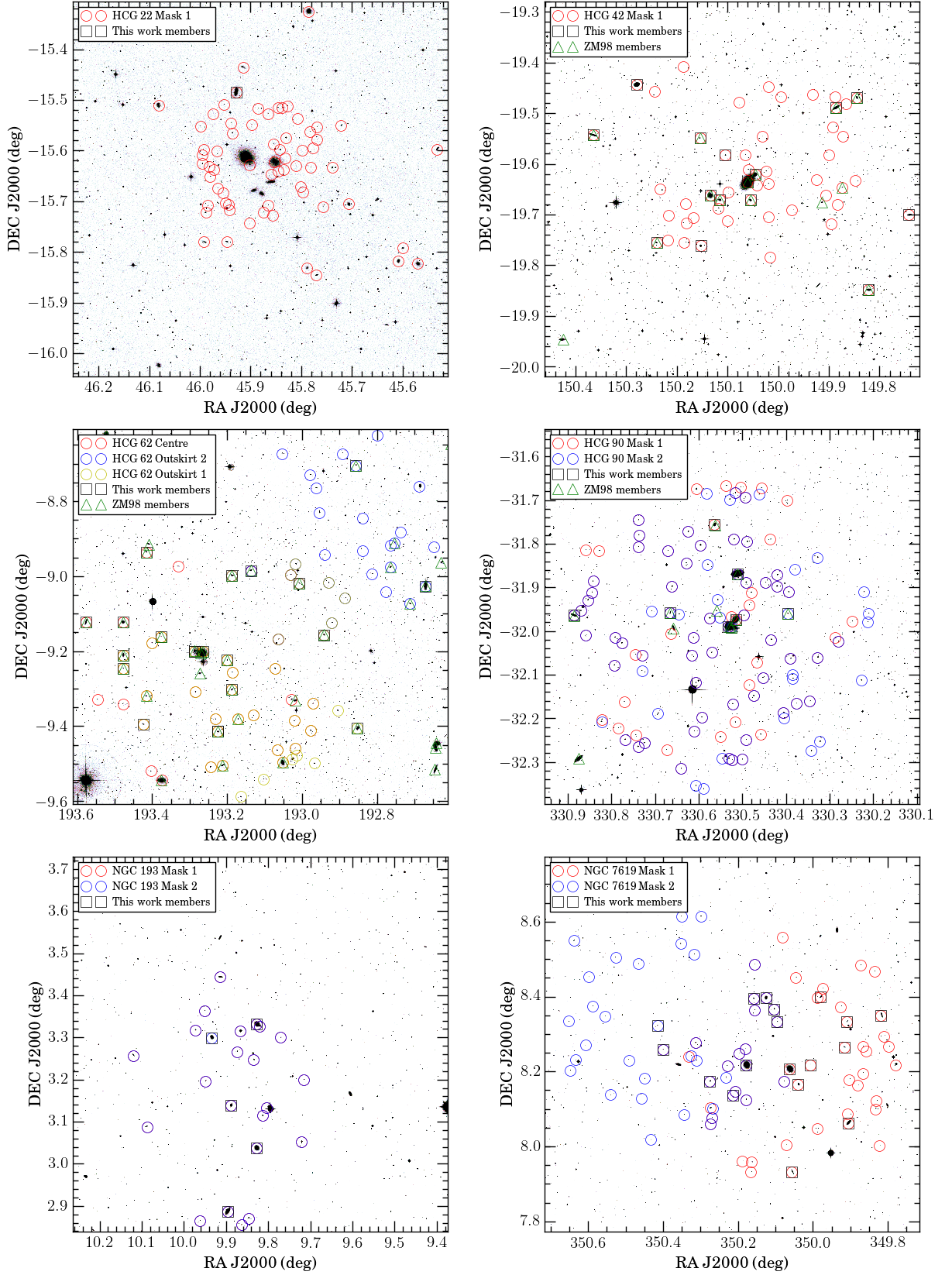


Figure 3.1: Observational masks of the six galaxy groups. The circles represent all the targeted objects, with colors indicating the masks according to the labels in the upper left part of each image. Black squares represent the confirmed members according to our analysis, and green triangles indicate member galaxies confirmed by ZM98.

Table 3.3 - Summary of the observations of six galaxy groups with the Blanco 4m telescope. (1) Number of the observing run. (2) Date of the run. (3) Observed galaxy group. (4) Identification of the observed mask. (5) Number of exposures and individual exposure times.

Run	Date	Group	Mask	Exposures
(1)	(2)	(3)	(4)	(5)
(1)	Mar 22 2010	HCG 62	Centre	8 x 1800s
(2)	Mar 23 2010	HCG 62	Outskirt 1	5 x 1800s
		HCG 62	Outskirt 2	5 x 1800s
(3)	Feb 02 2011	HCG 22	Mask 1	2 x 1500s
		HCG 42	Mask 1	4 x 1800, 1 x 2700s
(4)	Feb 03 2011	HCG 22	Mask 1	2 x 1800s
		HCG 42	Mask 1	3 x 1800, 4 x 2700s
(5)	Sep 01 2011	HCG 90	Mask 1	3 x 1800s
		NGC 7619	Mask 1	7 x 1800s
(6)	Sep 02 2011	NGC 193	Mask 1	3 x 1800s
(7)	Sep 03 2011	NGC 193	Mask 2	2 x 1800s
		HCG 90	Mask 2	4 x 1800s
		NGC 7619	Mask 2	6 x 1800s

of the spectra was not necessary because our analysis is based on the properties of the absorption lines in the spectra in relation to their local continuum. A part of the fibers in each mask is pointed to regions devoid of bright objects for the observation of the sky. However, the sky subtraction is performed only during the analysis of the kinematics of the galaxies, as detailed in Section 3.4.

3.3 Determination of Hydra-CTIO spectral resolution

The spectral resolution ($\Delta\lambda$) of the spectrograph, which describes the ability to resolve features of a spectrum, is an important factor that has to be considered for the proper measurement of the line-of-sight velocity distribution (LOSVD). In practice, the spectral resolution is quantified by the full width at half maximum (FWHM) of the line spread function (LSF), which describes the profile of a point source passing through the instrument in a given observational setup. Because the LOSVD is measured by the convolution of a set of templates to fit the observed spectrum, a difference in the spectral resolution of templates and observations results in systematic errors in the LOSVD moments. In

particular, the velocity dispersion of the galaxies, which is the proxy of the mass of the system, is overestimated in a typical case in which the templates have greater resolving power than the observations.

In the case of the Hydra-CTIO spectrograph, we have determined an initial value of $\Delta\lambda_{\text{Hydra}} \approx 3.6 \text{ \AA}$ with the measurement of the FWHM of emission lines in the arc lamps. However, the results of the kinematics in our data using this spectral resolution had inconsistencies, such as large differences in the velocity dispersion of the same galaxy observed on different nights. Also, the velocity dispersion of the galaxies varied in the same spectrum just by considering different wavelength domains in the fitting process. Therefore, the variation of the spectral resolution of the instrument was affecting the extraction of the kinematics.

To determine the spectral resolution of the instrument, we followed the method used by [Falc3n-Barroso et al. \(2011\)](#) to determine the spectral resolution of the MILES stellar library, which consists in using PPXF to calculate the broadening of stars using a set of templates with known resolution. In [Falc3n-Barroso et al. \(2011\)](#), they have used stars from the [Coelho et al. \(2005\)](#) library, with a fixed resolution of $\Delta\lambda = 1 \text{ \AA}$, to show that the stars in the MILES library has a nearly constant resolution of $\Delta\lambda_{\text{MILES}} = 2.51 \text{ \AA}$. Here, we have used stars from the MILES library to determine the spectral resolution using the Lick standard stars which we have observed for the calibration of the absorption line indices. Assuming that the LSF is approximately described by a Gaussian function for both the instrument and the stellar library, then the difference in the resolution may be calculated by the expression

$$\Delta\lambda_{\text{Hydra}}^2 = \Delta\lambda_*^2 + \Delta\lambda_{\text{MILES}}^2, \quad (3.1)$$

where $\Delta\lambda_*$ is the spectral resolution of Lick standard stars measured with PPXF. To connect the spectral resolution with the velocity dispersion, which is the actual measurement made by PPXF, it is necessary to remind that the resolving power, R , is given by

$$R = \frac{\lambda}{\Delta\lambda}, \quad (3.2)$$

where λ refers to the wavelength. Also, the resolving power can be described in physical terms to the Doppler effect as

$$R = \frac{c}{\Delta v}, \quad (3.3)$$

where c is the speed of light and Δv is the FWHM of the velocity broadening. In a Gaussian profile, $\text{FWHM} \approx 2.634\sigma$, where σ is the standard deviation of the LSF. Combining equations (3.2), (3.1) and (3.3), we obtain a wavelength-dependent spectral resolution for the Hydra-CTIO as

$$\Delta\lambda_{\text{Hydra}}(\lambda) = \sqrt{2.51^2 + \left(\frac{2.634\sigma_*}{c}\right)^2} \lambda^2, \quad (3.4)$$

where σ_* is the velocity dispersion of the stars measured with pPXF. Using the approximation that $\sigma_* \approx 0$, all the velocity dispersion measured with pPXF is due to the differences in the resolution of the instrument in relation to that of the templates.

We have determined σ_* for a set of 15 Lick standard stars, using as templates stars of the MILES library. In 10 cases, the stars are also present in the MILES library, and we have just compared the observations directly. In the other 5 stars, we have produced templates by interpolation of stars in the MILES library considering the effective temperature, surface gravity and iron abundances determined by [Worthey et al. \(1994\)](#) and [Worthey and Ottaviani \(1997\)](#). For each star, we have determined σ_* in intervals of 100 Å in the wavelength range between 4100 and 6900 Å. The results are shown in Figure 3.2, in which we display the velocity dispersion of the stars and the spectral resolution calculated with equation (3.4), both as a function of the wavelength. We have used the median velocity dispersion of the standard stars at each wavelength to calculate a polynomial expansion of order 5 to quantify the spectral resolution numerically as

$$\Delta\lambda_{\text{Hydra}}(\lambda) = \sum_{i=0}^5 w_i \lambda^i, \quad (3.5)$$

where the weights of the polynomial fitting are $w_0 = -270.74$, $w_1 = 0.36115$, $w_2 = 1.7355 \cdot 10^{-4}$, $w_3 = 3.94864 \cdot 10^{-8}$, $w_4 = -4.3297 \cdot 10^{-12}$ and $w_5 = 1.8489 \cdot 10^{-16}$. The result of this analysis indicate that, for the measurement of the kinematic properties, it is necessary to work in the wavelength region $4700 \lesssim \lambda(\text{Å}) \lesssim 6000$ because of the large variations in the spectral resolution out of this section. Moreover, this wavelength-dependent resolution is taken into account in the calculations of the line-strength indices in Section 3.7.

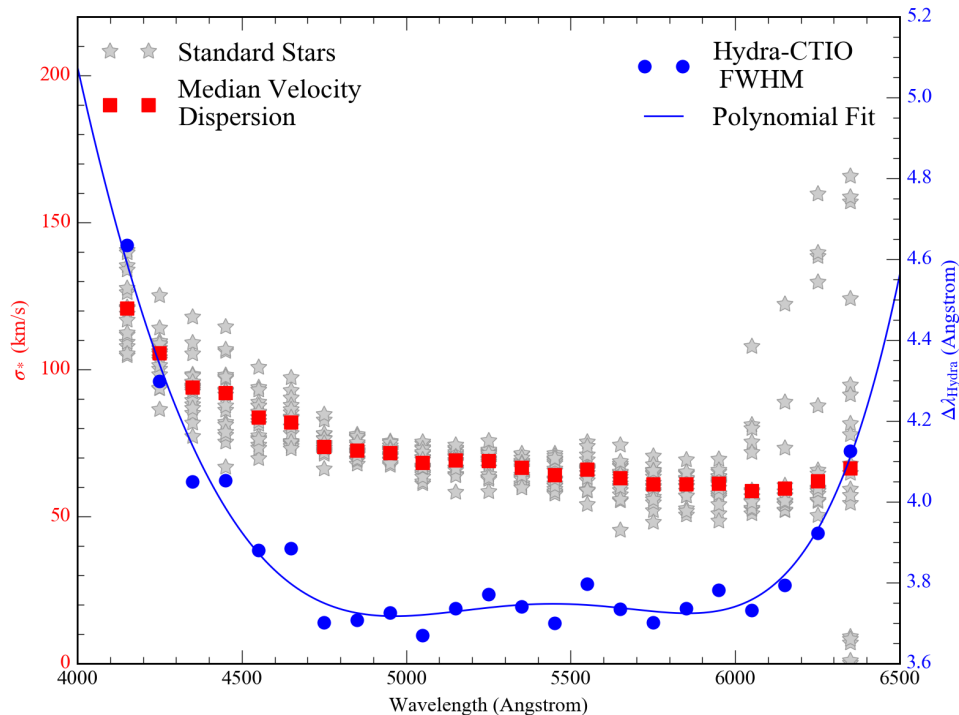


Figure 3.2: Wavelength-dependent spectral resolution of the Hydra-CTIO spectrograph. The left-side label indicates the velocity dispersion of the stars, displayed in gray, and the red squares indicate the median velocity dispersion for all stars. The blue circles indicate the spectral resolution, indicated by the scale in the right-side of the figure, and the polynomial fitting of order 5 is indicated by the solid blue line.

3.4 Group membership and kinematics

In this section, we detail the process to obtain the two most important kinematic properties of galaxies in groups, the systemic velocity and the velocity dispersion. The systemic velocity (V_{group}) of galaxies may be used to determine their membership within a group. For instance, in compact groups, the median velocity dispersion of the galaxies is $\sigma_{\text{group}} \approx 200 \text{ km s}^{-1}$, and galaxies with $|\Delta V| < 1000 \text{ km s}^{-1}$ are physically associated with the system (Hickson et al., 1992). Moreover, the central velocity dispersion of the galaxies (σ_0) indicates the mass of the systems.

To calculate the kinematics properties of all surveyed objects, we have used the PPXF code (Cappellari and Emsellem, 2004; Cappellari, 2012). We have used a set of simple stellar population (SSP) models as the templates for the fitting, created with stars from the MILES library (Sánchez-Blázquez et al., 2006; Falcón-Barroso et al., 2011) considering ages between 0.1 and 14 Gyr, metallicities in the range $-2.32 \leq [Z/H] \leq 0.2$, and assuming

a Salpeter initial mass function (IMF) with a logarithm slope of 1.3. In the cases where the emission line is evident, we have also used a second kinematic component including only templates of emission lines, considering the emission by [O III] ($\lambda = 4958.9, 5006.8\text{\AA}$), H β ($\lambda = 4691.3\text{\AA}$) and [N I] ($\lambda = 5200.25\text{\AA}$), produced with Gaussian profiles, with the additional constraint that $\sigma_{\text{gas}} < 100 \text{ km s}^{-1}$. The resolution of the templates is matched to the resolution of the observations ($\Delta\lambda \approx 3.9 \text{ \AA}$). The wavelength region have to be restricted to the region $4700 \lesssim \lambda(\text{\AA}) \lesssim 6000$ to avoid the varying resolution as discussed in Section 3.3.

We have also used pPXF to perform the sky subtraction of the spectra. Due to the different throughput of the fibers in the Hydra-CTIO spectrograph, the sky subtraction requires a normalization, which should be properly estimated to avoid contamination in the scientific spectra. Weijmans et al. (2009) have shown that using the sky as a special type of template in pPXF produces accurate solutions for the LOSVD even in cases with heavy contamination of the sky emission. To match the continuum of the data and the templates, we have used additive polynomials of order 20.

The results for the kinematics of the stellar components in the galaxies are summarized in Table 3.5. We have included all galaxies with systemic velocities within $|\Delta V| \geq 1000 \text{ km s}^{-1}$ in relation to the systemic velocities of the groups given in Table 3.1. A total of 90 spectra were kept for the remaining of the analysis, containing 59 different galaxies. The number of galaxies observed in each group is shown in the second column of Table 3.4, which only excludes HCG 22 for which a single galaxy have been detected in our survey. The minimum signal-to-noise ratio (S/N) between 4700 and 6000 \AA is 11.3, and 72% of the galaxies have $S/N \leq 15$.

Considering the inconsistencies observed in the kinematics of the same galaxy in different observations and/or wavelength domains, we have tested the compatibility of the systemic velocity and velocity dispersion for the 31 galaxies with multiple spectra. Figure 3.3 shows the results of the comparison, including an error bar in the y-axis that is calculated by the sum of the uncertainties in quadrature. These results show that only four galaxies have discrepancies larger than 2σ in the systemic velocity, and only two have such discrepancies for the velocity dispersion, indicating that the matching of the spectral resolution has resulted in consistent kinematics.

To observe in more detail the morphologies of the member galaxies, we have produced

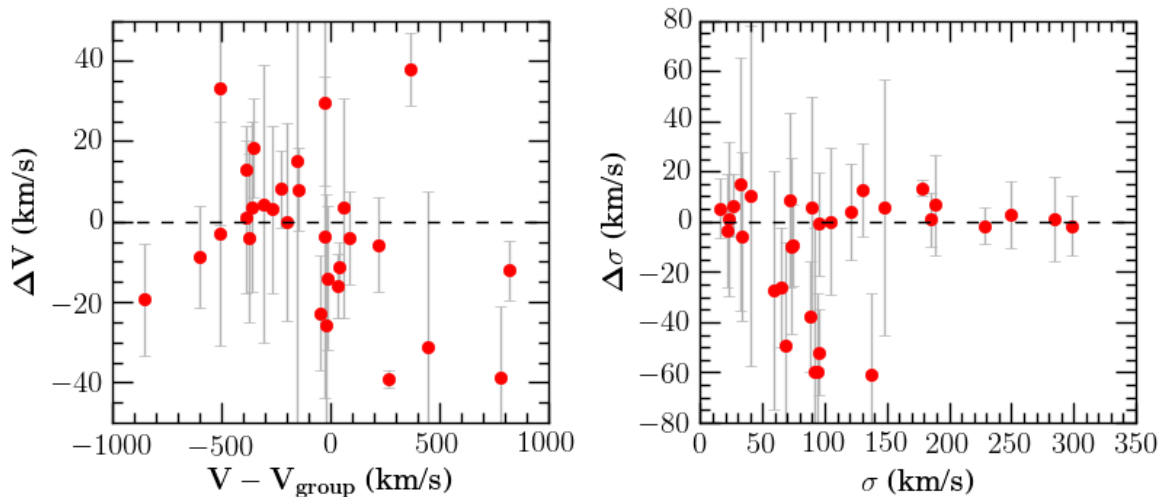


Figure 3.3: Comparison of the velocities and velocity dispersion for galaxies with multiple spectra. The x-axis indicates the velocity of one of the members, while the y-axis indicates the difference of the velocities. The error bars indicate the sum of the errors in quadrature.

stamps of these objects using red band images from the DSS. We have used the DSS2 (ESO, 2013b) program to obtain red band imaging of galaxies with a fixed size of 1 arcmin in order to check also nearby objects around each galaxy. The stamps for each group are presented in Figures 3.4 to 3.9. We observe that our sample include both early-type galaxy (ETG)s and late-type galaxy (LTG)s, and that the fibers are located at the center of these objects. In the following sections, however, we do not distinguish galaxies according to their morphologies, and thus the stellar populations are traced on both the bulges of spirals and on the central regions of elliptical.

3.5 Dynamical analysis

3.5.1 Formulae

The velocity dispersion of the galaxies is a probe of the group mass. Considering a system with N galaxies with velocities $\mathbf{V} = (V_1, V_2, \dots, V_N)$, the velocity dispersion of the group may be calculated with the biweight scale estimator (Beers et al., 1990), given by the equation

$$\sigma_{\text{group}} = N^{1/2} \frac{\left[\sum_{|u_i| < 1} (v_i - V_{\text{group}})^2 (1 - u_i^2)^4 \right]^{1/2}}{\left| \sum_{|u_i| < 1} (1 - u_i^2)(1 - 5u_i^2) \right|}, \quad (3.6)$$

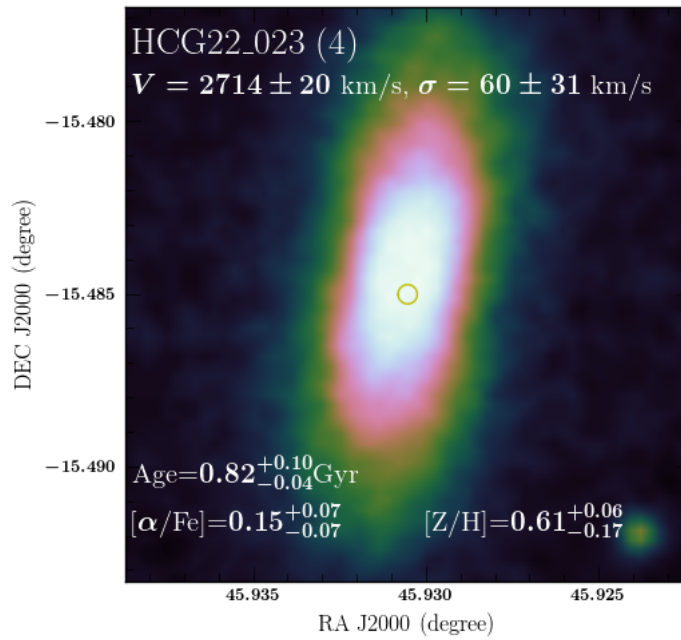


Figure 3.4: Stamp of the member galaxy in the group HCG 22 produced with red band DSS imaging. The yellow circle indicates the fiber position in real scale (diameter of 2”). The most important measured properties, including the systemic velocity, velocity dispersion, age, total metallicity and alpha-element enhancement are also displayed.

where V_{group} is the median velocity of the group galaxies, and the weights u_i are defined as

$$u_i = \frac{V_i - V_{\text{group}}}{c \cdot \text{MAD}}. \quad (3.7)$$

In the above sentence, c is a “turning constant” which defines which galaxies should be excluded from the calculations as outliers, and MAD is the median absolute deviation, defined generally for a vector \mathbf{X} as

$$\text{MAD} = \text{median}(|\mathbf{X}_i - \text{median}(\mathbf{X})|). \quad (3.8)$$

The median absolute deviation is a robust estimator for the variability of a sample, which is more appropriate than the standard deviation (SD) of a normal distribution in cases where outliers are expected. In a normally distributed random variable without outliers, $\text{SD} \approx 1.4826\text{MAD}$. We follow [Beers et al. \(1990\)](#) by adopting $c = 9$, which is approximately the equivalent of excluding galaxies with $|\Delta V| > 6\sigma_{\text{group}}$.

Considering that all galaxies are test particles in a dark matter halo, the projected gravitational radius of a group can be defined according to [Tully \(2015\)](#) as

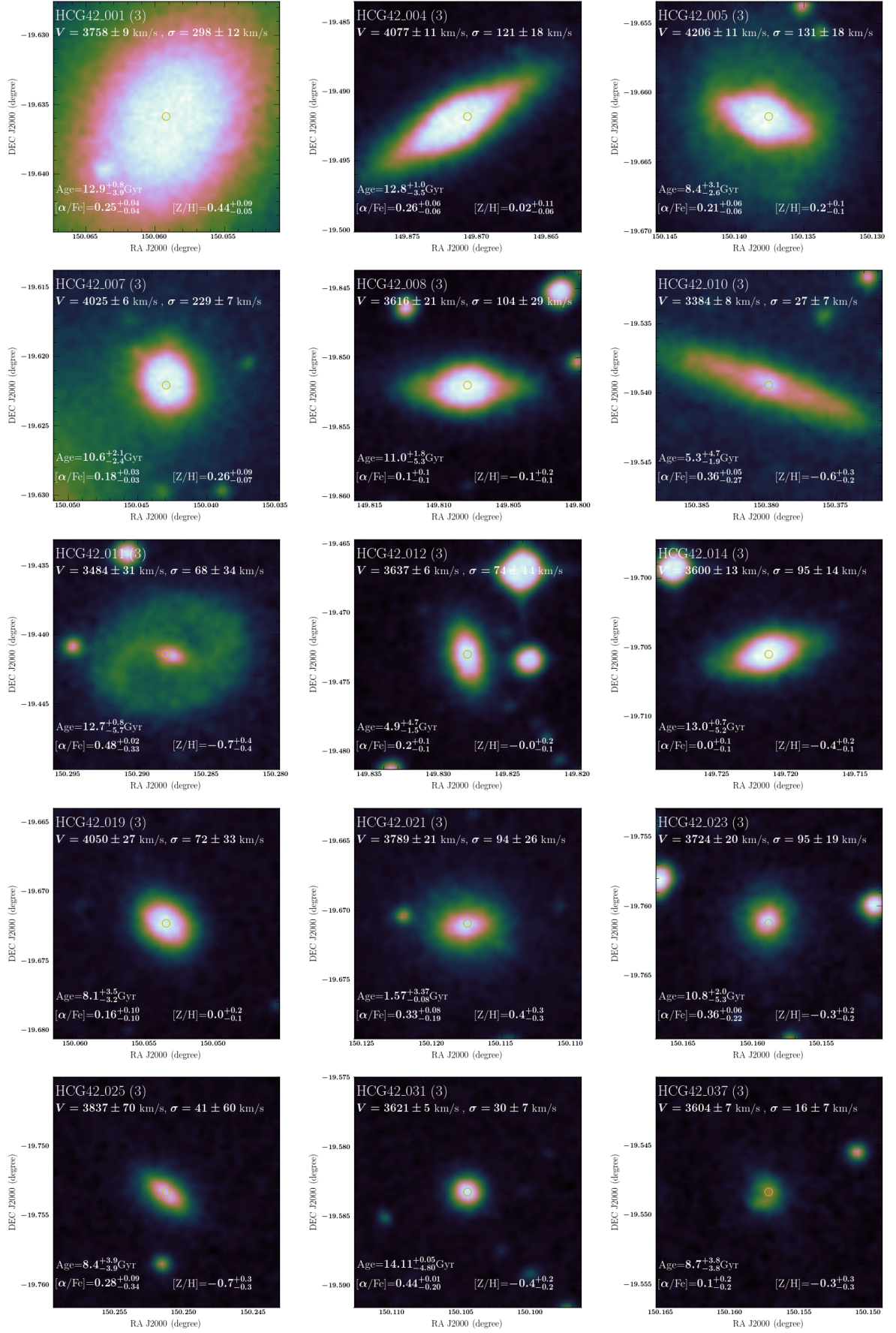


Figure 3.5: Same as Figure 3.4 for galaxies in group HCG 42.

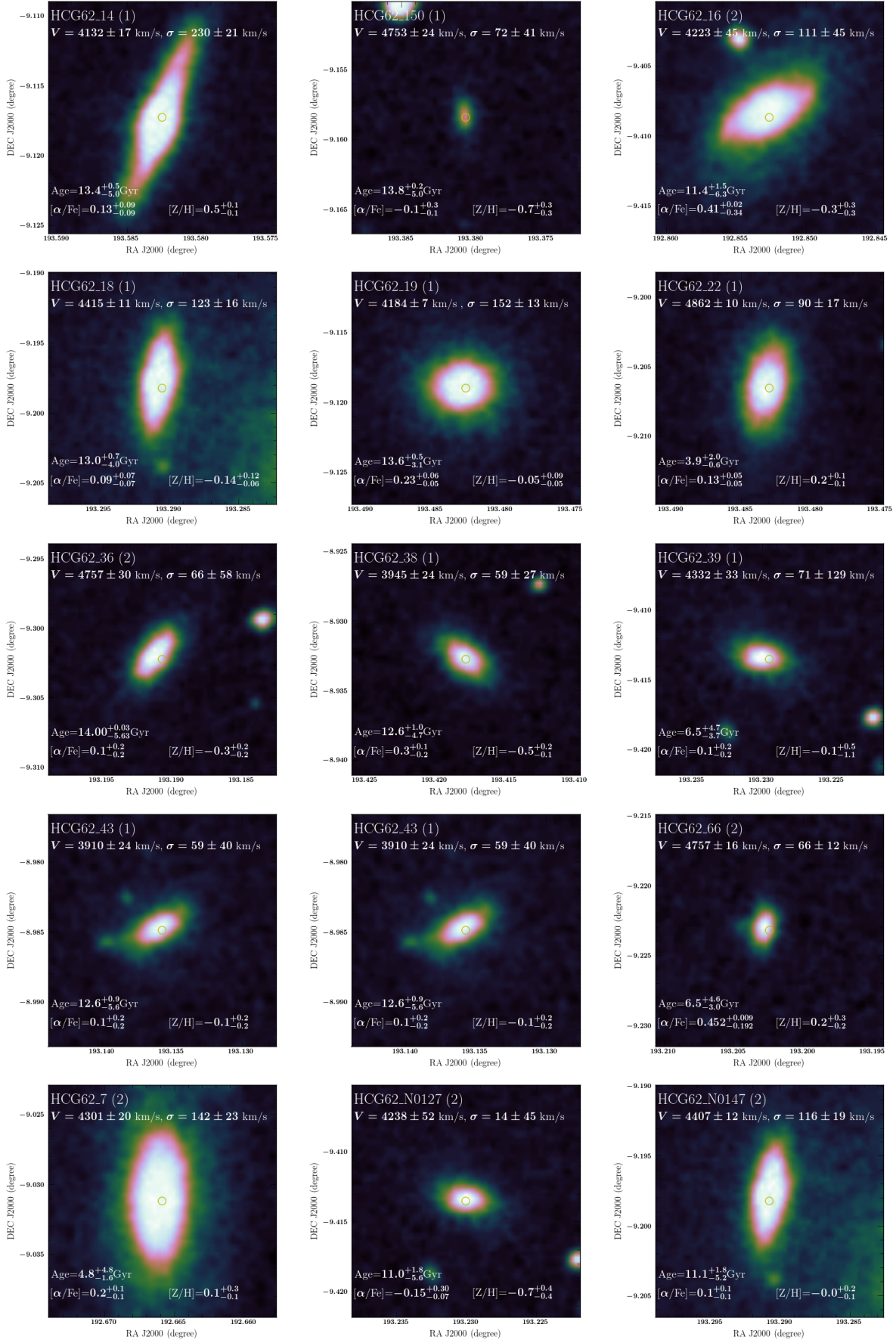


Figure 3.6: Same as Figure 3.4 for galaxies in group HCG 62.

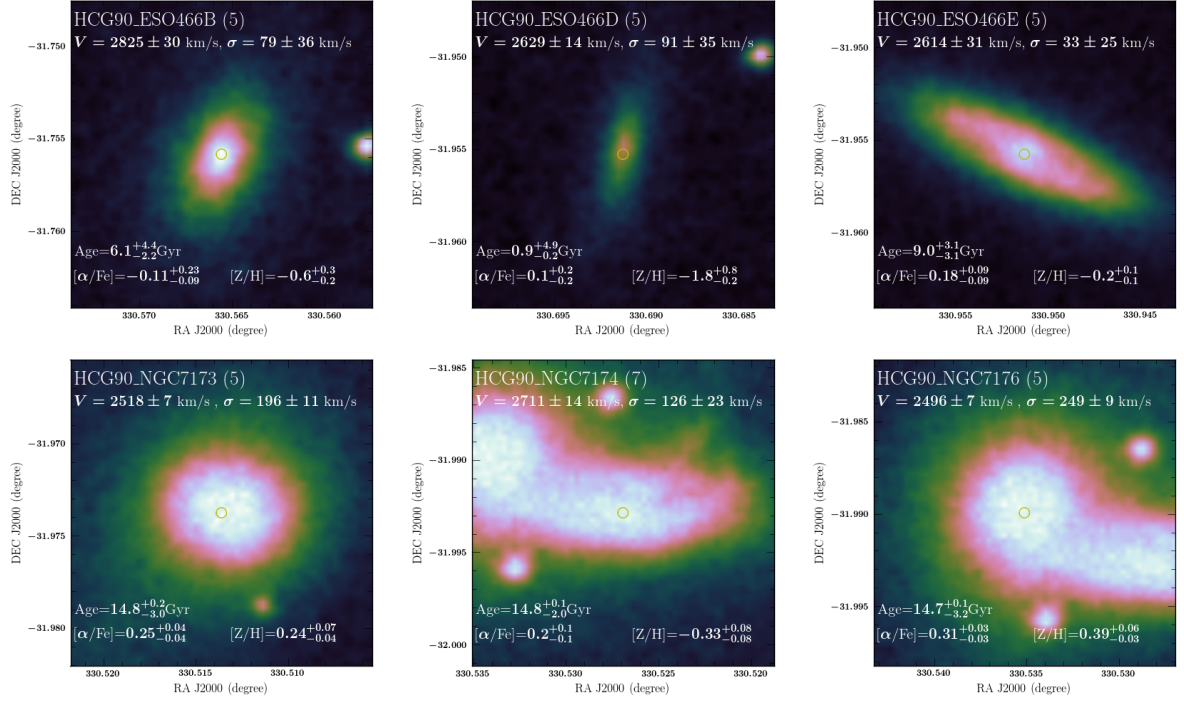


Figure 3.7: Same as Figure 3.4 for galaxies in group HCG 90.

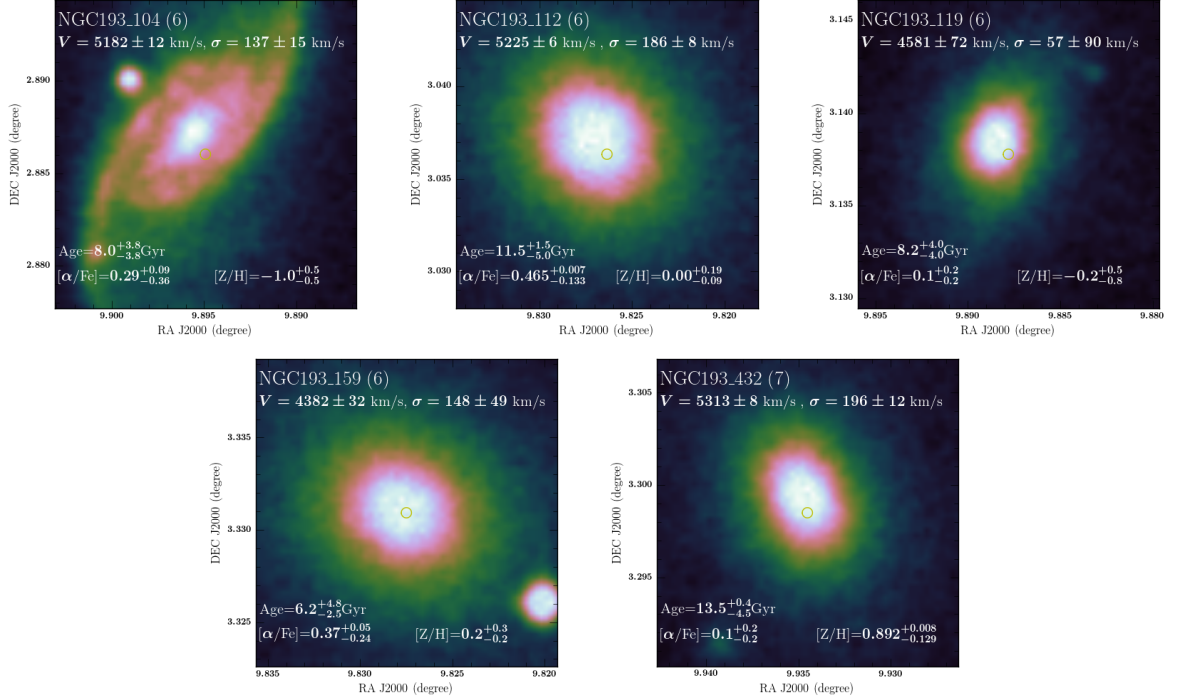


Figure 3.8: Same as Figure 3.4 for galaxies in group NGC 193.

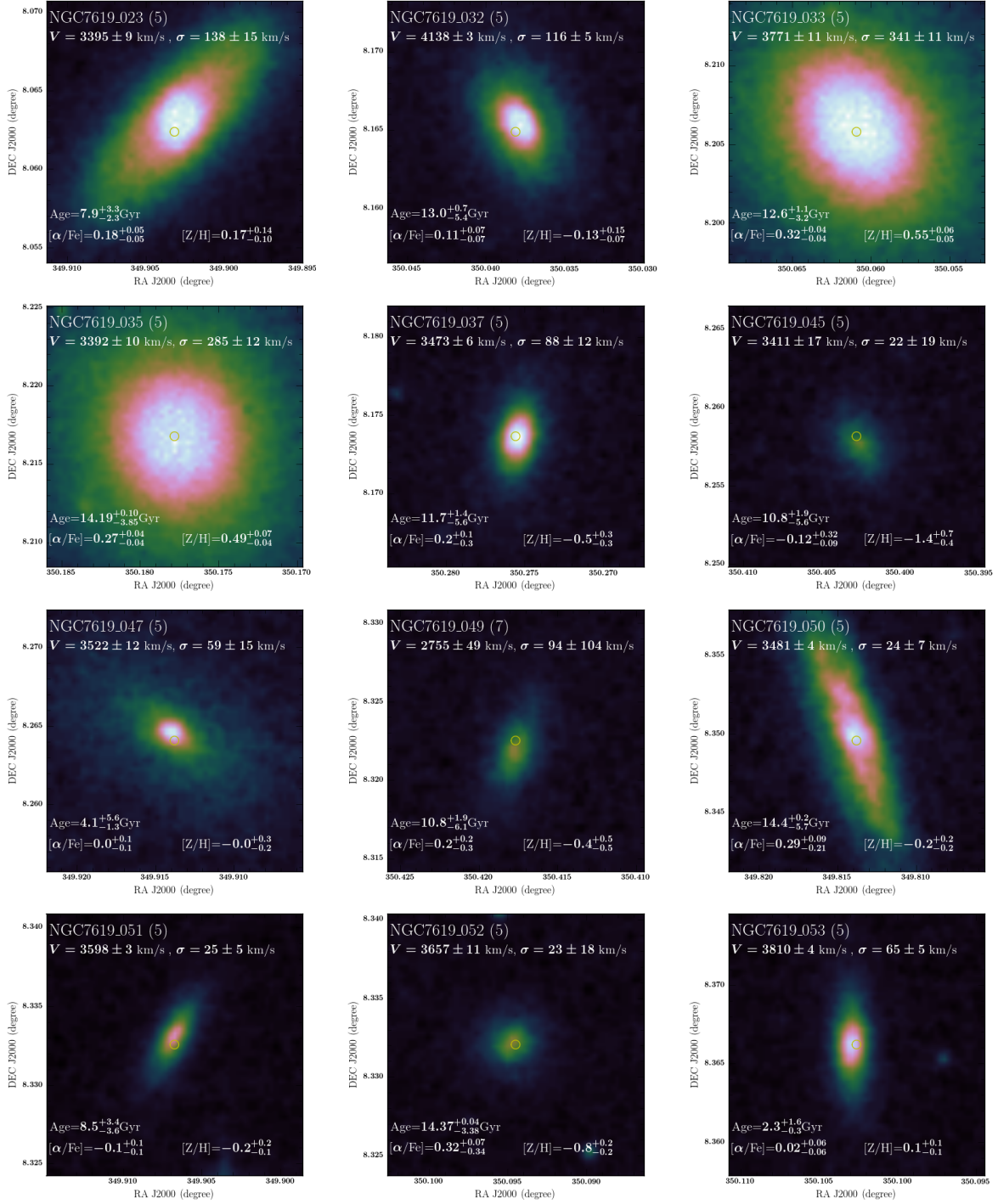


Figure 3.9: Same as Figure 3.4 for galaxies in group NGC 7619.

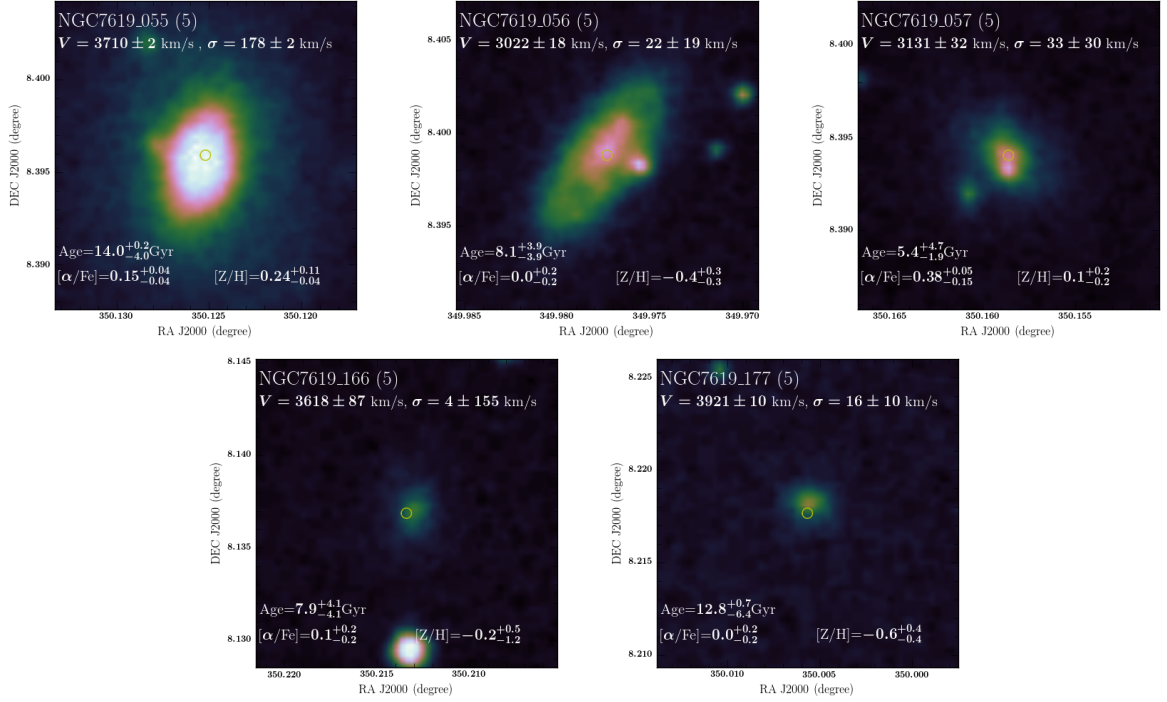


Figure 3.9: Same as Figure 3.4 for galaxies in group NGC 7619. (*cont.*)

$$R_g = \frac{N^2}{\sum_{i < j} 1/R_{ij}}, \quad (3.9)$$

where R_{ij} is the projected distance between two galaxies in the group. Then, the virial mass of the system is given by Heisler et al. (1985).

$$M_v = \frac{\alpha \pi R_g \sigma_v^2}{2G}, \quad (3.10)$$

where $G \approx 4.302 \times 10^{-3} \text{ pc M}_\odot^2 \text{ km}^2 \text{ s}^{-2}$ is the gravitational constant and α is a parameter that depends on the orbits of the galaxies. For orbits isotropically distributed in an dark matter with isothermal distribution, as assumed by Heisler et al. (1985), $\alpha = 3$. In more realistic cases, such as an anisotropic model or a Navarro-Frenk-White (NFW) density profile (Navarro et al., 1996), $\alpha \approx 5/2$ (Mamon and Łokas, 2005; Mauduit and Mamon, 2007) which is the value we adopt in our calculations.

Finally, we also measure the crossing times of the galaxy groups. According to Ramella et al. (1989), this quantity is given by

$$t_c = \frac{3}{5^{3/2}} \frac{R_h H_0}{\sigma_v}, \quad (3.11)$$

where the harmonic radius R_h is defined as

$$R_h = \frac{\pi \langle v \rangle}{H_0} \sin \left[\frac{N(N-1)}{4} \left(\sum_{i=1}^N \sum_{j>i} \theta_{ij}^{-1} \right)^{-1} \right], \quad (3.12)$$

where R_{ij} is the projected distance between two galaxies in the group, and θ_{ij} is the angular distance between two member galaxies. Another related quantity defined by [Ramella et al. \(1989\)](#) is the mean projected separation, given by

$$R_p = \frac{8 \langle v \rangle}{\pi H_0} \sin \left[\frac{1}{N(N-1)} \sum_{i=1}^N \sum_{j>i} \theta_{ij} \right]. \quad (3.13)$$

In the next sections, we show the results from the dynamical calculations of our galaxy groups with the above formulae.

3.5.2 Validation of calculations and results

The calculation of the dynamical properties was carried out using a few custom Python codes, and therefore a cautionary validation of the software was necessary. We have used the data from [ZM98](#) for this purpose, by using the coordinates and the systemic velocity of their observations, provided in their Table 1, to reproduce the dynamical properties presented in their Table 2.

The data in Table 1 of [ZM98](#) included both members and non-members of all groups. We have selected members of the groups using relative velocities smaller than 1500 km s^{-1} in comparison with the mean velocity of the groups (given by [ZM98](#)). This approach is slightly different from that used by [ZM98](#), who used an iterative sigma clipping method. However, as indicates in the panel A of Figure 3.10, our method is sufficient to obtain equivalent mean velocities for all groups. We then proceed to the calculation of the groups' velocity dispersion using the biweight scale estimator, presented in equation (3.6), which also agreed with the results from the literature, as indicated in the panel B of Figure 3.10, except for the NGC 7582. In this system, we were able to select the same eight galaxies as [ZM98](#) using our simple selection method because this system is isolated in the systemic velocity parameter space. Nevertheless, we have obtained $\sigma_v = 83 \pm 40 \text{ km s}^{-1}$, which is only 3 km s^{-1} higher than the value that would be obtained by a simple standard deviation calculation. Therefore, we believe that there is either a typo in the quoted velocity dispersion of the group in Table 2 of [ZM98](#), which shows $\sigma_v = 38_{-36}^{+37} \text{ km s}^{-1}$ for NGC 7582, or there is another problem in their Table 1 which we could not identify.

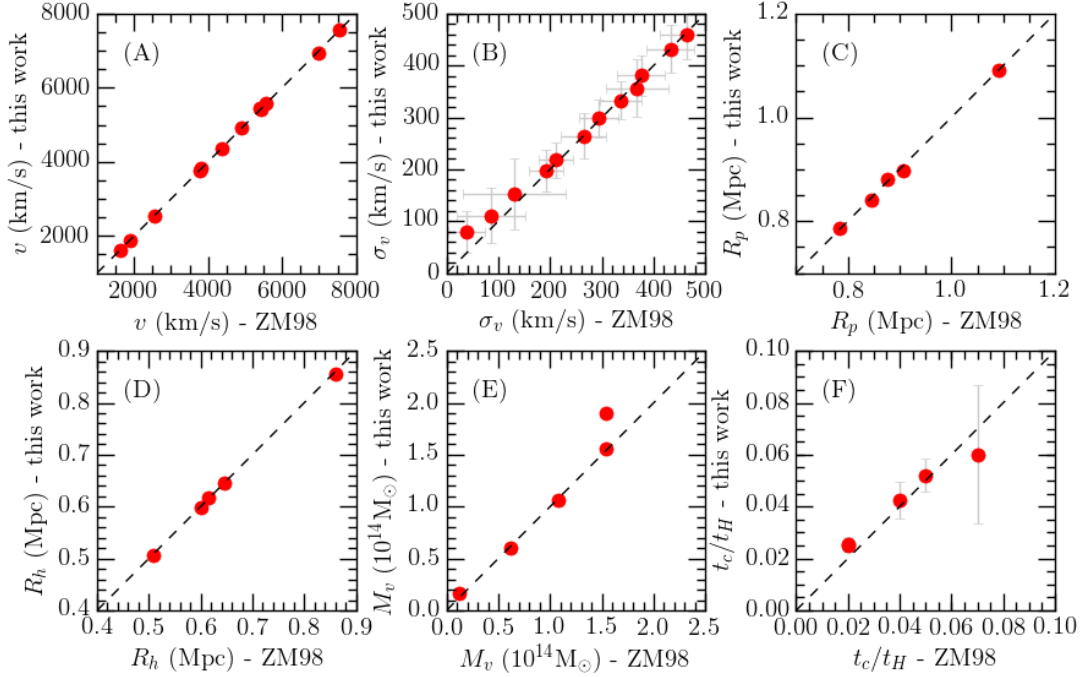


Figure 3.10: Validation of the dynamical properties of galaxy groups using data from ZM98. The dashed line indicates the equality. (A) Mean systemic velocity. (B) Velocity dispersion of the groups. (C) Mean projected separation among galaxies in the groups. (D) Harmonic radius. (E) Virial mass. (F) Crossing times in units of Hubble times.

The next two panels of Figure 3.10 indicate the comparison of the mean projected separation (C) and the harmonic radius (D), defined in equations (3.12) and (3.13), showing good agreement. ZM98 have calculated these properties in only five cases because they have restricted the calculations for groups with enough spatial sampling, defined by the cases where the radial sampling of groups is larger than $2/3$ of the median pairwise radius of the groups.

Finally, panels E and F of Figure 3.10 show the comparison of the virial mass and the crossing times calculated using equations (3.10) and (3.11) respectively. As in panels C and D, the number of groups analyzed by ZM98 is restricted to five. There is a good agreement in most cases, with the exception of the Virial mass of NGC 533, which is more massive according to our calculations than the reported value. Considering that both the Virial radius and the velocity dispersion are equivalent to ours, we believe that the reported value may be incorrect.

The dynamical parameters for our observations are summarized in Table 3.4. Systemic velocities and velocity dispersions are in good agreement with the previous results from

Table 3.4 - Dynamical properties for five galaxy groups. (1) Galaxy group. (2) Number of galaxies in the group. (3) Mean velocity. (4) Velocity dispersion. (5) Harmonic radius. (6) Gravitational radius. (7) Virial mass. (8) Crossing times relative in units of the Hubble time.

Group	N	V_{group} (km s^{-1})	σ_{group} (km s^{-1})	R_h (Mpc)	R_g (Mpc)	M_v ($10^{12}M_{\odot}$)	t_c/t_H
(1)	(2)	(3)	(4)	(5)	(6)	(7)	(8)
hcg42	15	3763 ± 59	243 ± 63	0.236 ± 0.004	0.31 ± 0.02	0.017 ± 0.009	0.018 ± 0.005
hcg62	15	4317 ± 91	373 ± 84	0.0341 ± 0.0007	0.045 ± 0.003	0.006 ± 0.003	0.0017 ± 0.0004
hcg90	6	2631 ± 45	115 ± 44	0.059 ± 0.001	0.087 ± 0.006	0.0011 ± 0.0008	0.009 ± 0.004
ngc193	5	4929 ± 177	482 ± 192	0.40 ± 0.01	0.56 ± 0.04	0.12 ± 0.10	0.015 ± 0.006
ngc7619	17	3520 ± 80	322 ± 76	0.250 ± 0.006	0.33 ± 0.02	0.03 ± 0.02	0.014 ± 0.003

the literature. However, the smaller FOV of our observations have biased our estimates of both the harmonic and gravitational radii significantly. In the three groups in common with ZM98, our gravitational radius is about the value as computed by ZM98 and, as a consequence, the mass estimates for our groups is considered only as a lower limit for the groups.

3.6 Lick indices

We have measured the Lick indices for all group members using our custom routine PYLECTOR (see Chapter 2). The spectra were broadened to match the wavelength-dependent image dissector scanner (IDS) resolution (Worthey and Ottaviani, 1997) using the instrumental resolution given by equation (3.5) and considering also the systemic velocity of the spectra. Emission lines were removed before the measurements using the best fit templates for the gas obtained with pPXF. Instrumental offsets were estimated with a set of 21 standard stars in the sample of Worthey et al. (1994) observed with the same observational apparatus. Finally, the effect of the broadening due to the internal kinematics of the galaxies was corrected using equation (2.7), which automatically includes non-Gaussian effects in the LOSVD. In the following analysis, we do not consider aperture effects in our measurements.

Numerous other authors have detected tight correlations between Lick indices and velocity dispersion (e.g., Kuntschner, 2000; Trager et al., 2000; Proctor and Sansom, 2002; Thomas et al., 2005). In particular, the relation between σ_0 and the index Mg2 is well documented and discussed in the literature (e.g. Gallazzi et al., 2006). In Figure 3.11, we show the relation between all Lick indices and the central velocity dispersion of the

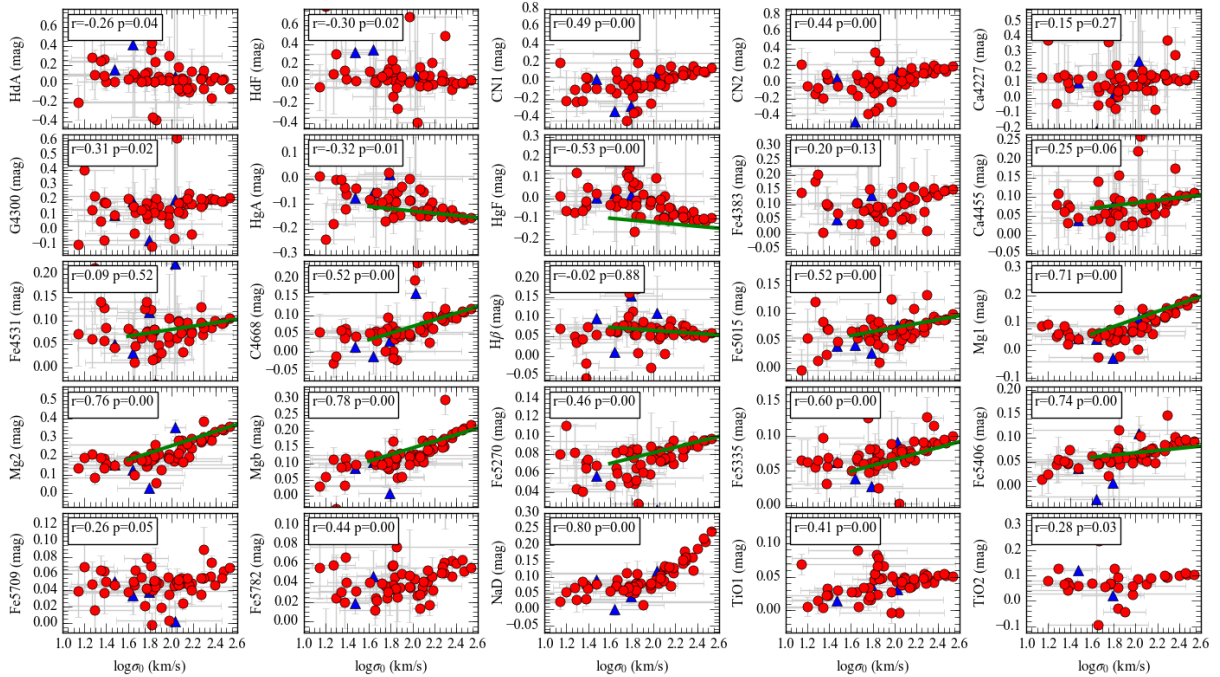


Figure 3.11: Scaling relations between the Lick indices and the central velocity dispersion for galaxies in groups. Red circles (blue triangles) indicate galaxies without (with) emission lines in our analysis of the optical spectra. Solid green lines indicate the relations obtained by Kuntschner (2000) for galaxies in the Fornax cluster. The upper left box in each panel display the Spearman’s rank correlation coefficient (r) and its p-value (p).

galaxies. We convert all Lick indices measured in equivalent widths to magnitudes using the relation

$$I(\text{mag}) = -2.5 \log \left[1 - \frac{I(\text{\AA})}{\Delta w} \right], \quad (3.14)$$

where Δw represent the width of the central bands.

One important aspect of Figure 3.11 is that it extends recent works to galaxies with low velocities, i.e., low-mass galaxies. Gallazzi et al. (2006), for example, have observed the σ_0 -Mg₂ in the Sloan digital sky survey (SDSS) data with galaxies with velocity dispersion of $\log \sigma_0 \gtrsim 1.8$. Similarly, McDermid et al. (2015) have used data from the Atlas3D survey to study 5 absorption line features in elliptical galaxies with velocity dispersions $\sigma_0 \gtrsim 1.7$. Our sample includes objects with velocity dispersion as low as $\sigma_0 \approx 15 \text{ km s}^{-1}$. Also, we are able to characterize all the indices, contrary to most literature data, which ensures that our results are robust, as most of our conclusions are supported by more than a single index.

Most of the panels of Figure 3.11 indicate the existence of a scaling relation, that is, a correlation between the Lick index with the velocity dispersion. In the upper left panels, we indicate the Spearman's rank coefficient (r), which quantifies the degree of correlation in the data, and the resultant p-value (p), which indicates the probability that the null hypothesis (uncorrelated data) can generate the same r . This simple statistic test indicate that in most cases the correlation is very weak ($|r| \leq 0.1$) for only two indices (Fe4531 and H β), weak ($0.1 < |r| \leq 0.3$) for nine indices (H δ_A , H δ_F , Ca4227, HgA, HgF, Fe4383, Ca4455, Fe5709 and TiO2), moderate ($0.3 < |r| \leq 0.5$) for six cases (CN1, CN2, G4300, Fe5270, Fe5782 and TiO1), and strong ($|r| > 0.5$) in eight cases (C4668, Fe5015, Mg1, Mg2, Mgb, Fe5335, Fe5406 and NaD). In most cases, these scaling relations for $\log \sigma_0 \gtrsim 1.8$ are well defined and tight, while the relations for lower masses are more scattered, which indicates that galaxies at lower masses have a larger range of properties, while more massive galaxies are increasingly more similar (McDermid et al., 2015). Also, the trends in Figure 3.11 varies more or less accordingly to the three categories of indices defined by Trager et al. (1998): Balmer indices, iron-like indices, and alpha-element-like indices.

Indices of the Balmer series (H δ_A , H δ_F , H γ_A , H γ_F and H β) are known to anti-correlate with the ages of the stellar populations (Trager et al., 1998). With the exception of H β , which only displays a very weak correlation, all other indices anti-correlate with the dynamical masses of the galaxies. The trends in all cases are consistent at low and high masses. These indices are known to correlate with the stellar population age of the galaxies and, therefore, the results for the correlation of the Balmer series indices confirm the idea that more massive galaxies are also older.

The iron-like indices (Ca, G band, TiO1 and Fe) correlate positively with the velocity dispersion. The existence of such relation may be seen as an extension of the well-known mass-metallicity relation, in which more massive galaxies are also more metal rich. According to Tremonti et al. (2004), the existence of such scaling relation occurs because more massive galaxies are in more massive dark matter halos, and thus are better suited to retain the iron that is expelled in winds due to supernovae. In most cases, the low and high masses are well described by a simple linear relation, but the indices Fe5270 and Fe5335 indicate that low-mass galaxies have stronger features. As indicated by Korn et al. (2005), the indices become more sensitive to alpha-elements for low-mass regimes, which

may explain the break in the scaling relations for galaxies with $\log \sigma_0 < 1.6$.

The alpha-element-like indices (CN, Mg, NaD) indicate two basic trends. The CN indices have positive correlation over all masses, while NaD and Mg indices clearly break at low mass regimes ($\log \sigma_0 \lesssim 1.6$). Interestingly, indices that are sensitive to C have varied behavior (CN and Mg1), illustrating the difficulty of interpreting the results based on the indices alone. Nevertheless, the existence of such a break in these scaling relations of alpha-element-like indices is not found in the literature, where relations such as the σ_0 -Mg₂ are usually linear in the entire studied ranges. The comparison of our results with the data from [Kuntschner \(2000\)](#), which performed a study of elliptical galaxies in the Fornax cluster, indicates that there is a good agreement at large velocity dispersions, but the lack of data for less massive objects does not allow for a comparison which could indicate if this change in the slope is related to a group-specific process, or if it is present also in more dense environments. These unexpected results may indicate some important feature in the history of enrichment of low mass galaxies that occurs at least in groups of galaxies, which we plan to explore in future works.

3.7 Stellar Populations

To obtain ages, metallicities, and alpha-element abundance, we have used the Bayesian method described in Section 2.3 using the models of [Thomas et al. \(2011\)](#). For this analysis, we have restricted the calculations to a subset of Lick indices that are less sensitive to carbon and nitrogen, including HdA, HdF, Fe4383, H β , Mgb, Fe5270, Fe5335, and Fe5406, because these elements are fixed in the models.

In Figure 3.12, we illustrate the relation between the abundances ($[Z/H]$, $[\alpha/Fe]$ and $[Fe/H]$) as a function of the velocity dispersion and as a function of the age. The green lines indicate the relations obtained by [Proctor et al. \(2004\)](#) for Hickson compact groups. In all cases, our results are comparable to the findings of [Proctor et al. \(2004\)](#), even considering the different models and techniques involved in the process. Similarly to the results of the previous section, our analysis allows the extension of the scaling relations to lower masses than previous works.

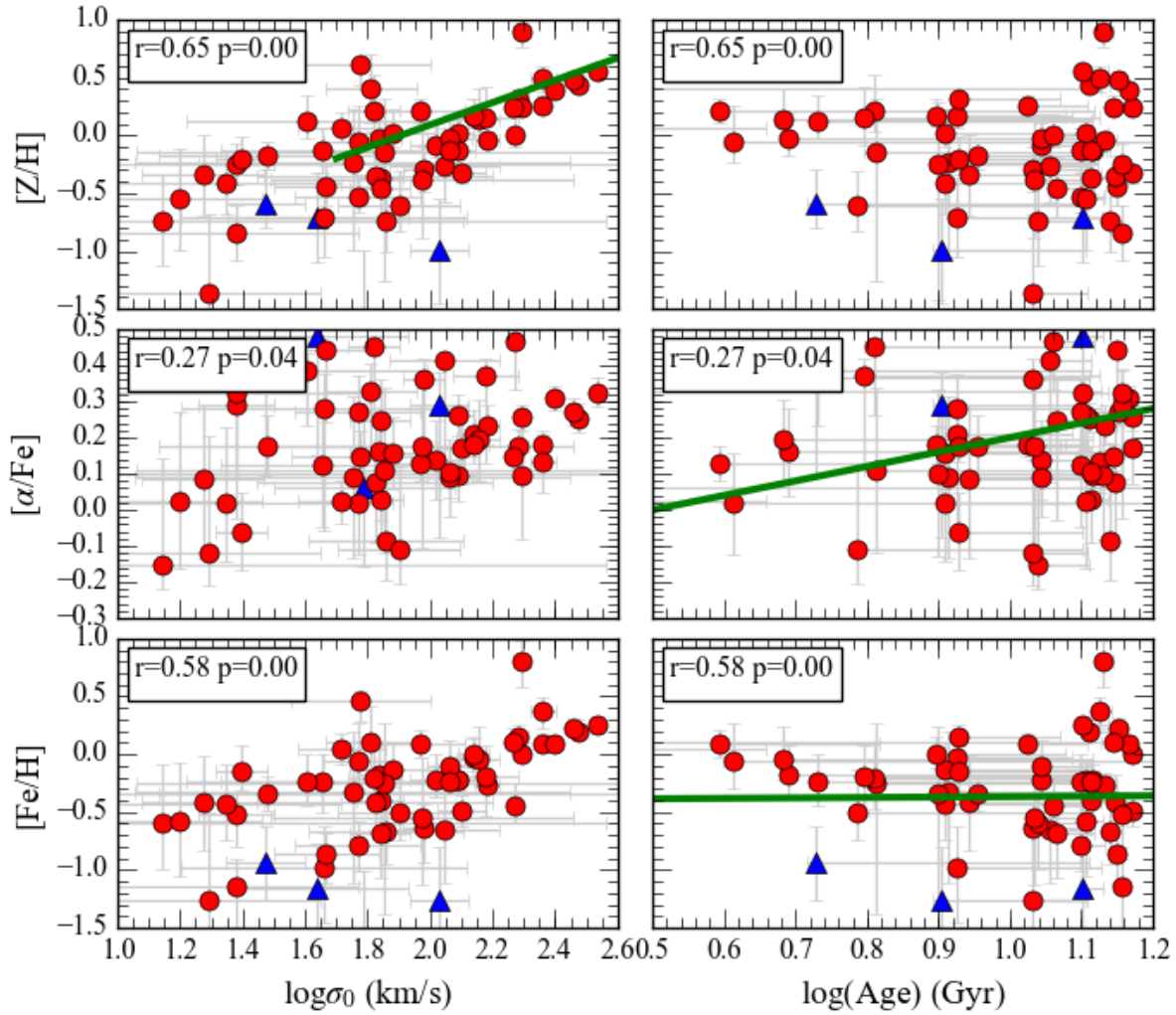


Figure 3.12: Luminosity weighted stellar populations abundances as a function of the velocity dispersion (left) and age (right). Red circles (blue triangles) indicate galaxies without (with) emission lines. The solid green lines indicate the correlations observed by Proctor et al. (2004) observed in elliptical galaxies of compact groups. The upper left box in each panel display the Spearman's rank correlation coefficient (r) and its p-value (p).

Table 3.5 - Identification, coordinates and kinematics of galaxies that are members of groups. (1) Identification of the galaxy. (2) Observational run according to Table 3.3. (3-4) Right ascension and declination of the galaxy. (5) Radial velocity. (6) Velocity dispersion. (7-8) Gauss-Hermite coefficients h_3 and h_4 . (9) Signal-to-noise ratio. (10) Indication of the presence of emission lines.

Galaxy	Run	RA (J2000)	DEC (J2000)	V (km/s)	σ (km/s)	h_3	h_4	S/N (\AA^{-1})	Emission
(1)	(2)	(3)	(4)	(5)	(6)	(7)	(8)	(9)	(10)
HCG22_023	(4)	0h04m06.4164s	45d55m49.95s	2714 ± 20	60 ± 31	0.0 ± 0.2	-0.0 ± 0.2	14.8	no
HCG42_001	(3)	0h02m21.3s	150d03m33s	3758 ± 9	298 ± 12	-0.02 ± 0.03	0.03 ± 0.03	20.9	no
HCG42_001	(4)	0h02m27.456s	150d03m33s	3766 ± 2	296 ± 3	-0.012 ± 0.007	0.008 ± 0.008	22.4	no
HCG42_004	(3)	0h03m22.878s	149d52m15s	4077 ± 11	121 ± 18	-0.13 ± 0.07	0.1 ± 0.1	17.2	no
HCG42_004	(4)	0h02m47.112s	149d52m15s	4073 ± 3	125 ± 5	-0.05 ± 0.02	0.09 ± 0.03	20.7	no
HCG42_005	(3)	0h03m50.6916s	150d08m15s	4206 ± 11	131 ± 18	-0.07 ± 0.07	0.04 ± 0.10	14.9	no
HCG42_005	(4)	0h03m20.0376s	150d08m15s	4200 ± 3	143 ± 3	-0.07 ± 0.02	-0.09 ± 0.02	18.2	no
HCG42_007	(3)	0h01m54.3828s	150d02m34.5s	4025 ± 6	229 ± 7	-0.00 ± 0.02	-0.02 ± 0.03	25.4	no
HCG42_007	(4)	0h01m43.3128s	150d02m34.5s	4014 ± 2	227 ± 2	-0.003 ± 0.006	-0.013 ± 0.007	27.0	no
HCG42_008	(3)	0h06m34.668s	149d48m28.5s	3616 ± 21	104 ± 29	-0.0 ± 0.2	-0.1 ± 0.2	14.7	no
HCG42_008	(4)	0h03m37.5228s	149d48m28.5s	3612 ± 3	105 ± 4	0.10 ± 0.02	-0.08 ± 0.03	22.7	no
HCG42_010	(3)	0h03m05.1624s	150d22m48s	3384 ± 8	27 ± 7	-0.0 ± 0.2	-0.04 ± 0.07	13.6	yes
HCG42_010	(4)	0h07m19.884s	150d22m48s	3376 ± 10	33 ± 10	0.0 ± 0.2	-0.03 ± 0.09	19.7	yes
HCG42_011	(3)	-0h01m15.3192s	150d17m16.5s	3484 ± 31	68 ± 34	0.0 ± 0.3	-0.1 ± 0.2	13.1	yes
HCG42_011	(4)	0h00m23.49s	150d17m16.5s	3517 ± 15	19 ± 23	-0.0 ± 0.4	0 ± 1	13.4	yes
HCG42_012	(3)	0h07m10.956s	149d49m40.5s	3637 ± 6	74 ± 14	0.09 ± 0.06	0.0 ± 0.1	12.5	no
HCG42_012	(4)	0h09m14.22s	149d49m40.5s	3655 ± 11	64 ± 8	0.0 ± 0.1	0.05 ± 0.07	17.6	no
HCG42_014	(3)	0h07m17.436s	149d43m16.5s	3600 ± 13	95 ± 14	0.1 ± 0.1	-0.15 ± 0.10	15.2	no
HCG42_014	(4)	0h07m00.444s	149d43m16.5s	3601 ± 14	43 ± 9	-0.0 ± 0.2	0.03 ± 0.09	20.2	no
HCG42_019	(3)	0h05m57.354s	150d03m12s	4050 ± 27	72 ± 33	0.0 ± 0.3	0.1 ± 0.3	13.3	no
HCG42_019	(4)	0h01m43.4928s	150d03m12s	4053 ± 6	80 ± 9	0.12 ± 0.06	-0.07 ± 0.07	18.7	no
HCG42_021	(3)	0h04m32.0484s	150d07m03s	3789 ± 21	94 ± 26	-0.0 ± 0.2	0.1 ± 0.2	15.0	no
HCG42_021	(4)	0h00m45.1728s	150d07m03s	3789 ± 13	35 ± 17	0.0 ± 0.2	-0.0 ± 0.2	21.3	no
HCG42_023	(3)	0h03m26.2548s	150d09m31.5s	3724 ± 20	95 ± 19	-0.1 ± 0.2	-0.2 ± 0.1	14.0	no

Galaxy	Run	RA (J2000)	DEC (J2000)	V (km/s)	σ (km/s)	h_3	h_4	S/N (\AA^{-1})	Emission
(1)	(2)	(3)	(4)	(5)	(6)	(7)	(8)	(9)	(10)
HCG42_023	(4)	0h09m31.176s	150d09m31.5s	3727 ± 6	94 ± 6	0.04 ± 0.05	-0.15 ± 0.04	11.8	no
HCG42_025	(3)	0h05m32.8524s	150d15m04.5s	3837 ± 70	41 ± 60	0.0 ± 1.0	-0.0 ± 0.4	18.3	no
HCG42_025	(4)	0h10m27.48s	150d15m04.5s	3852 ± 16	51 ± 31	0.0 ± 0.2	-0.0 ± 0.3	21.0	no
HCG42_031	(3)	0h00m44.6004s	150d06m16.5s	3621 ± 5	30 ± 7	-0.0 ± 0.1	-0.0 ± 0.1	12.7	no
HCG42_031	(4)	0h07m23.196s	150d06m16.5s	3629 ± 6	63 ± 24	-0.05 ± 0.06	-0.0 ± 0.2	20.2	no
HCG42_037	(3)	0h12m17.172s	150d09m25.5s	3604 ± 7	16 ± 7	-0.0 ± 0.3	-0.02 ± 0.07	16.1	no
HCG42_037	(4)	0h09m15.516s	150d09m25.5s	3617 ± 8	21 ± 10	0.0 ± 0.2	-0.0 ± 0.3	23.0	no
HCG62_14	(1)	0h05m11.4936s	193d34m57s	4132 ± 17	230 ± 21	-0.20 ± 0.06	0.10 ± 0.07	11.9	no
HCG62_150	(1)	0h16m08.76s	193d22m49.5s	4753 ± 24	72 ± 41	-0.0 ± 0.3	-0.0 ± 0.3	22.9	no
HCG62_16	(2)	0h01m05.7396s	192d51m09s	4223 ± 45	111 ± 45	0.0 ± 0.4	-0.1 ± 0.2	12.5	no
HCG62_18	(1)	0h04m06.366s	193d17m25.5s	4415 ± 11	123 ± 16	0.06 ± 0.08	-0.02 ± 0.10	15.1	no
HCG62_19	(1)	0h03m31.2552s	193d28m57s	4184 ± 7	152 ± 13	-0.01 ± 0.04	0.08 ± 0.06	16.8	no
HCG62_22	(1)	0h02m50.676s	193d28m58.5s	4862 ± 10	90 ± 17	0.02 ± 0.09	-0.0 ± 0.1	19.0	no
HCG62_22	(2)	0h01m54.534s	193d28m58.5s	4831 ± 38	96 ± 40	0.2 ± 0.3	-0.2 ± 0.3	18.8	no
HCG62_36	(2)	0h10m33.168s	193d11m27s	4757 ± 30	66 ± 58	0.0 ± 0.3	0.0 ± 0.5	22.6	no
HCG62_38	(1)	0h06m00.036s	193d25m04.5s	3945 ± 24	59 ± 27	0.2 ± 0.3	-0.2 ± 0.2	21.3	no
HCG62_39	(1)	0h13m44.004s	193d13m46.5s	4332 ± 33	71 ± 129	0.1 ± 0.2	0 ± 1	12.0	no
HCG62_43	(1)	0h09m22.176s	193d08m09s	3910 ± 24	59 ± 40	0.1 ± 0.3	0.0 ± 0.4	19.7	no
HCG62_43	(2)	0h09m34.488s	193d08m09s	3907 ± 14	31 ± 25	0.0 ± 0.3	-0.0 ± 0.4	26.4	no
HCG62_4	(1)	0h02m40.92s	193d16m06s	3560 ± 6	189 ± 9	0.02 ± 0.03	0.04 ± 0.04	16.7	no
HCG62_4	(2)	0h04m20.118s	193d16m06s	3540 ± 13	196 ± 18	0.00 ± 0.06	0.02 ± 0.07	19.9	no
HCG62_66	(2)	0h00m33.3144s	193d12m09s	4757 ± 16	66 ± 12	0.0 ± 0.2	0.03 ± 0.08	22.8	no
HCG62_7	(2)	0h06m22.572s	192d39m57s	4301 ± 20	142 ± 23	0.2 ± 0.1	-0.1 ± 0.1	17.2	no
HCG62_N0127	(2)	0h17m42.648s	193d13m48s	4238 ± 52	14 ± 45	0 ± 2	-0.0 ± 0.4	21.6	no
HCG62_N0147	(2)	0h06m24.372s	193d17m27s	4407 ± 12	116 ± 19	0.02 ± 0.09	0.0 ± 0.1	20.7	no
HCG90_ESO466B	(5)	0h13m33.132s	330d33m56.1s	2825 ± 30	79 ± 36	-0.2 ± 0.3	-0.1 ± 0.3	13.0	no
HCG90_ESO466D	(5)	0h14m06.36s	330d41m28.5s	2629 ± 14	91 ± 35	0.06 ± 0.09	0.0 ± 0.2	21.4	yes
HCG90_ESO466D	(7)	0h13m46.632s	330d41m28.5s	2615 ± 11	32 ± 46	0.02 ± 0.09	-0.0 ± 0.6	11.6	yes
HCG90_ESO466E	(5)	0h05m07.152s	330d57m04.65s	2614 ± 31	33 ± 25	0.0 ± 0.6	-0.0 ± 0.2	20.2	no

Galaxy	Run	RA (J2000)	DEC (J2000)	V (km/s)	σ (km/s)	h_3	h_4	S/N (\AA^{-1})	Emission
(1)	(2)	(3)	(4)	(5)	(6)	(7)	(8)	(9)	(10)
HCG90_ESO466E	(7)	0h04m47.9208s	330d57m04.65s	2610 ± 26	27 ± 22	-0.0 ± 0.5	-0.1 ± 0.2	13.8	no
HCG90_NGC7173	(5)	0h02m06.0036s	330d30m49.35s	2518 ± 7	196 ± 11	0.03 ± 0.03	0.05 ± 0.04	25.5	no
HCG90_NGC7174	(7)	0h06m07.092s	330d31m37.35s	2711 ± 14	126 ± 23	0.13 ± 0.09	0.2 ± 0.1	12.4	no
HCG90_NGC7176	(5)	0h02m01.8132s	330d32m06.75s	2496 ± 7	249 ± 9	0.01 ± 0.02	0.03 ± 0.03	23.8	no
HCG90_NGC7176	(7)	0h02m06.9468s	330d32m06.75s	2504 ± 8	252 ± 10	-0.00 ± 0.03	0.02 ± 0.03	22.8	no
NGC193_104	(6)	0h05m20.6376s	9d53m41.4s	5182 ± 12	137 ± 15	-0.12 ± 0.07	-0.07 ± 0.09	17.1	yes
NGC193_104	(7)	0h15m36.468s	9d53m41.4s	5144 ± 13	76 ± 29	0.1 ± 0.1	-0.0 ± 0.2	15.1	yes
NGC193_112	(6)	0h00m25.8905s	9d49m35.25s	5225 ± 6	186 ± 8	-0.15 ± 0.02	0.06 ± 0.03	18.3	no
NGC193_112	(7)	0h07m29.784s	9d49m35.25s	5213 ± 5	186 ± 8	-0.02 ± 0.02	0.05 ± 0.03	15.7	no
NGC193_119	(6)	0h13m24.024s	9d53m16.5s	4581 ± 72	57 ± 90	0.0 ± 0.8	0.0 ± 0.7	13.5	no
NGC193_159	(6)	0h03m01.7424s	9d49m39.45s	4382 ± 32	148 ± 49	0.1 ± 0.2	0.1 ± 0.2	16.9	no
NGC193_159	(7)	0h01m42.492s	9d49m39.45s	4356 ± 8	154 ± 12	-0.10 ± 0.04	0.15 ± 0.05	15.2	no
NGC193_432	(7)	0h10m34.464s	9d56m04.35s	5313 ± 8	196 ± 12	-0.14 ± 0.03	0.05 ± 0.04	12.0	no
NGC7619_023	(5)	0h03m08.5356s	349d54m11.85s	3395 ± 9	138 ± 15	-0.05 ± 0.06	0.03 ± 0.08	37.0	no
NGC7619_032	(5)	0h04m22.098s	350d02m17.25s	4138 ± 3	116 ± 5	-0.02 ± 0.02	-0.00 ± 0.03	33.9	no
NGC7619_033	(5)	0h02m27.5244s	350d03m39.6s	3771 ± 11	341 ± 11	-0.02 ± 0.03	-0.04 ± 0.03	24.1	no
NGC7619_035	(5)	0h02m16.9584s	350d10m39.9s	3392 ± 10	285 ± 12	-0.02 ± 0.03	0.00 ± 0.03	22.3	no
NGC7619_035	(7)	0h02m40.1028s	350d10m39.9s	3369 ± 10	286 ± 12	-0.00 ± 0.03	0.01 ± 0.03	22.3	no
NGC7619_037	(5)	0h06m43.668s	350d16m32.55s	3473 ± 6	88 ± 12	-0.03 ± 0.05	0.01 ± 0.09	12.5	no
NGC7619_037	(7)	0h01m29.5968s	350d16m32.55s	3457 ± 5	50 ± 18	-0.04 ± 0.07	0.0 ± 0.2	23.4	no
NGC7619_045	(5)	0h19m08.4s	350d24m09.75s	3411 ± 17	22 ± 19	0.0 ± 0.5	-0.0 ± 0.4	41.5	no
NGC7619_045	(7)	0h15m37.692s	350d24m09.75s	3441 ± 12	18 ± 13	-0.0 ± 0.4	-0.0 ± 0.3	20.4	no
NGC7619_047	(5)	0h08m29.256s	349d54m50.1s	3522 ± 12	59 ± 15	0.0 ± 0.1	-0.1 ± 0.1	43.8	no
NGC7619_049	(7)	0h09m38.052s	350d25m03.6s	2755 ± 49	94 ± 104	0.0 ± 0.3	0.0 ± 0.7	18.4	no
NGC7619_050	(5)	0h05m32.4096s	349d48m50.1s	3481 ± 4	24 ± 7	-0.02 ± 0.06	-0.0 ± 0.2	36.0	no
NGC7619_051	(5)	0h06m29.664s	349d54m24s	3598 ± 3	25 ± 5	-0.04 ± 0.06	0.0 ± 0.1	41.9	no
NGC7619_052	(5)	0h04m09.2424s	350d05m40.65s	3657 ± 11	23 ± 18	0.0 ± 0.2	-0.0 ± 0.4	36.4	no
NGC7619_052	(7)	0h14m19.68s	350d05m40.65s	3726 ± 17	24 ± 25	0.0 ± 0.4	-0.0 ± 0.5	14.9	no
NGC7619_053	(5)	0h03m36.3024s	350d06m09.9s	3810 ± 4	65 ± 5	0.03 ± 0.04	-0.14 ± 0.03	39.3	no

Galaxy	Run	RA (J2000)	DEC (J2000)	V (km/s)	σ (km/s)	h_3	h_4	S/N (\AA^{-1})	Emission
(1)	(2)	(3)	(4)	(5)	(6)	(7)	(8)	(9)	(10)
NGC7619_053	(7)	0h05m31.3512s	350d06m09.9s	3848 ± 8	39 ± 23	-0.1 ± 0.2	-0.0 ± 0.2	16.8	no
NGC7619_055	(5)	0h02m14.4636s	350d07m30.9s	3710 ± 2	178 ± 2	0.003 ± 0.008	0.010 ± 0.009	30.6	no
NGC7619_055	(7)	0h02m21.336s	350d07m30.9s	3671 ± 1	191 ± 2	-0.021 ± 0.007	0.020 ± 0.008	24.3	no
NGC7619_056	(5)	0h12m42.516s	349d58m37.95s	3022 ± 18	22 ± 19	-0.0 ± 0.5	-0.1 ± 0.5	54.8	no
NGC7619_057	(5)	0h03m01.7604s	350d09m31.2s	3131 ± 32	33 ± 30	0.0 ± 0.6	-0.0 ± 0.3	44.7	no
NGC7619_057	(7)	0h00m08.4802s	350d09m31.2s	3135 ± 12	48 ± 40	0.0 ± 0.1	0.0 ± 0.4	17.8	no
NGC7619_166	(5)	0h13m43.824s	350d12m48s	3618 ± 87	4 ± 155	0 ± 1	0 ± 4	50.2	no
NGC7619_177	(5)	0h14m45.276s	350d00m20.4s	3921 ± 10	16 ± 10	-0.0 ± 0.4	-0.01 ± 0.07	43.2	no

Chapter 4

Kinematic evidence of substructure in the stellar halo of the Hydra I cluster core

4.1 Introduction

Galaxy clusters are the largest virialized structures in the universe, containing hundreds to thousands gravitationally bound galaxies concentrated into a relatively small volume with a radius of a few megaparsecs. The formation of galaxy clusters is related to the collapse of the largest overdensities in the initial density field determined by the cosmic microwave background (CMB) and are the site of complex interactions involving gravity and baryonic-related processes. Consequently, galaxy clusters are the intersection between cosmology and galaxy formation.

The central region of galaxy clusters usually hosts a brightest cluster galaxy (BCG), the most luminous and massive galaxy of the system. These galaxies are usually close to the bottom of the gravitational potential of the cluster traced by their X-ray emission (Lin and Mohr, 2004). Commonly, BCGs are classified as cD galaxies, morphologically similar to other ETGs but with an extended and diffuse stellar halo, which are believed to be formed by the continuous merging of other galaxies in a process usually called cannibalism (Ostriker and Hausman, 1977). This hierarchical build-up of BCGs is supported by dynamical studies (Dressler, 1979; Bender et al., 2015), stellar populations (Cocato et al., 2010; Barbosa et al., 2016; Edwards et al., 2016) and is well described by simulations (De Lucia and Blaizot, 2007; Cooper et al., 2013, see also Figure 1.2).

From a cosmological perspective, cD galaxies may be used to test predictions of the

Lambda cold dark matter (Λ CDM) model regarding the radial density profile of dark matter halos. The dark matter halos formed in cosmological simulations (e.g., [Springel et al., 2005](#)) are well described by a NFW density profile ([Navarro et al., 1996](#)), given by

$$\rho(r) = \frac{\rho_0}{(r/r_s)(1 + r/r_s)^2}, \quad (4.1)$$

where r is the radial distance to the center of the halo, and r_s and ρ_0 are the scale radius and the amplitude parameters which vary from halo to halo. One important test for cosmology is to test whether the NFW profile produces cuspy cores at the center, that is, to check whether $\rho \propto r^{-1}$ in the limit when $r \rightarrow 0$. However, this prediction is difficult to test in practice because the dark matter halos that are observed contain baryons, which lead to degenerated models owing to the uncertain light-to-mass ratio. To minimize this problem, galaxies with large mass-to-light ratios are preferred, such as low surface brightness galaxies, including cD galaxies.

The problem is that most observational studies support radial density profiles containing halos with cores, i.e., $\rho \approx r^0$ in the limit when $r \rightarrow 0$. For example, at the scale of galaxy clusters, [Sand et al. \(2004\)](#) have determined that the density profiles are incompatible with the NFW profile using strong lensing. At galactic scales, cored profiles have been supported in studies of low surface brightness galaxies ([de Blok et al., 2001](#)), spirals ([Spano et al., 2008](#)) and cD galaxies ([Kelson et al., 2002](#)). This divergence, known as the cusp-core problem or the small-scale cosmological problem, poses an important challenge for both theory and observations. Some authors have proposed explanations for the observation of cored halos, such as feedback effects ([Governato et al., 2010](#), e.g.) or warm dark matter (e.g. [Primack, 2009](#)). Recently, [Pineda et al. \(2016\)](#) have indicated that the problem may be related to an observational bias which would always lead to the presence of cores. Still, the question remains largely open as none of the alternatives have been conclusively tested.

In this context, the galaxy NGC 3311 is one of the most attractive targets for the study of dark matter halos. NGC 3311 is the nearest cD galaxy, located in the center of the Hydra I cluster core, at a distance of ~ 50 Mpc. Besides its low and extended surface brightness profile ([Vasterberg et al., 1991](#); [Arnaboldi et al., 2012](#)), NGC 3311 has a variety of dynamical tracers that allows probing its kinematics at large distances from the center of the system, such as globular clusters ([Wehner et al., 2008](#)) and planetary nebulae ([Ventimiglia et al., 2011](#)). Moreover, the velocity dispersion profile of NGC3311 increases

as a function of the radius (Loubser et al., 2008), which indicates that the dynamical properties of the stars in the central region are dominated by the cluster’s gravitational potential.

Richtler et al. (2011) have performed a dynamical modeling of NGC 3311 using the non-rotating spherical Jeans equation (see Mamon and Łokas, 2005), based on the analysis of the stellar light from long-slit observations and the globular cluster kinematics from Misgeld et al. (2011), which favored the presence of a density profile with a core. However, shortly before the publication of that dynamical analysis, Ventimiglia et al. (2010) have published the stellar kinematics of NGC 3311 based on long-slit observations of the stellar halo that is inconsistent with the results from Richtler et al. (2011): in the region close to the center of NGC 3311, the velocity dispersion of both works agree, but at a distance of ~ 16 kpc, which represents approximately two effective radii, the velocity dispersion differs by ~ 100 km s $^{-1}$. Such a difference at large galactic scale may alter drastically the conclusions regarding the nature of the dark matter density profile of the cluster and, as such, requires proper verification.

One important difference between the observations of Richtler et al. (2011) and Ventimiglia et al. (2010) is the different orientation of the slits used for the observations. Richtler et al. (2011) have used two long slit observations, one along the major axis of NGC 3311 at a position angle of 40° , and another connecting the center of NGC 3311 with NGC 3309, the second most luminous galaxy of the Hydra I cluster core (green slits in Figure 4.3). On the other hand, Ventimiglia et al. (2010) have placed one long slit centered at NGC 3311 with a position angle of 63° in order to also study HCC 26, a dwarf galaxy in the vicinity of the cD galaxy, and another slit centered at HCC26 avoiding the central region of NGC 3311 in order to study the outer stellar halo (blue slits in Figure 4.3). Assuming that both works have been performed correctly, this large deviation of the velocity dispersion profile indicates that velocity field is not spherical, and a large perturbation on the gravitational potential is occurring.

This divergence in the velocity dispersion profiles also put in question if the main assumptions of the dynamical analysis applied to large elliptical galaxies hold in reality, such as virial equilibrium and spherical symmetry. The round and smooth appearance of cD galaxies and the distribution of the X-ray hot gas at large scale may justify those hypotheses. However, in the case of NGC 3311, there is evidence that the system has

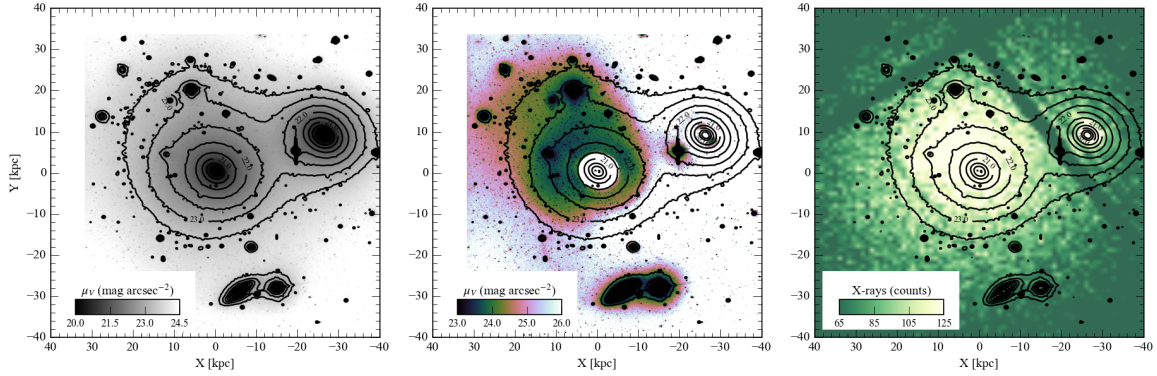


Figure 4.1: V-band and X-ray imaging of the central region of the Hydra I cluster core. *Left:* V-band imaging of the central 40 kpc around NGC 3311 by [Arnaboldi et al. \(2012\)](#). *Center:* Residuals from a maximum symmetric model of the V-band photometry indicating the location of the northeast substructure. *Right:* X-ray imaging obtained with the Chandra telescope from [Hayakawa et al. \(2004\)](#).

some peculiarities and, thus, it is not in virial equilibrium. A deep photometric study of the galaxy by [Arnaboldi et al. \(2012\)](#) has indicated that the residuals of the maximum symmetric model of the light distribution result in residuals largely concentrated in an offset substructure displaced from the center of the galaxy towards the northeast direction, as illustrated in Figure 4.1. Moreover, there is an excess of light in the residuals which may be related to a tidal tail of the lenticular galaxy HCC 007 at the bottom of the FOV. This result is corroborated by the distribution of the X-ray gas by [Hayakawa et al. \(2004\)](#). In the remaining of this chapter, we shall refer to this particular feature in the photometry as the northeast (NE) substructure. The idea that the central region of the Hydra I cluster is perturbed is supported by the analysis of the planetary nebulae from [Ventimiglia et al. \(2011\)](#), whose observation favors the presence of three dynamical components.

In this chapter, we aim to clarify the divergence in the velocity dispersion profiles of NGC 3311 in previous studies by the study of its large-scale kinematics using a bi-dimensional homogeneous data set. We will also verify if this kinematic analysis supports the idea that the central region of NGC 3311 is currently under interaction. The structure of this chapter is as follows. In Section 4.2, we present the observations and the data reduction process. In Section 4.3, we detail the extraction of the kinematics and the production of the maps of the moments of the LOSVD based on smoothing. In Section 4.4, we present our results and compare with previous works and in Section 4.5, we summarize our work. Throughout this chapter, we adopt the distance to the Hydra I cluster of

$D = 50.7$ Mpc, and the effective radius of NGC 3311 of $R_e = 8.4$ kpc, that is the average value derived by [Arnaboldi et al. \(2012\)](#) for the inner region of the galaxy, and thus $1'' = 0.262$ kpc.

4.2 Observations and data reduction

In order to compare the velocity dispersion profiles obtained by [Ventimiglia et al. \(2010\)](#) and [Richtler et al. \(2011\)](#) using the stellar halo, it is necessary to observe NGC 3311 out to galactocentric distances of at least ~ 20 kpc $\approx 76'$. For this purpose, we have observed NGC 3311 using the focal reducer/ low dispersion spectrograph 2 (FORS2, [Appenzeller et al., 1998](#)) instrument, mounted at the Cassegrain focus of the UT1 telescope of 8.2m at the Very Large Telescope (VLT), which has a FOV of $6.8' \times 6.8'$, which is enough to cover the area required for the study of NGC 3311 out to $\sim 3R_e$ and also allows the observation of the sky simultaneously. The telescope time was obtained under European southern observatory (ESO) program ID 088.B-0448/B (PI: Richtler), and the observations were carried out on March 29, 2012.

To perform a bi-dimensional survey of the stellar halo, we have used FORS2 in the mask exchange unit (MXU) mode, which allows the use of masks for multi-object observations over selected areas over the FOV. Figure 4.2 shows our observational strategy, which consists of six masks that survey the stellar halo of NGC 3311 in concentric shells. The exposure time for each pointing is 1400 s. The central (cen1 and cen2) and inner (inn1 and inn2) masks were observed twice each to a total integration time of 2800 s, while the outer (out1 and out2) masks were observed six times each giving a total integration time of 8400 s. The design of the masks was performed with the FIMS program ([ESO, 2013a](#)) using pre-imaging images obtained in the same telescope in the B and R bands. The slits have typical dimensions of $1'' \times 5''$, but the size varied in some cases to avoid point sources and chip gaps. The slits are divided into four categories according to their function: 1) 138 sky slits, used for the sky subtraction and located at the extremes of the masks; 2) 140 stellar halo slits, observed in regions devoid of bright point sources; 3) 3 slits over HCC 007, located at the lenticular galaxy in the bottom of Figure 4.3; and 4) 50 point sources selected for the survey of ultra-compact dwarf galaxies and globular clusters.

In this chapter, we deal exclusively with the stellar halo slits, which are displayed in

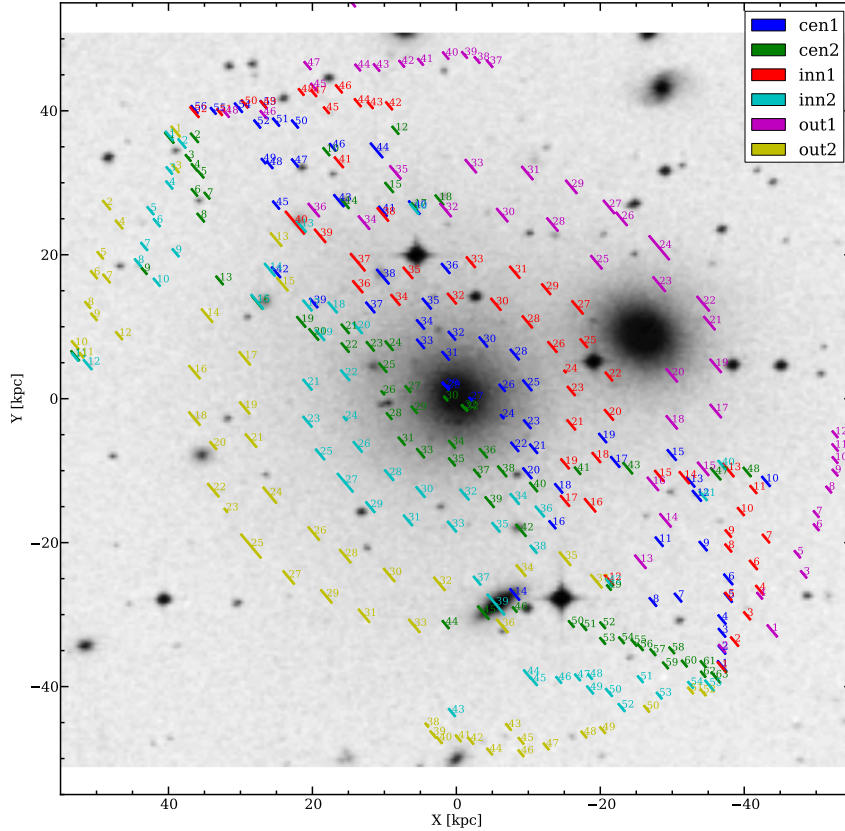


Figure 4.2: Observational strategy for the observation of the stellar halo of NGC 3311. Different colors indicate the observation mask according to the legend in the upper right panel. The small numbers are used for the identification of the spectra. For clarity, we omit the slits on top of point sources that are not studied in this work.

Figure 4.3. We also show the position of the long-slit observations of [Ventimiglia et al. \(2010\)](#), (blue) and [Richtler et al. \(2011\)](#), (green) to illustrate that our survey is able to cover a large radial range, but also allows the study of the properties of the kinematics at different azimuthal angles.

The data reduction, including bias subtraction, flat fielding correction, and dispersion calibrations were performed using the standard instrument pipelines FORS_CALIB and FORS_SCIENCE, and custom IRAF scripts were used for the process of combination and sky subtraction. We have combined all the spectra obtained in a slit, with the exception of the slits cen1s29 and cen2s32, which were divided in two because of their high S/N. The flux calibration using the MXU mode is impractical because it would require multiple exposures of standard stars, increasing the observational overheads, and thus we have used methods in our analysis that do not need flux calibration. Owing to large variations in both borders of the spectra, we set the working wavelength in the range $4700\text{\AA} \lesssim \lambda \lesssim 5700\text{\AA}$.

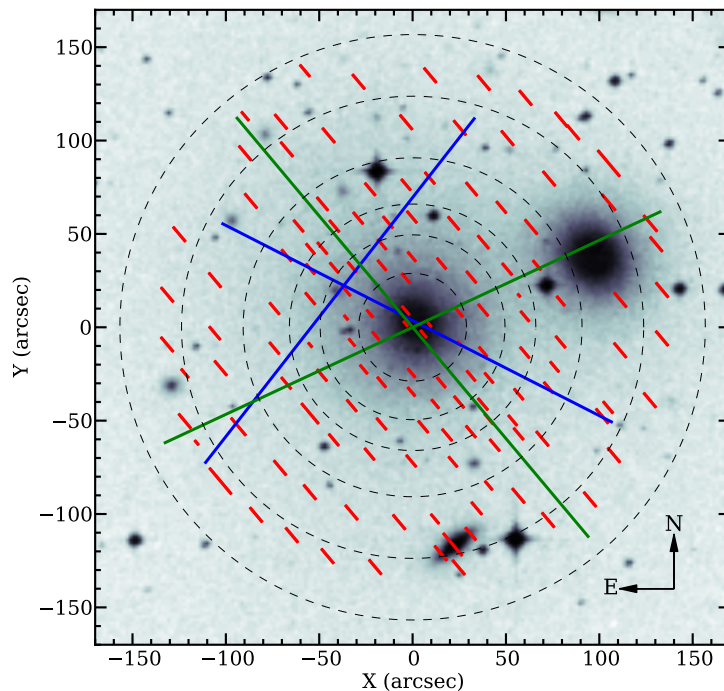


Figure 4.3: Positioning of the slits for the study of the stellar halo of NGC 3311. The small red slits represent our observations, while the two blue and green long slits represent the positioning of previous work by Ventimiglia et al. (2010) and Richtler et al. (2011) respectively.

Each slit in the stellar halo has at least one sky slit at the same X position in the CCD, ensuring that the dispersion of both science and sky spectra are aligned independently of the calibrations. Regions of very bright sky emission lines in the spectra are ignored in all other steps of the analysis.

4.3 Data analysis

We measured the LOSVD of our spectra using the penalized pixel-fitting code (pPXF, Cappellari and Emsellem, 2004), which allows the simultaneous fitting of a linear combination of stellar templates with a light-of-sight velocity distribution, in the wavelength range $4700 \lesssim \lambda(\text{\AA}) \lesssim 5700$, avoiding bright sky lines. For the templates, we used SSP templates produced with stars from the MILES library (Sánchez-Blázquez et al., 2006), calculated with a Salpeter IMF with a logarithmic slope of 1.3. The SSP templates were calculated for ages from 0.1 to 15 Gyr and metallicities in the range $-2.32 \leq [Z/H] \leq 0.22$. In the fitting process, we have considered a single kinematic component with four moments

including the systemic velocity (V_{LOS}), the velocity dispersion (σ_{LOS}) and two other high order Gauss-Hermite moments (h_3 and h_4). The variations in the continuum are adjusted by the use of additive polynomials of order 8. Uncertainties for the parameters were calculated using Monte Carlo simulations based on the signal-to-noise (S/N) for each spectrum. The summary of these measurements is presented on table 4.1.

The S/N of the spectra is estimated by the comparison of the median flux with the residuals of the fitting with pPXF. In Figure 4.4, we present the distribution of the S/N, which also illustrates the general method we have adopted for the presentation of the results. In our analysis, we only consider spectra with $S/N > 10$, which removed only problematic spectra usually due to the chip gaps. We have also opted in not combining spectra of different positions, as this process would remove the spatial information that we would like to understand, and we have used smoothing in order to analyze the main trends of the data. To produce maps of the moments of the LOSVD, we have produced polygons around each considered slit defined by a central Voronoi tessellation. In this particular map, we display all the slits to illustrate our initial sample but, in the following maps, we do not include polygons related to spectra with $S/N < 10$.

We have not combined the spectra of different slits in order to keep the spatial information, but the consequence is a more uncertain determination of the moments of the LOSVD. In order to observe the large-scale trends of our observations, we have processed the maps using the locally weighted scatterplot smoothing (LOESS, Cleveland, 1979; Cleveland and Devlin, 1988). The LOESS is a non-parametric regression method in which each data point is fitted to a low-order polynomial using least squares giving more weight to points near the point whose response is being estimated. Besides the degree of the polynomial for the regression, the only free parameter is the fraction of points in the sample that are going to be considered. In our work, we have used the implementation of the algorithm by Cappellari et al. (2013) using a third-order polynomial and considering 20% of the data around each point for the smoothing. For the systemic velocity and velocity dispersion maps, we have smoothed only data points with $S/N \leq 40$ in order to keep inhomogeneities which are well supported by the data, but in the maps of h_3 and h_4 we have smoothed all data points because of the large variations observed even in regions of high S/N.

The resulting maps are displayed in figures 4.5, 4.7, 4.9 and 4.10. In the left panel of each figure, we have included the original map (not smoothed) for reference, but central

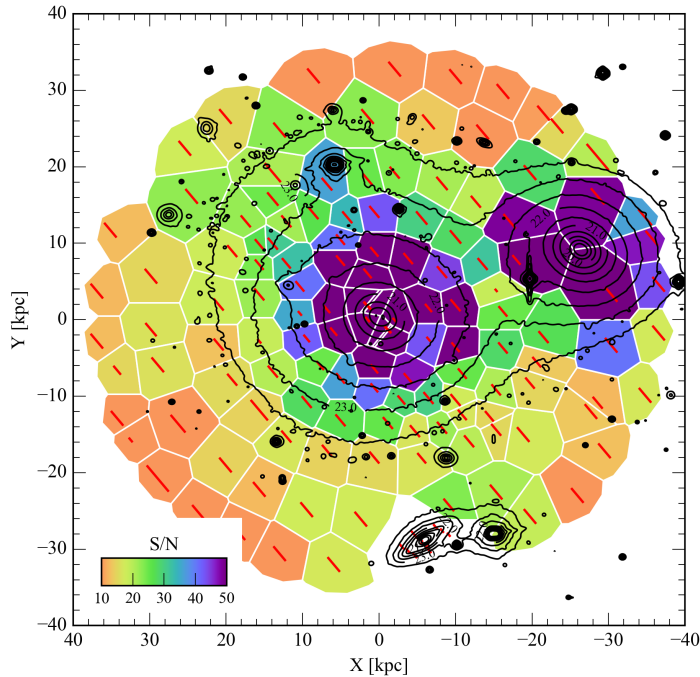


Figure 4.4: Distribution of the S/N in the spectra of the stellar halo of the Hydra I cluster core observed with FORS2. The polygons around each spectrum are constructed using central Voronoi tessellation. The black contours indicate the V-band isophotes in the range from 20 to 23.5 mag arcsec⁻² from [Arnaboldi et al. \(2012\)](#).

and right panels display the maps obtained with the LOESS smoothing. In the right panel of each figure, we have used V-band contours of the residuals from the analysis of [Arnaboldi et al. \(2012\)](#) in order to illustrate the position of the NE substructure, which coincides also with the X-rays excess. In figures 4.5 and 4.7, we also include the long-slit kinematics obtained by [Ventimiglia et al. \(2010\)](#) and [Richtler et al. \(2011\)](#) for comparison. In the next section, we are going to discuss these maps in detail and compare our results with the literature.

4.4 Discussion

4.4.1 Systemic velocity

Figure 4.5 indicates that there is no clear large scale rotation in the system. The large velocity dispersion in Figure 4.7 indicates that the system is supported by dispersion, as expected for massive galaxies ([Emsellem et al., 2007](#)). The center of NGC 3311 has an average systemic velocity of $V_{\text{LOS}} \approx 3840 \text{ km s}^{-1}$, in good agreement with previous measurements such as [Ventimiglia et al. \(2010\)](#) and [Richtler et al. \(2011\)](#). There is a small

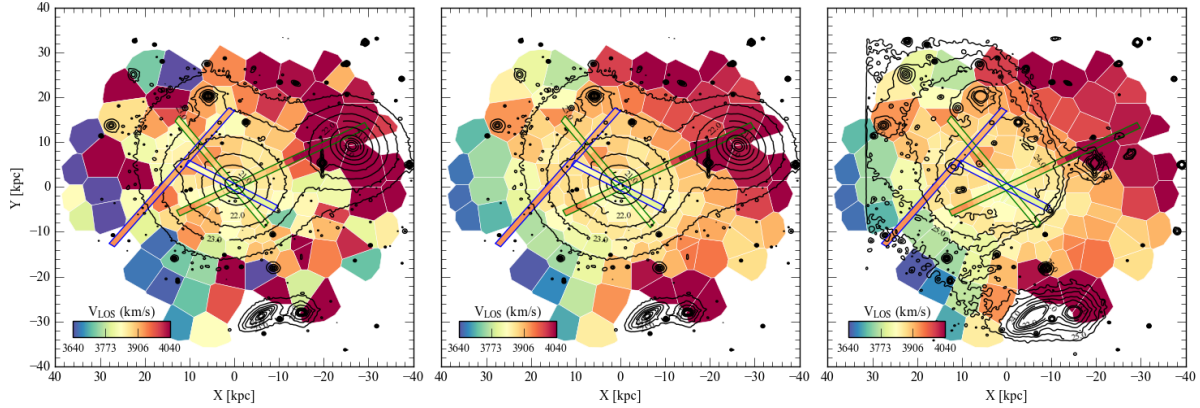


Figure 4.5: Distribution of the systemic velocities of the stellar halo around NGC 3311. *Left:* Velocities determined according to the measurements with pPXF displayed with V-band contours. *Center:* Smoothed maps obtained with LOESS regression displayed with V-band contours. *Right:* Smoothed maps obtained with LOESS displayed with contours from the maximum symmetric model from [Arnaboldi et al. \(2012\)](#). Long-slits represent the results from [Ventimiglia et al. \(2010\)](#) and [Richtler et al. \(2011\)](#).

variation in the velocity regarding the four innermost slits, with a variation of $\sim 30 \text{ km s}^{-1}$ between the lowest and the highest velocities, suggesting that the core of the system has some rotation. However, the low spatial sampling of this data set does not allow for a deeper analysis of this feature.

The systemic velocity distribution correlates better with the location of the NE substructure than with the location of the V-band isophotes, i.e., the spectra with velocities $\sim 3900 \text{ km s}^{-1}$ are approximately confined to the limits of the isophote of $25 \text{ mag arcsec}^{-2}$ in the residual image. On the other hand, there is a low-velocity pattern that extends from the bottom of the figure ($\text{PA} \approx 180^\circ$) to the left side ($\text{PA} \approx 90^\circ$) outside that same isophote, blue-shifted in relation to the center of the galaxy. These spectra at a velocity of $\sim 3700 \text{ km s}^{-1}$ are closer to the systemic velocity of the cluster of $V_{\text{Hydra1}} = 3777 \text{ km s}^{-1}$ ([Struble and Rood, 1999](#)). This is an indication that the light that composes the stellar halo around NGC 3311 is not gravitationally bound to the galactic halo but, instead, is bound to the cluster's potential. A few high-velocity spectra are presented in the bottom, which may be related to the lenticular galaxy HCC 007 at the bottom, which has a central velocity of $V \approx 4700 \text{ km s}^{-1}$. The red pattern on the upper right region of the figure is simply explained by the presence of NGC 3309, which has a velocity of $V \approx 4100 \text{ km s}^{-1}$.

Figure 4.6 compares the systemic velocities in our work with previous measurements by [Ventimiglia et al. \(2010\)](#) and [Richtler et al. \(2011\)](#). In the left panels, we display the

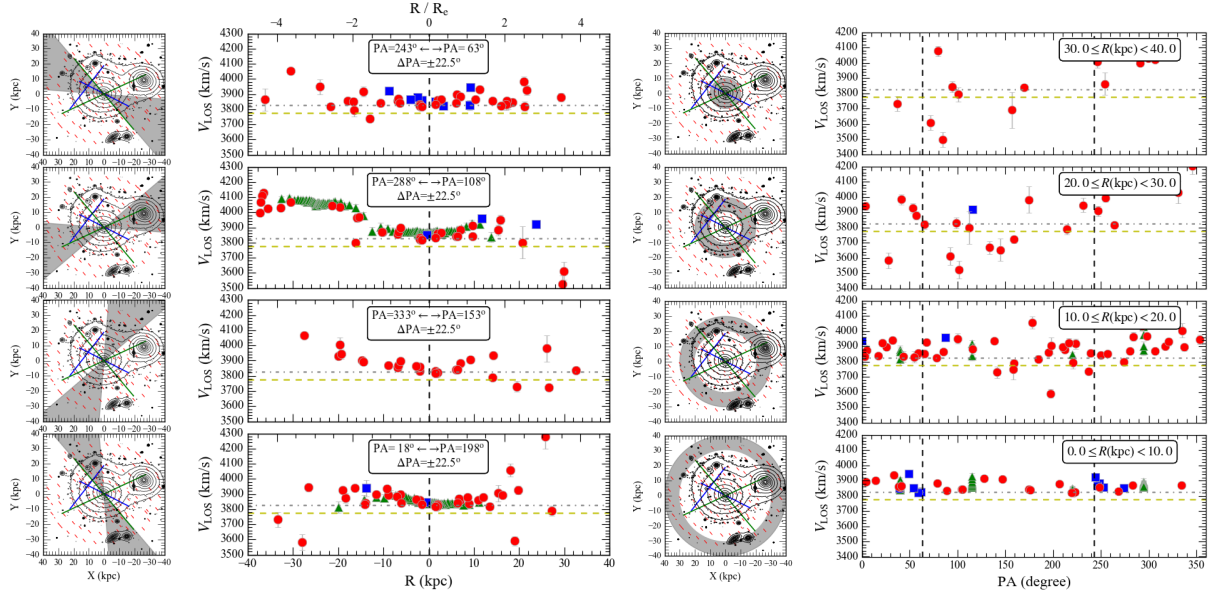


Figure 4.6: Comparison of the systemic velocities in our work (red circles) with the literature, including Ventimiglia et al. (2010, blue squares) and Richtler et al. (2011, green triangles). The first and second column panels show the radial profile of the systemic velocities at conic regions indicated by the gray shaded areas in the figures of the first column. The third and fourth column panels show the variation of the systemic velocity as a function of the position angle in radial bins indicated by the gray shaded areas in the figures of the third column. The gray dot-dashed line indicate the central systemic velocity of NGC 3311, while the yellow dashed line indicates the velocity of the cluster according to Struble and Rood (1999). For better visualization, we always include the four slits in the center of NGC 3311 for reference.

comparison in cones around four position angle in order to produce profiles similar to what is observed with long-slit observations. The right panels indicate the variation of the velocity as a function of the azimuthal angle for increasing radial bins, which does not show a sinusoidal pattern that could indicate a large scale rotation of the system. This comparison indicates a good agreement with the previous measurements, as expected. We now turn to the analysis of the velocity dispersion, which had shown discrepancies in previous works.

4.4.2 Velocity dispersion

The map of the velocity dispersion shown in Figure 4.7 indicates that the velocity dispersion in the center of NGC 3311 is smaller than that of the stellar halo, departing from a central value of $\sigma_{\text{LOS}} \approx 180 \text{ km s}^{-1}$ to values around $\sigma_{\text{LOS}} \approx 400 \text{ km s}^{-1}$ at $R \approx 12 \text{ kpc}$,

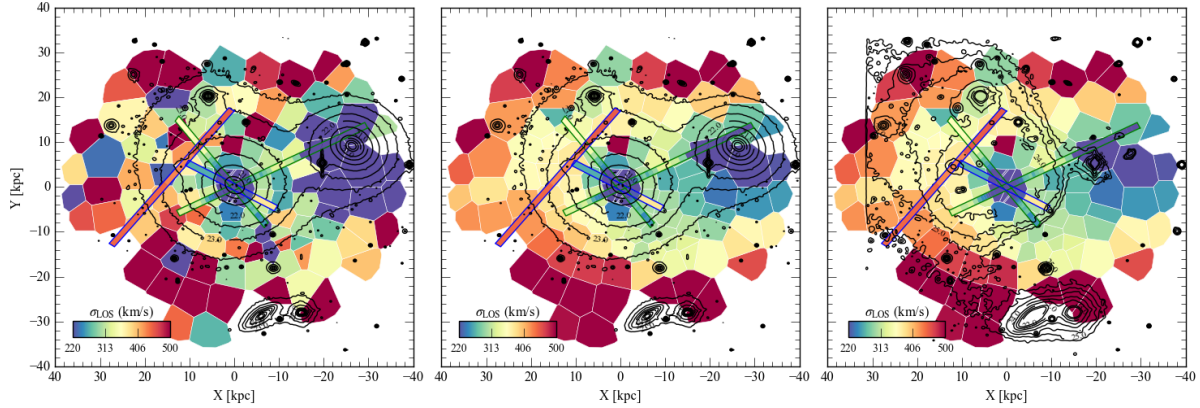


Figure 4.7: Same as Figure 4.5 for the velocity dispersion of NGC 3311.

confirming previous observations (Loubser et al., 2008; Richtler et al., 2011; Ventimiglia et al., 2011). Such an increase in the velocity dispersion in the stellar halo of cD galaxies has been observed before but it is rare (Dressler, 1979; Fisher et al., 1995; Kelson et al., 2002; Loubser et al., 2008).

Similarly to the results observed for the systemic velocity, the velocity dispersion distribution is better correlated with the location of the NE substructure than with the V-band isophotes. At a position angle of the semi-major axis, of 40° , it is clear that the velocity dispersion does not show point symmetry, indicating that the velocity dispersion is larger at the NE photometric substructure. The high-velocity dispersion, in this case, may be explained by the superposition of two kinematic components in the line-of-sight (LOS).

In Figure 4.8, we compare the velocity dispersion with the literature using cones and radial bins as in Figure 4.6. The radial profiles in the left side of the figure show that our observations are consistent with those of Ventimiglia et al. (2010) and Richtler et al. (2011). In particular, the comparison of the velocity dispersion around $PA=108^\circ$, and also around $PA=18^\circ$ indicates that variations of $\sim 100 \text{ km s}^{-1}$ are also observed in our data set only, indicating that the inconsistency of previous works is explained by the inhomogeneity of the velocity dispersion field. The azimuthal variation of the velocity dispersion in Figure 4.8 indicates also that this property is not compatible with a symmetric distribution of the light.

The stellar halo of other cD galaxies in the local universe, such as NGC 6166 in Abell 2199 (Bender et al., 2015) and M87 in the Virgo cluster (Murphy et al., 2014), reach the velocity dispersion of their parent clusters. This is not the case in NGC 3311, as the Hydra I cluster has a velocity dispersion of $\sigma_{\text{gal}} = 647 \text{ km s}^{-1}$ (Struble and Rood, 1999). However,

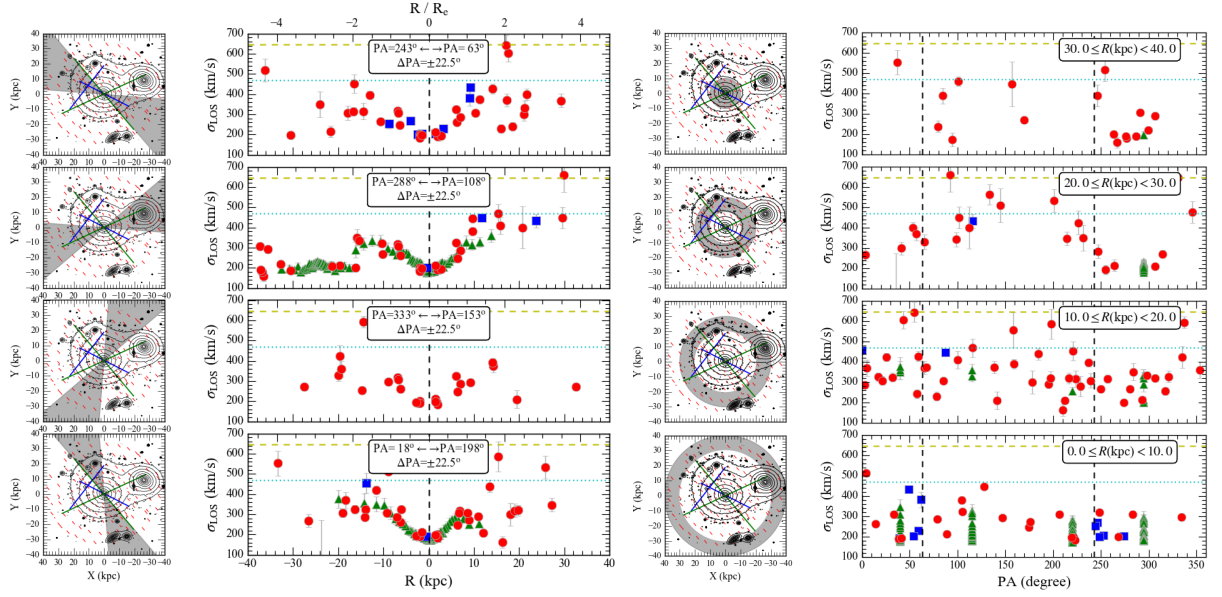


Figure 4.8: Same as Figure 4.6 for the velocity dispersion of NGC 3311. The dotted cyan line indicates the velocity dispersion of the central planetary nebulae component from Ventimiglia et al. (2011)

the velocity dispersion reaches the value of the velocity dispersion of the central kinematic component in the planetary nebulae observed by Ventimiglia et al. (2011), $\sigma_{\text{PNe}} \approx 470 \text{ km s}^{-1}$. We do not observe any flattening in the radial profiles, and thus it is not possible to conclude that the stellar halo is not relaxed yet. However, all the evidence obtained to this point indicate that the particular aspect of NGC 3311 is that it is not relaxed and that the presence of NE substructure is supported by photometry, X-rays and now also kinematically.

4.4.3 Skewness and kurtosis

Similar to the systemic velocity and velocity dispersion, the distribution of the smoothed maps of h_3 and h_4 in figures 4.9 and 4.10 respectively, indicate a spatial correlation with the NE substructure. The center of NGC 3311 shows a symmetric LOSVD, only slightly more concentrated than a Gaussian distribution with $(h_3, h_4) \approx (0, 0.05)$, while the NE substructure displays an asymmetric distribution, with $(h_3, h_4) \approx (-0.1, 0.05)$ (see Figure 2.1).

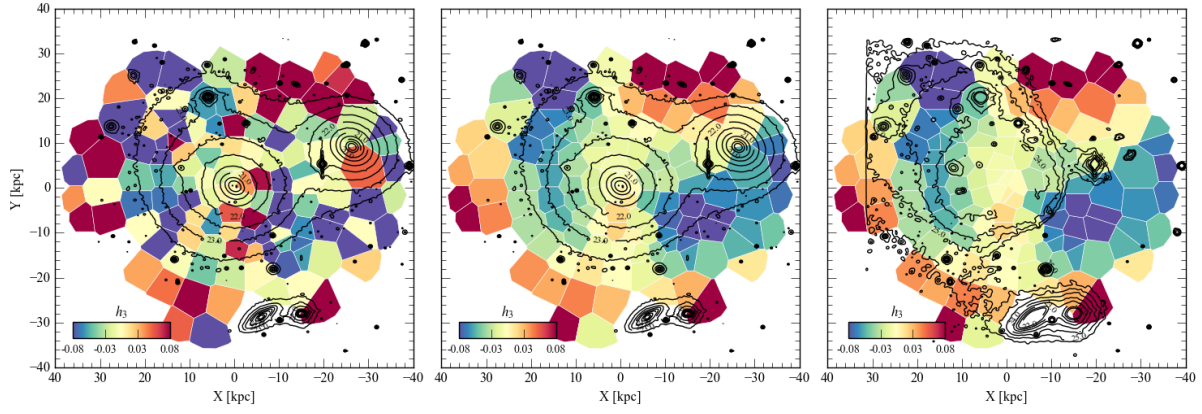


Figure 4.9: Same as Figure 4.5 for the skewness parameter h_3 of NGC 3311.

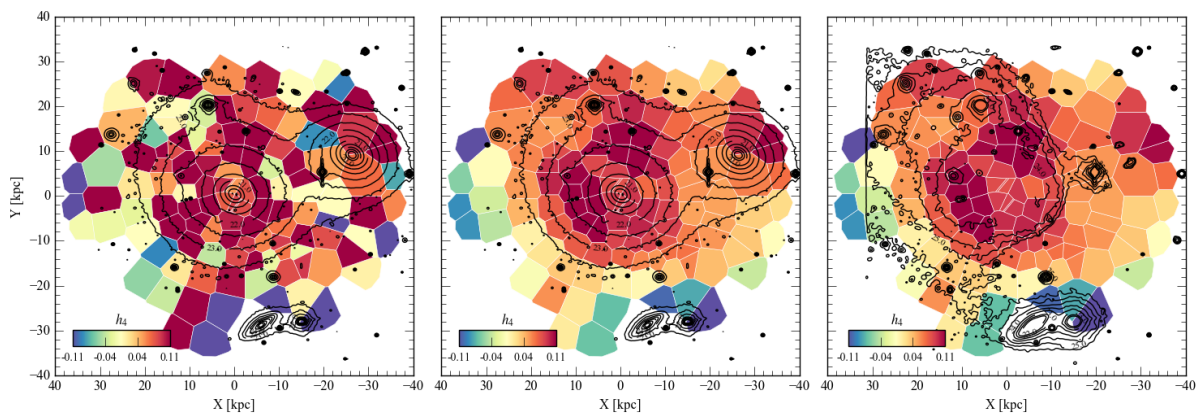


Figure 4.10: Same as Figure 4.6 for the kurtosis parameter h_4 of NGC 3311.

4.5 Summary and conclusion

In this chapter, we have shown the bi-dimensional distribution of the moments of the LOSVD for the central 30 kpc of the Hydra I cluster core, which includes the central galaxy NGC 3311 and its extended stellar halo. The use of a bi-dimensional survey of the kinematics indicates that the discrepancies in the velocity dispersion profiles from the works of [Richtler et al. \(2011\)](#) and [Ventimiglia et al. \(2010\)](#) are explained by real variations of the velocity distribution, and not to possible errors in the analysis.

The use of LOESS smoothing has indicated important large-scale trends in the kinematics. The rising velocity dispersion profile in this galaxy indicates that the stellar halo is related to the cluster gravitational potential, and not to the BCG potential. However, we were also able to show that the velocity dispersion, as well as all other moments of the LOSVD, are correlated with the presence of a large photometric substructure previously reported by [Arnaboldi et al. \(2012\)](#) and also present in the X-rays ([Hayakawa et al., 2004](#)).

The assumptions of virial equilibrium and spherical symmetry are not supported by our observations, which can also point to a larger problem. If NGC 3311 is a typical cD galaxy, and these ongoing processes of interactions are common in such a class of object, then every dynamical analysis using long-slits is subject to uncertainties that may alter the interpretation of the radial density profile of the dark matter halo. In the particular case of NGC 3311, we are currently working on the dynamical modeling of the system ([Hilker et al., prep](#)) to understand the impact of our observations. However, a proper verification of this issue requires the observation of other similar systems with IFU instruments.

In this chapter, we have restricted our analysis to the kinematical aspects of the observations. In the next chapter, we present the analysis of the stellar populations, which brings information about the mass assembly of the central region of the Hydra I cluster core.

Table 4.1 - Moments of the line-of-sight velocity distribution in the stellar halo of NGC 3311 calculated with pPXF. Values between square brackets indicate fixed parameters owing to limits imposed in the fitting process. (1) Identification of the slit. (2) Right ascension for the center of the slit. (3) Declination for the center of the slit. (4) Radial distance to NGC 3311 at RA=10h36m42.71s and DEC=-27d31m41.13s. (5) Position angle relative to the center of NGC 3311. (6) Line-of-sight systemic velocity. (7) Line-of-sight velocity dispersion. (8) Gauss-Hermite h_3 coefficient. (9) Gauss-Hermite h_4 coefficient. (10) Signal-to-noise.

ID	RA	DEC	R	PA	V_{LOS}	σ_{LOS}	h_3	h_4	S/N
	(J2000)	(J2000)	(arcsec)	($^\circ$)	(km s^{-1})	(km s^{-1})			
(1)	(2)	(3)	(4)	(5)	(6)	(7)	(8)	(9)	(10)
cen1 s18	159h09m43.2s	-27d32m33.4s	19.2	111.3	4082 ± 50	278 ± 51	-0.07 ± 0.06	-0.0 ± 0.1	15.0
cen1 s19	159h09m18.0s	-27d32m04.6s	21.4	99.7	3995 ± 27	194 ± 23	-0.25 ± 0.08	-0.1 ± 0.1	13.7
cen1 s20	159h10m01.2s	-27d32m24.7s	14.5	108.0	3918 ± 32	315 ± 41	-0.00 ± 0.08	0.09 ± 0.06	17.6
cen1 s21	159h09m57.6s	-27d32m10.7s	13.0	102.3	3737 ± 22	396 ± 20	-0.25 ± 0.03	0.06 ± 0.04	25.2
cen1 s23	159h10m01.2s	-27d31m56.6s	10.6	96.3	3841 ± 9	265 ± 12	-0.09 ± 0.03	0.14 ± 0.03	49.8
cen1 s24	159h10m15.6s	-27d31m52.3s	6.9	94.5	3857 ± 10	319 ± 13	-0.04 ± 0.02	0.11 ± 0.02	43.2
cen1 s25	159h10m01.2s	-27d31m34.3s	10.2	86.7	3868 ± 10	267 ± 10	-0.14 ± 0.02	0.01 ± 0.03	52.0
cen1 s26	159h10m15.6s	-27d31m35.8s	6.6	87.3	3869 ± 7	308 ± 9	0.08 ± 0.02	0.14 ± 0.02	69.0
cen1 s27	159h10m33.6s	-27d31m42.2s	2.0	90.1	3830 ± 2	200 ± 3	0.037 ± 0.009	0.08 ± 0.01	114.2
cen1 s28	159h10m08.4s	-27d31m16.7s	10.3	79.1	3870 ± 15	319 ± 15	-0.01 ± 0.04	-0.03 ± 0.03	44.5
cen1 s29	159h10m48.0s	-27d31m34.7s	2.3	86.8	3857 ± 2	190 ± 3	-0.009 ± 0.009	0.05 ± 0.01	94.1
cen1 s29a	159h10m46.9s	-27d31m35.6s	2.0	87.2	3858 ± 2	189 ± 3	-0.009 ± 0.009	0.05 ± 0.01	92.2
cen1 s29b	159h10m49.1s	-27d31m33.7s	2.7	86.4	3864 ± 2	193 ± 3	-0.02 ± 0.01	0.09 ± 0.01	85.7
cen1 s30	159h10m26.4s	-27d31m09.5s	8.9	76.2	3867 ± 10	295 ± 13	0.00 ± 0.03	0.11 ± 0.03	59.4
cen1 s31	159h10m48.0s	-27d31m17.4s	6.2	79.4	3900 ± 6	261 ± 7	-0.02 ± 0.02	0.05 ± 0.02	63.8
cen1 s32	159h10m44.4s	-27d31m05.9s	8.9	74.7	3892 ± 13	512 ± 15	0.02 ± 0.02	[0.3]	58.7
cen1 s33	159h11m02.4s	-27d31m10.6s	9.2	76.6	3937 ± 10	307 ± 13	-0.04 ± 0.02	0.10 ± 0.03	70.6
cen1 s34	159h11m02.4s	-27d30m59.4s	11.6	72.1	3897 ± 16	421 ± 20	0.01 ± 0.03	0.07 ± 0.03	40.8
cen1 s35	159h10m58.8s	-27d30m47.5s	14.0	67.6	3840 ± 16	324 ± 20	-0.06 ± 0.04	0.09 ± 0.04	33.9
cen1 s36	159h10m48.0s	-27d30m27.4s	18.4	60.5	3875 ± 32	370 ± 41	-0.06 ± 0.06	0.15 ± 0.07	25.1
cen1 s37	159h11m31.2s	-27d30m49.7s	17.7	68.4	3836 ± 35	605 ± 43	-0.15 ± 0.04	0.12 ± 0.04	21.5

Table 4.1 - continued.

ID	RA	DEC	R	PA	V_{LOS}	σ_{LOS}	h_3	h_4	S/N
	(J2000)	(J2000)	(arcsec)	($^\circ$)	(km s^{-1})	(km s^{-1})			
(1)	(2)	(3)	(4)	(5)	(6)	(7)	(8)	(9)	(10)
cen2 s21	159h11m45.6s	-27d31m01.9s	18.5	73.1	3845 ± 17	241 ± 21	-0.10 ± 0.07	[0.3]	27.0
cen2 s22	159h11m45.6s	-27d31m12.7s	17.2	77.5	3853 ± 27	371 ± 32	-0.10 ± 0.05	0.09 ± 0.05	24.1
cen2 s23	159h11m31.2s	-27d31m12.0s	14.2	77.2	3856 ± 18	426 ± 25	0.02 ± 0.03	0.13 ± 0.03	32.6
cen2 s25	159h11m24.0s	-27d31m24.2s	11.2	82.3	3930 ± 10	372 ± 12	-0.02 ± 0.02	0.30 ± 0.03	40.9
cen2 s26	159h11m24.0s	-27d31m38.6s	10.4	88.5	3866 ± 14	306 ± 14	-0.04 ± 0.03	0.01 ± 0.04	35.6
cen2 s27	159h11m09.6s	-27d31m36.5s	6.9	87.6	3883 ± 7	285 ± 9	-0.01 ± 0.02	0.10 ± 0.02	63.7
cen2 s28	159h11m20.4s	-27d31m52.0s	9.8	94.3	3841 ± 13	380 ± 17	-0.09 ± 0.03	0.17 ± 0.03	42.4
cen2 s29	159h11m06.0s	-27d31m48.4s	6.1	92.8	3842 ± 6	323 ± 8	-0.01 ± 0.01	0.18 ± 0.02	68.8
cen2 s30	159h10m48.0s	-27d31m41.9s	1.5	90.0	3832 ± 2	211 ± 3	0.006 ± 0.008	0.073 ± 0.009	91.2
cen2 s31	159h11m13.2s	-27d32m06.4s	9.8	100.5	3914 ± 13	444 ± 15	0.01 ± 0.03	[0.3]	25.0
cen2 s32	159h10m37.2s	-27d31m47.3s	1.7	92.3	3820 ± 2	195 ± 3	-0.003 ± 0.009	0.08 ± 0.01	93.3
cen2 s32a	159h10m36.2s	-27d31m48.1s	2.0	92.6	3823 ± 2	181 ± 3	-0.016 ± 0.009	0.08 ± 0.01	83.1
cen2 s32b	159h10m38.2s	-27d31m46.5s	1.4	91.9	3819 ± 2	196 ± 3	-0.003 ± 0.009	0.08 ± 0.01	93.3
cen2 s33	159h11m02.4s	-27d32m13.2s	9.2	103.3	3907 ± 10	293 ± 12	-0.06 ± 0.03	0.06 ± 0.03	36.4
cen2 s34	159h10m44.4s	-27d32m08.2s	6.5	101.2	3842 ± 6	246 ± 7	0.06 ± 0.02	0.10 ± 0.02	68.5
cen2 s35	159h10m44.4s	-27d32m18.2s	8.9	105.4	3839 ± 10	270 ± 13	0.02 ± 0.03	0.13 ± 0.03	41.0
cen2 s36	159h10m26.4s	-27d32m13.2s	8.6	103.3	3878 ± 9	307 ± 12	0.09 ± 0.02	0.15 ± 0.03	47.2
cen2 s37	159h10m30.0s	-27d32m24.7s	10.9	108.0	3862 ± 15	287 ± 15	-0.20 ± 0.03	0.09 ± 0.04	29.0
cen2 s38	159h10m15.6s	-27d32m23.6s	12.1	107.5	3878 ± 13	209 ± 17	-0.08 ± 0.04	0.06 ± 0.05	30.4
cen2 s39	159h10m22.8s	-27d32m41.3s	15.3	114.2	3905 ± 53	585 ± 74	0.03 ± 0.07	0.13 ± 0.05	16.5
cen2 s40	159h09m57.6s	-27d32m32.6s	16.5	111.0	3792 ± 39	451 ± 47	-0.05 ± 0.05	0.06 ± 0.06	16.6
inn1 s15	159h08m45.6s	-27d32m26.2s	30.6	108.5	3806 ± 100	391 ± 78	0.0 ± 0.1	0.0 ± 0.2	12.2
inn1 s16	159h09m25.2s	-27d32m43.1s	24.1	114.9	3947 ± 48	349 ± 62	-0.0 ± 0.1	0.05 ± 0.07	17.1
inn1 s17	159h09m39.6s	-27d32m40.6s	21.0	113.9	4102 ± 46	424 ± 58	-0.06 ± 0.07	0.09 ± 0.06	15.0
inn1 s18	159h09m21.6s	-27d32m15.7s	21.4	104.3	3909 ± 32	282 ± 34	-0.18 ± 0.08	0.08 ± 0.09	14.7
inn1 s19	159h09m39.6s	-27d32m19.3s	17.8	105.8	3855 ± 21	307 ± 36	-0.06 ± 0.06	0.22 ± 0.07	20.6
inn1 s20	159h09m14.4s	-27d31m51.2s	21.6	94.0	3817 ± 21	214 ± 27	-0.01 ± 0.10	0.0 ± 0.1	27.3

Table 4.1 - continued.

ID	RA	DEC	R	PA	V_{LOS}	σ_{LOS}	h_3	h_4	S/N
	(J2000)	(J2000)	(arcsec)	($^\circ$)	(km s^{-1})	(km s^{-1})			
(1)	(2)	(3)	(4)	(5)	(6)	(7)	(8)	(9)	(10)
inn1 s21	159h09m36.0s	-27d31m57.0s	16.6	96.5	3851 ± 23	314 ± 20	-0.04 ± 0.04	0.05 ± 0.06	28.4
inn1 s23	159h09m36.0s	-27d31m37.6s	16.2	88.1	3800 ± 12	200 ± 14	-0.00 ± 0.05	0.00 ± 0.05	25.0
inn1 s24	159h09m39.6s	-27d31m26.4s	15.8	83.3	3965 ± 29	350 ± 40	-0.05 ± 0.06	0.15 ± 0.05	18.6
inn1 s25	159h09m28.8s	-27d31m10.2s	19.6	76.4	4035 ± 7	211 ± 9	-0.00 ± 0.03	0.05 ± 0.03	59.4
inn1 s26	159h09m46.8s	-27d31m12.4s	15.4	77.3	3968 ± 14	333 ± 17	-0.02 ± 0.03	0.23 ± 0.04	32.0
inn1 s27	159h09m32.4s	-27d30m49.7s	21.4	68.4	4046 ± 9	209 ± 9	-0.04 ± 0.04	-0.09 ± 0.03	48.7
inn1 s28	159h10m01.2s	-27d30m58.0s	14.7	71.5	3900 ± 14	254 ± 18	-0.11 ± 0.04	0.09 ± 0.05	28.3
inn1 s29	159h09m50.4s	-27d30m39.2s	20.0	64.6	3930 ± 24	327 ± 27	-0.02 ± 0.05	0.04 ± 0.05	19.5
inn1 s30	159h10m19.2s	-27d30m47.9s	14.4	67.7	3894 ± 22	594 ± 28	-0.04 ± 0.03	0.21 ± 0.03	30.2
inn1 s31	159h10m08.4s	-27d30m29.5s	19.6	61.2	4005 ± 47	423 ± 53	0.12 ± 0.06	0.07 ± 0.08	21.2
inn1 s32	159h10m44.4s	-27d30m44.6s	14.1	66.5	3833 ± 12	286 ± 14	0.13 ± 0.04	0.22 ± 0.04	43.1
inn1 s33	159h10m33.6s	-27d30m23.8s	19.3	59.3	3944 ± 31	359 ± 39	0.02 ± 0.06	0.08 ± 0.05	23.5
inn1 s34	159h11m16.8s	-27d30m45.4s	16.4	66.8	3941 ± 22	323 ± 21	-0.01 ± 0.05	-0.02 ± 0.04	26.6
inn1 s35	159h11m09.6s	-27d30m29.9s	19.0	61.3	3925 ± 22	307 ± 21	-0.06 ± 0.04	-0.03 ± 0.06	36.2
inn1 s36	159h11m38.4s	-27d30m37.8s	21.0	64.1	3985 ± 32	298 ± 32	-0.08 ± 0.05	0.01 ± 0.08	24.8
inn1 s37	159h11m38.4s	-27d30m23.8s	23.7	59.3	5865 ± 242	7 ± 264	0.0 ± 0.7	0.0 ± 0.5	20.8
inn2 s18	159h11m52.8s	-27d30m49.7s	21.7	68.4	3927 ± 34	398 ± 29	0.02 ± 0.06	-0.06 ± 0.05	22.3
inn2 s19	159h12m00.0s	-27d31m05.5s	21.2	74.5	3819 ± 31	330 ± 37	-0.14 ± 0.07	0.13 ± 0.08	17.9
inn2 s20	159h11m38.4s	-27d31m01.6s	17.1	73.0	3831 ± 37	643 ± 48	0.10 ± 0.04	0.08 ± 0.04	31.1
inn2 s21	159h12m07.2s	-27d31m34.0s	21.1	86.5	4080 ± 104	415 ± 106	-0.04 ± 0.07	0.0 ± 0.2	18.1
inn2 s22	159h11m45.6s	-27d31m28.6s	16.0	84.2	3825 ± 18	230 ± 21	-0.06 ± 0.05	0.05 ± 0.07	21.9
inn2 s23	159h12m07.2s	-27d31m55.2s	21.2	95.7	3831 ± 36	341 ± 35	-0.07 ± 0.05	-0.02 ± 0.08	13.1
inn2 s24	159h11m45.6s	-27d31m53.4s	15.9	94.9	3951 ± 32	409 ± 44	-0.07 ± 0.06	0.18 ± 0.07	18.7
inn2 s25	159h12m00.0s	-27d32m13.9s	20.7	103.6	3800 ± 106	400 ± 104	0.0 ± 0.1	-0.0 ± 0.1	15.2
inn2 s26	159h11m38.4s	-27d32m09.6s	15.5	101.8	3883 ± 36	469 ± 45	-0.11 ± 0.06	0.12 ± 0.04	20.3
inn2 s27	159h11m45.6s	-27d32m30.1s	19.6	110.0	3662 ± 56	[1000.0]	-0.13 ± 0.09	-0.1 ± 0.1	14.5
inn2 s28	159h11m20.4s	-27d32m25.8s	14.3	108.4	3935 ± 21	374 ± 30	0.02 ± 0.04	0.17 ± 0.04	27.9

Table 4.1 - continued.

ID	RA	DEC	R	PA	V_{LOS}	σ_{LOS}	h_3	h_4	S/N
	(J2000)	(J2000)	(arcsec)	($^\circ$)	(km s^{-1})	(km s^{-1})			
(1)	(2)	(3)	(4)	(5)	(6)	(7)	(8)	(9)	(10)
inn2 s29	159h11m31.2s	-27d32m44.2s	19.5	115.2	3731 ± 37	209 ± 44	-0.0 ± 0.1	0.0 ± 0.1	16.8
inn2 s30	159h11m02.4s	-27d32m35.5s	14.1	112.1	3789 ± 25	390 ± 23	-0.02 ± 0.04	-0.04 ± 0.04	26.8
inn2 s31	159h11m09.6s	-27d32m51.7s	18.4	117.9	3750 ± 67	556 ± 87	-0.04 ± 0.08	0.07 ± 0.07	14.5
inn2 s32	159h10m37.2s	-27d32m37.0s	13.6	112.6	3818 ± 24	438 ± 29	0.07 ± 0.04	0.08 ± 0.04	25.3
inn2 s33	159h10m44.4s	-27d32m55.3s	18.0	119.1	4058 ± 41	300 ± 57	-0.0 ± 0.1	0.10 ± 0.06	15.1
inn2 s34	159h10m08.4s	-27d32m39.5s	16.4	113.6	3895 ± 23	162 ± 28	-0.09 ± 0.06	-0.0 ± 0.1	21.9
inn2 s35	159h10m19.2s	-27d32m55.7s	19.0	119.2	3590 ± 30	319 ± 35	0.00 ± 0.09	-0.03 ± 0.06	16.5
inn2 s36	159h09m54.0s	-27d32m46.7s	19.8	116.1	3925 ± 28	319 ± 26	-0.07 ± 0.04	0.08 ± 0.07	19.7
out1 s14	159h08m42.0s	-27d32m51.7s	34.1	117.9	3722 ± 52	404 ± 55	0.02 ± 0.08	0.01 ± 0.08	12.8
out1 s15	159h08m20.4s	-27d32m22.2s	36.2	107.0	3863 ± 74	517 ± 57	-0.11 ± 0.08	-0.11 ± 0.08	17.0
out1 s16	159h08m49.2s	-27d32m30.8s	30.2	110.3	4011 ± 41	389 ± 54	-0.12 ± 0.07	0.13 ± 0.07	13.5
out1 s17	159h08m13.2s	-27d31m49.1s	36.6	93.1	4130 ± 21	159 ± 27	-0.0 ± 0.1	0.06 ± 0.07	17.3
out1 s18	159h08m38.4s	-27d31m55.6s	30.5	95.9	4051 ± 12	198 ± 15	-0.10 ± 0.04	0.11 ± 0.05	40.8
out1 s19	159h08m13.2s	-27d31m23.2s	36.8	81.9	4108 ± 10	178 ± 9	-0.12 ± 0.04	-0.07 ± 0.05	43.6
out1 s20	159h08m38.4s	-27d31m28.6s	30.5	84.2	4067 ± 3	188 ± 5	0.05 ± 0.01	0.07 ± 0.02	82.2
out1 s21	159h08m16.8s	-27d30m58.7s	37.2	71.8	4068 ± 6	191 ± 9	-0.04 ± 0.03	0.11 ± 0.03	47.0
out1 s22	159h08m20.4s	-27d30m47.5s	37.3	67.6	3998 ± 10	308 ± 12	-0.20 ± 0.03	0.21 ± 0.03	36.4
out1 s23	159h08m45.6s	-27d30m36.4s	32.8	63.5	4030 ± 5	219 ± 7	-0.02 ± 0.02	0.09 ± 0.02	48.8
out1 s24	159h08m45.6s	-27d30m15.5s	35.6	56.7	4024 ± 16	291 ± 20	0.12 ± 0.04	0.19 ± 0.04	20.1
out1 s25	159h09m21.6s	-27d30m23.8s	27.6	59.3	4068 ± 13	271 ± 17	0.12 ± 0.04	0.14 ± 0.04	28.5
out1 s26	159h09m07.2s	-27d29m58.9s	34.4	52.0	3915 ± 60	423 ± 56	0.1 ± 0.1	-0.1 ± 0.1	15.1
out1 s27	159h09m14.4s	-27d29m52.1s	34.5	50.2	4905 ± 138	916 ± 168	0.05 ± 0.07	-0.0 ± 0.1	10.5
out1 s28	159h09m46.8s	-27d30m02.2s	28.0	52.9	4032 ± 72	645 ± 82	0.10 ± 0.05	0.00 ± 0.08	10.0
out1 s30	159h10m15.6s	-27d29m56.8s	26.7	51.4	4203 ± 55	476 ± 53	0.18 ± 0.06	0.10 ± 0.09	13.7
out1 s32	159h10m48.0s	-27d29m53.9s	26.6	50.7	3943 ± 27	267 ± 32	-0.03 ± 0.07	0.06 ± 0.06	23.0
out1 s34	159h11m34.8s	-27d30m01.1s	28.0	52.6	3584 ± 52	874 ± 63	-0.21 ± 0.05	0.19 ± 0.06	23.0
out1 s36	159h12m03.6s	-27d29m53.9s	33.3	50.7	3732 ± 49	552 ± 60	-0.11 ± 0.06	0.10 ± 0.06	15.1

Table 4.1 - continued.

ID	RA	DEC	R	PA	V_{LOS}	σ_{LOS}	h_3	h_4	S/N
	(J2000)	(J2000)	(arcsec)	($^{\circ}$)	(km s^{-1})	(km s^{-1})			
(1)	(2)	(3)	(4)	(5)	(6)	(7)	(8)	(9)	(10)
out2 s13	159h12m25.2s	-27d30m10.8s	33.9	55.3	4184 ± 101	456 ± 123	0.04 ± 0.06	0.0 ± 0.2	17.7
out2 s14	159h13m04.8s	-27d30m54.4s	37.0	70.1	3609 ± 51	794 ± 75	0.08 ± 0.05	0.19 ± 0.04	12.5
out2 s15	159h12m21.6s	-27d30m36.4s	29.3	63.5	3879 ± 28	368 ± 33	-0.11 ± 0.04	0.04 ± 0.06	22.6
out2 s16	159h13m12.0s	-27d31m26.8s	37.1	83.4	3498 ± 48	388 ± 40	-0.2 ± 0.1	-0.2 ± 0.1	12.2
out2 s17	159h12m43.2s	-27d31m18.8s	30.4	80.0	4078 ± 32	237 ± 28	0.08 ± 0.07	-0.0 ± 0.1	14.8
out2 s18	159h13m12.0s	-27d31m53.4s	37.0	94.9	3844 ± 38	174 ± 33	0.0 ± 0.1	-0.17 ± 0.09	12.5
out2 s19	159h12m43.2s	-27d31m47.3s	29.8	92.3	3613 ± 57	658 ± 83	0.00 ± 0.08	0.20 ± 0.05	16.3
out2 s20	159h13m01.2s	-27d32m08.9s	34.9	101.5	3794 ± 47	460 ± 23	0.11 ± 0.09	-0.01 ± 0.07	14.9
out2 s21	159h12m39.6s	-27d32m06.0s	29.5	100.3	3524 ± 57	448 ± 53	0.09 ± 0.05	-0.02 ± 0.09	16.0
out2 s26	159h12m03.6s	-27d32m59.3s	27.6	120.4	3669 ± 44	562 ± 50	0.03 ± 0.05	-0.05 ± 0.07	14.4
out2 s28	159h11m45.6s	-27d33m12.2s	27.2	124.4	3654 ± 72	508 ± 83	0.05 ± 0.07	-0.0 ± 0.1	12.5
out2 s30	159h11m20.4s	-27d33m23.0s	26.6	127.5	3722 ± 23	748 ± 38	0.19 ± 0.06	0.30 ± 0.05	17.8
out2 s31	159h11m34.8s	-27d33m46.4s	33.2	133.3	3691 ± 118	446 ± 111	0.1 ± 0.2	0.3 ± 0.2	10.0
out2 s32	159h10m51.6s	-27d33m28.1s	26.2	128.8	3982 ± 87	810 ± 58	0.03 ± 0.07	-0.14 ± 0.05	17.6
out2 s33	159h11m06.0s	-27d33m52.2s	32.6	134.6	3838 ± 13	270 ± 15	-0.23 ± 0.06	[-0.3]	17.0
out2 s34	159h10m04.8s	-27d33m20.5s	25.9	126.8	4277 ± 79	533 ± 56	-0.0 ± 0.1	-0.15 ± 0.06	23.5
out2 s35	159h09m39.6s	-27d33m13.7s	27.2	124.8	3789 ± 32	347 ± 33	0.00 ± 0.09	0.01 ± 0.09	21.1
out2 s37	159h09m21.6s	-27d33m26.6s	32.4	128.4	4300 ± 82	[1000.0]	0.13 ± 0.06	-0.16 ± 0.06	18.8

Chapter 5

The Hydra I cluster core. I Stellar populations in the
cD galaxy NGC 3311 (article)¹

¹ Reproduced by permission of Astronomy & Astrophysics, ©ESO

The Hydra I cluster core

I. Stellar populations in the cD galaxy NGC 3311^{★,★★}

C. E. Barbosa^{1,2}, M. Arnaboldi^{1,3}, L. Coccato¹, M. Hilker¹, C. Mendes de Oliveira², and T. Richtler⁴

¹ European Southern Observatory, Karl-Schwarzschild-Straße 2, 85748 Garching, Germany
e-mail: carlos.barbosa@usp.br

² Universidade de São Paulo, IAG, Departamento de Astronomia, Rua do Matão 1226, São Paulo, SP, Brazil

³ INAF, Osservatorio Astronomico di Torino, Strada Osservatorio 20, 10025 Pino Torinese, Italy

⁴ Departamento de Astronomia, Universidad de Concepción, Concepción, Chile

Received 15 January 2016 / Accepted 7 March 2016

ABSTRACT

Context. The history of the mass assembly of brightest cluster galaxies may be studied by mapping the stellar populations at large radial distances from the galaxy centre, where the dynamical times are long and preserve the chemodynamical signatures of the accretion events.

Aims. We provide extended and robust measurements of the stellar population parameters in NGC 3311, the cD galaxy at the centre of the Hydra I cluster, and out to three effective radii. We wish to characterize the processes that drove the build-up of the stellar light at all these radii.

Methods. We obtained the spectra from several regions in NGC 3311 covering an area of ~ 3 arcmin² in the wavelength range $4800 \leq \lambda(\text{\AA}) \leq 5800$, using the FORS2 spectrograph at the Very Large Telescope in the Mask exchange unit (MXU) mode. We measured the equivalent widths of seven absorption-features defined in the Lick/IDS system, which were modelled by single stellar populations, to provide luminosity-weighted ages, metallicities, and alpha element abundances.

Results. The trends in the Lick indices and the distribution of the stellar population parameters indicate that the stars of NGC 3311 may be divided in two radial regimes, one within and the another beyond one effective radius, $R_e = 8.4$ kpc, similar to the distinction between the inner galaxy and the external halo derived from the NGC 3311 velocity dispersion profile. The inner galaxy ($R \leq R_e$) is old (age ~ 14 Gyr), has negative metallicity gradients and positive alpha element gradients. The external halo is also very old, but has a negative age gradient. The metal and element abundances of the external halo both have a large scatter, indicating that stars from a variety of satellites with different masses have been accreted. The region in the extended halo associated with the off-centred envelope at $0^\circ < PA < 90^\circ$ has higher metallicity with respect to the symmetric external halo.

Conclusions. The different stellar populations in the inner galaxy and extended halo reflect the dominance of in situ stars in the former and the accreted origin for the large majority of the stars in the latter. The low value of the velocity dispersion in the inner galaxy indicates that its stars are bound to the galaxy's gravitational potential, and the abundances and gradients suggest that the inner galaxy is formed in an outside-in scenario of merging gas-rich lumps, reminiscent of the first phase of galaxy formation. The external halo has a higher velocity dispersion, it is dynamically hotter than the galaxy and its stars are gravitationally driven by the cluster's gravitational potential. The stars in the external halo were removed from their parent galaxies, either disks with truncated star formation, or the outer regions of early-type galaxies. Late mass accretion at large radii is now coming from the tidal stripping of stars from dwarfs and S0 galaxies. These results provide supporting evidence for the recent theoretical models of formation of massive ellipticals as a two-phase process.

Key words. galaxies: clusters: individual: Hydra I – galaxies: individual: NGC 3311 – galaxies: haloes – galaxies: evolution – galaxies: formation – galaxies: stellar content

1. Introduction

Brightest cluster galaxies (BCGs) are the giant early-type galaxies found at the core of galaxy clusters. BCGs often display extended, diffuse stellar haloes, known as cD envelopes, which are believed to be composed of stars that were stripped from satellite galaxies interacting with the cluster's halo by tidal interactions and dynamical friction (Gallagher & Ostriker 1972;

Dressler 1979). Owing to the long relaxation times at large radii, stellar haloes are not well-mixed and, therefore, preserve chemodynamical signatures of the past accretion events, which have survived to the present day and can be used to access the history of the galaxy mass assembly.

The initial processes of galaxy formation through monolithic collapse set abundance gradients, which are modified by the subsequent history of accretion over time. Initial strong metallicity gradients arise naturally in galaxies formed by the collapse of gas clouds in the monolithic scenario (Larson 1974) or by the merging of numerous gas-rich sub-galaxies (Kobayashi 2004). The occurrence of major mergers is able to dilute metallicity

* Based on observations made with ESO Telescopes at the La Silla Paranal Observatory under programme ID 088.B-0448(B) PI Richtler.

** Table 1 is only available at the CDS via anonymous ftp to cdsarc.u-strasbg.fr (130.79.128.5) or via <http://cdsarc.u-strasbg.fr/viz-bin/qcat?J/A+A/589/A139>

gradients by mixing stars in the central regions of galaxies (White 1980; Kobayashi 2004), while minor mergers may form gradients at larger radii by depositing stars with different abundances (Villumsen 1983; Hirschmann et al. 2015). Observations in the last ten years, such as the population of compact massive objects at high redshift (van Dokkum et al. 2008; van der Wel et al. 2014) and the evolution of sizes and concentrations with redshift (Naab et al. 2009), suggest that massive ellipticals are formed by different processes over time in the two-phase scenario (De Lucia & Blaizot 2007; Oser et al. 2010). Galaxies are formed at high redshift ($z \gtrsim 3$) during star formation events triggered by rapid dissipative processes, such as cold accretion of gas through filaments (Kereš et al. 2005; Dekel et al. 2009) or gas-rich major mergers (Robertson et al. 2006), followed by an extended accretion of stars of smaller galaxies, usually at large galactic radii.

In the two-phase scenario, stars inhabiting a halo can be divided into two categories according to the sub-halo in which they were formed: in situ and accreted. The in situ stars were formed in the most massive sub-halo of a galaxy during the first phase of galaxy formation, which resulted in stars with relatively high metallicity, owing to their deep gravitational potential that can retain the metals ejected by supernovae (Tremonti et al. 2004), and high alpha element abundance that results from the rapid time-scales of star formation (see, e.g. Thomas et al. 2005). The accreted stars were formed in galaxies with a variety of masses and, consequently, have different abundances and ages. Spatially, in situ stars are centrally concentrated and usually dominate the light in the central ~ 5 – 10 kpc of elliptical galaxies, contributing significantly to the stellar halo out to ~ 30 kpc, while the accreted stars are less centrally concentrated and dominate the light in the outer regions (Oser et al. 2010; Cooper et al. 2013). From a dynamical point of view, in situ stars have experienced violent relaxation processes in the early phases of the galaxy formation, while the accreted stars may still be unrelaxed, especially at the largest radii, and thus may exhibit an inhomogeneous spatial distribution, which survived to the present day (Cooper et al. 2015).

The observational test for this model of galaxy formation relies on the measurement of stellar population parameters in early-type galaxies out to large radii, but the low surface brightness in these regions makes spectroscopic measurements difficult. Nevertheless, current state-of-the-art investigations seem in agreement with predictions from the two-phase scenario. In the case of NGC 4889 in the Coma cluster, Coccato et al. (2010b) show that there are different populations in the core and halo, consistent with the idea of accreted stars dominating the light at radii $R > 18$ kpc. Similarly, differences between the inner and outer stellar populations have been found for other cD galaxies such as NGC 3311 (Coccato et al. 2011), M49 (Mihos et al. 2013), M87 (Virgo cluster, Montes et al. 2014), and NGC 6166 (Abell 2199, Bender et al. 2015), and even in several non-BCGs (Pastorello et al. 2014). However, these studies provide limited information about the distribution of the metal abundances and ages, because they were performed either by photometry, which has good spatial information but does not provide detailed abundances and ages, or by long-slit spectroscopy, which is limited to the slit position, but provides abundance and age information in detail. Ideally we would like to be able to collect the metal abundance and age information over the entire spatial extension of the galaxy light, for an extensive mapping of its physical properties.

In this work we study the galaxy NGC 3311, the BCG of the Hydra I cluster, to provide the first bi-dimensional and large-scale view of the stellar populations of this system which, together with the detailed kinematic study (Paper II), can shed

further insights into a number of specific formation scenarios that have been recently proposed for this system. NGC 3311 has a radial velocity of ~ 3800 km s $^{-1}$ and a positive velocity dispersion profile (Ventimiglia et al. 2010), indicating that its extended halo is driven by the cluster potential at $R > 8$ kpc and may be composed of the debris shredded from satellite galaxies falling into the cluster's centre (Coccato et al. 2011). Furthermore, this kind of rising velocity dispersion profile seems to be asymmetric at large radii, as observed at different position angles (Ventimiglia et al. 2010; Richtler et al. 2011). A scenario of ongoing interactions and extended build-up of the stellar mass is also supported by the presence of multiple components in the line-of-sight velocity distribution (LOSVD) of the planetary nebulae in NGC 3311 (Ventimiglia et al. 2011), of substructures and tails in the halo light distribution (Arnaboldi et al. 2012), and by the distribution of dwarf galaxies around NGC 3311 (Misgeld et al. 2008).

In the accompanying paper on the kinematics of NGC 3311 (Paper II, Hilker et al., in prep.), we focus on the kinematic properties, discuss the implications for the mass profile of NGC 3311, and explore possible formation histories of the massive star clusters observed by Misgeld et al. (2011). In the current paper, we present the spatial map of the stellar population parameters, ages, and abundances out to large radii. The article is organized as follows: in Sect. 2, we describe our data set and the methods of data reduction. In Sect. 3, we describe the measurements for the absorption features using Lick indices and, in Sect. 4, we convert this information into physical parameters of the stellar populations. In Sect. 5, we discuss the correspondence of the stellar populations with kinematic and morphological structures, which are discussed in detail in Sect. 6. In Sect. 7, we discuss our main findings in line with recent observational and theoretical works and provide an updated view of the NGC 3311 halo formation, based on recent works. Finally, we proceed to an overview and conclusion of this work in Sect. 8. We assume a distance to the core of the Hydra cluster of 50.7 Mpc, calculated by the Hubble flow, considering a radial velocity of 3777 km s $^{-1}$ (Struble & Rood 1999) and $H_0 = 70.5$ km s $^{-1}$ Mpc $^{-1}$ (Komatsu et al. 2009). The adopted effective radius for NGC 3311 is $R_e = 8.4$ kpc, which is the mean value of the isophotal analysis in the V-band from Arnaboldi et al. (2012).

2. Observations and data reduction

In this study, we explore a new spectroscopic data set for the Hydra I cluster. The data were observed at the Very Large Telescope at Paranal, Chile, using the UT1 8.2 m telescope with the FOCal Reducer/low dispersion Spectrograph 2 (FOR2, Appenzeller et al. 1998) in the multi-object spectroscopic mode with the mask exchange unit (MXU), obtained under ESO programme ID 088.B-0448B (PI: Richtler).

NGC 3311 spans a large area of the sky, and thus its observation out to large galactocentric distances requires a field of view beyond the area of most integral field units available to date. To survey an area of 3×3 arcmin 2 around NGC 3311, which translates into projected distances of ~ 30 kpc, we sampled regions of the stellar halo that were devoid of contamination of point sources with small slits, with a typical size of $1'' \times 5''$, using six masks that sample the stellar halo in shells: cen1, cen2, inn1, inn2, out1, and out2. We used the grism 1400V with the standard collimator to obtain a dispersion of 0.25 Å pixel $^{-1}$, which gives a spectral resolution of $R = 2100$ at 5200 Å. The exposure times for the cen; and inn; masks, which cover the central

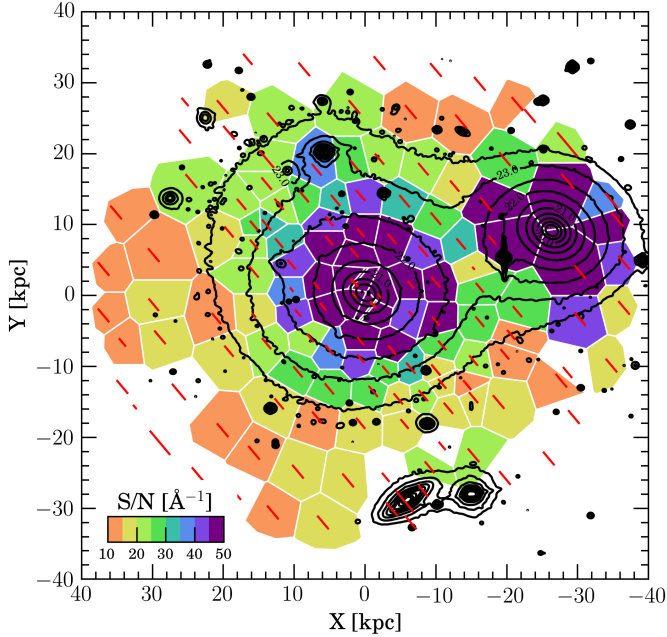


Fig. 1. Distribution of the signal-to-noise (S/N) of the scientific spectra in our sample. The position of the slits is shown as red bars, and the colours of the polygon, calculated by Voronoi Tessellation, indicate the S/N according to the scale in the colour bar in the bottom left corner. Slits with white background were excluded from the analysis owing to their low quality ($S/N < 10$). Black lines show the V-band contours in the range from 20 to 23.5 mag arcsec⁻² in intervals of 0.5 mag arcsec⁻², from Arnaboldi et al. (2012). The geometry of the polygons is shown hereafter in all the other maps in this study.

region, are 2×1400 s, while they are 6×1400 s for the out-masks. This observing strategy resulted in 135 slitlets dedicated to the observation of NGC 3311 and NGC 3309. The numbers of extracted spectra is smaller though, because we set a minimum signal-to-noise (S/N) of 10 in our observations, to constrain the stellar population parameters. A total of 118 spectra are used in our analysis. They are indicated by the red slits in Fig. 1.

The reduction processes for extracting the scientific spectra, including bias subtraction, flat fielding correction, and wavelength calibration, were performed using custom IRAF scripts. We used the long-slit spectrum of a spectrophotometric standard star, HD 102070, to test the effect of the flux calibration on the Lick indices, which are used for the analysis of the stellar populations. This test shows that the median change in the equivalent width of the indices is of 0.5% and, therefore, there is no need to flux to calibrate our spectra. The spectrum for sky subtraction of each slit was obtained simultaneously to the observations at slits in the periphery of the CCD, using the same x -axis position of the data, which ensured that science and sky spectra share the same wavelength range and exposure time for the subtraction. The wavelength range for spectra varies slightly as a function of the x -axis in the CCD, but in most cases the interval $4800 \lesssim \lambda$ (Å) $\lesssim 5800$ is available. For consistency, we calculated the signal-to-noise ratio per angstrom (S/N) of each spectrum in the range $5200 \leq \lambda$ (Å) ≤ 5500 , and the distribution of the S/N is presented by the polygons in Fig. 1. In this case, and in all the maps shown in this work, we present the distribution of parameters using these polygons, which were calculated using Voronoi tessellation and the V-band contours from observations in Arnaboldi et al. (2012) to improve the visualization.

3. Line strength indices

3.1. Equivalent widths of Lick indices

The stellar population properties are studied by the analysis of spectral absorption features using line-strength indices in the Lick/IDS system (Worthey 1994; Trager et al. 1998), which consists of calculating the equivalent widths (EW) of absorption features in a given central band amidst two pseudo-continuum sidebands. This process was carried out as follows:

We obtained the LOSVD for each spectrum using the pPXF code (Cappellari & Emsellem 2004) taking into account four Gauss-Hermite LOSVD moments and additive polynomials of order 12 to compensate for the variations in the continuum. The adopted templates are single stellar population (SSP) models computed with the MILES stellar library (Sánchez-Blázquez et al. 2006), with ages from 1 to 15 Gyr, metallicities in the range $-0.7 \leq [Z/H] \leq 0.2$, and computed with a Salpeter Initial Mass Function with logarithmic slope of -1.3 . The template spectra from the MILES library have a resolution of $FWHM = 2.5$ Å, which is slightly larger than that our observations, $FWHM = 2.1$ Å. We then convolved our spectra with a Gaussian filter to match the resolution of the MILES stellar library. In most cases, the best fit was obtained by a linear combination of a small number of SSPs, but in a few cases a secondary nebular component was accounted for in the templates, which included emission lines for H β (4861 Å), NI (5200 Å), and [OIII] (4957 Å and 5007 Å at fixed ratio of 1:3), which are subtracted off the observed spectrum, if present. For the measurement of the Lick indices, we convolve our spectra to match the resolution of the Lick/IDS system, using Gaussian filters of varied resolution according to Worthey & Ottaviani (1997), before measuring the EWs using a custom Python code.

To correct for the intrinsic broadening of the absorption features, we used the ratio of the equivalent widths in the best fit from pPXF before and after the LOSVD convolution, as in Coccato et al. (2010a), using the relation

$$I = \frac{I'_0}{I'_{\text{LOSVD}}} \cdot I_{\text{meas}}, \quad (1)$$

where I'_{LOSVD} and I'_0 are the indices measured in the best fit spectra from pPXF with and without the LOSVD convolution, and I_{meas} and I are the measured and the corrected indices for the extracted spectra.

Finally, we also corrected the indices for the instrumental offsets by the observation of the standard star, HD 102070, for which Lick indices were determined by Schiavon (2007). Although not all indices are determined for HD 102070 in the spectral region of our data set, the relatively small value of the correction in most cases and the good agreement with previous measurements for NGC 3311 from Loubser & Sánchez-Blázquez (2012) assure us that any systematics are relatively small. Uncertainties for the Lick indices were estimated using Monte Carlo simulations with perturbations in the velocity dispersion and the addition of a bootstrapped noise, based on the residuals of the pPXF models. In Fig. 2, we show typical examples of the extracted spectrum in our data set, including the best fit and residuals calculated with pPXF and the position of the Lick indices bands. In Cols. 5 to 11 of Table 1 we show the values for the corrected Lick indices of our extracted spectra.

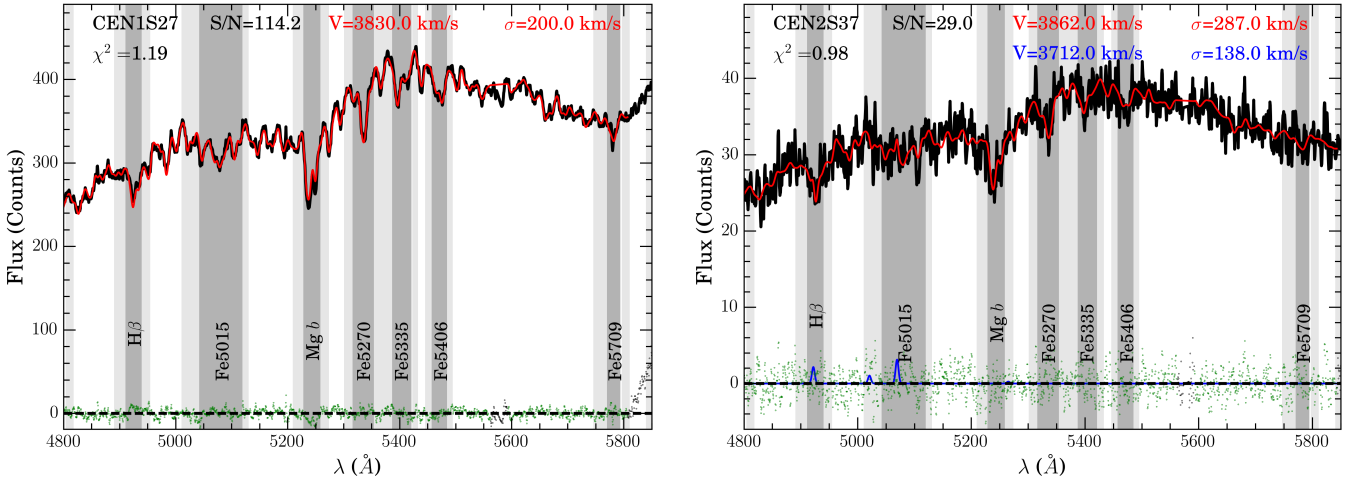


Fig. 2. Examples of the LOSVD fitting process with pPXF in our data set. The sky subtracted spectra (black) are superposed by the best fit templates (red) obtained by a combination of SSP spectra from the MILES library (Sánchez-Blázquez et al. 2006), emission lines, and an additive polynomial of order 12, convolved with the line-of-sight velocity distribution with four moments. The best fit emission lines (blue) are subtracted from the spectra to avoid contamination on top of the absorption features. Residuals from the fits are shown in the bottom (green dots). The Lick indices are measured at the location of the vertical shades by the measurement of the equivalent width in central bands (dark grey) compared to the level of the two pseudo continuum side bands (light grey).

3.2. Effect of systematic errors resulting from sky subtraction

Elliptical galaxies usually present large variances in their stellar population properties at large radii, as observed in high S/N integral field observations from the SAURON survey (Kuntschner et al. 2006, 2010), and our results show similar trends. One question is whether varying S/N from the inner regions to large radii may be the primary source of scatter in the derived stellar population parameters, as function of radius. To verify whether this result is related to different S/N, we performed the following test. Since the main source of uncertainty is the sky subtraction, we performed several measurements of the Lick indices with different values of under/over sky subtraction at the level of $\pm 1\%$ of the total sky in each spectrum. This percentage was obtained by a visual inspection of our spectra after the inclusion of this systematic error, which showed that errors of this magnitude would leave recognizable features that resemble the sky spectra in the 2D spectra of low signal-to-noise spectra ($S/N \sim 15$).

The result of this test is presented in Fig. A.1, where the difference of the EW of the indices, δI_{Lick} , is plotted as a function of radius. The deviations are calculated using a running standard deviation, indicated by the grey shaded area. For a typical spectrum with $S/N \sim 20$, the variations of the measured EWs for the Lick indices are $\delta H\beta = 0.21 \text{ \AA}$ (12%), $\delta Fe5015 = 0.43 \text{ \AA}$ (25%), $\delta Mg b = 0.35 \text{ \AA}$ (11%), $\delta Fe5270 = 0.22 \text{ \AA}$ (18%), $\delta Fe5335 = 0.30 \text{ \AA}$ (8%), $\delta Fe5406 = 0.20 \text{ \AA}$ (10%), and $\delta Fe5709 = 0.06 \text{ \AA}$ (6%). The same test is also performed for the stellar population parameters, using the methods described in Sect. 4, resulting in changes of $\delta \log \text{Age (years)} = 0.05 \text{ dex}$, $\delta [Z/H] = 0.48 \text{ dex}$, $\delta [\alpha/Fe] = 0.14 \text{ dex}$, and $\delta [Fe/H] = 0.45 \text{ dex}$ (see Fig. A.2). In the following analysis, we include the results of this test in Figs. 4 and 7, when we compare this systematic effect with the observed scatter of the Lick indices and with the scatter of the stellar population parameters respectively.

3.3. Spatial distribution and gradients of the Lick indices

The maps of the EWs for six measured Lick indices are presented in Fig. 3, including $H\beta$, Fe5015, Mg *b*, Fe5270, Fe5335,

and Fe5406. The index Fe5709 is not displayed in the figure because it is measured only in a fraction of our spectra, owing to issues with the red continuum for some observational masks, but it is also used for the modelling of stellar populations whenever possible. These maps indicate that each index has a particular pattern, and that the central region of NGC 3311 stands out by having a relatively weaker $H\beta$ absorption and stronger metal line indices than the outskirts.

The large-scale behaviour of the Lick indices can be observed in Fig. 4, where the Lick indices are displayed as a function of the projected galactic log-radial distance from the centre of NGC 3311, in units of effective radius. The results from our measurements are shown as circles of different colours according to the S/N of the spectra. We also include a comparison with the long-slit data from the literature including Loubser et al. (2009), Coccatto et al. (2011), and Loubser & Sánchez-Blázquez (2012). Our indices are not only in good agreement with the literature, but also complement the data from Loubser & Sánchez-Blázquez (2012) by extending the radial coverage.

As we already commented in Sect. 3.2, one important characteristic of Fig. 4 is the large scatter in the external halo. This scatter is larger than that caused by the systematic effects of over/under subtraction of the sky by $\pm 1\%$, shown in the figure by the grey shaded areas. Hence we also expect a large true scatter in the abundance and age distributions at large radii. Further evidence for the intrinsic nature of the scatter at $R \sim R_e$ and outwards is the significant variance of the stellar population parameters derived for the highest S/N spectra in the data set, shown by the dark blue circles.

Another important feature of Fig. 4 is the presence of a break in the radial gradients, from the inner to the outer profiles. This break occurs at about one effective radius ($R_e = 8.4 \text{ kpc}$), which is close to the expected transition between the in situ and accreted components according to models (e.g. Cooper et al. 2015). Therefore, to quantify the mean trends of the Lick indices, we divided them into two radial regions, the inner galaxy ($R \leq R_e$), and the extended halo ($R > R_e$). In each of these regions, we

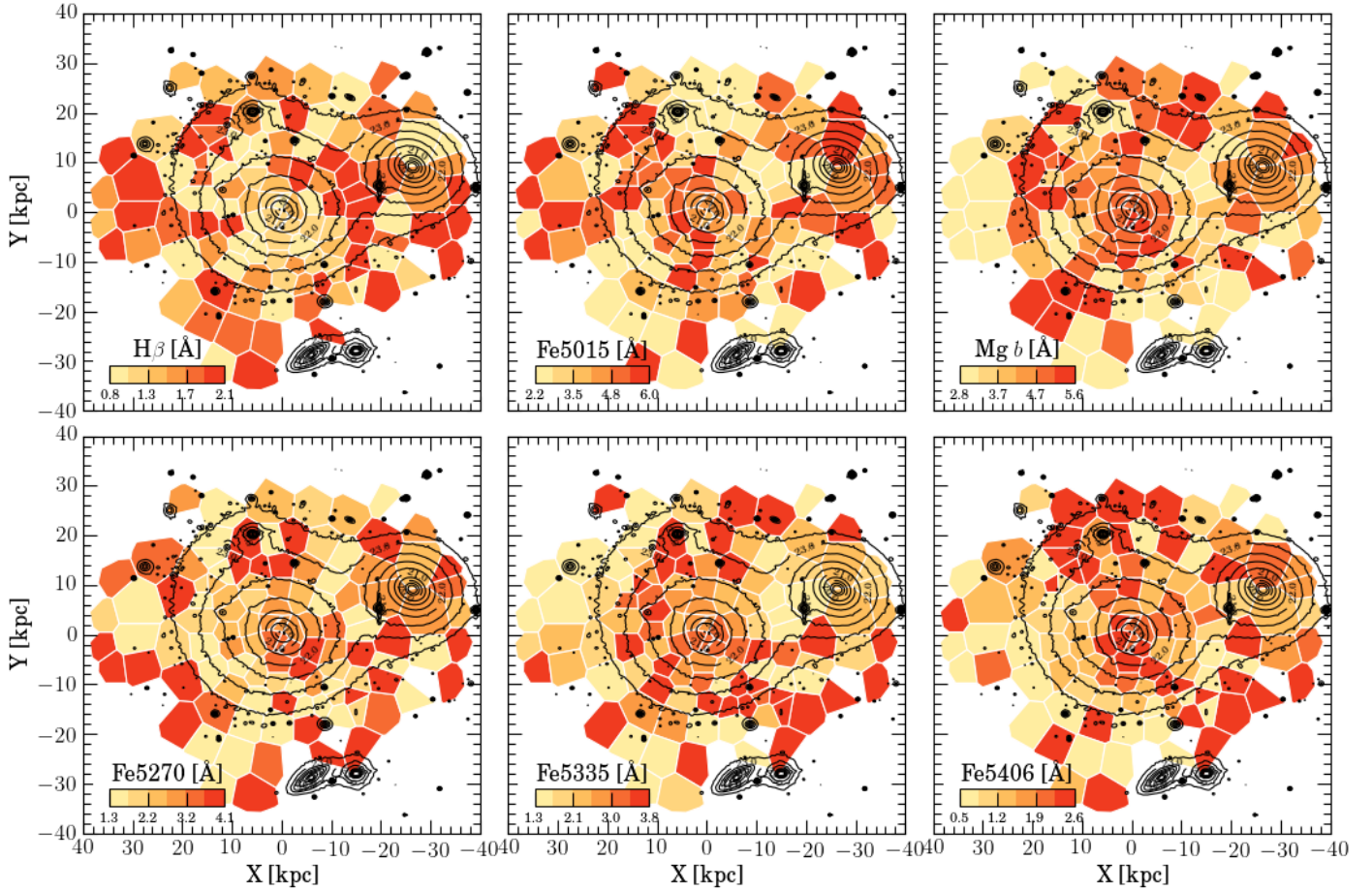


Fig. 3. Spatial distribution of the equivalent width of six Lick indices: $H\beta$, Fe5015, Mg b , Fe5270, Fe5335, and Fe5406. Black lines indicate the contours of the V -band image from [Arnaboldi et al. \(2012\)](#) between 20 to 23.5 mag arcsec $^{-2}$ in steps of 0.5 mag arcsec $^{-2}$. These maps illustrate the presence of a homogeneous inner region and a large scatter at large radii, for all indices.

measured the radial gradients using the equation

$$I_{\text{Lick}}(X) = I_{\text{Lick}}(0) + \Delta I_{\text{Lick}} \cdot X, \quad (2)$$

where $X = \log(R/R_e)$ is the logarithm of the projected galactocentric distance R , normalized by the effective radius R_e , $I_{\text{Lick}}(X)$ are the corrected Lick indices as a function of X , and ΔI_{Lick} is the calculated gradient. The gradient is determined from a χ^2 minimization weighted by the uncertainties of the data points. We do not remove any outliers, but we implement a geometric selection by excluding the spectra that are i) very close to NGC 3309 and ii) on top of HCC 007. The coefficients of the linear regressions are presented in [Table 2](#) and the best fit is shown by the black dashed lines in [Fig. 4](#).

The main result of this section is summarized in [Fig. 4](#). The distribution of the measured values for the Lick indices in the inner galaxy are different from the distribution of the values of the same indices in the external halo. The break occurs at $R = R_e$ for all indices. This implies that independent of the stellar population models that may translate the equivalent widths of the absorption features into other physically relevant quantities, there is going to be a break in the stellar population properties with different values for the inner galaxy and the external halo.

4. Stellar populations

We adopted the model from [Thomas et al. \(2011\)](#) to derive luminosity-weighted stellar population parameters, i.e. age,

Table 2. Linear regression coefficients for the Lick indices as function of radius.

Index	Inner galaxy (1)		Extended halo (2)	
	$I_{\text{Lick}}(0)$ (Å)	ΔI_{Lick} (Å/dex)	$I_{\text{Lick}}(0)$ (Å)	ΔI_{Lick} (Å/dex)
$H\beta$	1.1 ± 0.1	-0.1 ± 0.2	1.5 ± 0.1	0.2 ± 0.5
Fe5015	5.6 ± 0.3	1.9 ± 0.5	4.1 ± 0.4	-2.8 ± 1.3
Mg b	4.7 ± 0.1	-0.7 ± 0.2	4.4 ± 0.2	-1.8 ± 0.8
Fe5270	2.7 ± 0.2	-0.7 ± 0.4	2.4 ± 0.2	1.5 ± 0.9
Fe5335	2.7 ± 0.1	-0.4 ± 0.2	2.7 ± 0.2	-0.1 ± 0.9
Fe5406	2.0 ± 0.2	-0.4 ± 0.3	1.8 ± 0.2	0.5 ± 0.8
Fe5709	0.7 ± 0.1	-0.1 ± 0.1	0.6 ± 0.1	1.1 ± 0.6

Notes. (1) Linear regression coefficients for the Lick indices as function of radius in the inner galaxy ($R \leq R_e$), derived according to [Eq. \(2\)](#), where $I_{\text{Lick}}(0)$ indicates the value of the indices at one effective radius and ΔI_{Lick} indicates the gradients. (2) Same as (1) for the external halo ($R > R_e$) region.

total metallicity ($[Z/H]$), and alpha element abundance ($[\alpha/Fe]$), which are computed using a Salpeter initial stellar mass function. We also estimated the iron abundance using the relation ([Thomas et al. 2003](#))

$$[Z/H] = [Fe/H] + A[\alpha/Fe], \quad (3)$$

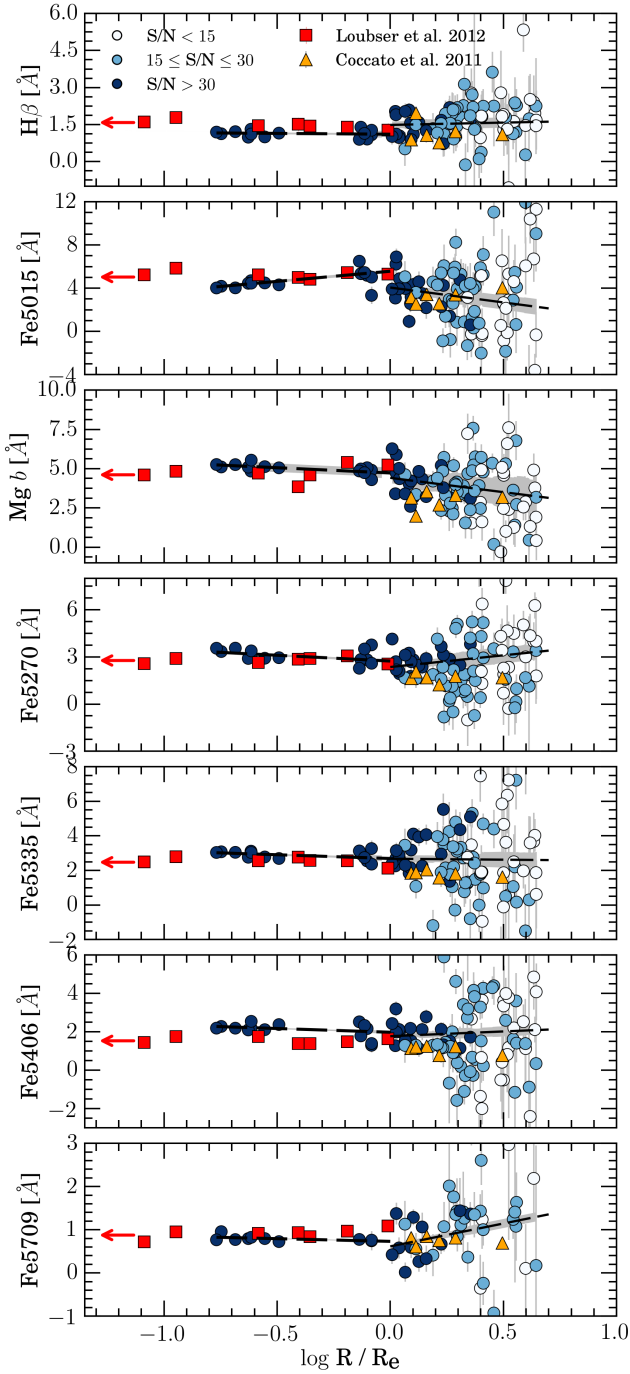


Fig. 4. Lick indices as a function of the distance from the centre of NGC 3311. The EWs measured for our spectra are shown by full circles, with different colours according to their S/N, as indicated in the top panel. Long-slit data from the literature is also displayed, including Coccatto et al. (2011), as orange triangles, Loubser & Sánchez-Blázquez (2012) as red squares and Loubser et al. (2009) as red arrows. The two black dashed lines indicate the gradients obtained by linear regression in the two regions corresponding to the inner galaxy and the external halo. The grey shaded areas around the dashed lines represent the variance in the equivalent width generated by a systematic error in the sky subtraction by $\pm 1\%$. The different gradients indicate different mechanisms for the assembly of the stellar haloes.

considering the factor $A = 0.94$ (Trager et al. 2000). All those parameters will help us to understand the mass assembly history of stars in NGC 3311. The inferred ages may constrain the

time since the last burst of star formation, the metallicities, are a proxy for the mass of the parent halo where these stars were formed and the alpha element abundances set constraints on the star formation time-scales (Thomas et al. 2005).

Before we describe in detail the methods to compute the stellar population parameters, we list the distinct features of this modelling approach. We assume that the SSP approximation is valid locally for each of our spectra, while we may be observing composite stellar populations (CSP). Each of the SSP parameters is sensitive to a different stellar population, which may or may not be the one dominating the stellar mass. In our discussion, we are going to use the interpretation of the stellar population parameters according to Serra & Trager (2007), which relate SSP-equivalent parameters to CSPs as follows. Ages are biased towards the age of the youngest stellar populations, even in cases where they only have a small fraction of the mass, and therefore spectra with very low ages are not considered as young, but instead old populations with a contribution of young stars. In case of element abundances, these reflect the distribution of the most massive components in the composite stellar populations and, therefore, approximately reflect the mass-weighted properties.

4.1. Determination of SSP properties using Markov Chains

We used Monte Carlo Markov chains (MCMC, Markov 1913) to obtain SSP parameters, $\theta = (\log \text{Age}, [\text{Fe}/\text{H}], [\alpha/\text{Fe}])$ from the information contained in the set of Lick indices, D , available for each spectrum. A complete discussion of the MCMC method can be obtained elsewhere (e.g. MacKay 2003; Wall & Jenkins 2012), and here we only summarize the main concepts. The idea is to infer the posterior probability distribution of the parameters given the data, $p(\theta|D)$, using Bayes' theorem,

$$p(\theta|D) \propto p(\theta)p(D|\theta), \quad (4)$$

where $p(\theta)$ is the prior distribution and $p(D|\theta)$ is the likelihood distribution. We assume that the priors are uniform within the ranges of the models from Thomas et al. (2011), extrapolated in metallicity, $0.1 \leq \text{Age}(\text{Gyr}) \leq 15$, $-2.25 \leq [Z/H] \leq 0.90$ and $-0.3 \leq [\alpha/\text{Fe}] \leq 0.5$, and that the likelihood distributions are Gaussian functions with standard deviations equal to the uncertainties of the measurements of the Lick indices. The calculations of the samples were performed with the PyMC package (Patil et al. 2010) using the Metropolis-Hastings algorithm with SSP models linearly interpolated for sub-grid resolution.

Figure 5 illustrates the posterior distribution in two cases. The panels in the lower left show projections of the parameter space, which indicate that parameters are not independent of each other. In particular, a small age-metallicity degeneracy is present (Worthey 1994). However, the relevant statistics are obtained by the marginalization of the parameters, indicated by the histograms, which already take these effects into account. For symmetric posterior distributions, such as the metallicities in both examples of Fig. 5, we fit a simple Gaussian to obtain the mode and the standard deviation. However, in several cases the distributions are skewed towards the limits of the models, such as the ages in Fig. 5, which required a fit of a generalized extreme value (GEV) function. In these cases, we used the mode as the relevant statistic, and the uncertainties are calculated by determining two iso-probability values encompassing the maximum probabilities for which the posterior distribution integrals add up to 68% of the area under the curve, similar to the 1σ deviations of a Gaussian distribution.

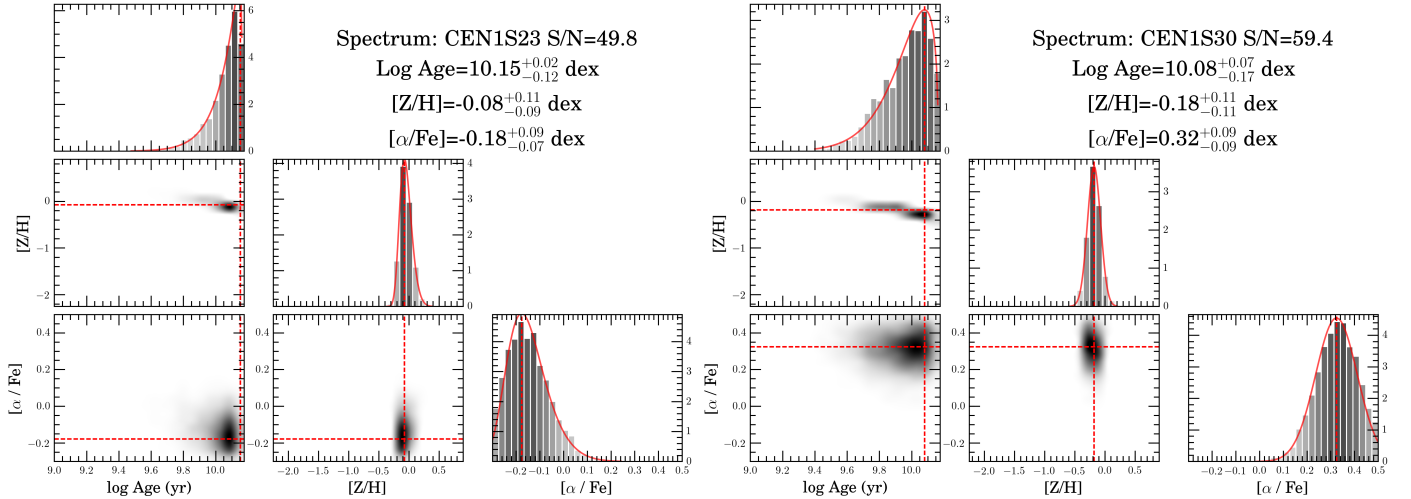


Fig. 5. Examples of the posterior distributions for two spectra using the MCMC method. The panels in the main diagonal show histograms of the marginalized distributions, which are used to determine the representative values and their uncertainties. The thick red lines show the best fit to the posterior samples, either a Gaussian or a generalized extreme value function. Projections of the posterior distributions in the *lower left panels* show the correlations among parameters. The histograms in the upper right corner of each panel indicate the maximum probabilities and the 1σ deviations of the stellar population parameters in each case.

The results of this analysis are presented in Cols. 12 to 14 of Table 1. In low S/N regimes, the posterior distributions become flat owing to the larger uncertainties in the Lick indices. To avoid such unconstrained parameters in the analysis, we set a maximum limit of 0.2, 0.7, 0.2, and 0.8 dex in the uncertainties of $\log(\text{Age})$, $[\alpha/\text{Fe}]$, $[\text{Z}/\text{H}]$, and $[\text{Fe}/\text{H}]$, respectively.

4.2. Spatial distribution and gradients of SSP parameters

In Fig. 6, we present the spatial distribution of the four stellar population parameters, i.e. $\log(\text{Age})$, $[\text{Z}/\text{H}]$, $[\alpha/\text{Fe}]$, and $[\text{Fe}/\text{H}]$. As observed in the distribution of Lick indices, the large scale distribution of the stellar populations is scattered, predominantly in the outer regions, while the inner galaxy displays a more regular behaviour. The central region shows rather old ages and super solar abundances. The external halo is much more diverse, presenting some large scale structures uncorrelated to the isophotes. However, considering the low spatial resolution of our observations, the relatively small S/N in several of these spectra, and the expected spread in stellar populations, we consider that most of the apparent structures may be explained by random fluctuations.

To describe the large-scale distribution, we again refer to the analysis of the radial trends and their gradients. In Fig. 7, we plot the stellar population parameter values determined from this work: in circles with different colours according to their S/N, as function of both the radial distance from the centre of NGC 3311, and also as a function of the V-band surface brightness at the location of the slits (left and central panels, respectively). We also show the stellar population parameters derived from the observations of Loubser & Sánchez-Blázquez (2012) and Thomas et al. (2011), as squares and triangles respectively, calculated from their published values of the Lick indices, using our MCMC approach for consistency. We also show the central stellar population parameters from Loubser et al. (2009) using an arrow indicating the published value in their paper.

There is considerable scatter in the external halo properties, similarly to that of the Lick indices plotted in Fig. 4. Once more, we compare this scatter with the systematic effect of an incorrect

sky subtraction by $\pm 1\%$, as displayed by the grey shaded areas. The comparison shows that the observed scatter is larger than that caused by a systematic effect in the sky subtraction of $\pm 1\%$. To reproduce a scatter similar to the one measured in the external halo, an error of $\sim 6\%$ is necessary, which is much larger than any of the residuals in our extracted spectra. Therefore, we have evidence that the scatter at large radii is an intrinsic property of the external stellar halo.

Similarly to the method deployed for the Lick indices, we quantify the radial trends in the stellar population properties using gradients which are computed separately for the inner galaxy and the external halo. The separation between these two regions is set at the projected distance of $1R_e$ from the centre, which is approximately represented by the isophotal surface brightness level of $\mu_v \approx 22.2 \text{ mag arcsec}^{-2}$. We used Eq. (2) to parametrize the gradients; this time we used two parameters for the abscissa, $X = \{\log(R/R_e), \mu_v\}$. For this calculation of the gradients, we excluded the slits around NGC 3309 and the three slits covering the dwarf galaxy HCC 007 at the south of NGC 3311 to avoid contamination. We note that the stellar population gradients as a function of the radius from the centre of NGC 3311 is our primary diagnostic to characterize the global variations in stellar population parameters and, as such, this is discussed in detail below. We expect the gradients as function of the local surface brightness values to be affected by the presence of substructures, as is the case for the external halo of NGC 3311 (see Arnaboldi et al. 2012), and hence have a larger scatter than radial gradients.

5. Correspondence among stellar populations, surface brightness components, and kinematical structures in the inner galaxy and external halo of NGC 3311

The presence of a break in the measured Lick indices and the clearly distinct distribution of the stellar population parameters for the inner galaxy ($R < R_e$) and the external halo point towards different formation channels for the stars in these two regions. We derive consistent values for the ages, the total metallicity,

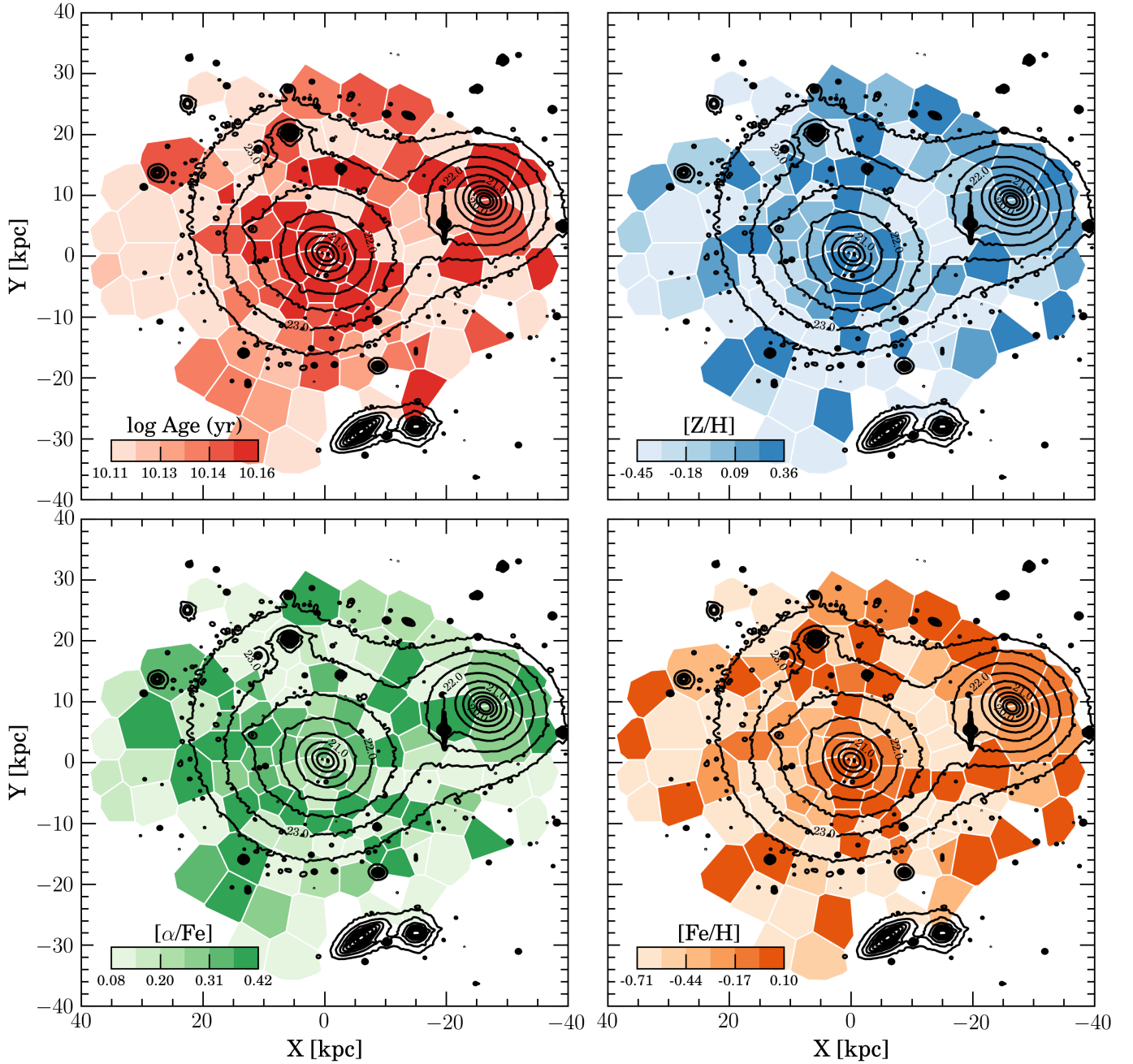


Fig. 6. Maps of the modelled luminosity-weighted stellar population properties: ages (*top left*), total metallicity (*top right*), alpha-element abundance (*bottom left*), and iron abundance (*bottom right*). Black lines display the *V*-band surface brightness contours from [Arnaboldi et al. \(2012\)](#) in the range from 20 to 23.5 in steps of 0.5 mag arcsec⁻². Colours indicate the SSP equivalent parameters according to the colour bars in the bottom left section of each panel. The inner galaxy ($R < \sim 10$ kpc) is characterized by homogenous old age, high metallicity, and super solar $[\alpha/\text{Fe}]$; the outer halo shows a more complex behaviour; see extended discussion in Sect. 6.

Table 3. Linear regression coefficients for the fitting of the stellar population parameters.

Property	Inner galaxy (1)		External halo (2)	
	$I(0)$ (dex)	ΔI (dex/dex)	$I(0)$ (dex)	ΔI (dex/dex)
log Age (yr)	10.16 ± 0.01	0.00 ± 0.01	10.14 ± 0.01	-0.02 ± 0.02
[Z/H]	0.07 ± 0.11	-0.23 ± 0.18	0.00 ± 0.15	-0.46 ± 0.39
$[\alpha/\text{Fe}]$	0.41 ± 0.03	0.18 ± 0.06	0.38 ± 0.08	-0.20 ± 0.22
[Fe/H]	-0.15 ± 0.08	-0.16 ± 0.08	-0.36 ± 0.16	0.14 ± 0.43

Notes. (1) Linear regression coefficients for the fitting of the stellar population parameters in the inner galaxy ($R \leq R_c$) according to Eq. (2), parametrized by the logarithm of the radius to the centre of NGC 3311. $I(0)$ indicates the value of the stellar population properties at one effective radius, while ΔI indicates the gradient. (2) Same as (1) for the outer halo ($R > R_c$) region.

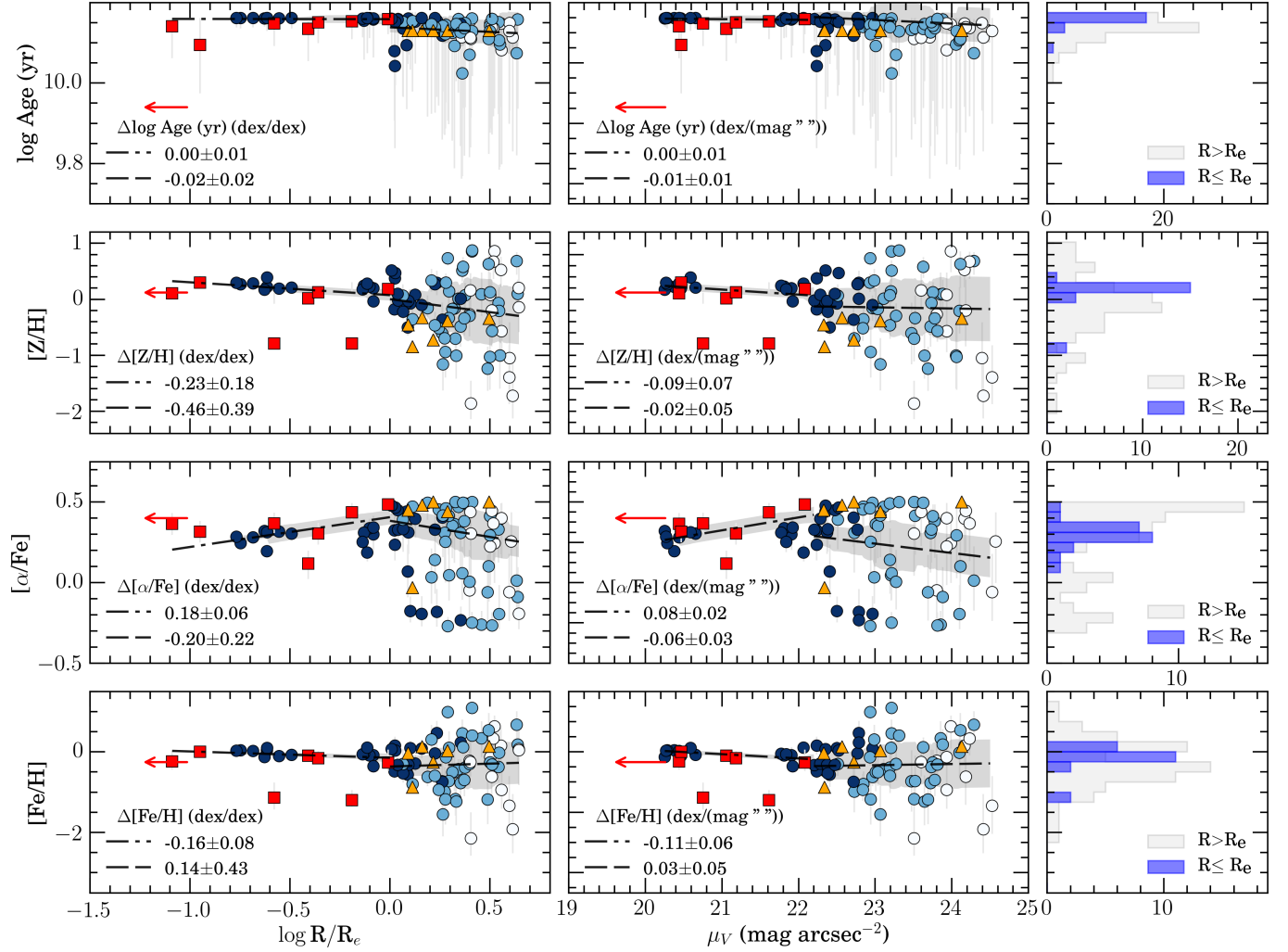


Fig. 7. Gradients of the stellar population parameters. *Left:* ages, $[Z/H]$, $[\alpha/Fe]$, and $[Fe/H]$ as function of the log-distance to the centre of NGC 3311. Circles indicate data points from this work, coloured according to their S/N as dark blue ($S/N > 30$), light blue ($15 \leq S/N \leq 30$) and white ($S/N < 15$). Data from Loubser et al. (2009) and Coccato et al. (2011) are shown by red arrow and orange triangles, respectively. New calculated values for the stellar population parameters based on data from Loubser & Sánchez-Blázquez (2012) are indicated by red squares. Dot-dashed and dashed lines indicate the regression for the inner and external halo, respectively, with the gradients displayed in the bottom left of each panel. The grey shades represent the systematic error of under/over subtraction of the sky by 1%. *Centre:* same as for the left panels, but with gradients measured as a function of the V -band surface brightness. *Right:* histograms of the distribution of the stellar population parameters, combining our data with those of Loubser & Sánchez-Blázquez (2012), with the inner galaxy and external halo shown in blue and grey bins, respectively. The gradients in the inner galaxy are consistent with the predictions from a quasi-monolithic collapse model, while the shallow azimuthally-averaged gradients and the large scatter in the outer halo are consistent with the results of accreted stars from a variety of different progenitors.

and gradients in $[\alpha/Fe]$ and $[Fe/H]$, with very small scatter for the inner galaxy. The distribution of values derived for the external halo have a very large scatter in comparison. The findings for the inner galaxy are consistent with the expectations from the in situ formation, which maintains gradients from the time of initial rapid star formation. Conversely, the larger scatter of the values in the external halo suggests that these stars come from the debris of gravitationally disrupted galaxies, as suggested by the classical model (Dressler 1979) for the formation of cD haloes. Thus the breaks at $1R_e$ are interpreted as transition from the in situ to the accreted stellar populations, and are observed in other giant ellipticals from the MASSIVE survey (Greene et al. 2013, 2015).

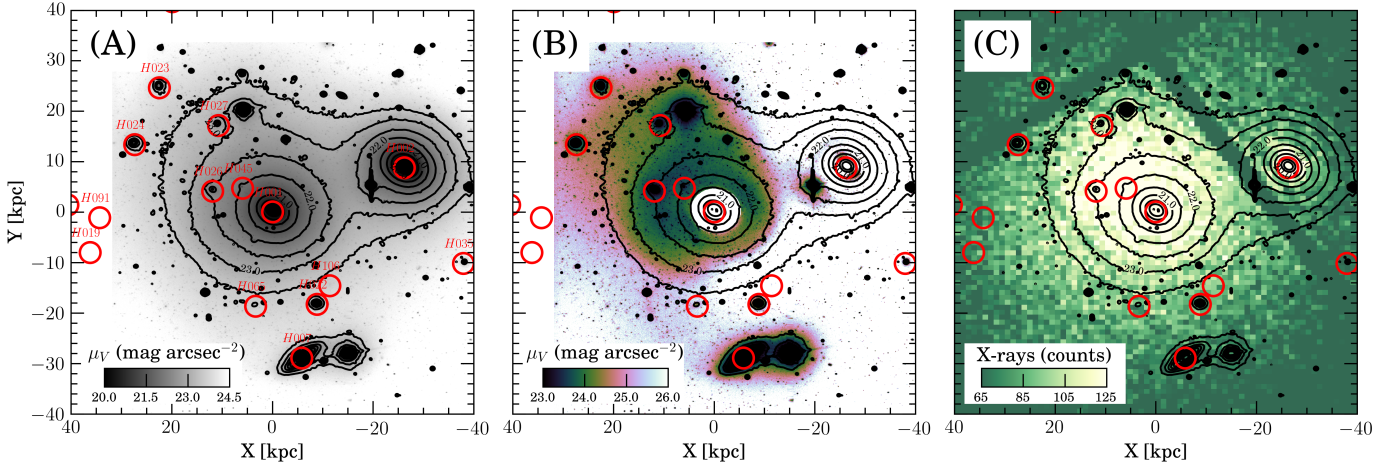
In NGC 3311, this type of break in the stellar properties of the inner galaxy and the external halo correlates with variations in the velocity dispersion profile. Within one R_e , stars

move under the influence of the galaxy mass, reaching a $\sigma_0 \approx 160 \text{ km s}^{-1}$ at the centre. At one R_e and slightly larger radii, the line-of-sight (LOS) velocity dispersion has a positive gradient reaching $\sigma(R) \approx 400 \text{ km s}^{-1}$ at 30 kpc (Ventimiglia et al. 2010; Richtler et al. 2011; Paper II). This increase in $\sigma(R)$ with radius indicates that the stars are progressively driven by the massive external halo associated with the Hydra I cluster, as mapped by the hot X-ray emission (Hayakawa et al. 2004).

We now discuss the properties of the external halo of NGC 3311, defined as the region $R > R_e$. This halo is not homogeneous and the presence of additional components can be physically motivated. Using deep V -band imaging, Arnaboldi et al. (2012) show that the light of NGC 3311 is described primarily by a single Sérsic function with index $n \approx 10$ at all radii. No break or no photometric signature of the two-component structure is expected in a cD galaxy: the cluster dominated halo is not

Table 4. Linear regression coefficients as presented in Table 3, parametrized by the V-band surface brightness.

Property	Inner galaxy ($\mu_V \leq 22.2$ mag arcsec $^{-2}$)		External halo ($\mu_V > 22.2$ mag arcsec $^{-2}$)	
	$I(22.2)$ (dex)	ΔI (dex/(mag arcsec $^{-2}$))	$I(22.2)$ (dex)	ΔI (dex (mag arcsec $^{-2}$))
log Age (yr)	10.19 ± 0.05	0.00 ± 0.01	10.36 ± 0.11	-0.01 ± 0.01
[Z/H]	2.06 ± 1.50	-0.09 ± 0.07	0.33 ± 1.20	-0.02 ± 0.05
[α /Fe]	-1.36 ± 0.47	0.08 ± 0.02	1.58 ± 0.62	-0.06 ± 0.03
[Fe/H]	2.16 ± 1.25	-0.11 ± 0.06	-1.01 ± 1.27	0.03 ± 0.05


Fig. 8. Evidence of a large-scale component in the external halo of NGC 3311. **A), B)** V-band image and residual from the Sérsic $n = 10$ model from Arnaboldi et al. (2012) illustrate the presence of an off-centred envelope. **C)** X-rays image from Hayakawa et al. (2006) indicates an excess emission at the same position of the off-centred envelope. Red circles indicate the position of dwarf galaxies from the catalogue of Misgeld et al. (2008).

obvious in the photometry. This Sérsic $n = 10$ component centred on NGC 3311 fits most of the light in all directions and is responsible for the featureless appearance observed in Panel A of Fig. 8. However, once the symmetric main component is subtracted, Arnaboldi et al. (2012) detected an additional feature in the galaxy light, the off-centred envelope, which is located at a projected distance of 18 kpc from the centre of NGC 3311, towards the north-east direction (panel B of Fig. 8). At the location of the off-centred envelope, there is an excess emission in X-rays (Hayakawa et al. 2004, 2006, see panel C) and a group of dwarf galaxies are found around this position with high relative LOS velocities of ~ 1000 km s $^{-1}$ (Misgeld et al. 2008), compared to the systemic velocity of the Hydra I cluster. At the optical wavelengths, the off-centred envelope is fainter than the symmetric main halo, contributing up to $\approx 30\%$ of the light (Coccatto et al. 2011; Arnaboldi et al. 2012).

The off-centred envelope is also associated with kinematical signatures. Ventimiglia et al. (2011) show that the LOSVD of planetary nebulae in the cluster core around NGC 3311 halo is multi-peaked, with three distinct components: a broad asymmetric component with velocities of ~ 3100 km s $^{-1}$, a blue-shifted north-south elongated component at ~ 1800 km s $^{-1}$, and a red-shifted component at ~ 5000 km s $^{-1}$, at the location of the off-centred envelope. Furthermore Arnaboldi et al. (2012) show that asymmetric features in the velocity dispersion and the LOS velocity profiles correlate with the spatial location of the off-centred envelope. That is, at the location of the envelope, the LOSVs are redshifted with respect to the centre of NGC 3311 and the velocity dispersion is larger than at the symmetric location in the external halo, opposite the galaxy centre. These features can be explained by the superposition along the LOS of

two distinct structural components, the Sérsic $n = 10$ halo and the off-centred envelope, with different LOSVs by ≥ 50 km s $^{-1}$.

Therefore, the external halo properties may be associated with two structural components: the “symmetric” Sérsic $n = 10$ halo, which is found at all azimuthal angles, and the off-centred envelope in the north-east quadrant. The exact boundaries of these components are not well defined, hence we adopt a simple scheme to seek out their signatures in the distribution of the parameters for the stellar populations. The properties of the stellar population in the symmetric external halo are derived for $R > R_e$ and $90^\circ \leq \text{PA} \leq 360^\circ$, while the population of the off-centred halo is studied in the quadrant at $0^\circ < \text{PA} < 90^\circ$. As the symmetric halo contributes 70% or even larger amounts to the light at the location of the off-centred envelope, we would expect to only detect small variations in the distributions of the stellar population parameters at the location of the off-centred envelope, compared to the symmetric halo distribution.

6. Properties of the stellar populations of the stellar light in NGC 3311

6.1. Stellar populations in the inner galaxy

The stellar population properties of the inner galaxy ($R \lesssim R_e$) have well-constrained values as indicated by the blue histograms on the right side of Fig. 7. The radial linear gradients of the stellar parameters are minor. There are three deviating data points: one at the position of the dust lane in the central kpc of NGC 3311 (Arnaboldi et al. 2012), and two in other regions further out, see Loubser et al. (2009) and Loubser & Sánchez-Blázquez (2012).

The stars of the inner galaxy are old, compatible with the oldest modelled stellar populations (15 Gyr), with no gradient in age. The total metallicity of the stars is super solar, with a mild gradient of -0.23 ± 0.18 dex dex $^{-1}$, while the alpha element abundance is high at the centre, $[\alpha/\text{Fe}] \approx 0.2$ dex, with a positive gradient of 0.18 ± 0.06 dex dex $^{-1}$. The resulting iron abundance is close to solar, with a gradient of -0.16 ± 0.08 dex dex $^{-1}$.

The very old age of NGC 3311 is expected for BCGs. Oliva-Altamirano et al. (2015) observe that one-third of their BCG sample has similarly old stellar populations (age > 12 Gyr), while Loubser et al. (2009) find that about 50% of the BCGs have central old stellar populations. The flat age gradient and the abundance gradients are consistent with the values observed in BCGs by Oliva-Altamirano et al. (2015).

6.2. Stellar populations in the external halo

The properties of the outer stellar halo of NGC 3311 are considerably different from those inferred for the inner galaxy, as shown in Fig. 7, left and central panels at $R \gtrsim R_e$ and $\mu_v \gtrsim 22.2$ mag arcsec $^{-2}$. We detect a shallow age gradient of $\Delta \log \text{Age} = -0.02 \pm 0.02$ dex dex $^{-1}$ in the external halo, which is compatible with the flat gradient in the inner galaxy. The total metallicity gradient is steeper than that of the inner galaxy, with $\Delta[\text{Z}/\text{H}] = -0.46 \pm 0.39$ dex dex $^{-1}$, and an inversion of the radial trends is observed in the alpha element abundance, with $\Delta[\alpha/\text{Fe}] = -0.20 \pm 0.22$ dex dex $^{-1}$, and in the abundance of iron, with $\Delta[\text{Fe}/\text{H}] = 0.14 \pm 0.43$ dex dex $^{-1}$.

In addition to the average radial trends, the clear feature of the outer stellar halo of NGC 3311 is the considerable larger scatter of the stellar population parameters. The histograms on the right side of Fig. 7 show the distribution of stellar population properties for the inner galaxy (blue) and outer stellar halo (grey). The large scatter is present for the SSP parameters of high S/N (≥ 40) spectra and at a radius of $R \sim 0.6R_e = 5.3$ kpc, as indicated by the dark blue circles in the radial plots for $[\text{Z}/\text{H}]$, $[\alpha/\text{Fe}]$, and $[\text{Fe}/\text{H}]$ in Fig. 7. Moreover, the width of the distribution of the stellar population parameters is larger than expected from a systematic error in the sky subtraction of $\pm 1\%$, as indicated by the grey shaded areas shown around the mean gradients.

In the histograms on the right side of Fig. 7, the positions of the mean peak of the distributions and their widths are different in the inner galaxy and external halo. A common characteristic of these distributions is that their widths for the external halo are twice as large as those for the inner galaxy. In the case of the $[\text{Z}/\text{H}]$ and $[\alpha/\text{Fe}]$ distributions, there are multiple peaks for the external halo. Therefore, contrary to the inner galaxy, which can be explained by a rapid process of collapse and merger of gas-rich lumps, the outer stellar halo was most likely built up by an accretion of stars from a variety of progenitors, with different masses and star formation histories.

We now investigate whether there are differences in the stellar population parameters between the off-centred envelope and the rest of the external halo of NGC 3311. Figure 9 shows the distribution of the stellar population parameters for the off-centred envelope (red) and the rest of the external halo (grey). To determine the number of peaks that are statistically significant in each case, we used Gaussian mixture models (GMM) to estimate the number of populations which minimize the Bayesian information criteria (BIC), results of which are summarized in Table 5. The $[\alpha/\text{Fe}]$ distributions for the off-centred envelope and symmetric halo are those for which two components are statistically favoured with respect to the single peak distribution. The distributions for the ages and metallicities can be relatively well

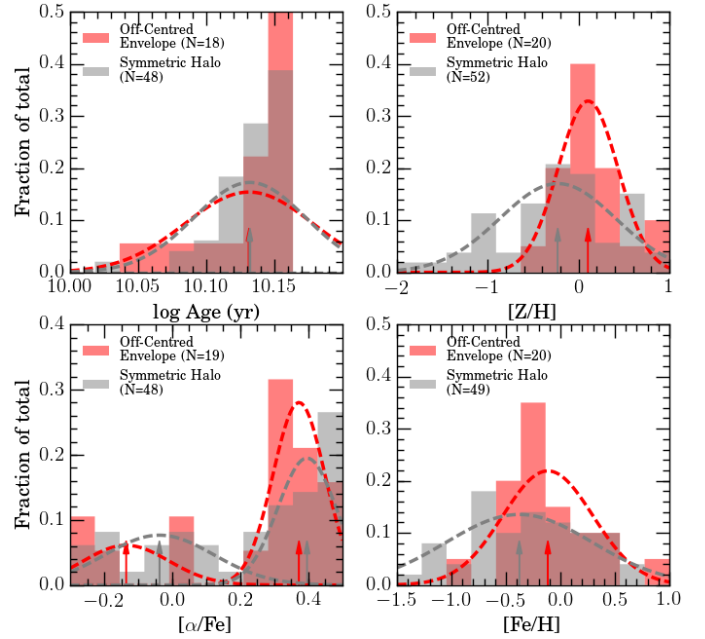


Fig. 9. Distribution of stellar population parameters of the off-centred envelope (red) and the symmetric halo (grey). The histograms are normalized and the number of spectra (N) used in each case is shown in the legend of each panel. Dashed lines indicate the components of the GMM analysis, while the arrows indicate the position of the peak of each component. The off-centred envelope is responsible for a significant shift of the metallicity where it is located, while ages and alpha-element abundance distributions are similar to those inferred for the symmetric halo.

Table 5. Properties of the Gaussian mixture models with lowest Bayesian information criteria for the off-centred envelope and the symmetric halo.

Property (1)	Halo (2)	N (3)	Mean (4)	Sigma (5)	Weight (6)
log Age (Gyr)	Envelope	18	10.13	0.05	1.0
	Sym. Halo	48	10.13	0.04	1.0
$[\text{Z}/\text{H}]$	Envelope	20	0.10	0.33	1.0
	Sym. Halo	52	-0.24	0.64	1.0
$[\alpha/\text{Fe}]$	Envelope	19	0.37	0.08	0.74
			-0.14	0.13	0.26
	Sym. Halo	48	0.39	0.09	0.57
$[\text{Fe}/\text{H}]$	Envelope	20	-0.12	0.41	1.0
	Sym. Halo	49	-0.38	0.68	1.0

Notes. (1) Stellar population parameters. (2) External halo component ($R > R_e$), defined as an envelope for the NE quadrant of our observation, and a symmetric halo otherwise. (3) Number of data points used in the statistics. (4), (5) Mean and standard deviation of the Gaussian mixture model component. (6) Weight of the component in the Gaussian mixture model.

described by single Gaussian functions instead. The GMM models are shown in Fig. 9 by dashed lines, with arrows indicating the position of the peak for each component.

We used the Kolmogorov-Smirnov (KS) test to statistically compare the distributions of the stellar population parameters

for the off-centred envelope and the symmetric halo. The result of the KS tests indicates that the age and the alpha element abundances of these two components may have been drawn from the same parent distribution, with probabilities of 78 and 32% respectively. In both components, stars are predominantly old with ages of ~ 14 Gyr, which is compatible with the oldest stellar populations in the models of [Thomas et al. \(2011\)](#). This old age distribution extends the results from [Coccatto et al. \(2011\)](#) to the entire halo and is also supported by the lack of features in the UV emission from GALEX observations ([Gil de Paz et al. 2007](#)). The age is the only external halo property for which the gradient is representative of the vast majority of the observed data points.

The distribution of alpha element abundance in the symmetric halo and in the off-centred envelope show similar multimodal distributions, modelled as a mixture of two Gaussian components. The main contribution to the alpha element abundance are stars with $[\alpha/\text{Fe}] \approx 0.4$ dex and spread of 0.1 dex, observed in 64% of cases, while the secondary population has an abundance of $[\alpha/\text{Fe}] \approx -0.1$ dex and a spread of 0.15 dex. The explanation for almost identical alpha element abundance at the off-centred envelope and in the symmetric halo is that this property is robust against a contamination of a minor component in the total integrated light, as indicated by the simulations of [Coccatto et al. \(2011\)](#). Comparing the SSP parameters of a superposition of a typical, alpha-enhanced symmetric halo spectrum ($[Z/\text{H}] = -0.34$ dex, $[\alpha/\text{Fe}] = 0.50$ dex) with the properties of the dwarf galaxy HCC 026 ($[Z/\text{H}] = -0.85$ dex, $[\alpha/\text{Fe}] = 0.03$ dex), they noticed that 35% of the light is necessary to decrease the element abundance by only 0.05 dex. There may be specific regions in the off-centred envelope where this amount may be slightly larger, especially in those regions with the largest velocity dispersion observed in Paper II but, considering the total light, the fraction of light at the substructure should not exceed 30%, confirming the findings of [Coccatto et al. \(2011\)](#), and in agreement with the estimates of [Arnaboldi et al. \(2012\)](#).

In contrast to the age and $[\alpha/\text{Fe}]$ distributions, the total metallicity and the iron abundance distributions do differ between the off-centred envelope and the symmetric halo. The probability that these distributions are drawn from the same parent distributions are low, i.e. $\sim 1\%$ and $\sim 3\%$, respectively. The total metallicity distribution of the off-centred envelope is most discrepant. The difference is clearly shown in Fig. 9: the metallicity distribution of the stellar populations at the location of the off-set envelope is a single peaked distribution centred at $[Z/\text{H}] = 0.1$ dex and width of 0.33 dex, while the metallicity of the symmetric halo is a much broader distribution, with mean value $[Z/\text{H}] = -0.24$ dex and width of 0.64 dex. The stars in the quadrant where the off-centred envelope is located have higher metallicities than most of the stars at the same radii, except for the stars sampled by spectra extracted in proximity of the giant companion, NGC 3309. A similar result holds for the iron abundance with the symmetric halo, which has $[\text{Fe}/\text{H}] = -0.38$ dex and dispersion of 0.68 dex, while the mean abundances of the off-centred envelope is $[\text{Fe}/\text{H}] = -0.12$ dex, with a dispersion of 0.41 dex. Since the light at the location of the off-centred envelope is given by the superposition of this component and the symmetric halo, the intrinsic metallicity of the stars in the envelope may be significantly higher than solar.

Our derived stellar population parameters for the external halo of NGC 3311 are compatible with previous results from [Coccatto et al. \(2011\)](#), and are similar to the stellar populations of other cD galaxy haloes, such as NGC 4889 in the Coma cluster ([Coccatto et al. 2010b](#)) and NGC 6166 in the Abell 2199 cluster ([Bender et al. 2015](#)). These physical properties are also similar to

those inferred for the stellar populations in other BCGs ([Spolaor et al. 2008](#)) and massive early-type galaxies ([Spolaor et al. 2010](#); [Greene et al. 2012, 2013, 2015](#)).

7. Implications for the assembly history of NGC 3311

Recent cosmological models for the formation of large early-type galaxies predict that the majority of stars in external haloes originated from satellite galaxies in the so-called two-phase scenario (e.g. [De Lucia & Blaizot 2007](#); [Naab et al. 2009](#); [Oser et al. 2010](#); [Cooper et al. 2013](#)). In the following sections, we compare our results with recent modelling of BCGs to relate the inferred distributions of the stellar population parameters with the physical mechanisms involved in the formation of extended haloes of BCGs in clusters.

7.1. The inner galaxy

As presented in previous sections, the distribution and the distinct radial gradients of the age, $[Z/\text{H}]$, $[\text{Fe}/\text{H}]$, and $[\alpha/\text{Fe}]$ of stellar populations in the inner galaxy are consistent with stars born in situ. According to the models of [Cooper et al. \(2013\)](#), the large number of in situ stars in the central regions of BCGs are expected to occur up to a stellar mass threshold of $M_{200} \lesssim 10^{13} M_{\odot}$ since, for more massive galaxies, the accreted stars become increasingly dominant even in their innermost regions ([Cooper et al. 2015](#)). NGC 3311 is very close to this boundary, with $M_{200} \approx 0.63 M_{500} = 6.3 \times 10^{13} M_{\odot}$ ([Piffaretti et al. 2011](#)), and our determination of the stellar population parameters shows the presence of in situ and accreted stars in two radial regions, and thus in agreement with the predictions of [Cooper et al. \(2013\)](#).

We can also compare our results with those for other massive early-type galaxies. The total metallicity gradient of the inner galaxy in NGC 3311, $\Delta[Z/\text{H}] = -0.23 \pm 0.18$ dex dex $^{-1}$, is comparable to the gradients of other BCG galaxies ([Oliva-Altamirano et al. 2015](#)) and non-BCGs ([Kuntschner et al. 2010](#)). Positive $[\alpha/\text{Fe}]$ gradients are also common among early-type galaxies ([Kuntschner et al. 2010](#)) and BCGs ([Brough et al. 2007](#)) and, therefore, the mechanisms that set the gradients in BCGs must be similar to those that form ordinary early-type galaxies. In a simple, quasi-monolithic scenario, such gradients can be explained in an outside-in scenario (e.g. [Pipino et al. 2006, 2008, 2010](#)). In this context, early-type galaxies are formed by the merging of gas-rich lumps, which produces an intense star formation, but with a differential rate at different radii. Star formation in the outer regions around $1R_{\text{e}}$ is characterized by short time-scales and strong stellar winds that deplete the iron efficiently, whereas star formation in the core is prolonged and metals, in particular iron, are kept owing to the strong gravitational potential. This produces positive alpha element gradients and negative total metallicity gradients. The abundance gradients of the inner galaxy of NGC 3311 are compatible with the results of these models, considering a few episodes of dry mergers ([Pipino et al. 2010](#)).

7.2. The extended symmetric halo

With reference to the main peak of the alpha element abundance distribution, see Fig. 9, the extended halo can be described as a mix of old stars with metallicities of $[Z/\text{H}] \approx -0.25$ and $[\alpha/\text{Fe}] \approx 0.4$, at first order. As discussed earlier, the high value for the α abundance does not imply that all stars were

formed in galaxies with high $[\alpha/\text{Fe}]$, since this quantity does not change a lot by the contamination of less alpha-enhanced stars. Nevertheless, the majority of stars in the external halo may indeed have high $[\alpha/\text{Fe}]$. In the nearby universe, high $[\alpha/\text{Fe}]$ stars are those:

1. Stars that are produced in disk galaxies with truncated star formation. [Greene et al. \(2012, 2013\)](#) show that the metallicity and the alpha element abundance at the outskirts of massive galaxies are similar to those found in the Milk-Way thick disk, which is predicted to have been formed in short time-scales ([Chiappini et al. 1997](#)). These disks could have been destroyed in interactions and mergers very early on, since galaxy encounters at high redshift were much more common than in the present day universe.
2. Stars from galaxies in compact groups. [De la Rosa et al. \(2007\)](#) have found that galaxies with $\sigma_0 \lesssim 160 \text{ km s}^{-1}$ in Hickson Compact Groups have larger $[\text{Mg}/\text{Fe}]$ and lower $[\text{Z}/\text{H}]$ compared to field galaxies of similar masses, and proposed that such galaxies may have their otherwise extended star formation quenched by mergers.
3. Stars on the outskirts of massive early-type galaxies with declining metallicity gradients and flat-to-positive alpha element gradients ([Coccatto et al. 2011](#)). Negative metallicity gradients extending to the outer radii are found in most early-type galaxies (e.g. [Baes et al. 2007](#); [La Barbera et al. 2012](#)). Flat and positive $[\alpha/\text{Fe}]$ gradients are commonly found in early-type galaxies at small radii ([Kuntschner et al. 2010](#)), and there is evidence that, at least, metallicity gradients extend to larger radii ([La Barbera et al. 2012](#); [Pastorello et al. 2014](#)). In other nearby clusters, such as Virgo and Fornax, declining metallicity gradients and flat alpha element abundances are found in almost all cases ([Spolaor et al. 2010](#)), but there is no such information for the giant ellipticals in the Hydra I cluster. If these have similar gradients, the central stellar populations of the Hydra I ellipticals should exhibit high $[\text{Z}/\text{H}]$ and $[\alpha/\text{Fe}]$, similar to those found in the extended halo of NGC 3311 ([Coccatto et al. 2011](#)).

All of the above galaxies could have provided stars that have now been found to have contributed most of the light of the symmetric external halo. They do not exclude each other necessarily, since they could have been different parts of the same process in a hierarchical scenario. More importantly, however, is that the high $[\alpha/\text{Fe}]$ indicates star formation that is happening on short time-scales of ≈ 0.1 Gyr, according to the approximation of [Thomas et al. \(2005\)](#). We can also estimate the most likely masses of the progenitors of the stars in the external halo from the metallicity distribution in Fig. 9. Translating these metallicities into stellar masses according to the relations from [Gallazzi et al. \(2005\)](#), the typical galaxies contributing to the formation of the extended symmetric halo are Milky Way-like galaxies, including mostly galaxies in the range $\sim 10^{10} M_{\odot}$ to $\sim 10^{12} M_{\odot}$.

The extrapolation of the inner galaxy gradient in $[\alpha/\text{Fe}]$ matches the position of the dominant alpha element abundance in the external halo, indicating that these stars may have similar origins. Cosmological hydrodynamical simulations from [Murante et al. \(2007\)](#) indeed indicate that most of the diffuse halo is composed of stars that were liberated from the most massive galaxies in episodes of major mergers that were related to the formation of the cD galaxy, where tidal shocking and stripping of massive galaxies are able to unbound up to 30% of their stellar mass. In agreement with several predictions from the models of [Murante et al. \(2007\)](#), the semi-analytical models of [Contini et al. \(2014\)](#), including disruption of galaxies and

tidal interactions, are able to reproduce both the typical masses of the progenitors in our observations, as well as the typical total metallicities. Therefore, our observations are in agreement with models in which the assembly of the BCG is directly connected with the formation of the diffuse halo.

The $[\alpha/\text{Fe}]$ distribution of the symmetric halo indicates the presence of a secondary population, with solar and sub-solar α -abundances. These lower alpha element abundances suggest a much more extended star formation, i.e. ~ 15 Gyr, according to the approximation of [Thomas et al. \(2005\)](#). In this case, there is already one galaxy in the Hydra I cluster that has similar properties, the dwarf galaxy HCC 026. This dwarf galaxy has solar alpha-abundance, $[\alpha/\text{Fe}] = -0.03 \pm 0.05$ dex, and low metallicity, $[\text{Z}/\text{H}] = -0.85 \pm 0.03$ ([Coccatto et al. 2011](#)). HCC 026 is part of a group of dwarf galaxies in the same location of the off-centred envelope ([Misgeld et al. 2008](#)) and it has strong tidal tails that indicate that this galaxy is being disrupted by the tidal field close to the cluster centre ([Arnaboldi et al. 2012](#)). Hence HCC 026 is the typical object that contributes to the late accretion events that build-up the halo today.

These types of solar and sub-solar α abundance populations are inferred from a substantial fraction of the extracted spectra in about 40% of the total sample in the external halo. Hence the accretion of stars from disrupted dwarfs or irregular galaxies is an important channel for the late build-up of the external halo. Very recent observations of the planetary nebulae in the halo of M 87 and the intracluster light in the Virgo core show that the contribution from Magellanic cloud-like irregular galaxies is responsible for a sizeable fraction of the halo light being added in the last Gyr to the M 87 halo and ICL ([Longobardi et al. 2015a,b](#)). Models from [Murante et al. \(2007\)](#) indicate that low-mass galaxies ($M_* < 10^{10} M_{\odot}$) may contribute to the formation of the diffuse halo, but numerical issues related to the particle resolution of low-mass galaxies did not allow them to set proper constraints on this secondary population.

Our current results for NGC 3311 and the recent findings for M 87 indicate that it is important to study the details of the late mass accretion, which is responsible for a sizeable amount of the chemical composition and kinematics of the haloes of massive nearby galaxies.

7.3. The metallicity distribution of the off-centred envelope

The stellar populations located at the off-centred envelope show an enhancement of metals in comparison with the rest of the symmetric halo, while the alpha element abundance and age distributions are similar. The strongly peaked metallicity distribution centred around $[\text{Z}/\text{H}] \approx 0.1$ indicates that the stars associated with the substructure were formed in massive galaxies. According to [Murante et al. \(2007\)](#), massive ellipticals can lose up to 30% of their stars during their merging events with the cD, and these stars then contribute to the build-up of the external halo. The question then is, how this external high metallicity halo component acquired an offset and became off-centred with respect to the high surface brightness, highly concentrated inner galaxy.

Off-centred outer components in BGCs are quite frequent: from a sample of 24 clusters, [Gonzalez et al. \(2005\)](#) show that a two-component fit to the light profiles of BCGs provides an improved match to the data and that the two photometric components are misaligned in 60% of the sample. In the [Gonzalez et al. \(2005\)](#) sample, the cluster Abell 1651 has a cD galaxy where the two components have different centres,

with the outer component being off-centred by 15 kpc linear distance in projection, i.e. very similar to what is observed for NGC 3311. As observed in cosmological simulations (e.g. Murante et al. 2007), the highly radial orbits of the dark haloes of massive ellipticals and their tidal interaction with the cD dark halo may cause a deflection of the central part of the cD from its dark halo, while the outer envelopes maintain their orbital directions, thus creating an offset between core and halo in the cD galaxy. Candidate dark haloes responsible for a tidal interaction with NGC 3311 are the dark halo associated with the group of infalling dwarfs or the dark halo associated with NGC 3309. These tidal interactions would then be similar to what is observed in the Coma cluster core (Gerhard et al. 2007). Such mechanisms may also explain the gas stripping of NGC 3311, as observed in the X-rays (Hayakawa et al. 2004, 2006), since the mass of the gas is compatible with the mass of NGC 3311.

8. Summary and conclusions

We performed a spatially extended survey of the stellar populations in NGC 3311, the brightest galaxy of the Hydra I cluster. By analysing the absorption line equivalent widths using a Bayesian framework with Monte Carlo Markov Chains, we probed luminosity-weighted parameters, i.e. age, $[Z/H]$, $[\alpha/Fe]$, and $[Fe/H]$ out to $\sim 3R_e$. This enabled the characterization of the stellar content of three physically motivated components of this system: the inner galaxy, the symmetric external halo, and the off-centred envelope.

The inner stellar halo ($R < R_e$) presents stellar populations typical of massive early-type galaxies, including old ages, high metallicities, and high alpha-element abundances. Similar to other BCGs, the inner galaxy has a well-defined negative metallicity and a positive alpha element abundance gradient which can be explained by a quasi-monolithic scenario involving a few dry mergers. These gradients, and the smaller velocity dispersion of the inner galaxy, are clear indications that the stars in this region were formed in situ in the early phases of galaxy formation.

The stellar component of the outer symmetric stellar halo is characterized by a large spread of the stellar parameter values rather than by clearly defined radial gradients. This region is also characterized by high velocity dispersions which are indicative of these stars being driven by the cluster's potential and being generated by accumulation of tidal debris. While the mean value of the metallicity distribution in this region indicates subsolar abundances, the $[\alpha/Fe]$ distribution of the symmetric halo is bimodal, with high (~ 0.4) and low (~ 0) components. The majority of stars in the symmetric halo are generated in galaxies with a rapid star formation and short time-scales, in agreement models for the formation of cD envelopes (e.g. Murante et al. 2004, 2007; Contini et al. 2014). However, a substantial number of stars, about 40%, have a low $[\alpha/Fe]$ value, which indicates that stars from less massive galaxies have also been added to the cD halo. Their association with dwarf galaxies that are currently being disrupted at the position of the off-set envelope indicates that the growth of the cD halo is an ongoing process, which is fed by late mass accretion.

Finally, the stellar populations at the position of the off-centred envelope, a substructure also observed in photometry, X-rays and kinematics, indicates that the dark matter halo of an infalling group may have interacted with the BCG halo, causing the stripping of gas and stars.

We conclude that massive satellite galaxies in the vicinity of NGC 3311 merged with the central cD in early times and formed

its symmetric outer halo, while the build-up process of the extended halo is still ongoing, as indicated by the presence of an infalling group of dwarfs that are currently adding their stars to the halo. Tidal interactions between the dark haloes of the infalling group, of NGC 3309, and NGC 3311 may be responsible for the stripping of stars and gas in the halo of NGC 3311. Although very challenging from an observational point of view, the haloes of cD galaxies provide important constraints on the formation and morphological transformation of galaxies in nearby clusters.

Acknowledgements. We would like to thank Dr. Ilani Loubser for kindly sharing data from the inner regions of NGC 3311. We would like to thank the referee for his/her constructive comments. This research has made use of the NASA/IPAC Extragalactic Database (NED) which is operated by the Jet Propulsion Laboratory, California Institute of Technology, under contract with the National Aeronautics and Space Administration. CEB and CMdO are grateful to the São Paulo Research Foundation (FAPESP) funding (Procs. 2011/21325-0, 2012/22676-3 and 2014/07684-5). T.R. acknowledges financial support from FONDECYT project No. 1100620, and from the BASAL Centro de Astrofísica y Tecnologías Afines (CATA) PFB-06/2007. T.R. also thanks ESO/Garching for a visitorship.

References

- Appenzeller, I., Fricke, K., Fürtig, W., et al. 1998, *The Messenger*, **94**, 1
- Arnaboldi, M., Ventimiglia, G., Iodice, E., Gerhard, O., & Coccato, L. 2012, *A&A*, **545**, A37
- Baes, M., Sil'chenko, O. K., Moiseev, A. V., & Manakova, E. A. 2007, *A&A*, **467**, 991
- Bender, R., Kormendy, J., Cornell, M. E., & Fisher, D. B. 2015, *ApJ*, **807**, 56
- Brough, S., Proctor, R., Forbes, D. A., et al. 2007, *MNRAS*, **378**, 1507
- Cappellari, M., & Emsellem, E. 2004, *PASP*, **116**, 138
- Chiappini, C., Matteucci, F., & Gratton, R. 1997, *ApJ*, **477**, 765
- Coccato, L., Arnaboldi, M., Gerhard, O., et al. 2010a, *A&A*, **519**, A95
- Coccato, L., Gerhard, O., & Arnaboldi, M. 2010b, *MNRAS*, **407**, L26
- Coccato, L., Gerhard, O., Arnaboldi, M., & Ventimiglia, G. 2011, *A&A*, **533**, A138
- Contini, E., De Lucia, G., Villalobos, Á., & Borgani, S. 2014, *MNRAS*, **437**, 3787
- Cooper, A. P., D'Souza, R., Kauffmann, G., et al. 2013, *MNRAS*, **434**, 3348
- Cooper, A. P., Gao, L., Guo, Q., et al. 2015, *MNRAS*, **451**, 2703
- de la Rosa, I. G., de Carvalho, R. R., Vazdekis, A., & Barbuy, B. 2007, *AJ*, **133**, 330
- De Lucia, G., & Blaizot, J. 2007, *MNRAS*, **375**, 2
- Dekel, A., Birnboim, Y., Engel, G., et al. 2009, *Nature*, **457**, 451
- Dressler, A. 1979, *ApJ*, **231**, 659
- Gallagher, III, J. S., & Ostriker, J. P. 1972, *AJ*, **77**, 288
- Gallazzi, A., Charlot, S., Brinchmann, J., White, S. D. M., & Tremonti, C. A. 2005, *MNRAS*, **362**, 41
- Gerhard, O., Arnaboldi, M., Freeman, K. C., et al. 2007, *A&A*, **468**, 815
- Gil de Paz, A., Boissier, S., Madore, B. F., et al. 2007, *ApJS*, **173**, 185
- Gonzalez, A. H., Zabludoff, A. I., & Zaritsky, D. 2005, *ApJ*, **618**, 195
- Greene, J. E., Murphy, J. D., Comerford, J. M., Gebhardt, K., & Adams, J. J. 2012, *ApJ*, **750**, 32
- Greene, J. E., Murphy, J. D., Graves, G. J., et al. 2013, *ApJ*, **776**, 64
- Greene, J. E., Janish, R., Ma, C.-P., et al. 2015, *ApJ*, **807**, 11
- Hayakawa, A., Furusho, T., Yamasaki, N. Y., Ishida, M., & Ohashi, T. 2004, *PASJ*, **56**, 743
- Hayakawa, A., Hoshino, A., Ishida, M., et al. 2006, *PASJ*, **58**, 695
- Hirschmann, M., Naab, T., Ostriker, J. P., et al. 2015, *MNRAS*, **449**, 528
- Kereš, D., Katz, N., Weinberg, D. H., & Davé, R. 2005, *MNRAS*, **363**, 2
- Kobayashi, C. 2004, *MNRAS*, **347**, 740
- Komatsu, E., Dunkley, J., Nolte, M. R., et al. 2009, *ApJS*, **180**, 330
- Kuntschner, H., Emsellem, E., Bacon, R., et al. 2006, *MNRAS*, **369**, 497
- Kuntschner, H., Emsellem, E., Bacon, R., et al. 2010, *MNRAS*, **408**, 97
- La Barbera, F., Ferreras, I., de Carvalho, R. R., et al. 2012, *MNRAS*, **426**, 2300
- Larson, R. B. 1974, *MNRAS*, **166**, 585
- Longobardi, A., Arnaboldi, M., Gerhard, O., & Hanuschik, R. 2015a, *A&A*, **579**, A135
- Longobardi, A., Arnaboldi, M., Gerhard, O., & Mihos, J. C. 2015b, *A&A*, **579**, L3
- Loubser, S. I., Sánchez-Blázquez, P., Sansom, A. E., & Soechting, I. K. 2009, *MNRAS*, **398**, 133

- Loubser, S. I., & Sánchez-Blázquez, P. 2012, *MNRAS*, **425**, 841
- MacKay, D. 2003, *Information theory, inference, and learning algorithms* (Cambridge, UK, New York: Cambridge University Press)
- Markov, A. A. 1913, *Proceedings of the Academy of Sciences of St. Petersburg*, **7**, 153
- Mihos, J. C., Harding, P., Rudick, C. S., & Feldmeier, J. J. 2013, *ApJ*, **764**, L20
- Misgeld, I., Mieske, S., & Hilker, M. 2008, *A&A*, **486**, 697
- Misgeld, I., Mieske, S., Hilker, M., et al. 2011, *A&A*, **531**, A4
- Montes, M., Trujillo, I., Prieto, M. A., & Acosta-Pulido, J. A. 2014, *MNRAS*, **439**, 990
- Murante, G., Arnaboldi, M., Gerhard, O., et al. 2004, *ApJ*, **607**, L83
- Murante, G., Giovalli, M., Gerhard, O., et al. 2007, *MNRAS*, **377**, 2
- Naab, T., Johansson, P. H., & Ostriker, J. P. 2009, *ApJ*, **699**, L178
- Oliva-Altamirano, P., Brough, S., Jimmy, Kim-Vy, T., et al. 2015, *MNRAS*, **449**, 3347
- Oser, L., Ostriker, J. P., Naab, T., Johansson, P. H., & Burkert, A. 2010, *ApJ*, **725**, 2312
- Pastorello, N., Forbes, D. A., Foster, C., et al. 2014, *MNRAS*, **442**, 1003
- Patil, A., Huard, D., & Fonnesbeck, C. J. 2010, *J. Stat. Software*, **35**, 1
- Piffaretti, R., Arnaud, M., Pratt, G. W., Pointecouteau, E., & Melin, J.-B. 2011, *A&A*, **534**, A109
- Pipino, A., Matteucci, F., & Chiappini, C. 2006, *ApJ*, **638**, 739
- Pipino, A., D'Ercole, A., & Matteucci, F. 2008, *A&A*, **484**, 679
- Pipino, A., D'Ercole, A., Chiappini, C., & Matteucci, F. 2010, *MNRAS*, **407**, 1347
- Richtler, T., Salinas, R., Misgeld, I., et al. 2011, *A&A*, **531**, A119
- Robertson, B., Bullock, J. S., Cox, T. J., et al. 2006, *ApJ*, **645**, 986
- Sánchez-Blázquez, P., Peletier, R. F., Jiménez-Vicente, J., et al. 2006, *MNRAS*, **371**, 703
- Schiavon, R. P. 2007, *ApJS*, **171**, 146
- Serra, P., & Trager, S. C. 2007, *MNRAS*, **374**, 769
- Spolaor, M., Forbes, D. A., Proctor, R. N., Hau, G. K. T., & Brough, S. 2008, *MNRAS*, **385**, 675
- Spolaor, M., Kobayashi, C., Forbes, D. A., Couch, W. J., & Hau, G. K. T. 2010, *MNRAS*, **408**, 272
- Struble, M. F., & Rood, H. J. 1999, *ApJS*, **125**, 35
- Thomas, D., Maraston, C., & Bender, R. 2003, *MNRAS*, **339**, 897
- Thomas, D., Maraston, C., Bender, R., & Mendes de Oliveira, C. 2005, *ApJ*, **621**, 673
- Thomas, D., Maraston, C., & Johansson, J. 2011, *MNRAS*, **412**, 2183
- Trager, S. C., Worthey, G., Faber, S. M., Burstein, D., & González, J. J. 1998, *ApJS*, **116**, 1
- Trager, S. C., Faber, S. M., Worthey, G., & González, J. J. 2000, *AJ*, **120**, 165
- Tremonti, C. A., Heckman, T. M., Kauffmann, G., et al. 2004, *ApJ*, **613**, 898
- van der Wel, A., Franx, M., van Dokkum, P. G., et al. 2014, *ApJ*, **788**, 28
- van Dokkum, P. G., Franx, M., Kriek, M., et al. 2008, *ApJ*, **677**, L5
- Ventimiglia, G., Gerhard, O., Arnaboldi, M., & Coccato, L. 2010, *A&A*, **520**, L9
- Ventimiglia, G., Arnaboldi, M., & Gerhard, O. 2011, *A&A*, **528**, A24
- Villumsen, J. V. 1983, *MNRAS*, **204**, 219
- Wall, J. V., & Jenkins, C. R. 2012, *Practical Statistics for Astronomers* (Cambridge University Press)
- White, S. D. M. 1980, *MNRAS*, **191**, 1
- Worthey, G. 1994, *ApJS*, **95**, 107
- Worthey, G., & Ottaviani, D. L. 1997, *ApJS*, **111**, 377

Appendix A: Simulations of the variance of Lick indices and stellar populations generated by a systematic error of the sky subtraction at the $\pm 1\%$ level

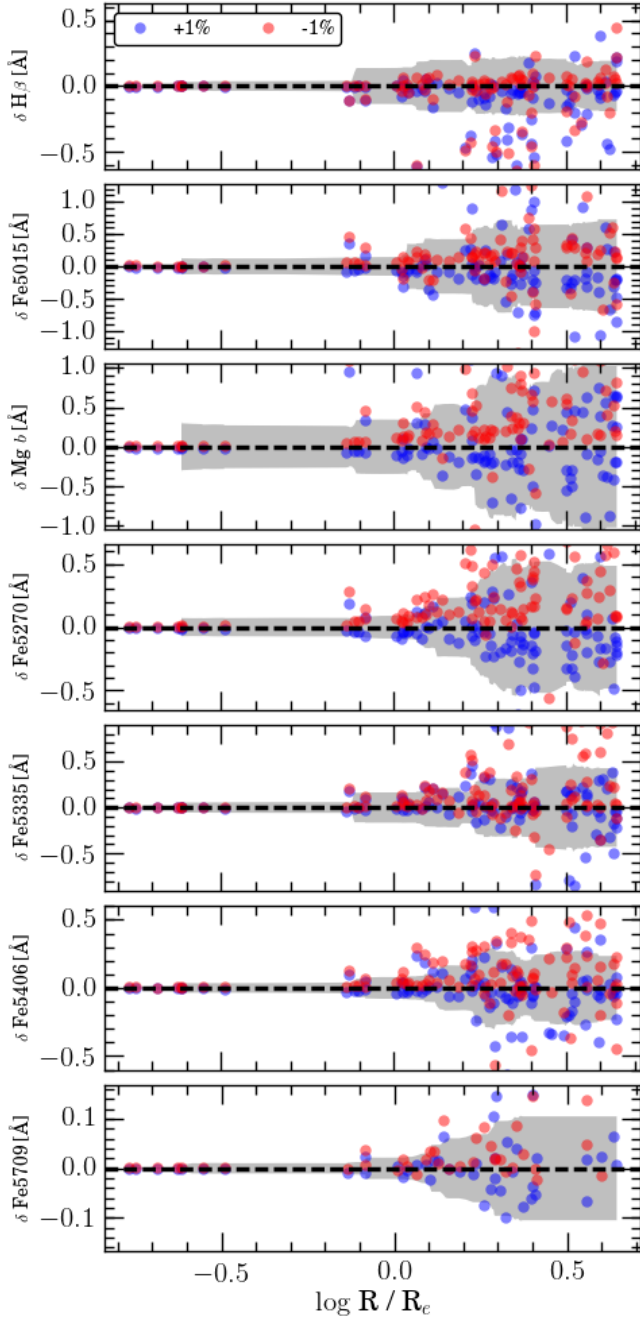


Fig. A.1. Difference of the Lick indices values generated by a systematic error in the sky subtraction of $\pm 1\%$ as a function of the distance to the centre of NGC 3311. The blue (red) circles represent the measurements performed by the addition (subtraction) of 1% of the sky spectra. The grey shaded areas represent the rolling standard deviation in the measurements.

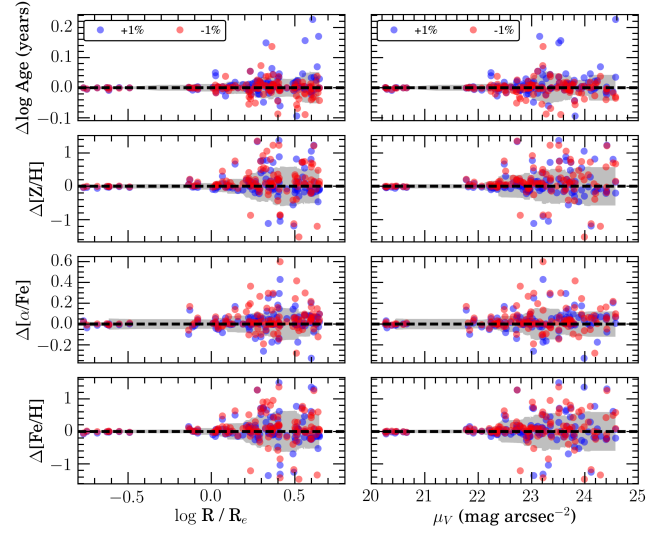


Fig. A.2. Difference of the stellar population parameters generated by a systematic error in the sky subtraction of $\pm 1\%$ as a function of the distance to the centre of NGC 3311 (*left*) and as a function of the *V*-band surface brightness (*right*). The blue (red) circles represent the measurements performed by the addition (subtraction) of 1% of the sky spectra. The grey shaded areas represent the rolling standard deviation in the measurements.

Chapter 6

A MUSE view of NGC 3311

6.1 Introduction

In chapters 4 and 5, we have shown the stellar halo of the cD galaxy NGC 3311 supports the idea that the mass assembly of this massive ETG follows the predictions of the two-phase model (Naab et al., 2009; Oser et al., 2010), in which galaxies are initially formed in rapid dissipative processes, followed by a long process of accretion mostly by dry mergers which deposit stars at large radii. In this particular case, the large velocity dispersion of the diffuse stellar halo indicates that the stars have been accreted by the action of the cluster’s gravitational potential, and the presence of a large substructure supports the idea that this process is still happening. However, there are important questions regarding the formation of cD galaxies that are still open.

One important question is if there is an observable transition between the in situ and the accreted components. Such a transition has important implications for the current understanding of the formation of cD galaxies. The classic picture for cD galaxies indicates that their surface brightness profiles may be decomposed into two components (e.g. Gonzalez et al., 2005) and the transition between these two photometric components would also mark the transition of the velocity dispersion. However, this picture was questioned by Bender et al. (2015), who studied the prototype cD galaxy NGC 6166 and obtained a smooth photometric transition between the inner and outer stellar halos, while still favoring two kinematic components. The confirmation of such finding in another system can clarify the definition of a cD galaxy.

Another important aspect is the connection between the low-metallicity peak in the

outer halo population with the galaxies in the infalling group. If the stellar populations of the dwarf galaxies were indeed compatible with the metallicity of the outer halo, we would have another strong evidence of a galaxy-cluster interaction at play. However, in our previous study, we had only one dwarf galaxy with known abundances, and thus the study of the stellar population of galaxies in the infalling group was required.

To study these questions, we have recently obtained new observations for the central region of the Hydra I cluster with the multi unit spectroscopic explorer (MUSE), a large field integral field spectrograph. In this chapter, we are going to show our preliminary results which will be fully explored in a forthcoming article. In Section 6.2, we present our observations and the data reduction process. In section 6.3, we explain the process used in the determination of the kinematics and emission lines. In Section 6.4, we present our results for the kinematics of the stars and the analysis of the velocity field using KINEMETRY. In Section 6.5, we show the distribution of fluxes of the emission lines and the resulting BPT diagram. In Section 6.6, we present the distribution of Lick indices and in Section 6.7 we present the resulting modeling of the indices in terms of ages and abundances. Finally, in Section 6.8, we present the summary and conclusions of this chapter. As in previous chapters, we adopt the distance to the Hydra I cluster of $D = 50.7$ Mpc, which results in $1'' = 0.262$ kpc, and we assume an effective radius of NGC 3311 of $R_e = 8.4$ kpc (Arnaboldi et al., 2012).

6.2 Observations and data reduction

We have obtained integral field observations of the core of the Hydra I cluster using the MUSE instrument (Henault et al., 2003; Bacon et al., 2004), mounted at the Nasmyth focus of the UT4 8m telescope of the Very Large Telescope array, under ESO program ID 094.B-0711A (PI: Arnaboldi). Observations were carried out using the wide field mode, which allows the observation of a FOV of 1×1 arcmin² with spatial sampling of 0.2×0.2 arcsec², which in the case of NGC 3311, corresponds to a box with dimensions 15.7×15.7 kpc². The spectra are observed in the wavelength range $4650 \leq \lambda(\text{\AA}) \leq 9300$ with resolving power varying from 2000 to 4000. Figure 6.1 shows the strategy used in our observations: three fields, A, B and C, positioned along the major axis of NGC 3311 which is able to probe the center of NGC 3311 and the NE substructure, plus an additional field, D,

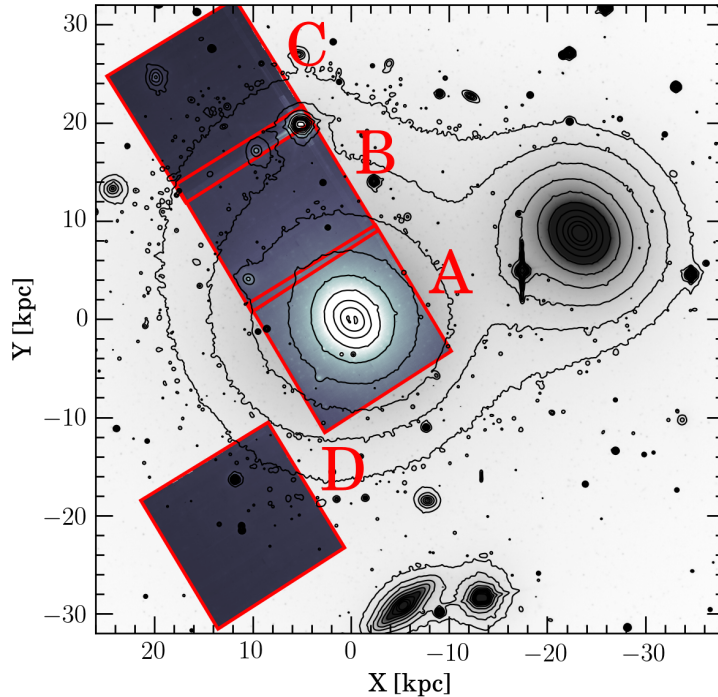


Figure 6.1: Scheme of the strategy for the observations of NGC 3311 at the Hydra I cluster using MUSE. Observations are based on four fields, three aligned with the major axis (A, B, and C) to survey the central region of the galaxy and the NE substructure. Another field (D) is targeted to observe the tidal tail of the lenticular galaxy HCC 007. The V-band image from Arnaboldi et al. (2012) is used in the background, while the small images inside the squares are obtained with the median flux of the data cubes in the interval $4500 \leq \lambda(\text{\AA}) \leq 5500$. Black lines show the V-band contours in the range from 20 to 23.5 mag arcsec⁻² in intervals of 0.5 mag arcsec^{-2filei}.

intended to observe the tidal tail of the lenticular galaxy HCC 007.

The data reduction was executed with the ESO Reflex package (Freudling et al., 2013), an environment based on the Kepler¹ workflow platform that provides a real-time visualization of the data processing. We have used the standard recipes for the instrument for the reduction, which includes flat fielding, bias correction, wavelength calibration, sky subtraction, flux calibration and combination of the cubes. The final four cubes are composed of ≈ 95 thousand spectra each, and most of the FOV is usable in our analysis. We have to mask out from the analysis only the saturated star observed in the upper region of field B and its diffraction spikes that are also observed in field C. In this chapter, we restricted the analysis to the wavelength range $4800 \leq \lambda(\text{\AA}) \leq 7000$ because of problems in the sky-subtraction in the near-infrared, not yet solved in the version of the pipeline by

¹ <https://kepler-project.org/>

the time we processed the data.

The Hydra I cluster core has a large population of low-mass systems in the central region, including dwarf galaxies (Misgeld et al., 2008) and ultra-compact dwarfs (Misgeld et al., 2011), which we have to avoid, in a first moment, for the analysis of the extended stellar halo. We have used SEXTRACTOR (Bertin and Arnouts, 1996) in the images produced by the collapsing of the cubes in order to produce a segmentation image, which is used as a way to separate different sources. We have also performed changes in the segmentation image to separate a few objects that were blended in the SEXTRACTOR analysis, and we also separated the central dust lanes from the remaining of the galaxy in order to avoid contamination in the central region.

We combined spectra using the Voronoi binning method (Cappellari and Copin, 2003) in order to obtain $S/N \sim 50$ in each spectrum. In fields A and B, this process was carried out over the entire FOV, but such a large S/N is not achieved in fields C and D even with the combination of all the spectra in the cube. In those cases, we have separated the spectra in a few radial bins in order to keep some information about the radial distribution but, in this preliminary analysis, we excluded spectra with $S/N < 10$. The binning scheme and the resulting S/N distribution of the stellar halo of NGC 3311 halo is shown in Figure 6.2. Notice that this S/N distribution is measured from the spectra after the combination of the data, and thus it is different from the expected value calculated in the Voronoi binning.

6.3 Data analysis

As in previous chapters, we have used the pPXF code (Cappellari and Emsellem, 2004) to extract the stellar and gas kinematics. In this case, we have used two kinematic components, one for the stellar and another for the gas emission. The stellar component was calculated using a set of SSP templates constructed with stars from the MILES library (Sánchez-Blázquez et al., 2006; Falcón-Barroso et al., 2011), calculated with a bimodal IMF (Vazdekis et al., 1996), metallicities in the range $-0.66 \leq [Z/H] \leq 0.40$, ages between 0.1 and 14 Gyr and varied alpha-element abundances ($[\alpha/Fe]=0, 0.4$). The gas component was fitted using a set of Gaussian emission line templates including $H\beta$ ($\lambda 4861$), $[O III]$ ($\lambda 4959, \lambda 5007$), $H\alpha$ ($\lambda 6565$), $[N II]$ ($\lambda 6585, \lambda 6550$) and $[S II]$ ($\lambda 6718, \lambda 6733$), considering

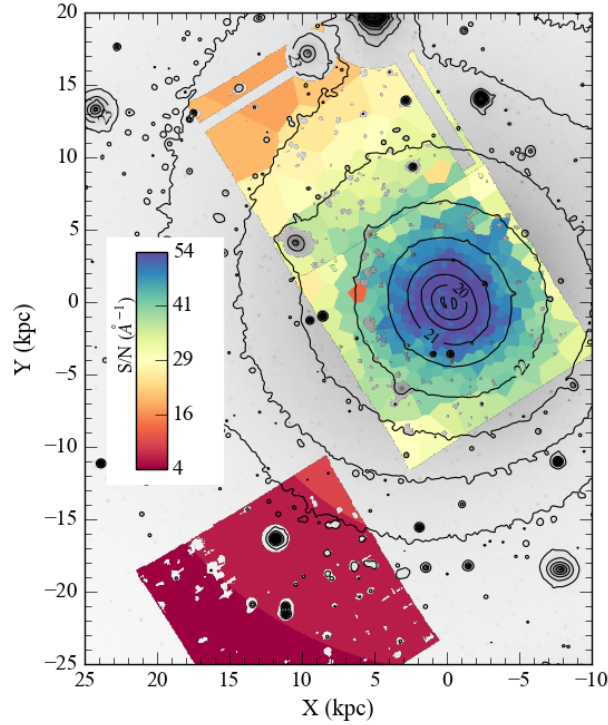


Figure 6.2: Binning scheme and resulting S/N distribution of the stellar halo of Hydra I cluster core with MUSE observations. Masked regions include low signal to noise ($S/N < 10$), dwarf galaxies and globular clusters detected with SExtractor and saturated stars and their trails.

a two-moment LOSVD with an additional constraint that $\sigma_{\text{gas}} < 80 \text{ km s}^{-1}$. We have used additive polynomials to correct for small variations in the flux calibration, and regions of the spectra containing strong sky lines were masked during the calculations. Figure 6.3 illustrates the results of this procedure for one of our combined spectra.

The MUSE data have a resolution that varies as a function of the wavelength. Therefore, for a proper calculation of the LOSVD, we have homogenized the spectral resolution of the observations to a unique value. We have convolved the observations with Gaussian filters to obtain a spectral resolution of $\text{FWHM} \approx 2.9$, corresponding to the resolution of the blue part of the spectra where the resolution is the lowest. Both the stellar and the emission templates were also prepared to match this resolution.

6.4 Stellar kinematics

Figure 6.4 shows the distribution of the four moments of the Gaussian-Hermite expansion obtained from the stellar component. The systemic velocity in the center of NGC

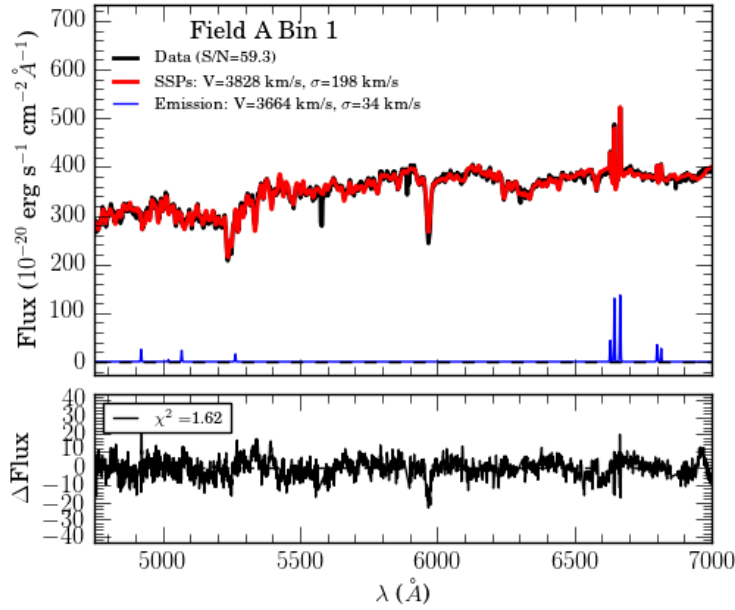


Figure 6.3: Example of the fitting process with pPXF for the MUSE observations of the Hydra I cluster core. The upper panel displays the observed spectrum (black), the best fit for the stellar component (red) and the best fit for the emission lines (blue). The lower panel shows the residuals of the fitting.

3311 shows a complex distribution that suggests a pattern of rotation in the center. The velocity dispersion indicates that the galactic halo dominates the light only in the very central region, while the high-velocity dispersion of the extended halo is observed in the region of the NE structure. The high S/N in the center in these observations indicate that the skewness parameter h_3 is slightly negative in the center ($h_3 \approx -0.02$) and the kurtosis parameter is indeed positive ($h_4 \approx 0.10$). This consistency is clearly shown in Figure 6.5, where we compare the radial profiles of the four moments of the MUSE data with those obtained with FORS2.

The systemic velocity of the central galaxy is shown in the first panel of Figure 6.4. The central heliocentric systemic velocity is approximately 3835 km s^{-1} , in agreement with previous measurements (Ventimiglia et al., 2010; Richtler et al., 2011) and indeed offset in relation to the cluster's systemic velocity of 3777 km s^{-1} (Struble and Rood, 1999). As indicated in Chapter 4, the four central slits indicated some ordered rotation, but the systemic velocity map suggests that the central region of NGC 3311 rotates. Figure 6.6 shows the systemic velocity as a function of the position angle at different isophotal V-band levels, which indicates a sinusoidal pattern. To improve visualization, we have smoothed the data to produce the solid lines and folded the plots around the maximum velocity

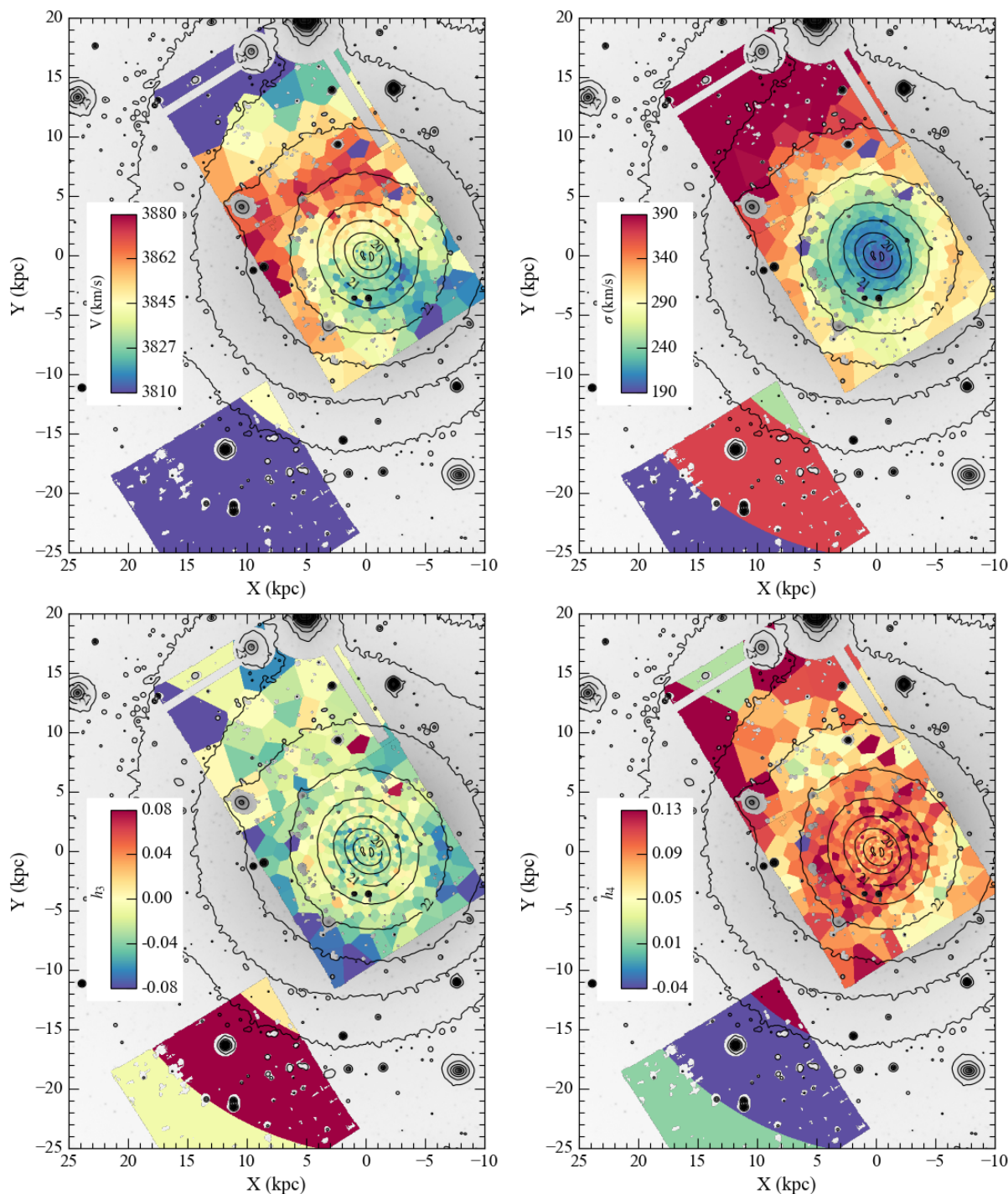


Figure 6.4: Maps for the four moments of the LOSVD: systemic velocity (V), velocity dispersion (σ), skewness (h_3) and kurtosis (h_4).

position angle (PA_{vmax}) to compare the symmetry of the rotation. For $V < 19.5$ mag arcsec $^{-2}$, there is very little evidence of rotation, but this region may not be reliable for the calculations due the known dust lanes that heavily obscure the core of NGC 3311. However, the systemic velocity displays some patterns that resemble a coherent rotation in

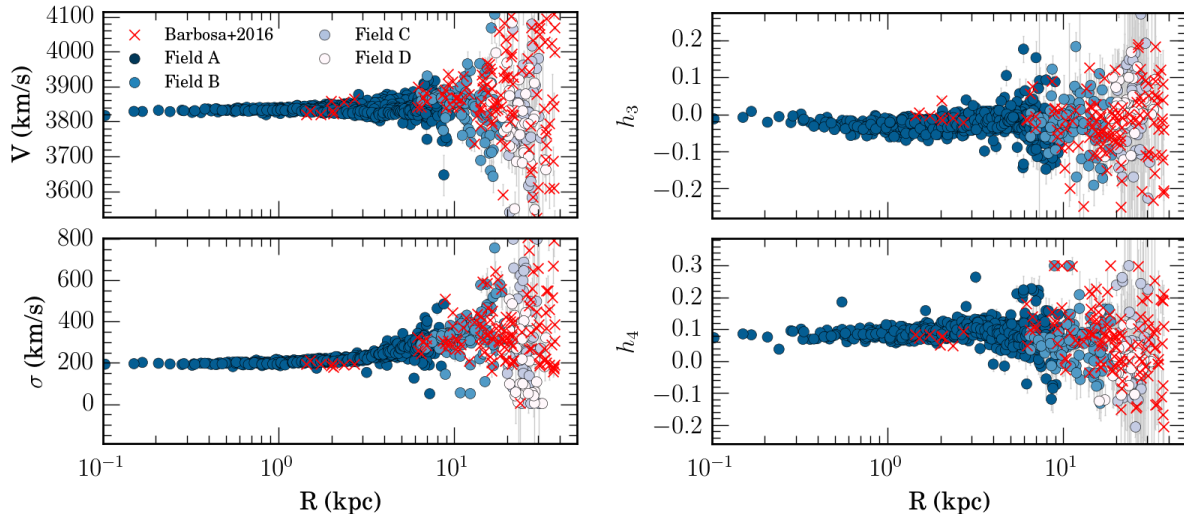


Figure 6.5: Comparison of the kinematics of the Hydra I cluster core obtained with MUSE and FORS2 data. Circles indicate the results from the MUSE data, with colors representing the observed field, and the red crosses indicate the data from the previous analysis in chapter 4.

the interval $20 \leq V(\text{mag arcsec}^{-2}) \leq 21.5$, which may be an indicative that the system may have a kinematically decoupled core (KDC), that is, a system with a nuclear kinematics different from the remaining of the velocity field.

To verify this hypothesis in a more quantitative way, we have analyzed the velocity map using KINOMETRY (Krajinović et al., 2006), which generalizes the method of ellipse fitting (e.g. Jedrzejewski, 1987) by modeling the velocity field (K) in successive elliptical rings along the kinematic major axis (a), each fitted with a harmonic series given by

$$K(a, \phi) = A_0(a) + \sum_{n=1}^N k_n(a) \cos[n(\phi - \phi_n(a))], \quad (6.1)$$

where A_0 and k_n are amplitude coefficients, $\phi_n(a)$ are the phase coefficients and ϕ is the kinematic position angle. The two most important terms in our analysis are k_1 , which describes the rotation velocity, and k_5 , which measures the residuals in relation to the rotation velocity. A low k_5/k_1 indicates that rotation is supported by the models, while large k_5/k_1 indicates the opposite. For reference, the SAURON survey uses the criteria $k_5/k_1 < 0.02$ to define the regular rotators (Krajinović et al., 2008), while the Atlas3D survey uses the criteria $k_5/k_1 < 0.04$ (Emsellem et al., 2011).

Figure 6.7 shows the result of our analysis, in which we have fixed only the center of the system to be the center of NGC 3311 while leaving the axial ratio $q = 1 - a/b$ free to

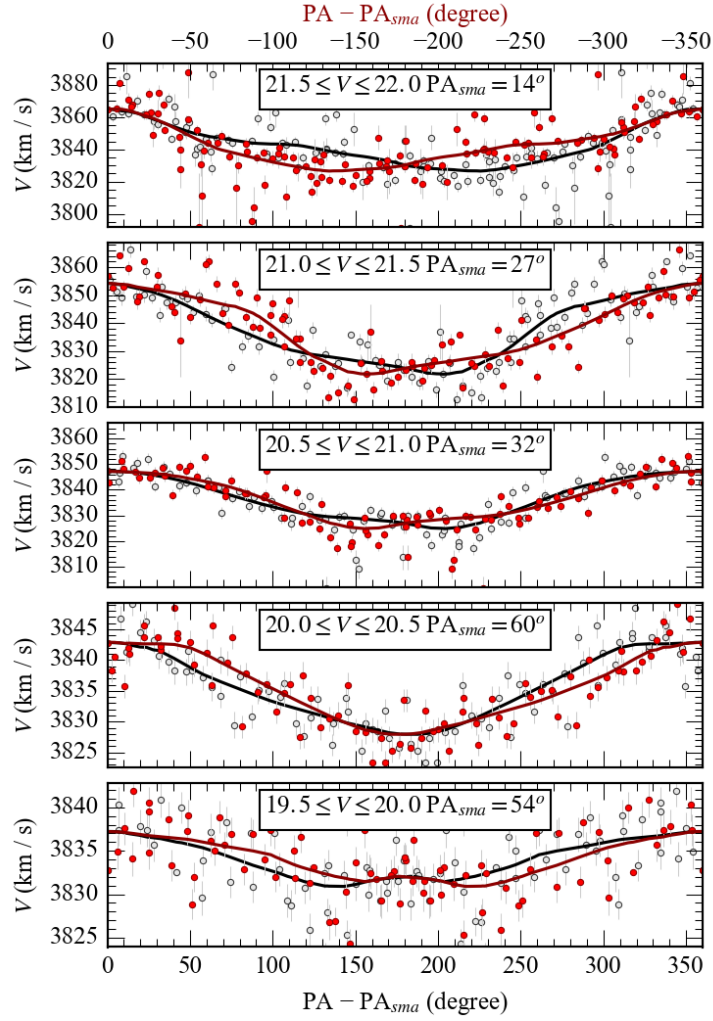


Figure 6.6: Velocity as a function of the position angle for various radial sections.

be adjusted. In these figures, it is possible to notice that the rotation is small, reaching a maximum value of $\approx 30 \text{ km s}^{-1}$, and the axial ratio and the kinematic position angle ϕ_1 are not well defined, as they do not converge to a stable value. Moreover, the ratio k_5/k_1 is always larger than 0.04, indicating that the velocity field of NGC 3311 does not indicate the presence of a KDC.

6.5 Emission line analysis

Our main motivation for the inclusion of emission line spectra in the pPXF fitting was to avoid contamination of such lines over the absorption line features. However, emission lines may, in fact, give some additional information about the physical state of the gas in the galaxy, star formation rate, and gas-phase metallicity.

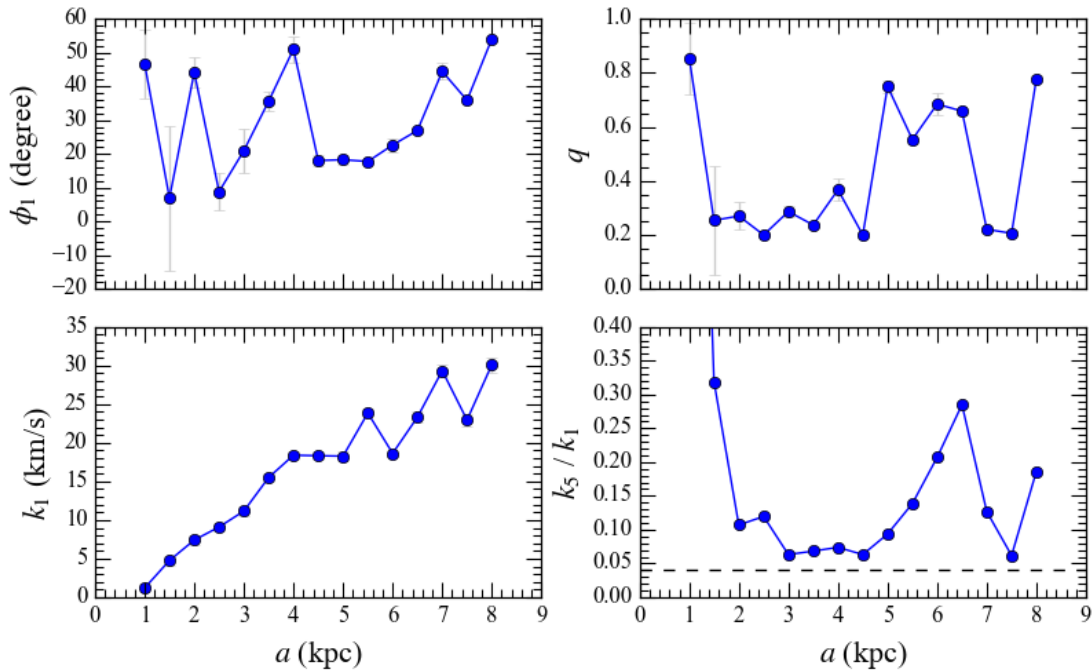


Figure 6.7: Analysis of the velocity field of NGC 3311 using KINEMETRY. The k_1 coefficient indicates the degree of rotation in the field, ϕ_1 is the position angle of the velocity field, q represents the axial ratio and the ratio k_5/k_1 indicates the deviations from the rotation field as a function of the semi major axis a . The dashed black line in the bottom right figure indicates the maximum threshold for a typical regular rotator in the SAURON and Atlas3D surveys.

We have measured the total flux using the weights for the emission line templates in the pPXF fitting. To correct these fluxes for the interstellar extinction, we have determined the nebular color excess $E(B - V)$ using the Balmer decrement, which remains approximately constant in star-forming galaxies. Following Osterbrock (1989), we assume a temperature $T = 10^4$ K, an electron density $n_e = 10^2 \text{ cm}^{-3}$, and an intrinsic ratio $(\text{H}\alpha/\text{H}\beta)_{\text{int}} = 2.86$, the nebular color excess is given by

$$E(B - V) = 1.97 \log \left[\frac{(\text{H}\alpha/\text{H}\beta)_{\text{obs}}}{2.86} \right], \quad (6.2)$$

where $(\text{H}\alpha/\text{H}\beta)_{\text{obs}}$ is the observed line ratio. Using these color excesses, we have then corrected the emission line for the extinction using the empirical extinction law

$$F(\lambda) = F_{\text{obs}}(\lambda) 10^{0.4k(\lambda)E(B-V)}, \quad (6.3)$$

where $F(\lambda)$ is the total flux of an emission line with wavelength λ and $k(\lambda)$ is the reddening curve. In this work, we have adopted the reddening curve given by Cardelli et al. (1989)

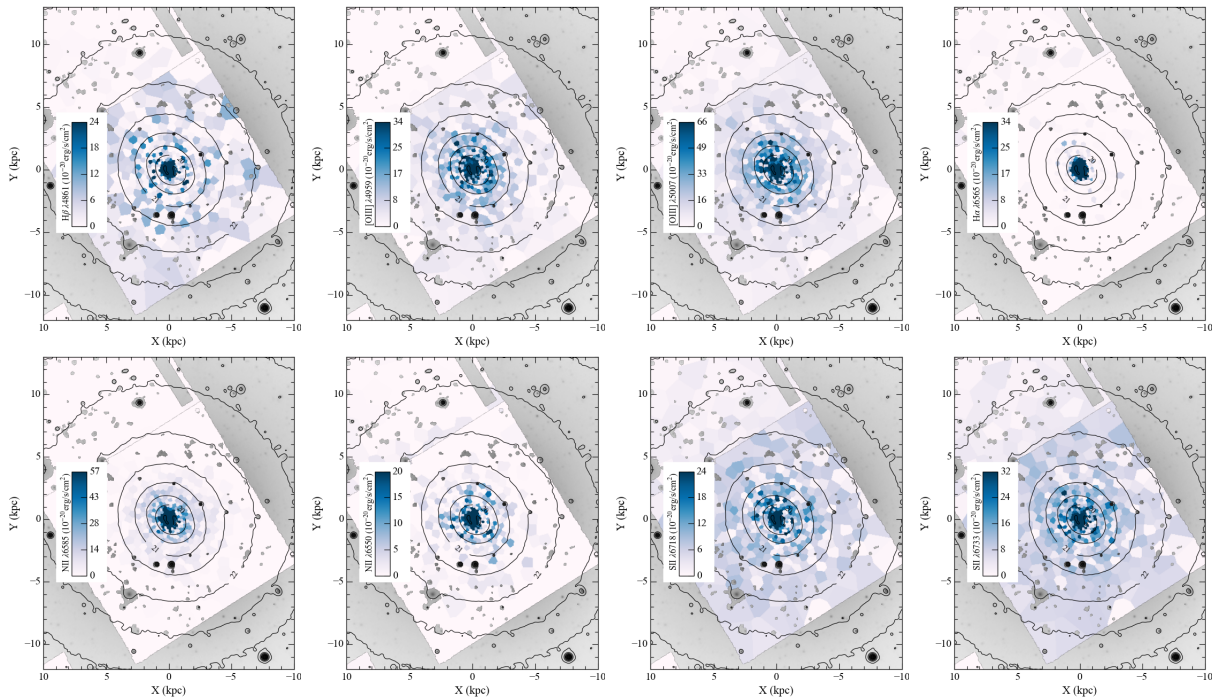


Figure 6.8: Emission line fluxes corrected for the interstellar extinction using Balmer decrement and reddening curves given by [Cardelli et al. \(1989\)](#).

assuming an extinction factor of $R_V = 3.1$ like that found for our Galaxy. Figure 6.8 shows the distribution of the fluxes in the emission lines for all cases considered in our analysis. It is clear that the gas is concentrated in the center of NGC 3311, especially $H\alpha$ which reaches fluxes of $\approx 6600 \text{ erg s}^{-1} \text{ cm}^{-2}$ in the central kiloparsec, but falls to zero at 4 kpc.

To obtain more information about the physics of the gas, we use Baldwin-Phillips-Terlevich diagram (BPT [Baldwin et al., 1981](#)), displayed in Figure 6.9. We have restricted our analysis to emission lines with amplitudes at least as high as the mean noise of the spectra, restricting our analysis to two kiloparsecs around the center of NGC 3311. We have included the empirical line that separates star formation from AGN from [Kauffmann et al. \(2003\)](#) and the photoionization models from [Kewley et al. \(2001\)](#) in the BPT diagram. The star-forming region of NGC 3311 is limited to the inner kiloparsec, but the source of ionization already changes at 2 kpc to another source of ionization. The observed BPT diagram for NGC 3311 is characteristic of a star-forming galaxy according to the classification of [Belfiore et al. \(2016\)](#), who have observed the spatially resolved BPT diagrams in the MaNGA survey.

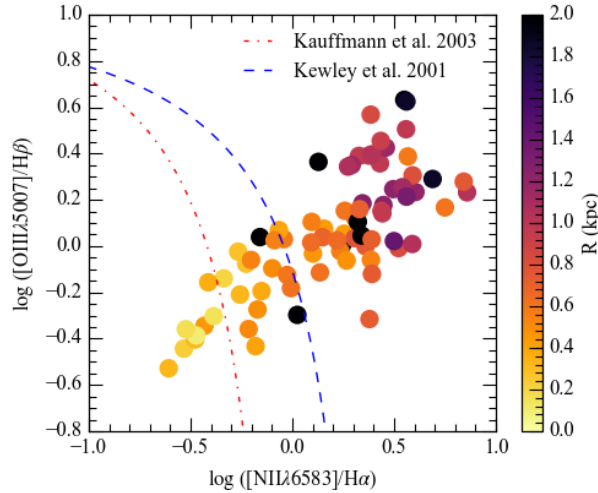


Figure 6.9: The BPT diagram for the galaxy NGC 3311 restricted to emission lines with amplitude larger than the noise. Colors of the circles indicate the distance to the center of the system according to the color bar on the right. Blue dashed lines indicate the division of star-forming galaxies according to Kewley et al. (2001), while the red dot-dashed lines indicate the empirical division according to Kauffmann et al. (2003).

6.6 Lick indices

We have used our routine PYLECTOR to measure the Lick indices in the new MUSE data set for the Hydra I cluster core. We have corrected for the effects of emission line contamination using the observations in the Section 6.5, and we have used the best fit templates and equation (2.7) for the correction of the indices for the effect of broadening. In this case, we do not need to match the resolution of the MUSE spectrograph with that of the Lick/IDS system because we have flux calibrated spectra which can be modeled with models from Thomas et al. (2011). The results are shown in Figure 6.10.

In Chapter 5, we have shown that the Lick indices already indicated the changing in the stellar content from the central galaxy to the outer stellar halo, with a transition around $R \approx R_e = 8.4$ kpc. Figure 6.11 shows the radial profile of the Lick indices for the stellar halo spectra, also including the results from the FORS2 analysis. To compare with the measurements in the previous work we have measured the Lick indices in the FORS2 data without matching the resolution of the instrument with the resolution of the Lick system. Despite the large scatter of the FORS2 data, there is a good consistency in the results for most indices. The MUSE data reveals that the gradients observed from 1.5 to 8.4 kpc (what we called "inner galaxy" in chapter 5) are not extended to the central region of the galaxy, where the slope is much flatter for all indices. The gradients tend to extend

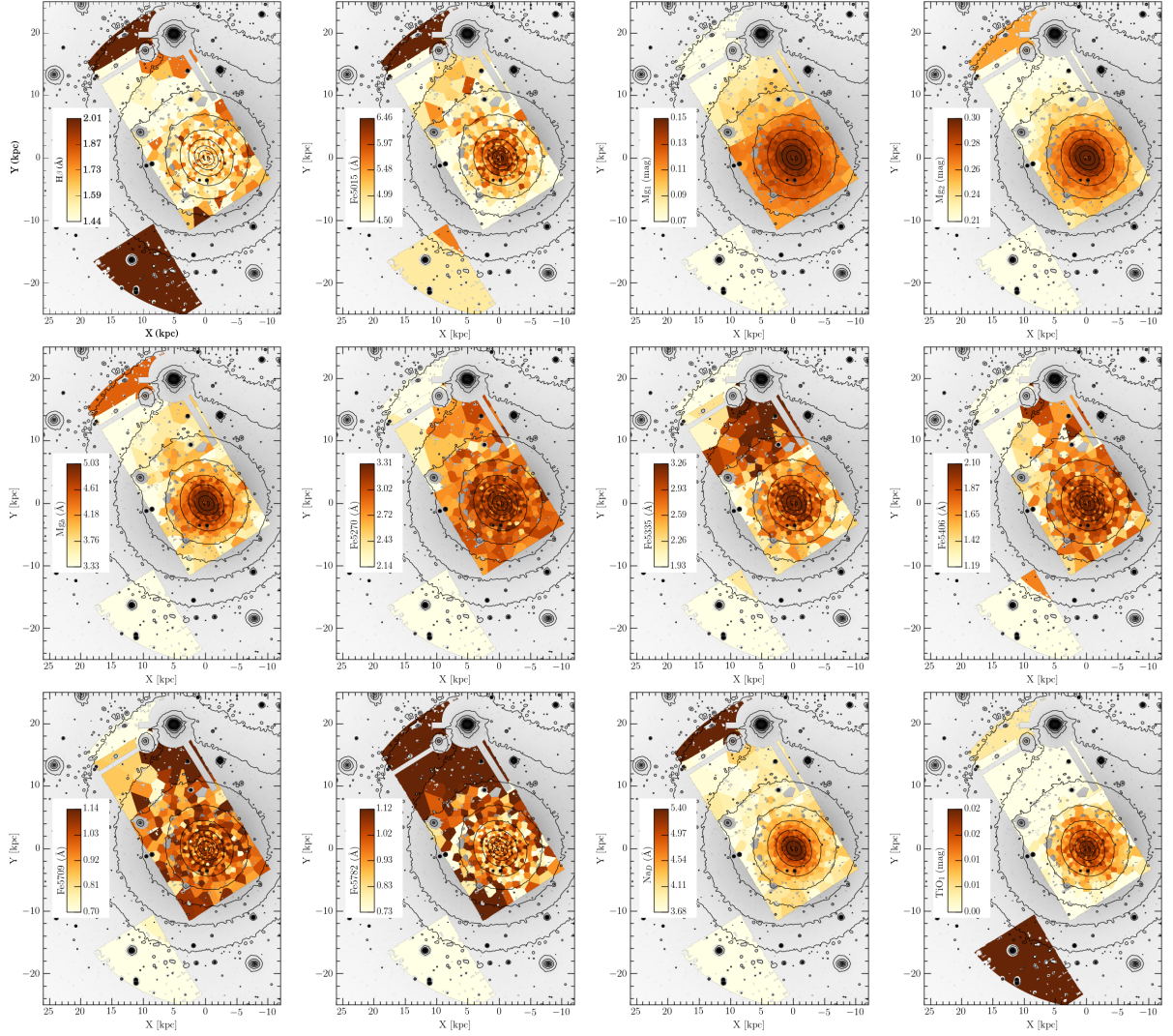


Figure 6.10: Distribution of the Lick indices in the Hydra I cluster core for the MUSE data set.

outwards, out to 11 kpc, but the iron indices Fe5015, Fe5335 and Fe5782 clearly indicate a pronounced change of slope around one 9 kpc. These new observations also allow the observation of the NaD, which also indicates a flattening of the gradient at large radius, and the titanium index TiO1, which seems to become steeper.

6.7 Stellar populations

We have modeled the Lick indices using the models from [Thomas et al. \(2011\)](#) using our Monte Carlo Markov chain (MCMC) method described in Chapter 2. In this preliminary analysis, we have used only a subset of the Lick indices that are not sensitive to changes in the nitrogen and carbon abundances for simplicity, including H β , Mgb, Fe5270, Fe5335, and Fe5406. We have assumed the same simple model described in Chapter 2, where

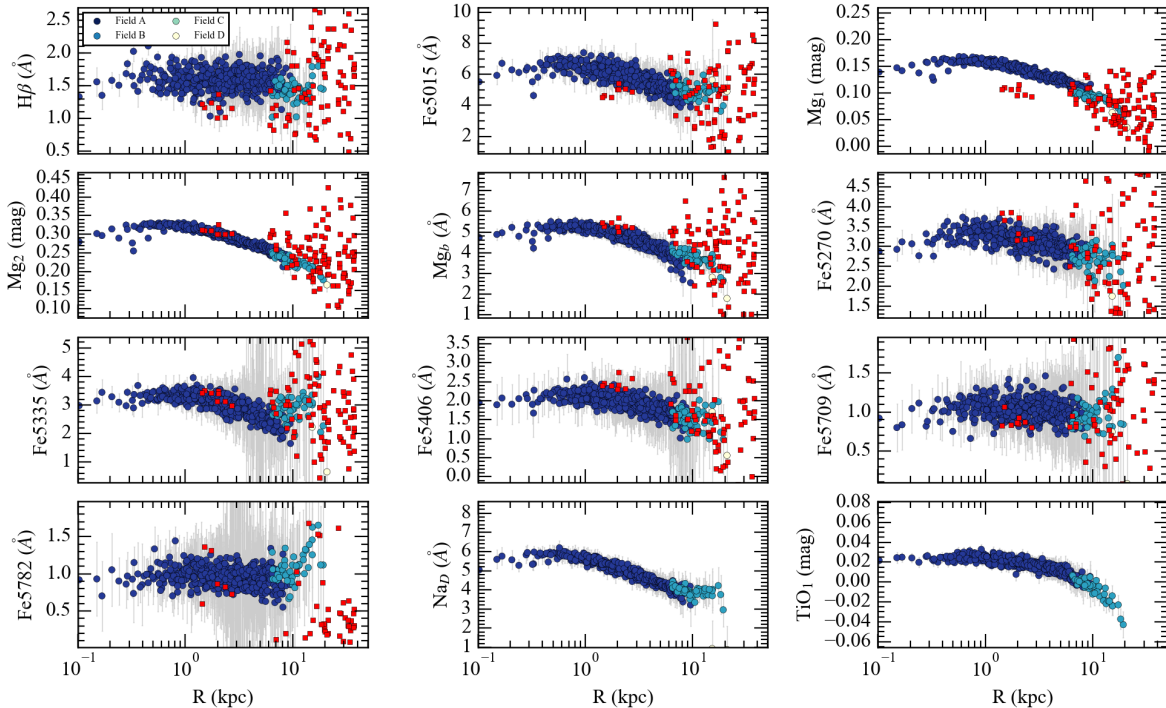


Figure 6.11: Radial profile of the Lick indices in the Hydra I cluster core including the MUSE and FORS2 data sets. Circles indicate the MUSE data set, with colors indicating the observed field. Red squares indicate the results from the FORS2 analysis.

we assume noninformative priors for the stellar populations, and Gaussian uncertainties for the Lick indices. We use the maximum posterior probability for each parameter, and uncertainties are calculated using the highest probability density interval which covers 68% of the probability. The results of this analysis are shown in Figure 6.12.

In general terms, the stellar population properties of Figure 6.12 are in good agreement with the previous modeling in Chapter 5, as expected, as the Lick indices used in the modeling are similar. However, these new maps display a number of substructures not observed before. The age and the total metallicity in the center of galaxy NGC3311 display a common structure. This may indicate an effect of the age-metallicity degeneracy that was not broken in the previous analysis with so few indices. Interestingly, the alpha-element abundance displays a pattern that seems to correlate with the velocity field in the southwest of field A, which may indicate the presence of a stellar population kinematically decoupled from the remaining of the central population, containing stars formed in much less massive halos than those in NGC 3311. The abundance of iron is more homogenous, but there is a clear low iron abundance region in the location close to the dwarf galaxy in field B.

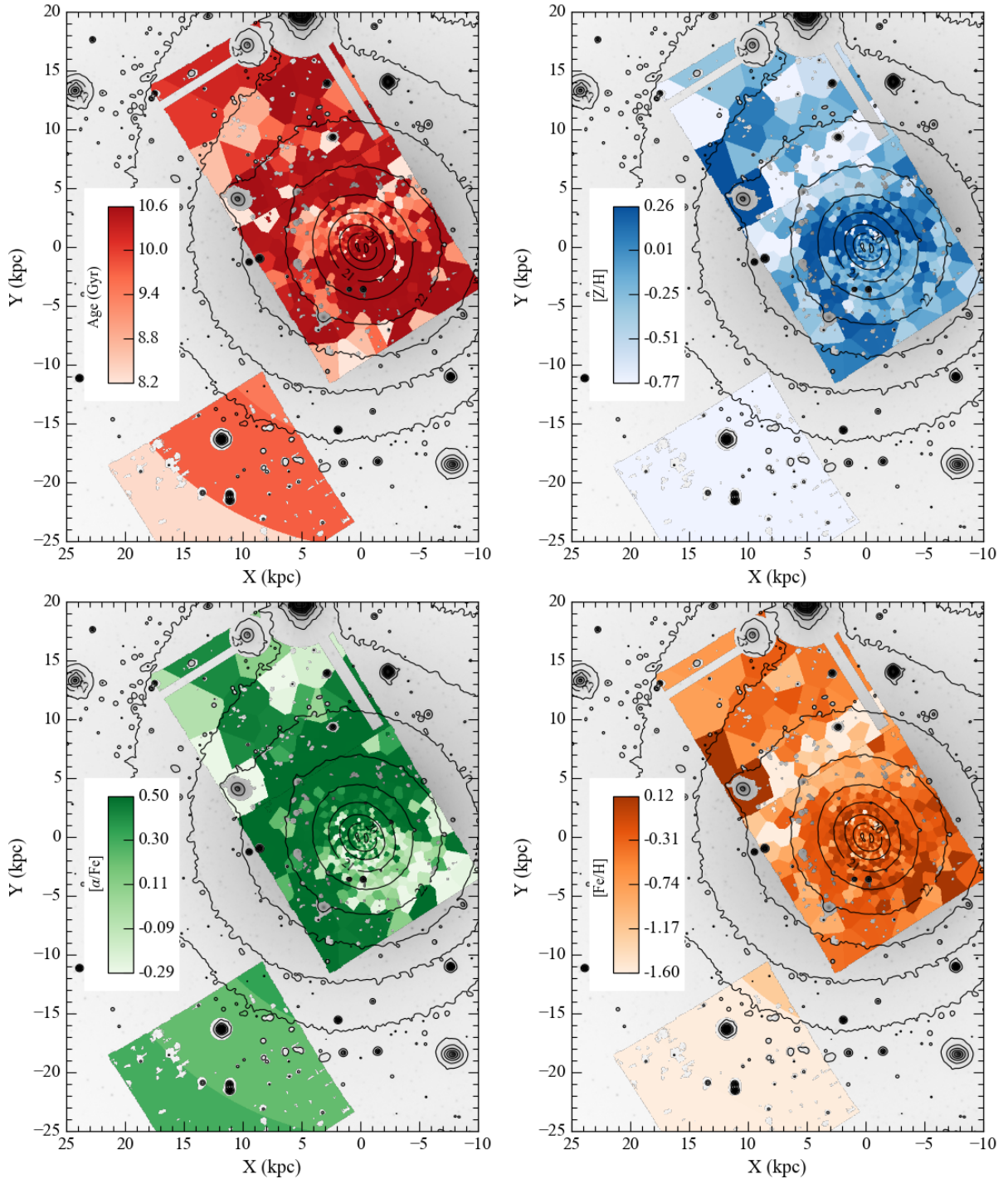


Figure 6.12: Distribution of the stellar population properties in the Hydra I cluster core for the MUSE data set.

6.8 Summary and future perspectives

In this chapter, we have shown the preliminary results from our analysis of the Hydra I cluster core using new observations using the MUSE spectrograph, which allows the study of the system with unprecedented detail. The stellar kinematics analysis has shown good

agreement with our previous work using FORS2 data, which indicates that the galactic halo has a complex LOSVD. The central region of NGC 3311 is not a regular rotator, and the velocity dispersion profile indicates the presence of a small galactic halo in the middle of a large number of stars bound to the cluster's gravitational potential. The center of NGC 3311 contains cold gas, which indicates current star formation. Finally, the stellar population indicates a complex distribution of metals and old stellar populations.

This chapter has shown the potential of the observations using integral field spectrographs for the study of cD galaxies. In future work, we plan to improve the modeling of the stellar populations, including testing other theoretical models and also other methods, to attempt to clarify if the age-degeneracy observed if the age-degeneracy is playing a role in our results. We also would like to extend our analysis more to the red, including the analysis of the Ca II triplet, in order to have additional information about the metallicity and possibly about the IMF. This would require a proper modeling of the sky subtraction, which may be resolved with the new code ZAP ([Soto et al., 2016](#)).

Chapter 7

Conclusion and perspectives

In this thesis, we have conducted an observational study of the formation and evolution of galaxies in the local universe through the analysis of their kinematic properties and stellar populations. In the following, we review our main results and discuss some future perspectives for our research.

The methodology described in Chapter 2 indicates an important achievement, which was the development of a Bayesian framework to study stellar populations. This is one of the most promising aspects of this work, and we plan to extend and refine the method to other purposes as described below. In the recent and comprehensive review on spectral energy distribution (SED) fitting, [Walcher et al. \(2011\)](#) have shown the necessity of going beyond the use of SSPs for the determination of more realistic stellar formation histories of ETGs, which may be incorporated in a Bayesian context naturally. Also, the methods used in this thesis may be extended to other types of data, such as broad and narrow band photometry, which we plan to explore in the future in the context of large photometric surveys, such as the Southern photometric local universe survey (S-PLUS) and Javalambre physics of the accelerating universe astrophysical survey (J-PAS).

In Chapter 3, we have performed the study of galaxies in groups. The importance of groups of galaxies in the cosmological context have become clear in the last decade, and a number of articles have been devoted to the theme. However, there are few attempts to understand the stellar population properties of these systems extending to low mass galaxies. In this work, we have shown that previous scaling relations between stellar populations and velocity dispersions may be extended to less massive systems. The verification of these results may be used to impose constraints onto models of galaxy evolution in this

particular environment, which can be used to explain the existence of the bimodality of the colors of galaxies. We plan to extend this work by further investigating the correlations pointed out here for the lowest mass bin. This, however, requires new observations in 8m class telescopes.

The following chapters were dedicated to the study of the Hydra I cluster core, including the BCG galaxy NGC 3311 and the extended and diffuse stellar halo surrounding it. In Chapter 4, we have presented the kinematic analysis of the system, in which we have observed the large-scale kinematic properties. Our two-dimensional study has shown that the large difference in the velocity dispersion profiles in previous works of [Ventimiglia et al. \(2010\)](#) and [Richtler et al. \(2011\)](#) is explained by the presence of a large substructure identified in the photometry by [Arnaboldi et al. \(2012\)](#). In Chapter 5 we have shown our study of the stellar populations in the system, which demonstrated that the outer stellar halo is composed of stars both from major mergers in the formation of the BCGs and also from the recent infall of less massive systems, which may be related to the existence of an infalling group. Finally, in Chapter 6, we have shown preliminary results of our current work on the Hydra I cluster core using integral field observations with MUSE, in which we have shown the complexity of the stellar population distribution in the system. All these results support the idea that the assembly of mass occurs in the hierarchical growth set by the Λ CDM cosmology, and in particular that the two-phase model can explain the current state of NGC 3311. This thesis has shown the wealthy of information contained in spatially resolved stellar populations extended to large radii, an aspect that we would like to explore in future projects.

Bibliography

- Abazajian K. N., Adelman-McCarthy J. K., Agüeros M. A., Allam S. S., Allende Prieto C., Anderson K. S. J., Anderson S. F., Annis J., Bahcall N. A., et al. The Seventh Data Release of the Sloan Digital Sky Survey, *ApJS*, 2009, vol. 182, p. 543
- Appenzeller I., Fricke K., Fürtig W., Gässler W., Häfner R., Harke R., Hess H.-J., Hummel W., Jürgens P., Kudritzki R.-P., Mantel K.-H., Meisl W., Muschelok B., Nicklas H., Rupprecht G., Seifert W., et al., Successful commissioning of FORS1 - the first optical instrument on the VLT., *The Messenger*, 1998, vol. 94, p. 1
- Arnaboldi M., Ventimiglia G., Iodice E., Gerhard O., Coccato L., A tale of two tails and an off-centered envelope: diffuse light around the cD galaxy NGC 3311 in the Hydra I cluster, *A&A*, 2012, vol. 545, p. A37
- Baade W., The Resolution of Messier 32, NGC 205, and the Central Region of the Andromeda Nebula., *ApJ*, 1944, vol. 100, p. 137
- Bacon R., Bauer S.-M., Bower R., Cabrit S., Cappellari M., Carollo M., Combes F., Davies R. L., Delabre B., Dekker H., Devriendt J., Djidel S., Duchateau M., Dubois J.-P., Emsellem E., et al., The second-generation VLT instrument MUSE: science drivers and instrument design. In *Ground-based Instrumentation for Astronomy* , vol. 5492 of *Proc. SPIE*, 2004, p. 1145
- Baldwin J. A., Phillips M. M., Terlevich R., Classification parameters for the emission-line spectra of extragalactic objects, *PASP*, 1981, vol. 93, p. 5
- Balogh M. L., Morris S. L., Yee H. K. C., Carlberg R. G., Ellingson E., Star Formation in Cluster Galaxies at $0.2 < Z < 0.55$, *ApJ*, 1997, vol. 488, p. L75
- Barbosa C. E., Arnaboldi M., Coccato L., Hilker M., Mendes de Oliveira C., Richtler T., The Hydra I cluster core. I. Stellar populations in the cD galaxy NGC 3311, *A&A*, 2016, vol. 589, p. A139
- Beers T. C., Flynn K., Gebhardt K., Measures of location and scale for velocities in clusters of galaxies - A robust approach, *AJ*, 1990, vol. 100, p. 32
- Belfiore F., Maiolino R., Maraston C., Emsellem E., Bershadsky M. A., Masters K. L., Yan R., Bizyaev D., Boquien M., Brownstein J. R., Bundy K., Drory N., Heckman T. M., Law D. R., Roman-Lopes A., Pan K., et al., SDSS IV MaNGA - spatially resolved diagnostic diagrams: a proof that many galaxies are LIERS, *MNRAS*, 2016, vol. 461, p. 3111

- Bell E. F., Wolf C., Meisenheimer K., Rix H.-W., Borch A., Dye S., Kleinheinrich M., Wisotzki L., McIntosh D. H., Nearly 5000 Distant Early-Type Galaxies in COMBO-17: A Red Sequence and Its Evolution since $z \sim 1$, *ApJ*, 2004, vol. 608, p. 752
- Bender R., Kormendy J., Cornell M. E., Fisher D. B., Structure and Formation of cD Galaxies: NGC 6166 in ABELL 2199, *ApJ*, 2015, vol. 807, p. 56
- Benson A. J., Galaxy formation theory, *Phys. Rep.*, 2010, vol. 495, p. 33
- Bertin E., Arnouts S., SExtractor: Software for source extraction., *A&AS*, 1996, vol. 117, p. 393
- Binney J., Tremaine S., *Galactic Dynamics: Second Edition*. Princeton University Press, 2008
- Blanton M. R., Hogg D. W., Bahcall N. A., Baldry I. K., Brinkmann J., Csabai I., Eisenstein D., Fukugita M., Gunn J. E., Ivezić Ž., Lamb D. Q., Lupton R. H., Loveday J., Munn J. A., et al., The Broadband Optical Properties of Galaxies with Redshifts $0.02 < z < 0.22$, *ApJ*, 2003, vol. 594, p. 186
- Blumenthal G. R., Faber S. M., Primack J. R., Rees M. J., Formation of galaxies and large-scale structure with cold dark matter, *Nature*, 1984, vol. 311, p. 517
- Blumenthal G. R., Pagels H., Primack J. R., Galaxy formation by dissipationless particles heavier than neutrinos, *Nature*, 1982, vol. 299, p. 37
- Bond J. R., Szalay A. S., Turner M. S., Formation of galaxies in a gravitino-dominated universe, *Physical Review Letters*, 1982, vol. 48, p. 1636
- Buzzoni A., Lick-index entanglement and biased diagnostic of stellar populations in galaxies, *MNRAS*, 2015, vol. 449, p. 296
- Byrd G., Valtonen M., Tidal generation of active spirals and S0 galaxies by rich clusters, *ApJ*, 1990, vol. 350, p. 89
- Cappellari M., , 2012 pPXF: Penalized Pixel-Fitting stellar kinematics extraction *Astrophysics Source Code Library*
- Cappellari M., Copin Y., Adaptive spatial binning of integral-field spectroscopic data using Voronoi tessellations, *MNRAS*, 2003, vol. 342, p. 345
- Cappellari M., Emsellem E., Parametric Recovery of Line-of-Sight Velocity Distributions from Absorption-Line Spectra of Galaxies via Penalized Likelihood, *PASP*, 2004, vol. 116, p. 138

-
- Cappellari M., McDermid R. M., Alatalo K., Blitz L., Bois M., Bournaud F., Bureau M., Crocker A. F., Davies R. L., Davis T. A., de Zeeuw P. T., Duc P.-A., Emsellem E., Khochfar S., et al., The ATLAS^{3D} project - XX. Mass-size and mass- σ distributions of early-type galaxies: bulge fraction drives kinematics, mass-to-light ratio, molecular gas fraction and stellar initial mass function, *MNRAS*, 2013, vol. 432, p. 1862
- Cardelli J. A., Clayton G. C., Mathis J. S., The relationship between infrared, optical, and ultraviolet extinction, *ApJ*, 1989, vol. 345, p. 245
- Cardiel N., , 2010 indexf: Line-strength Indices in Fully Calibrated FITS Spectra Astrophysics Source Code Library
- Cardiel N., Gorgas J., Cenarro J., Gonzalez J. J., Reliable random error estimation in the measurement of line-strength indices, *A&AS*, 1998, vol. 127, p. 597
- Chabrier G., The Galactic Disk Mass Budget. I. Stellar Mass Function and Density, *ApJ*, 2001, vol. 554, p. 1274
- Cigan P., , 2004 Reducing Multi-fiber Spectra in IRAF with DOHYDRA: A Guide by Phil Cigan last modified March 11, 2008, accessed March 24, 2016, <http://www.astro.wisc.edu/~cigan/reducing/reducing.html>
- Cleveland W. S., Robust Locally Weighted Regression and Smoothing Scatterplots, *Journal of the American Statistical Association*, 1979, vol. 74, p. 829
- Cleveland W. S., Devlin S. J., Locally Weighted Regression: An Approach to Regression Analysis by Local Fitting, *Journal of the American Statistical Association*, 1988, vol. 83, p. 596
- Coccatto L., Gerhard O., Arnaboldi M., Distinct core and halo stellar populations and the formation history of the bright Coma cluster early-type galaxy NGC 4889, *MNRAS*, 2010, vol. 407, p. L26
- Coelho P., Barbuy B., Meléndez J., Schiavon R. P., Castilho B. V., A library of high resolution synthetic stellar spectra from 300 nm to 1.8 μm with solar and α -enhanced composition, *A&A*, 2005, vol. 443, p. 735
- Cohen J. G., Blakeslee J. P., Ryzhov A., The Ages and Abundances of a Large Sample of M87 Globular Clusters, *ApJ*, 1998, vol. 496, p. 808

- Coil A. L., Weiner B. J., Holz D. E., Cooper M. C., Yan R., Aird J., Outflowing Galactic Winds in Post-starburst and Active Galactic Nucleus Host Galaxies at $0.2 < z < 0.8$, *ApJ*, 2011, vol. 743, p. 46
- Cooper A. P., D'Souza R., Kauffmann G., Wang J., Boylan-Kolchin M., Guo Q., Frenk C. S., White S. D. M., Galactic accretion and the outer structure of galaxies in the CDM model, *MNRAS*, 2013, vol. 434, p. 3348
- Cooper M. C., Griffith R. L., Newman J. A., Coil A. L., Davis M., Dutton A. A., Faber S. M., Guhathakurta P., Koo D. C., Lotz J. M., Weiner B. J., Willmer C. N. A., Yan R., The DEEP3 Galaxy Redshift Survey: the impact of environment on the size evolution of massive early-type galaxies at intermediate redshift, *MNRAS*, 2012, vol. 419, p. 3018
- Crook A. C., Huchra J. P., Martimbeau N., Masters K. L., Jarrett T., Macri L. M., Groups of Galaxies in the Two Micron All Sky Redshift Survey, *ApJ*, 2007, vol. 655, p. 790
- Daddi E., Renzini A., Pirzkal N., Cimatti A., Malhotra S., Stiavelli M., Xu C., Pasquali A., Rhoads J. E., Brusa M., di Serego Alighieri S., Ferguson H. C., Koekemoer A. M., Moustakas L. A., Panagia N., Windhorst R. A., Passively Evolving Early-Type Galaxies at $1.4 < z < 2.5$ in the Hubble Ultra Deep Field, *ApJ*, 2005, vol. 626, p. 680
- Davies R. L., Burstein D., Dressler A., Faber S. M., Lynden-Bell D., Terlevich R. J., Wegner G., Spectroscopy and photometry of elliptical galaxies. II - The spectroscopic parameters, *ApJS*, 1987, vol. 64, p. 581
- de Blok W. J. G., McGaugh S. S., Bosma A., Rubin V. C., Mass Density Profiles of Low Surface Brightness Galaxies, *ApJ*, 2001, vol. 552, p. L23
- de la Rosa I. G., de Carvalho R. R., Vazdekis A., Barbuy B., Truncated Star Formation in Compact Groups of Galaxies: A Stellar Population Study, *AJ*, 2007, vol. 133, p. 330
- De Lucia G., Blaizot J., The hierarchical formation of the brightest cluster galaxies, *MNRAS*, 2007, vol. 375, p. 2
- Dressler A., The dynamics and structure of the cD galaxy in Abell 2029, *ApJ*, 1979, vol. 231, p. 659
- Dressler A., Galaxy morphology in rich clusters - Implications for the formation and evolution of galaxies, *ApJ*, 1980, vol. 236, p. 351

- Dressler A., The Morphology-Density Relation: From Present to Past. In American Astronomical Society Meeting Abstracts #204 , vol. 36 of Bulletin of the American Astronomical Society, 2004, p. 781
- Edwards L. O. V., Alpert H. S., Trierweiler I. L., Abraham T., Beizer V. G., Stellar populations of BCGs, close companions and intracluster light in Abell 85, Abell 2457 and IIZw108, MNRAS, 2016, vol. 461, p. 230
- Einstein A., Die Grundlage der allgemeinen Relativitätstheorie, Annalen der Physik, 1916, vol. 354, p. 769
- Elmegreen B. G., Scalo J., Interstellar Turbulence I: Observations and Processes, ARA&A, 2004, vol. 42, p. 211
- Emsellem E., Cappellari M., Krajnović D., Alatalo K., Blitz L., Bois M., Bournaud F., Bureau M., Davies R. L., Davis T. A., de Zeeuw P. T., Khochfar S., Kuntschner H., Lablanche P.-Y., McDermid R. M., et al., The ATLAS^{3D} project - III. A census of the stellar angular momentum within the effective radius of early-type galaxies: unveiling the distribution of fast and slow rotators, MNRAS, 2011, vol. 414, p. 888
- Emsellem E., Cappellari M., Krajnović D., van de Ven G., Bacon R., Bureau M., Davies R. L., de Zeeuw P. T., Falcón-Barroso J., Kuntschner H., McDermid R., Peletier R. F., Sarzi M., The SAURON project - IX. A kinematic classification for early-type galaxies, MNRAS, 2007, vol. 379, p. 401
- ESO, 2013a FIMS: FORS Instrument Mask Simulator last modified March 12, 2014, accessed September 6, 2016, <https://www.eso.org/sci/observing/phase2/SMGuidelines/FIMS.html>
- ESO, 2013b The ESO DSS Batch Tool last modified February 2, 2013, accessed May 24, 2016, <http://archive.eso.org/cms/tools-documentation/the-eso-st-ecf-digitized-sky-survey-application.html>
- Faber S. M., Burstein D., Dressler A., Spectrum of the halo of the cD galaxy in Abell 401, AJ, 1977, vol. 82, p. 941
- Faber S. M., Friel E. D., Burstein D., Gaskell C. M., Old stellar populations. II - an analysis of K-giant spectra, ApJS, 1985, vol. 57, p. 711
- Faber S. M., Willmer C. N. A., Wolf C., Koo D. C., Weiner B. J., Newman J. A., Im M., Coil A. L., Conroy C., Cooper M. C., Davis M., Finkbeiner D. P., Gerke B. F., Gebhardt K.,

- Groth E. J., Guhathakurta P., et al., Galaxy Luminosity Functions to $z \sim 1$ from DEEP2 and COMBO-17: Implications for Red Galaxy Formation, *ApJ*, 2007, vol. 665, p. 265
- Falc3n-Barroso J., S3nchez-Bl3nquez P., Vazdekis A., Ricciardelli E., Cardiel N., Cenarro A. J., Gorgas J., Peletier R. F., An updated MILES stellar library and stellar population models, *A&A*, 2011, vol. 532, p. A95
- Famaey B., McGaugh S. S., Modified Newtonian Dynamics (MOND): Observational Phenomenology and Relativistic Extensions, *Living Reviews in Relativity*, 2012, vol. 15
- Fisher D., Illingworth G., Franx M., Kinematics of 13 brightest cluster galaxies, *ApJ*, 1995, vol. 438, p. 539
- Freeman K., Slipher and the Nature of the Nebulae. In *Origins of the Expanding Universe: 1912-1932*, vol. 471 of *Astronomical Society of the Pacific Conference Series*, 2013, p. 63
- Freudling W., Romaniello M., Bramich D. M., Ballester P., Forchi V., Garc3a-Dabl3 C. E., Moehler S., Neeser M. J., Automated data reduction workflows for astronomy. The ESO Reflex environment, *A&A*, 2013, vol. 559, p. A96
- Friedmann A., 3ber die Kr3mmung des Raumes, *Zeitschrift fur Physik*, 1922, vol. 10, p. 377
- Gaffney V., Fitch S., Ramsey E., Yorston R., Ch'ng E., Baldwin E., Bates R., Gaffney C., Ruggles C., Sparrow T., McMillan A., Cowley D., Fraser S., Murray C., Murray H., Hopla E., Howard A., Time and a Place: A luni-solar 'time-reckoner' from 8th millennium BC Scotland, *IA*, 2013
- Gallazzi A., Charlot S., Brinchmann J., White S. D. M., Ages and metallicities of early-type galaxies in the Sloan Digital Sky Survey: new insight into the physical origin of the colour-magnitude and the $Mg_2 - \sigma_V$ relations, *MNRAS*, 2006, vol. 370, p. 1106
- Garcia A. M., General study of group membership. II - Determination of nearby groups, *A&AS*, 1993, vol. 100, p. 47
- Gelman A., Carlin J. B., Stern H. S., Rubin D. B., *Bayesian Data Analysis, Second Edition* (Chapman & Hall/CRC Texts in Statistical Science). Chapman and Hall/CRC, 2003
- Gerhard O. E., Line-of-sight velocity profiles in spherical galaxies: breaking the degeneracy between anisotropy and mass., *MNRAS*, 1993, vol. 265, p. 213
- Girichidis P., Federrath C., Banerjee R., Klessen R. S., Importance of the initial conditions for star formation - I. Cloud evolution and morphology, *MNRAS*, 2011, vol. 413, p. 2741

-
- Gonzalez A. H., Zabludoff A. I., Zaritsky D., Intracluster Light in Nearby Galaxy Clusters: Relationship to the Halos of Brightest Cluster Galaxies, *ApJ*, 2005, vol. 618, p. 195
- Gordon K. J., Messier 33, History of our Understanding of a Spiral Galaxy, *QJRAS*, 1969, vol. 10, p. 293
- Gorgas J., Efstathiou G., Aragon Salamanca A., Line strengths in early-type galaxies, *MNRAS*, 1990, vol. 245, p. 217
- Governato F., Brook C., Mayer L., Brooks A., Rhee G., Wadsley J., Jonsson P., Willman B., Stinson G., Quinn T., Madau P., Bulgeless dwarf galaxies and dark matter cores from supernova-driven outflows, *Nature*, 2010, vol. 463, p. 203
- Gunn J. E., Gott III J. R., On the Infall of Matter Into Clusters of Galaxies and Some Effects on Their Evolution, *ApJ*, 1972, vol. 176, p. 1
- Guth A. H., Inflationary universe: A possible solution to the horizon and flatness problems, *Phys. Rev. D*, 1981, vol. 23, p. 347
- Hastings W. K., Monte Carlo sampling methods using Markov chains and their applications, *Biometrika*, 1970, vol. 57, p. 97
- Hayakawa A., Furusho T., Yamasaki N. Y., Ishida M., Ohashi T., Inhomogeneity in the Hot Intracluster Medium of Abell 1060 Observed with Chandra, *PASJ*, 2004, vol. 56, p. 743
- Heisler J., Tremaine S., Bahcall J. N., Estimating the masses of galaxy groups - Alternatives to the virial theorem, *ApJ*, 1985, vol. 298, p. 8
- Henault F., Bacon R., Bonneville C., Boudon D., Davies R. L., Ferruit P., Gilmore G. F., Le Fèvre O., Lemonnier J.-P., Lilly S., Morris S. L., Prieto E., Steinmetz M., de Zeeuw P. T., MUSE: a second-generation integral-field spectrograph for the VLT. In *Instrument Design and Performance for Optical/Infrared Ground-based Telescopes*, vol. 4841 of *Proc. SPIE*, 2003, p. 1096
- Hickson P., Systematic properties of compact groups of galaxies, *ApJ*, 1982, vol. 255, p. 382
- Hickson P., Mendes de Oliveira C., Huchra J. P., Palumbo G. G., Dynamical properties of compact groups of galaxies, *ApJ*, 1992, vol. 399, p. 353
- Hilker M., Richtler T., Barbosa C. E., Coccato L., Arnaboldi M., Mendes de Oliveira C., The Hydra I cluster core - II. Kinematics and dynamical analysis, *A&A*, in prep.

- Hinshaw G., Larson D., Komatsu E., Spergel D. N., Bennett C. L., Dunkley J., Nolte M. R., Halpern M., Hill R. S., Odegard N., Page L., Smith K. M., Weiland J. L., Gold B., Jarosik N., Kogut A., Limon M., Meyer S. S., Tucker G. S., et al., Nine-year Wilkinson Microwave Anisotropy Probe (WMAP) Observations: Cosmological Parameter Results, *ApJS*, 2013, vol. 208, p. 19
- Hubble E., A Relation between Distance and Radial Velocity among Extra-Galactic Nebulae, *Proceedings of the National Academy of Science*, 1929, vol. 15, p. 168
- Jedrzejewski R. I., CCD surface photometry of elliptical galaxies. I - Observations, reduction and results, *MNRAS*, 1987, vol. 226, p. 747
- Kauffmann G., Heckman T. M., White S. D. M., Charlot S., Tremonti C., Peng E. W., Seibert M., Brinkmann J., Nichol R. C., SubbaRao M., York D., The dependence of star formation history and internal structure on stellar mass for 10^5 low-redshift galaxies, *MNRAS*, 2003, vol. 341, p. 54
- Kelson D. D., Zabludoff A. I., Williams K. A., Trager S. C., Mulchaey J. S., Bolte M., Determination of the Dark Matter Profile of A2199 from Integrated Starlight, *ApJ*, 2002, vol. 576, p. 720
- Kereš D., Katz N., Weinberg D. H., Davé R., How do galaxies get their gas?, *MNRAS*, 2005, vol. 363, p. 2
- Kewley L. J., Dopita M. A., Sutherland R. S., Heisler C. A., Trevena J., Theoretical Modeling of Starburst Galaxies, *ApJ*, 2001, vol. 556, p. 121
- Klypin A. A., Shandarin S. F., Three-dimensional numerical model of the formation of large-scale structure in the Universe, *MNRAS*, 1983, vol. 204, p. 891
- Kormendy J., Kennicutt Jr. R. C., Secular Evolution and the Formation of Pseudobulges in Disk Galaxies, *ARA&A*, 2004, vol. 42, p. 603
- Korn A. J., Maraston C., Thomas D., The sensitivity of Lick indices to abundance variations, *A&A*, 2005, vol. 438, p. 685
- Krajnović D., Bacon R., Cappellari M., Davies R. L., de Zeeuw P. T., Emsellem E., Falcón-Barroso J., Kuntschner H., McDermid R. M., Peletier R. F., Sarzi M., van den Bosch R. C. E., van de Ven G., The SAURON project - XII. Kinematic substructures in early-type galaxies: evidence for discs in fast rotators, *MNRAS*, 2008, vol. 390, p. 93

-
- Krajnović D., Cappellari M., de Zeeuw P. T., Copin Y., Kinemetry: a generalization of photometry to the higher moments of the line-of-sight velocity distribution, *MNRAS*, 2006, vol. 366, p. 787
- Kroupa P., On the variation of the initial mass function, *MNRAS*, 2001, vol. 322, p. 231
- Kuntschner H., The stellar populations of early-type galaxies in the Fornax cluster, *MNRAS*, 2000, vol. 315, p. 184
- Kuntschner H., Line-of-sight velocity distribution corrections for Lick/IDS indices of early-type galaxies, *A&A*, 2004, vol. 426, p. 737
- Lançon A., Hauschildt P. H., Ladjal D., Mouhcine M., Near-IR spectra of red supergiants and giants. I. Models with solar and with mixing-induced surface abundance ratios, *A&A*, 2007, vol. 468, p. 205
- Le Borgne J.-F., Bruzual G., Pelló R., Lançon A., Rocca-Volmerange B., Sanahuja B., Schaerer D., Soubiran C., Vílchez-Gómez R., STELIB: A library of stellar spectra at $R \sim 2000$, *A&A*, 2003, vol. 402, p. 433
- Lin Y.-T., Mohr J. J., K-band Properties of Galaxy Clusters and Groups: Brightest Cluster Galaxies and Intracluster Light, *ApJ*, 2004, vol. 617, p. 879
- Linde A. D., A new inflationary universe scenario: A possible solution of the horizon, flatness, homogeneity, isotropy and primordial monopole problems, *Physics Letters B*, 1982, vol. 108, p. 389
- Loubser S. I., Sansom A. E., Sánchez-Blázquez P., Soechting I. K., Bromage G. E., Radial kinematics of brightest cluster galaxies, *MNRAS*, 2008, vol. 391, p. 1009
- Mamon G. A., Łokas E. L., Dark matter in elliptical galaxies - II. Estimating the mass within the virial radius, *MNRAS*, 2005, vol. 363, p. 705
- Maraston C., Greggio L., Renzini A., Ortolani S., Saglia R. P., Puzia T. H., Kissler-Patig M., Integrated spectroscopy of bulge globular clusters and fields. II. Implications for population synthesis models and elliptical galaxies, *A&A*, 2003, vol. 400, p. 823
- Mauduit J.-C., Mamon G. A., Suppressed radio emission in supercluster galaxies: enhanced ram pressure in merging clusters?, *A&A*, 2007, vol. 475, p. 169

- McDermid R. M., Alatalo K., Blitz L., Bournaud F., Bureau M., Cappellari M., Crocker A. F., Davies R. L., Davis T. A., de Zeeuw P. T., Duc P.-A., Emsellem E. o., The ATLAS^{3D} Project - XXX. Star formation histories and stellar population scaling relations of early-type galaxies, *MNRAS*, 2015, vol. 448, p. 3484
- Mendel J. T., Proctor R. N., Forbes D. A., Brough S., The anatomy of the NGC5044 group - I. Group membership and dynamics, *MNRAS*, 2008, vol. 389, p. 749
- Mendel J. T., Proctor R. N., Rasmussen J., Brough S., Forbes D. A., The anatomy of the NGC5044 group - II. Stellar populations and star formation histories, *MNRAS*, 2009, vol. 396, p. 2103
- Metropolis N., Rosenbluth A. W., Rosenbluth M. N., Teller A. H., Teller E., Equation of State Calculations by Fast Computing Machines, *The Journal of Chemical Physics*, 1953, vol. 21, p. 1087
- Misgeld I., Mieske S., Hilker M., The early-type dwarf galaxy population of the Hydra I cluster, *A&A*, 2008, vol. 486, p. 697
- Misgeld I., Mieske S., Hilker M., Richtler T., Georgiev I. Y., Schubert Y., A large population of ultra-compact dwarf galaxies in the Hydra I cluster, *A&A*, 2011, vol. 531, p. A4
- Moore B., Katz N., Lake G., Dressler A., Oemler A., Galaxy harassment and the evolution of clusters of galaxies, *Nature*, 1996, vol. 379, p. 613
- Moustakas L. A., Casertano S., Conselice C. J., Dickinson M. E., Eisenhardt P., Ferguson H. C., Giavalisco M., Grogin N. A., Koekemoer A. M., Lucas R. A., Mobasher B., Papovich C., Renzini A., Somerville R. S., Stern D., Morphologies and Spectral Energy Distributions of Extremely Red Galaxies in the GOODS-South Field, *ApJ*, 2004, vol. 600, p. L131
- Murphy J. D., Gebhardt K., Cradit M., The Rising Stellar Velocity Dispersion of M87 from Integrated Starlight, *ApJ*, 2014, vol. 785, p. 143
- Naab T., Johansson P. H., Ostriker J. P., Minor Mergers and the Size Evolution of Elliptical Galaxies, *ApJ*, 2009, vol. 699, p. L178
- Navarro J. F., Frenk C. S., White S. D. M., The Structure of Cold Dark Matter Halos, *ApJ*, 1996, vol. 462, p. 563

-
- Oser L., Ostriker J. P., Naab T., Johansson P. H., Burkert A., The Two Phases of Galaxy Formation, *ApJ*, 2010, vol. 725, p. 2312
- Osterbrock D. E., *Astrophysics of gaseous nebulae and active galactic nuclei*, 1989
- Ostriker J. P., Hausman M. A., Cannibalism among the galaxies - Dynamically produced evolution of cluster luminosity functions, *ApJ*, 1977, vol. 217, p. L125
- Padoan P., Nordlund Å., The Stellar Initial Mass Function from Turbulent Fragmentation, *ApJ*, 2002, vol. 576, p. 870
- Paneth F. A., Thomas Wright of Durham and Immanuel Kant, *The Observatory*, 1941, vol. 64, p. 71
- Patil A., Huard D., Fonnesbeck C. J., PyMC: Bayesian Stochastic Modelling in Python, *Journal of Statistical Software*, 2010, vol. 35, p. 1
- Peebles P. J. E., Large-scale background temperature and mass fluctuations due to scale-invariant primeval perturbations, *ApJ*, 1982, vol. 263, p. L1
- Pineda J. C. B., Hayward C. C., Springel V., Mendes de Oliveira C., Rotation curve fitting and its fatal attraction to cores in realistically simulated galaxy observations, *ArXiv e-prints*, 2016
- Planck Collaboration Ade P. A. R., Aghanim N., Arnaud M., Ashdown M., Aumont J., Bacigalupi C., Banday A. J., Barreiro R. B., Bartlett J. G., et al. Planck 2015 results. XIII. Cosmological parameters, *ArXiv e-prints*, 2015
- Press W. H., Schechter P., Formation of Galaxies and Clusters of Galaxies by Self-Similar Gravitational Condensation, *ApJ*, 1974, vol. 187, p. 425
- Primack J. R., Cosmology: small-scale issues, *New Journal of Physics*, 2009, vol. 11, p. 105029
- Proctor R. N., Forbes D. A., Beasley M. A., A robust method for the analysis of integrated spectra from globular clusters using Lick indices, *MNRAS*, 2004, vol. 355, p. 1327
- Proctor R. N., Forbes D. A., Hau G. K. T., Beasley M. A., De Silva G. M., Contreras R., Terlevich A. I., Ages and metallicities of Hickson compact group galaxies, *MNRAS*, 2004, vol. 349, p. 1381
- Proctor R. N., Mendes de Oliveira C., Eigenthaler P., Spatially resolved stellar population parameters in the BCGs of two fossil groups, *MNRAS*, 2014, vol. 439, p. 2281

- Proctor R. N., Sansom A. E., A comparison of stellar populations in galaxy spheroids across a wide range of Hubble types, *MNRAS*, 2002, vol. 333, p. 517
- Prugniel P., Koleva M., Spectral models of stellar populations resolved in chemical abundances. In *The Spectral Energy Distribution of Galaxies - SED 2011* , vol. 284 of IAU Symposium, 2012, p. 16
- Puzia T. H., Saglia R. P., Kissler-Patig M., Maraston C., Greggio L., Renzini A., Ortolani S., Integrated spectroscopy of bulge globular clusters and fields. I. The data base and comparison of individual Lick indices in clusters and bulge, *A&A*, 2002, vol. 395, p. 45
- Ramella M., Geller M. J., Huchra J. P., Groups of galaxies in the Center for Astrophysics redshift survey, *ApJ*, 1989, vol. 344, p. 57
- Rees M. J., Ostriker J. P., Cooling, dynamics and fragmentation of massive gas clouds - Clues to the masses and radii of galaxies and clusters, *MNRAS*, 1977, vol. 179, p. 541
- Renzini A., Buzzoni A., Global properties of stellar populations and the spectral evolution of galaxies. In *Spectral Evolution of Galaxies* , vol. 122 of *Astrophysics and Space Science Library*, 1986, p. 195
- Richtler T., Salinas R., Misgeld I., Hilker M., Hau G. K. T., Romanowsky A. J., Schuberth Y., Spolaor M., The dark halo of the Hydra I galaxy cluster: core, cusp, cosmological? Dynamics of NGC 3311 and its globular cluster system, *A&A*, 2011, vol. 531, p. A119
- Salpeter E. E., The Luminosity Function and Stellar Evolution., *ApJ*, 1955, vol. 121, p. 161
- Sánchez-Blázquez P., Peletier R. F., Jiménez-Vicente J., Cardiel N., Cenarro A. J., Falcón-Barroso J., Gorgas J., Selam S., Vazdekis A., Medium-resolution Isaac Newton Telescope library of empirical spectra, *MNRAS*, 2006, vol. 371, p. 703
- Sand D. J., Treu T., Smith G. P., Ellis R. S., The Dark Matter Distribution in the Central Regions of Galaxy Clusters: Implications for Cold Dark Matter, *ApJ*, 2004, vol. 604, p. 88
- Scalo J., Perception of interstellar structure - Facing complexity. In *Physical Processes in Fragmentation and Star Formation* , vol. 162 of *Astrophysics and Space Science Library*, 1990, p. 151
- Schiavon R. P., Population Synthesis in the Blue. IV. Accurate Model Predictions for Lick Indices and UBV Colors in Single Stellar Populations, *ApJS*, 2007, vol. 171, p. 146

-
- Searle L., Sargent W. L. W., Bagnuolo W. G., The History of Star Formation and the Colors of Late-Type Galaxies, *ApJ*, 1973, vol. 179, p. 427
- Searle L., Zinn R., Compositions of halo clusters and the formation of the galactic halo, *ApJ*, 1978, vol. 225, p. 357
- Shapley H., Curtis H. D., The Scale of the Universe, *Bulletin of the National Research Council*, Vol. 2, Part 3, No. 11, p. 171-217, 1921, vol. 2, p. 171
- Skrutskie M. F., Cutri R. M., Stiening R., Weinberg M. D., Schneider S., et al., The Two Micron All Sky Survey (2MASS), *AJ*, 2006, vol. 131, p. 1163
- Slipher V. M., The radial velocity of the Andromeda Nebula, *Lowell Observatory Bulletin*, 1913, vol. 2, p. 56
- Slipher V. M., Nebulae, *Proceedings of the American Philosophical Society*, 1917, vol. 56, p. 403
- Smith R. W., Beyond the Galaxy: the development of extragalactic astronomy 1885 - 1965 Part 1, *Journal for the History of Astronomy*, 2008, vol. 39, p. 91
- Soto K. T., Lilly S. J., Bacon R., Richard J., Conseil S., ZAP - enhanced PCA sky subtraction for integral field spectroscopy, *MNRAS*, 2016, vol. 458, p. 3210
- Spano M., Marcelin M., Amram P., Carignan C., Epinat B., Hernandez O., GHASP: an $H\alpha$ kinematic survey of spiral and irregular galaxies - V. Dark matter distribution in 36 nearby spiral galaxies, *MNRAS*, 2008, vol. 383, p. 297
- Springel V., White S. D. M., Jenkins A., Frenk C. S., Yoshida N., Gao L., Navarro J., Thacker R., Croton D., Helly J., Peacock J. A., Cole S., Thomas P., Couchman H., Evrard A., Colberg J., Pearce F., Simulations of the formation, evolution and clustering of galaxies and quasars, *Nature*, 2005, vol. 435, p. 629
- Steinmetz M., Navarro J. F., The hierarchical origin of galaxy morphologies, *New A*, 2002, vol. 7, p. 155
- Struble M. F., Rood H. J., A Compilation of Redshifts and Velocity Dispersions for ACO Clusters, *ApJS*, 1999, vol. 125, p. 35
- Thomas D., Maraston C., Bender R., Stellar population models of Lick indices with variable element abundance ratios, *MNRAS*, 2003, vol. 339, p. 897

- Thomas D., Maraston C., Bender R., Mendes de Oliveira C., The Epochs of Early-Type Galaxy Formation as a Function of Environment, *ApJ*, 2005, vol. 621, p. 673
- Thomas D., Maraston C., Johansson J., Flux-calibrated stellar population models of Lick absorption-line indices with variable element abundance ratios, *MNRAS*, 2011, vol. 412, p. 2183
- Tinsley B. M., Galactic Evolution, *A&A*, 1972, vol. 20, p. 383
- Tody D., The IRAF Data Reduction and Analysis System. In *Instrumentation in astronomy VI*, vol. 627 of *Proc. SPIE*, 1986, p. 733
- Tody D., IRAF in the Nineties. In *Astronomical Data Analysis Software and Systems II*, vol. 52 of *Astronomical Society of the Pacific Conference Series*, 1993, p. 173
- Toomre A., Mergers and Some Consequences. In *Evolution of Galaxies and Stellar Populations*, 1977a, p. 401
- Toomre A., Theories of spiral structure, *ARA&A*, 1977b, vol. 15, p. 437
- Toomre A., Toomre J., Galactic Bridges and Tails, *ApJ*, 1972, vol. 178, p. 623
- Trager S. C., Faber S. M., Worthey G., González J. J., The Stellar Population Histories of Early-Type Galaxies. II. Controlling Parameters of the Stellar Populations, *AJ*, 2000, vol. 120, p. 165
- Trager S. C., Worthey G., Faber S. M., Burstein D., González J. J., Old Stellar Populations. VI. Absorption-Line Spectra of Galaxy Nuclei and Globular Clusters, *ApJS*, 1998, vol. 116, p. 1
- Tremonti C. A., Heckman T. M., Kauffmann G., Brinchmann J., Charlot S., White S. D. M., Seibert M., Peng E. W., Schlegel D. J., Uomoto A., Fukugita M., Brinkmann J., The Origin of the Mass-Metallicity Relation: Insights from 53,000 Star-forming Galaxies in the Sloan Digital Sky Survey, *ApJ*, 2004, vol. 613, p. 898
- Tripicco M. J., Bell R. A., Modeling the LICK/IDS Spectral Feature Indices Using Synthetic Spectra, *AJ*, 1995, vol. 110, p. 3035
- Tully R. B., Galaxy Groups, *AJ*, 2015, vol. 149, p. 54
- van der Marel R. P., Franx M., A new method for the identification of non-Gaussian line profiles in elliptical galaxies, *ApJ*, 1993, vol. 407, p. 525

-
- van Dokkum P. G., Cosmic-Ray Rejection by Laplacian Edge Detection, *PASP*, 2001, vol. 113, p. 1420
- van Dokkum P. G., Whitaker K. E., Brammer G., Franx M., Kriek M., Labbé I., Marchesini D., Quadri R., Bezanson R., Illingworth G. D., Muzzin A., Rudnick G., Tal T., Wake D., The Growth of Massive Galaxies Since $z = 2$, *ApJ*, 2010, vol. 709, p. 1018
- Vasterberg A. R., Lindblad P. O., Jorsater S., An optical study of the cD galaxy NGC3311 and the giant elliptical galaxy NGC3309 in the cluster Hydra I, *A&A*, 1991, vol. 247, p. 335
- Vazdekis A., Evolutionary Stellar Population Synthesis at 2 Å Spectral Resolution, *ApJ*, 1999, vol. 513, p. 224
- Vazdekis A., , 2011 LECTOR: Line-strengths in One-dimensional ASCII Spectra Astrophysics Source Code Library
- Vazdekis A., Casuso E., Peletier R. F., Beckman J. E., A New Chemo-evolutionary Population Synthesis Model for Early-Type Galaxies. I. Theoretical Basis, *ApJS*, 1996, vol. 106, p. 307
- Vazdekis A., Coelho P., Cassisi S., Ricciardelli E., Falcón-Barroso J., Sánchez-Blázquez P., Barbera F. L., Beasley M. A., Pietrinferni A., Evolutionary stellar population synthesis with MILES - II. Scaled-solar and α -enhanced models, *MNRAS*, 2015, vol. 449, p. 1177
- Vazdekis A., Sánchez-Blázquez P., Falcón-Barroso J., Cenarro A. J., Beasley M. A., Cardiel N., Gorgas J., Peletier R. F., Evolutionary stellar population synthesis with MILES - I. The base models and a new line index system, *MNRAS*, 2010, vol. 404, p. 1639
- Ventimiglia G., Arnaboldi M., Gerhard O., The unmixed kinematics and origins of diffuse stellar light in the core of the Hydra I cluster (Abell 1060), *A&A*, 2011, vol. 528, p. A24
- Ventimiglia G., Gerhard O., Arnaboldi M., Coccato L., The dynamically hot stellar halo around NGC 3311: a small cluster-dominated central galaxy, *A&A*, 2010, vol. 520, p. L9
- Walcher J., Groves B., Budavári T., Dale D., Fitting the integrated spectral energy distributions of galaxies, *Ap&SS*, 2011, vol. 331, p. 1
- Wehner E. M. H., Harris W. E., Whitmore B. C., Rothberg B., Woodley K. A., The Globular Cluster Systems around NGC 3311 and NGC 3309, *ApJ*, 2008, vol. 681, p. 1233

- Weijmans A.-M., Cappellari M., Bacon R., de Zeeuw P. T., Emsellem E., Falcón-Barroso J., Kuntschner H., McDermid R. M., van den Bosch R. C. E., van de Ven G., Stellar velocity profiles and line strengths out to four effective radii in the early-type galaxies NGC3379 and 821, *MNRAS*, 2009, vol. 398, p. 561
- White S. D. M., Rees M. J., Core condensation in heavy halos - A two-stage theory for galaxy formation and clustering, *MNRAS*, 1978, vol. 183, p. 341
- Worthey G., Comprehensive stellar population models and the disentanglement of age and metallicity effects, *ApJS*, 1994, vol. 95, p. 107
- Worthey G., Faber S. M., Gonzalez J. J., Burstein D., Old stellar populations. 5: Absorption feature indices for the complete LICK/IDS sample of stars, *ApJS*, 1994, vol. 94, p. 687
- Worthey G., Ottaviani D. L., $H\gamma$ and $H\delta$ Absorption Features in Stars and Stellar Populations, *ApJS*, 1997, vol. 111, p. 377
- Zabludoff A. I., Mulchaey J. S., The Properties of Poor Groups of Galaxies. I. Spectroscopic Survey and Results, *ApJ*, 1998, vol. 496, p. 39
- Zwicky F., *Morphological astronomy*. Berlin: Springer, 1957

Appendix A

GHASP: an H α survey of spiral galaxies - X. Surface photometry, decompositions and the Tully-Fisher relation in the R_c band ¹

¹ Article originally published on the Monthly Notes of the Royal Astronomical Society, volume 453, 2015. Reproduction by permission of Oxford University Press.

GHASP: an H α kinematic survey of spiral galaxies – X. Surface photometry, decompositions and the Tully–Fisher relation in the R_c band^{*}

C. E. Barbosa,¹† C. Mendes de Oliveira,¹ P. Amram,² F. Ferrari,³ D. Russeil,²
B. Epinat,² V. Perret,² C. Adami² and M. Marcelin²

¹Universidade de São Paulo, IAG, Departamento de Astronomia, Rua do Matão 1226, Cidade Universitária, 05508-090, São Paulo, SP, Brazil

²Aix Marseille Université, CNRS, LAM (Laboratoire d'Astrophysique de Marseille), 13388, Marseille, France

³Instituto de Matemática, Estatística e Física, FURG, 96201-900, Rio Grande, RS, Brazil

Accepted 2015 July 22. Received 2015 July 6; in original form 2015 February 22

ABSTRACT

We present R_c -band surface photometry for 170 of the 203 galaxies in GHASP, the Gassendi H-alpha survey of spirals, a sample of late-type galaxies for which high-resolution Fabry–Perot H α maps have previously been obtained. Our data set is constructed using new R_c -band observations taken at the Observatoire de Haute-Provence, supplemented with Sloan Digital Sky Survey archival data, obtained with the purpose of deriving homogeneous photometric profiles and parameters. Our results include R_c -band surface brightness profiles for 170 galaxies and $ugriz$ profiles for 108 of these objects. We catalogue several parameters of general interest for further reference, such as total magnitude, effective radius and isophotal parameters (magnitude, position angle, ellipticity and inclination). We also perform a structural decomposition of the surface brightness profiles using a multi-component method to separate discs from bulges and bars, and to observe the main scaling relations involving luminosities, sizes and maximum velocities. We determine the R_c -band Tully–Fisher relation using maximum velocities derived solely from H α rotation curves for a sample of 80 galaxies, resulting in a slope of -8.1 ± 0.5 , zero-point of -3.0 ± 1.0 and an estimated intrinsic scatter of 0.28 ± 0.07 . We note that, unlike the Tully–Fisher relation in the near-infrared derived for the same sample, no change in the slope of the relation is seen at the low-mass end (for galaxies with $V_{\max} < 125 \text{ km s}^{-1}$). We suggest that this different behaviour of the Tully–Fisher relation (with the optical relation being described by a single power law while the near-infrared has two), may be caused by differences in the stellar mass-to-light ratio for galaxies with $V_{\max} < 125 \text{ km s}^{-1}$.

Key words: galaxies: photometry – galaxies: structure.

1 INTRODUCTION

Historically, spiral galaxies performed a critical role in the studies of dark matter. Observations of the outer flat rotation curves of spiral galaxies (e.g. Rubin, Thonnard & Ford 1978) focused on the then overlooked missing mass problem (see, e.g. Zwicky 1937), which stresses that most of what we see (light) is just a fraction of what we would like to observe (mass). A critical further step, yet to be accomplished, is to understand the connection between ordinary and dark matter in the inner regions of galaxies and whether (and possibly how) light traces mass.

The kinematic decomposition of velocity fields of spiral galaxies is the general method used to map their distribution of dark matter

(e.g. van Albada et al. 1985; van Albada & Sancisi 1986; Kent 1986; Kassin, de Jong & Weiner 2006b). However, the stellar mass distribution is poorly constrained, and the under-determined stellar mass-to-light ratio translates into degeneracies, such as the disc-halo and the cusp-core problems, which prevent unique decompositions. In this context, high-resolution accurate rotation curves, such as those observed by the Gassendi H-alpha survey of spirals (GHASP), are necessary to alleviate the problem (Dutton et al. 2005).

Previous works have supported the scenario of cored dark matter profiles (e.g. Spano et al. 2008), but studies of the systematic errors with larger homogeneous samples are still needed to confirm these results. This series of papers on the GHASP survey has the goal of imposing tighter constraints on the study of dark matter distributions in spiral galaxies. In this paper, we build a new surface photometry data set for 128 GHASP galaxies in the R_c band, observed over several years at the Observatoire de Haute-Provence (OHP), which provides the basis for the determination of stellar masses in forthcoming work. Additionally, we complement this data with public

^{*}Based on observations performed at Observatoire de Haute Provence, France.

†E-mail: carlos.barbosa@usp.br

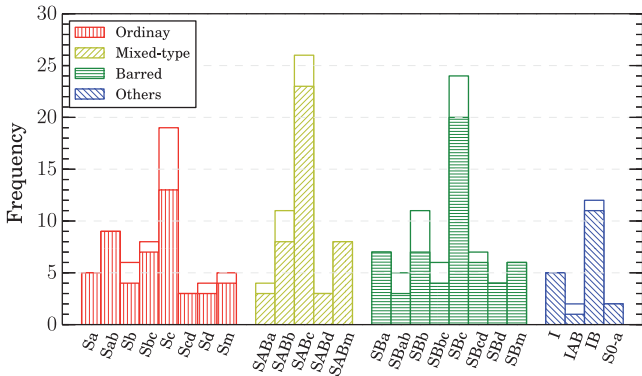


Figure 1. Frequency of galactic morphological types of the GHASP sample according to the Hyperleda classification, separated into ordinary spirals (59 galaxies), mixed types (52), barred (70), irregulars (19) and lenticulars (2).

Sloan Digital Sky Survey (SDSS) data to obtain *ugriz* photometry for 108 GHASP galaxies as well as to increase the R_c -band data to 170 galaxies (≈ 84 per cent of the survey).

Besides the surface brightness (SB) profiles, we also compile a homogeneous photometric catalogue including several photometric quantities of general interest, such as magnitudes, sizes and isophotal properties. In addition, we perform a multi-component light decomposition to separate the light from the discs (our main interest in dynamical decomposition) from other components such as bulges and bars. Finally, we perform a first set of applications to our data set by determining important scaling relations with luminosity, size and velocity of the galaxies, and by deriving the Tully–Fisher (TF) relation in the R_c band.

This paper is organized as follows. The GHASP sample is briefly outlined in Section 2. Following this, the details of the observations, data reduction and calibration are shown in Section 3. In Section 4, we present the methods used to determine the SB, position angle (PA), ellipticity and integrated magnitude profiles, and we detail the multi-component decomposition. In Section 5, we test our results against other similar works, and we check the internal consistency of our results. Finally, in Section 6, we derive several scaling relations involving luminosity, size and rotational velocity using the decomposition results, with special emphasis on the R_c -band TF relation.

2 THE GHASP SAMPLE

The GHASP sample consists of 203 spiral and irregular galaxies in the local Universe for which high-resolution $H\alpha$ maps have been observed with Fabry–Perot interferometry (Garrido et al. 2002, 2003, 2005; Garrido, Marcelin & Amram 2004; Spano et al. 2008; Epinat et al. 2008; Epinat, Amram & Marcelin 2008; Epinat et al. 2010; Torres-Flores et al. 2011). The GHASP sample was initially designed to be a subsample of the Westerbork survey (WHISP, van der Hulst, van Albada & Sancisi 2001) with the goal of providing a local Universe reference for the kinematics and dynamics of disc-like galaxies.

The GHASP sample was designed to cover a large range of morphological types, including ordinary, mixed-type and barred galaxies, thus excluding only early-type galaxies because of their low $H\alpha$ content, as illustrated in Fig. 1. The photometric sample presented here is built with data from two sources. Photometric

R_c -band data were obtained by the GHASP collaboration at the OHP over the last decade for 128 galaxies. To enlarge the sample, we also take advantage of the public data set from the seventh Data Release (DR7) of SDSS (Stoughton et al. 2002), which provides imaging and calibration in five pass bands (*ugriz*) for 108 of our galaxies. By combining both data sets, we are able to obtain photometry for a total of 170 GHASP galaxies, which are listed in Table 1 along with details of the observation. However, we note that, on average, the data observed at OHP in the R_c band go about half a magnitude deeper than the SDSS data.

3 DATA REDUCTION

3.1 Data from the OHP observatory

Broad-band imaging for 128 galaxies in the R_c band was obtained with the 1.2-m telescope at the OHP, France, in several observation runs as presented in Table 2. The images have a field of view of 11.7×11.7 arcmin, taken with a single CCD with 1024×1024 pixels, resulting in a pixel size of $0.685 \text{ arcsec}^{-1}$.

Basic data reduction was performed with IRAF tasks,¹ including flat-field, bias subtraction and cosmic ray cleaning. Images of one galaxy are then aligned and combined for the cases with roughly the same smallest seeing full width at half-maximum (FWHM), estimated from isolated field stars. A photometric stability check and zero-point calibration were obtained by observing several standard stars from the catalogue of Landolt (1992) at different times during the nights, considering the mean airmass correction coefficient of 0.145 for the R_c band (Chevalier & Ilovaisky 1991), and no colour term.

The determination of the sky level is the greatest source of uncertainty for SB profiles and magnitudes (Courteau 1996). For this purpose, we adopt the method of estimating the background by selecting sky boxes on the images, which are visually selected areas where the galaxy and stellar light contribution is minimal, and use those regions to calculate a smooth surface using the IRAF package IMSURFIT with polynomials of order 2, which is subtracted from the original images. This process resulted in an homogeneous background for which the typical residual standard deviation is in the range 0.5–1 per cent of the sky level.

We modelled the point spread function (PSF) of our images using the IRAF PSFMESURE task. We selected bright, unsaturated stars across the fields using the task DAOFIND, and then modelled their light profiles using a circular Moffat function (Moffat 1969), given by

$$\text{PSF}(r) = \frac{\beta - 1}{\pi \alpha^2} \left[1 + \left(\frac{r}{\alpha} \right)^2 \right]^{-\beta}, \quad (1)$$

where the radial scale length α and the slope β are free parameters, which can be related to the seeing by the relation $\text{FWHM} = 2\alpha\sqrt{2^{1/\beta} - 1}$ (see also Trujillo et al. 2001). This method has proved to be suitable in our case due to the presence of extended wings in the PSFs. Overall, the typical seeing of our observations is $\text{FWHM} \approx 3 \text{ arcsec}$, with the parameters α , β and FWHM having mean statistical uncertainties of 1.7, 9 and 3 per cent respectively.

¹ IRAF is distributed by the National Optical Astronomy Observatory, which is operated by the Association of Universities for Research in Astronomy (AURA) under a cooperative agreement with the National Science Foundation.

Table 1. Photometric sample of the GHASP survey. The printed version contains only an abridged version of the table, with the remaining material available online as supplementary material. (1) Galaxy name. (2, 3) Right ascension and declination of the galaxy according to the NASA/IPAC Extragalactic Database. (4, 5) Morphological classification according to the Hubble type and to the de Vaucouleurs numerical type from the Hyperleda data base. (6) Distance to the galaxy according to Epinat et al. (2008). (7) If the galaxy is in SDSS. (8–10) OHP R_c -band observation log, including the runs, total exposure time and seeing.

Galaxy	α (J2000)	δ (J2000)	Morphology	Morphology t	Distance (Mpc)	SDSS	OHP observation log.		
							Runs	Exposure time (s)	FWHM (arcsec)
(1)	(2)	(3)	(4)	(5)	(6)	(7)	(8)	(9)	(10)
UGC 89	00 ^h 09 ^m 53 ^s .4	+25°55′26″	SBa	1.2 ± 0.6	64.2	No	2, 5	600	2.7
UGC 94	00 ^h 10 ^m 25 ^s .9	+25°49′55″	S(r)ab	2.4 ± 0.6	64.2	No	5, 6	3300	2.3
IC 476	07 ^h 47 ^m 16 ^s .3	+26°57′03″	SABb	4.2 ± 2.6	63.9	Yes	–	–	–
UGC 508	00 ^h 49 ^m 47 ^s .8	+32°16′40″	SBab	1.5 ± 0.9	63.8	No	5	3600	2.3
UGC 528	00 ^h 52 ^m 04 ^s .3	+47°33′02″	SABb	2.9 ± 1.1	12.1	No	2	1500	1.9
NGC 542	01 ^h 26 ^m 30 ^s .9	+34°40′31″	Sb pec	2.8 ± 3.9	63.7	Yes	–	–	–
UGC 763	01 ^h 12 ^m 55 ^s .7	+00°58′54″	SABm	8.6 ± 1.0	12.7	Yes	2, 5	600	3.1
UGC 1013	01 ^h 26 ^m 21 ^s .8	+34°42′11″	SB(r)b pec	3.1 ± 0.2	70.8	Yes	2, 5	5100	2.5
UGC 1117	01 ^h 33 ^m 50 ^s .9	+30°39′37″	Sc	6.0 ± 0.4	0.9	No	5	4500	2.7
UGC 1249	01 ^h 47 ^m 29 ^s .9	+27°20′00″	SBm pec	8.8 ± 0.6	7.2	No	2	1800	2.1
...
UGC 11951	22 ^h 12 ^m 30 ^s .1	+45°19′42″	SBa	1.1 ± 0.8	17.4	No	2	2100	2.6
UGC 12060	22 ^h 30 ^m 34 ^s .0	+33°49′11″	IB	9.9 ± 0.5	15.7	No	6	6000	2.5
UGC 12082	22 ^h 34 ^m 10 ^s .8	+32°51′38″	SABm	8.7 ± 0.8	10.1	No	6	3000	3.7
UGC 12101	22 ^h 36 ^m 03 ^s .4	+33°56′53″	Scd	6.6 ± 0.9	15.1	Yes	2	1800	1.9
UGC 12212	22 ^h 50 ^m 30 ^s .3	+29°08′18″	Sm	8.7 ± 0.5	15.5	Yes	2	1800	2.2
UGC 12276	22 ^h 58 ^m 32 ^s .5	+35°48′09″	SB(r)a	1.1 ± 0.5	77.8	No	2	2700	2.0
UGC 12276c	22 ^h 58 ^m 32 ^s .5	+35°48′09″	S?	5.1 ± 5.0	77.8	No	2	2700	2.0
UGC 12343	23 ^h 04 ^m 56 ^s .7	+12°19′22″	SBbc	4.4 ± 0.9	26.9	No	2, 5	1500	2.7
UGC 12632	23 ^h 29 ^m 58 ^s .7	+40°59′25″	SABm	8.7 ± 0.5	8.0	No	5	4500	2.4
UGC 12754	23 ^h 43 ^m 54 ^s .4	+26°04′32″	SBC	6.0 ± 0.4	8.9	No	2	1200	2.3

Table 2. List of observational runs in which the R_c photometry of the GHASP galaxies was obtained at OHP.

Run	Dates	Number of galaxies observed
1	2002 March 7–13	29
2	2002 October 28 – November 10	38
3	2003 March 8–9	17
4	2003 March 29 – April 6	22
5	2003 September 22–28	25
6	2003 October 21–25	6
7	2008 June 2–4	11
8	2009 October 23	1
9	2010 March 19–21	16

3.2 Data from SDSS

To increase the number of galaxies in our photometric sample in the R_c band, we use SDSS DR7 (Abazajian et al. 2009) archival data for 108 GHASP galaxies we found in the data base and transformed SDSS *ugriz* data into R_c with a multi-band scaling relation (there are more details in Section 4.1). Among these 108 galaxies, 66 have also been observed in the OHP, thus 42 new ones are added to the final photometric sample. Calibrations and the PSF of the images are obtained directly from the data products of the survey. We performed a new sky determination for each image for consistency with the adopted method for R_c images, and also because a few authors have pointed out errors in the sky determinations for images with bright galaxies in early SDSS releases (e.g. Bernardi et al. 2007; Lauer et al. 2007; Lisker et al. 2007).

4 DATA ANALYSIS

4.1 Surface photometry

We study the photometric properties of the sample using the traditional method of elliptical isophote fitting (Kent 1984; Jedrzejewski 1987). SB profiles of the galaxies were obtained using the IRAF task ELLIPSE, which provides a number of parameters that describe the light of the galaxy as a function of the semi-major axis (which we simply refer to as the radius, r), including the ellipticity (ϵ), PA and the growth curve, which quantifies the total apparent magnitude inside each isophote.

Masks for foreground and background objects were produced interactively in two steps. First, most objects in the images were detected and masked out with SExtractor (Bertin & Arnouts 1996). Other important sources not detected by the program, such as saturated stars and stars/galaxies superposed on the galaxies of interest, were then masked during ELLIPSE runs. Finally, we checked the results by inspecting the residual image produced by subtracting an interpolated model of the galaxy produced with the task BMODEL. This process was carried out several times for each galaxy until no bright sources were observed in the resulting subtracted images except for spiral arms and/or bars of the galaxy that were not masked on purpose.

The centre of each galaxy was defined in a first iteration of ELLIPSE and was fixed for all later iterations. The PA and ellipticity of the isophotes were usually allowed to vary as a function of the radial distance, as usually done for late-type galaxy photometry (e.g. Balcells et al. 2003; MacArthur, Courteau & Holtzman 2003; McDonald, Courteau & Tully 2009), but in a few cases we were

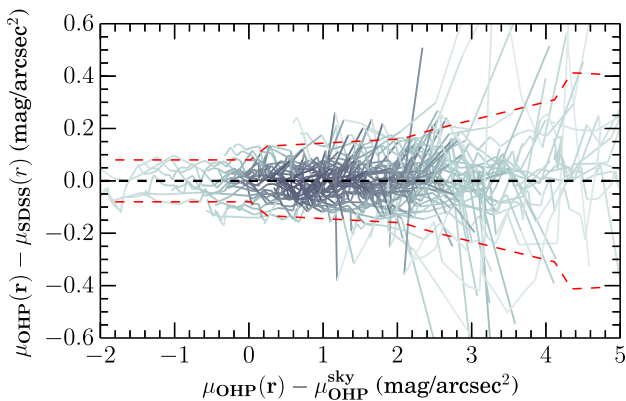


Figure 2. Difference between R_c SB profiles for OHP and SDSS data for 54 galaxies in common to both samples as a function of the OHP SB profile relative to the sky level. Profiles for the SDSS galaxies are obtained using equation (2). Each blue line represents the difference in the SB profiles of a single galaxy profile comparison. The dashed lines indicates the running rms difference between the profiles.

forced to fix the geometric parameters for part of or the whole galaxy to obtain convergence for the photometry. For the SDSS data, we adopt this method for the r -band images, due to the relatively high signal-to-noise ratio in the $ugriz$ system, but we fix the PAs and ellipticities according to the r -band parameters in the other pass bands to obtain consistent colours.

Uncertainties for the SB profiles include the isophote determination error given by `ELLIPSE`, the photon counting statistics of the detector, and the sky level subtraction uncertainty, which are all added in quadrature. All profiles are corrected for the Galactic foreground extinction using the dust reddening maps of Schlegel, Finkbeiner & Davis (1998), assuming a dust model with constant selective extinction of 3.1, and relative extinction for the different pass bands according to table 6 of Schlegel et al. (1998). However, we do not attempt to correct the SB profiles for the more uncertain problem of the galaxies' internal extinction.

Finally, to obtain R_c -band SB profiles from SDSS data, we use a slightly modified version of the relation derived by Jester et al. (2005), given by

$$\mu_R(r) = 0.42\mu_g(r) - 0.38\mu_r(r) + 0.96\mu_i(r) - 0.16, \quad (2)$$

where $\mu(r)$ represents the SB profile at radius r in the pass band indicated by the subscripts. The equation above was originally derived for stellar photometry, so we have tested its accuracy in surface photometry by comparing OHP SB profiles, obtained directly in the R_c band, with profiles derived from the SDSS $ugriz$ bands using a sample of 54 galaxies for which the geometric parameters of both data sets are similar. The results are presented in Fig. 2, which shows the difference between the profiles as a function of the OHP SB profiles relative to the sky level, which varies in the OHP observations, from one galaxy observation to another. The red line shows the running rms difference between the profiles, indicating that the error in transforming between the photometric systems is ~ 0.08 mag arcsec $^{-2}$ in the regions brighter than the sky level, ~ 0.15 mag arcsec $^{-2}$ for the regions down to 2 mag fainter than the sky, and ~ 0.4 mag arcsec $^{-2}$ for the regions 5 mag fainter than the sky level.

We present a sample of SB profiles for a variety of morphological types in Fig. 3, including also the ellipticity and PA variations. All

SB profiles are available in electronic format. In the next section, we detail other catalogued R_c -band photometric properties derived from SB profiles in this section.

4.2 Integrated and isophotal photometry in the R_c band

For the R_c -band SB profiles derived in this work, we obtained a number of properties of the galaxies that are of general interest by fixing a reference isophotal level. For the R_c band, the isophotal level of 23.5 mag arcsec $^{-2}$ is usually used as the reference, because it corresponds to an aperture similar to the B -band isophote of 25 mag arcsec $^{-2}$. However, this level was reached for only 72 per cent of our SB profiles. Therefore, to provide a more complete catalogue for our sample, we also use the isophotal level of 22.5 mag arcsec $^{-2}$ to provide parameters for 98 per cent of the sample.

We measured the isophotal radius (r_{iso}), position angle (PA_{iso}), ellipticity (ϵ_{iso}) and apparent magnitude ($m_{R, \text{iso}}$) directly from the SB profiles, with uncertainties estimated by Monte Carlo simulations of perturbations of the profile according to their uncertainties. Also, the inclination of the galaxies is estimated at a given isophotal level as (Tully & Fisher 1988)

$$\cos i_{\text{iso}} = \frac{(1 - \epsilon_{\text{iso}})^2 - q_0^2}{1^2 - q_0^2}, \quad (3)$$

where $q_0 = 0.2$ is the intrinsic flattening of edge-on discs (e.g. Haynes & Giovanelli 1984; Courteau 1996).

We also measured the total (asymptotic) apparent magnitudes of the galaxies ($m_{R, \text{total}}$), which were calculated by extrapolating the growth curve of the SB profiles using a derivative method similar to that in Cairós et al. (2001). However, this method failed for galaxies for which the growth curve did not converge. In these cases, we used the last isophote total magnitude to estimate the lower limit of the total magnitude. Also using the growth curve, we measured the effective radius of the galaxies (r_{50}), which is defined as the radius containing 50 per cent of the total light of the galaxy. Where we have not obtained a safe total magnitude, we estimated the lower limits of the effective radius. Uncertainties in these parameters are also based on Monte Carlo simulations.

Table 3 presents a sample of the results for the isophotal level of 22.5 mag arcsec $^{-2}$. The complete catalogue and the catalogue for the isophotal level of 23.5 mag arcsec $^{-2}$ are provided in the supplementary material.

4.3 Multi-component decomposition

In our forthcoming work (Pineda et al. in preparation), we plan to study the kinematic properties of a subsample of GHASP galaxies with specific photometric properties that depend on the relative importance of the discs in comparison with bulges and bars. To separate the SB profiles into different structural components, we used a multi-component decomposition of the SB profiles.

For this purpose, we use a parametric profile fitting method that includes as many components as necessary to separate the photometric components: discs, bulges, bars, spiral arms, lenses and nuclear sources. Ideally, one could use a complete 2D fitting to describe better the non-axisymmetric components, like a bar, but the reliability of the 1D method to recover the structural parameters is comparable to 2D, at least for the disc component (MacArthur et al. 2003), and also allows the integrated properties to be estimated with good accuracy.

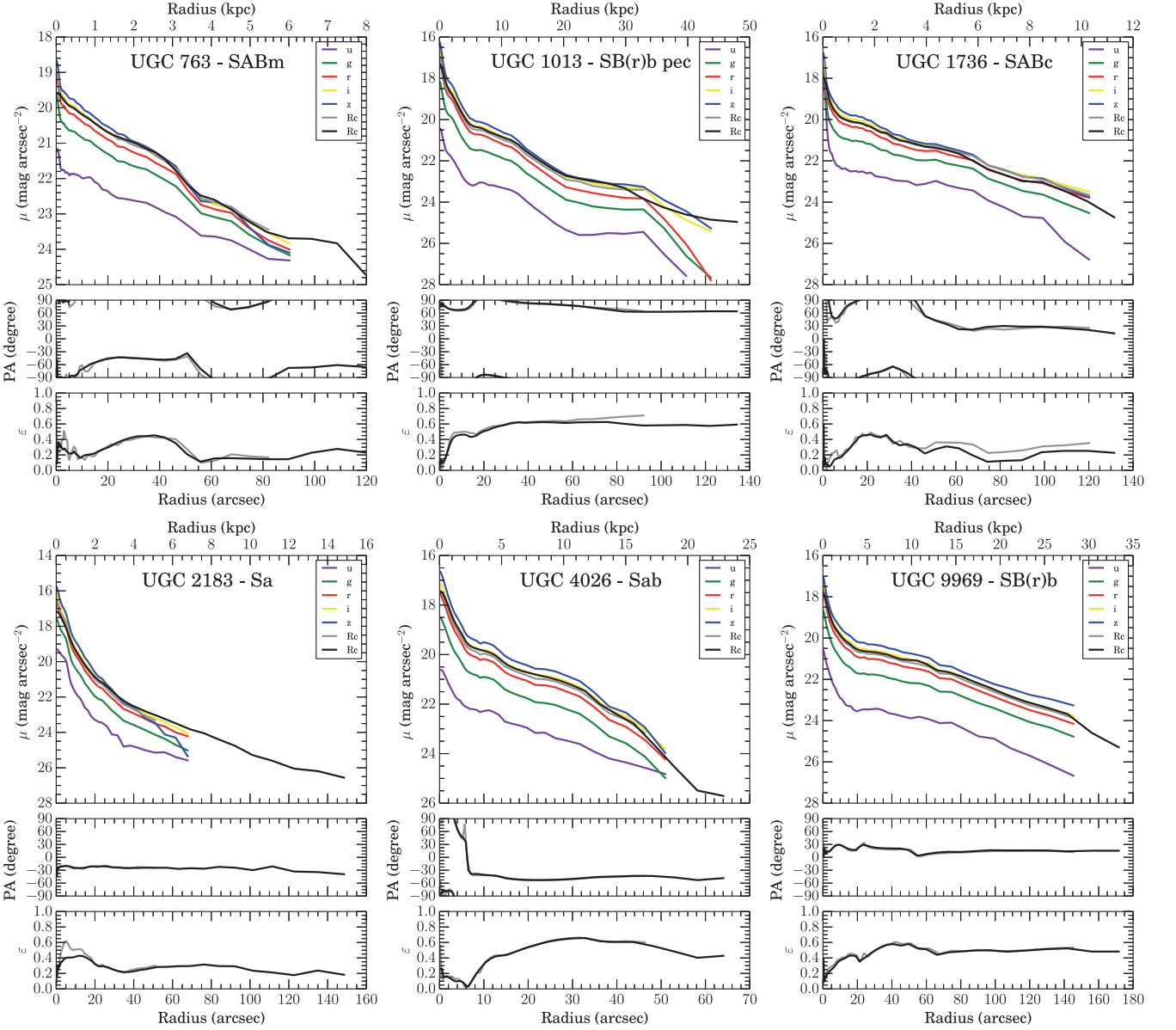


Figure 3. Examples of SB profiles in the R_c band, PA and ellipticity profiles for six galaxies for which data are available in both the OHP and SDSS data sets. The SB profiles are presented in different colours for each band according to the labels shown on the upper right. Uncertainties are not presented for clarity. The middle and lower panels of each galaxy show the PA and ellipticity profiles, respectively, with grey representing the r -band results and black representing the R_c -band geometry. All profiles are corrected for the Galactic foreground extinction according to the dust maps of Schlegel et al. (1998).

We performed the decomposition of all R_c -band profiles for the GHASP OHP sample. We developed a Python routine that performs a weighted chi-square minimization between the data and a model using the Levenberg–Marquardt algorithm (see, e.g. Press et al. 1992), using a PSF convolution of the models with a Moffat function (see Section 3.1). The input model is set manually according to the observation of photometric features in the SB profile and the images of the galaxies. Also, the observation of the varying ellipticity and PA as a function of the radius usually hinted at the different structural subcomponents of a galaxy. This process is illustrated in Fig. 4, where we present the structural decomposition of two barred galaxies, UGC 89 and UGC 10897. The structural parameters for all galaxies are listed in Table 4. In the next section, we give some details of the parametrizations used for the different components.

4.3.1 Discs

Since the early works of Patterson (1940) and de Vaucouleurs (1958), the intensity profiles of discs have been mostly described by a simple exponential law,

$$I_d(r) = I_0 \exp\left(-\frac{r}{h}\right), \quad (4)$$

where I_0 is the central ($r = 0$) intensity of the disc and h is the disc scale length. Usually, we refer to the central intensity in terms of SB using the relation $\mu_0 = -2.5 \log I_0$. For exponential discs, the total apparent magnitude is given by

$$m_{\text{disc}} = -2.5 \log \left(2\pi I_0 h^2 \frac{b}{a} \right), \quad (5)$$

where $b/a = 1 - \epsilon$ is the minor-to-major axis ratio of the galaxy.

Table 3. Isophotal and integrated photometric parameters in the R_c band. The printed version contains only an abridged version of the table, and the remaining material is available online. (1) Galaxy name. (2) Data source. (3–7) PA, ellipticity, inclination, radius and apparent integrated magnitude at the isophote of 22.5 mag arcsec $^{-2}$. (8) Effective radius. (9) Total apparent magnitude.

Galaxy	Data	PA _{22.5} (arcsec)	$\epsilon_{22.5}$ (degree)	$i_{22.5}$ (degree)	$r_{22.5}$ (arcsec)	$m_{R, 22.5}$ (mag)	r_{50} (arcsec)	$m_{R, total}$ (mag)
(1)	(2)	(3)	(4)	(5)	(6)	(7)	(8)	(9)
UGC 89	OHP	-27 ± 11	0.22 ± 0.03	40 ± 3	41 ± 2	11.60 ± 0.03	19 ± 5	11.4 ± 0.1
UGC 94	OHP	-84 ± 2	0.30 ± 0.02	46 ± 1	28 ± 1	13.12 ± 0.03	16 ± 7	12.7 ± 0.4
IC 476	SDSS	-79 ± 3	0.4 ± 0.1	52 ± 9	16 ± 2	14.7 ± 0.1	>10.0	<14.53
UGC 508	OHP	-61 ± 4	0.11 ± 0.05	28 ± 7	67 ± 1	11.17 ± 0.03	40 ± 1	10.91 ± 0.08
UGC 528	OHP	52 ± 2	0.03 ± 0.02	13 ± 3	65 ± 3	10.16 ± 0.01	21 ± 1	10.10 ± 0.04
NGC 542	SDSS	-34 ± 2	0.73 ± 0.01	79.1 ± 0.9	23 ± 2	14.39 ± 0.05	12 ± 6	14.2 ± 0.6
UGC 763	OHP	-75 ± 23	0.12 ± 0.02	29 ± 3	57 ± 4	11.61 ± 0.06	47 ± 5	11.1 ± 0.2
UGC 763	SDSS	-79 ± 35	0.12 ± 0.08	29 ± 10	56 ± 6	11.7 ± 0.1	>39.0	<11.46
UGC 1013	OHP	80 ± 2	0.62 ± 0.01	70.6 ± 0.8	53 ± 1	12.03 ± 0.01	27 ± 4	11.7 ± 0.1
UGC 1013	SDSS	80 ± 3	0.64 ± 0.01	72.2 ± 0.8	51 ± 5	12.17 ± 0.04	23 ± 3	11.9 ± 0.1
...
UGC 12082	OHP	18 ± 2	0.42 ± 0.01	56.1 ± 0.9	19 ± 3	15.0 ± 0.2	49 ± 23	12.8 ± 0.5
UGC 12101	OHP	-50 ± 2	0.53 ± 0.01	64.2 ± 0.8	51 ± 2	12.50 ± 0.03	29 ± 2	12.32 ± 0.09
UGC 12101	SDSS	-50 ± 3	0.52 ± 0.02	64 ± 1	49 ± 4	12.66 ± 0.06	28 ± 21	12.3 ± 0.9
UGC 12212	OHP	-80 ± 5	0.36 ± 0.02	52 ± 1	14 ± 1	15.8 ± 0.2	27 ± 26	14 ± 2
UGC 12212	SDSS	-71 ± 2	0.30 ± 0.01	46.8 ± 0.8	12 ± 5	15.9 ± 0.6	>16.0	<14.77
UGC 12276	OHP	-47 ± 6	0.23 ± 0.01	40.8 ± 0.9	30 ± 1	13.00 ± 0.03	19 ± 5	12.6 ± 0.2
UGC 12276c	OHP	82 ± 2	0.45 ± 0.01	58.3 ± 0.7	7 ± 1	17.0 ± 0.2	>5.0	<16.62
UGC 12343	OHP	38 ± 2	0.30 ± 0.03	47 ± 2	102 ± 1	10.33 ± 0.03	71 ± 9	10.2 ± 0.2
UGC 12632	OHP	22 ± 2	0.53 ± 0.05	64 ± 4	24 ± 5	14.8 ± 0.3	66 ± 59	13 ± 1
UGC 12754	OHP	-13 ± 3	0.29 ± 0.01	46 ± 1	89 ± 3	11.16 ± 0.03	47 ± 2	10.9 ± 0.1

However, deviations from a simple exponential disc were noticed by Freeman (1970), especially in the form of truncations or breaks in the inner profiles of galaxies. In a later study, van der Kruit & Searle (1982) also noticed breaks at large radii of discs, and more recently deviations at very low SB have been observed, including upward bends (e.g. Erwin, Beckman & Pohlen 2005).

Based on these observations, Erwin et al. (2008) proposed a reviewed classification of discs with three categories: Type I, simple discs described well by exponential discs; Type II, discs with downward truncations; and Type III, discs with upward bends. A local census of disc properties performed by Pohlen & Trujillo (2006) of late-type galaxies (Sb-Sm) estimated the fraction of Type I galaxies to be only 10 per cent, while 60 per cent are classified as Type II and 30 per cent are Type III according to this new classification scheme. Therefore, an updated profile for the discs is here adopted whenever breaks are clearly observed, by using broken exponential profiles, given by (Erwin et al. 2008)

$$I_d(r) = SI_0 \exp\left(-\frac{r}{h_i}\right) \times \{1 + \exp[\alpha(r - r_b)]\}^{\frac{1}{\alpha}\left(\frac{1}{h_i} - \frac{1}{h_o}\right)}, \quad (6)$$

where I_0 is the central intensity of the disc, h_i and h_o are the inner and outer disc scale lengths, respectively, r_b is the break radius, α is the sharpness of the disc transition between the inner and outer regions (where low α means a smooth transition from the inner to the outer disc and high α means an abrupt transition), and S is a scaling factor given by

$$S = [1 + \exp(-\alpha r_b)]^{-\frac{1}{\alpha}\left(\frac{1}{h_i} - \frac{1}{h_o}\right)}. \quad (7)$$

For the broken discs in our sample, the total luminosities were calculated numerically, given that a solution by integrating equation (6) is beyond the scope of this work.

In Table 4, we include a classification of the discs according to our observations. However, it is important to notice that breaks may occur at different radial distances, with different physical interpre-

tations: inner breaks ($\mu_r \sim 23$ mag arcsec $^{-2}$) may be related to star formation, while outer breaks ($\mu_r \sim 27$ mag arcsec $^{-2}$) may indicate a real drop in the stellar mass density (Martín-Navarro et al. 2012). Therefore, our classifications are restricted to the mean limiting SB of 24.5 mag arcsec $^{-2}$.

4.3.2 Other components

Apart from the disc, several other components are observed, including bulges, bars, arms, rings and lenses. We included those components in the decomposition using a Sérsic function (Sérsic 1968), given by

$$I_b(r) = I_e \exp\left(-b_n \left[\left(\frac{r}{r_e}\right)^{1/n} - 1\right]\right), \quad (8)$$

where r_e is the effective scale of the component (for which 50 per cent of the light is within r_e), I_e is the intensity at the effective radius, and n is the Sérsic index. The term b_n is not a free parameter, but a function of the Sérsic index due to the parametrization of the function at the effective radius instead of at the centre. In our calculations, we adopted the expressions for b_n presented in Appendix A1 of MacArthur et al. (2003). In a first-order approximation, $b_n \approx 2n - 0.33$, although the error may be considerable for $n < 0.5$. For simplification, we also rescale the effective intensity to SB using the expression $\mu_e = -2.5 \log I_e$. For equation (8), the total magnitude is given by (Ciotti 1991; MacArthur et al. 2003)

$$m_{\text{seraic}} = -2.5 \log \left(\frac{2\pi I_e r_e^2 e^{b_n} n \Gamma(2n) b}{b_n^{2n} a} \right), \quad (9)$$

where $\Gamma(x)$ is the complete gamma function of x . The Sérsic profile is a generalization of other commonly used profile functions, such as the exponential for $n = 1$, a Gaussian for $n = 1/2$ and de Vaucouleurs's profile (de Vaucouleurs 1948) for $n = 4$. Moreover,

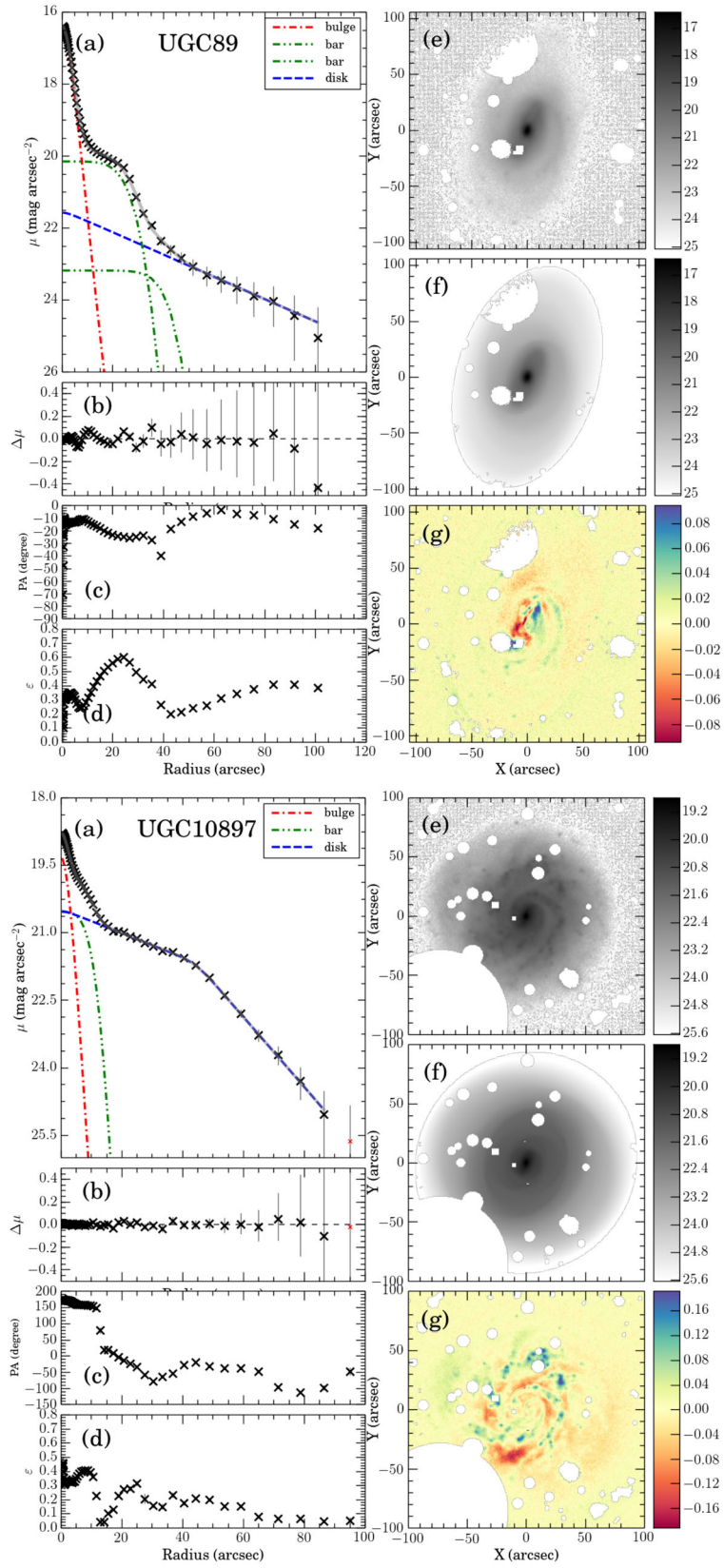


Figure 4. Examples of structural decomposition for two galaxies of the GHASP sample in the R_c -band, UGC 89 and UGC 10897. For each galaxy, we present seven panels, containing (a) surface brightness profiles and their decomposition components, (b) fitting residuals, (c) position angle profile, (d) ellipticity profile, (e) R_c -band image, (f) ELLIPSE model and (g) residual sigma image.

Table 4. Decomposition parameters for the GHASP sample in the R_c band obtained at the OHP observatory. The printed version contains only a sample of the table, and the remaining material is available online. (1) Galaxy name. (2–4) Parameters for the Sérsic function of bulges, bars and other components. (5) Visual classification of the components. (6–10) Parameters for the discs according to the broken exponential function. (11) Classification of the discs based on the type of breaks according to the scheme of Erwin, Pohlen & Beckman (2008, see text for details). (12) Magnitude of the central point source.

Galaxy	Sérsic				Disc						PS m_{ps} (mag)
	μ_e (mag arcsec $^{-2}$)	r_e (arcsec)	n	Type	μ_0	h_i (mag arcsec $^{-2}$)	h_o (arcsec)	r_b (arcsec)	α (arcsec)	Type	
(1)	(2)	(3)	(4)	(5)	(6)	(7)	(8)	(9)	(10)	(11)	(12)
UGC 89	16.7 ± 0.1	2.3 ± 0.1	1.0 ± 0.1	Bulge	21.5 ± 1.0	35 ± 25	–	–	–	Type I	–
	20.3 ± 0.2	19 ± 1	0.2 ± 0.1	Bar	–	–	–	–	–	–	–
	23 ± 1	29 ± 5	0.11 ± 0.07	Bar	–	–	–	–	–	–	–
UGC 94	18.7 ± 0.3	0.8 ± 0.3	1.6 ± 0.3	Bulge	20.3 ± 0.1	14.0 ± 0.8	–	–	–	Type I	–
	20.79 ± 0.09	8.3 ± 0.4	0.14 ± 0.09	Bar	–	–	–	–	–	–	–
UGC 508	18.6 ± 0.2	3.4 ± 0.1	2.65 ± 0.04	Bulge	19.60 ± 0.04	26.2 ± 0.2	–	–	–	Type I	–
	23.69 ± 0.08	20.2 ± 0.3	0.05 ± 0.05	Bar	–	–	–	–	–	–	–
	21.19 ± 0.06	7.6 ± 0.3	0.22 ± 0.02	Bar	–	–	–	–	–	–	–
UGC 528	19.0 ± 0.2	5.4 ± 0.6	2.7 ± 0.3	Bulge	18.6 ± 0.2	19 ± 2	–	–	–	Type I	–
	19.8 ± 0.2	13.1 ± 0.8	0.1 ± 0.2	Arms	–	–	–	–	–	–	–
	20.3 ± 0.4	22 ± 1	0.15 ± 0.09	Arms	–	–	–	–	–	–	–
UGC 763	28.0 ± 0.3	311 ± 183	5.3 ± 0.3	Bulge	19.99 ± 0.06	25 ± 2	–	–	–	Type I	–
	23 ± 2	18 ± 9	0.05 ± 0.06	Bar	–	–	–	–	–	–	–
...
UGC 12276	21.1 ± 0.1	5.4 ± 0.2	2.56 ± 0.01	Bulge	20.24 ± 0.09	14.0 ± 0.1	7.0 ± 0.3	45.0 ± 0.1	1.0 ± 0.2	Type II	–
	27.36 ± 0.05	0.1 ± 0.1	6.59 ± 0.04	Bar	–	–	–	–	–	–	–
UGC 12276c	22.74 ± 0.09	0.0 ± 0.1	2.99 ± 0.08	Bulge	20.60 ± 0.09	3.6 ± 0.2	–	–	–	Type I	–
UGC 12343	20.9 ± 0.4	12 ± 3	2.9 ± 0.3	Bulge	19.2 ± 0.1	30 ± 3	–	–	–	Type I	–
	21.7 ± 0.4	56 ± 3	0.2 ± 0.1	Bar	–	–	–	–	–	–	–
UGC 12632	23.1 ± 0.2	2.9 ± 0.6	0.05 ± 0.08	Nucleus	22.1 ± 0.1	58 ± 4	–	–	–	Type I	–
	23.4 ± 0.2	9.8 ± 0.4	0.10 ± 0.02	Bulge	–	–	–	–	–	–	–
UGC 12754	20.36 ± 0.07	11.8 ± 0.4	0.43 ± 0.04	Bar	20.6 ± 0.2	56 ± 7	–	–	–	Type I	15.7 ± 0.2
	22.4 ± 0.4	24 ± 1	0.05 ± 0.06	Bar	–	–	–	–	–	–	–

the Sérsic index can also be used as an indicator of the kind of component that is being observed. For example, in the optical and near-infrared wavelengths, Fisher & Drory (2010) have shown that $n \lesssim 2$ may indicate a pseudo-bulge, whereas $n \gtrsim 2$ may indicate a classic bulge for the spheroidal components. Besides, bars have typically $n \sim 0.7$ (Gadotti 2011). In Table 4, where the decomposition results are presented, we include a classification of the Sérsic function components according to a visual inspection of the images and profiles, such as bulges, bars, lenses and spiral arms.

For 38 galaxies, a nuclear source is also detected, which may be related to different physical processes, such as an active nucleus or stellar concentration. We have tested two approaches for parametrizing these components, using either a Sérsic component or a single delta function with a peak at $r = 0$. In 15 cases, the former approach resulted in a better description of the nucleus, because they have slightly larger FWHM than that of the modelled PSF and/or because of the different shape of the nuclear source compared to a star. These components are described as a nucleus in column 5 of Table 4. For 23 galaxies, however, the latter approach of using a delta function resulted in a better description of the nucleus. This delta function has only one free parameter, the magnitude of the source (m_{ps}), and its profile is that of a field star that is described as a Moffat function. These point source magnitudes are included in the last row of Table 4.

5 PHOTOMETRIC INTERNAL CONSISTENCY AND LITERATURE COMPARISON

In this section, we make a series of tests on our photometric results to verify their consistency and to compare them with similar results

in the literature. We have already made an internal consistency check of our SB profiles in Fig. 2, where we observed that the SB profiles from SDSS data are similar to those observed with direct measurements in the R_c band. Our SB profiles can also be compared with those derived for 12 galaxies in common with de Jong & van der Kruit (1994) in the R_c band, as shown in Fig. 5, where black and red lines show the difference between our data and the literature data for the OHP and SDSS data sets, respectively. For a proper comparison, we fixed the PA and the ellipticity of the galaxies to mimic the method of those authors instead of using a free PA and ellipticity as in Section 4.1. We also limited the comparison to regions greater than the seeing of our images.

The most deviant case is UGC 4256, but the internal consistency of our results for two different data sets indicates a possible systematic offset in the data of de Jong & van der Kruit (1994) for this galaxy. The deviation in the outer region of UGC 508 can be explained by the limited field of view in the images of de Jong & van der Kruit (1994), which cuts part of the galaxy. In this case, it is also possible to see a large variation of the isophotes fainter than $21 \text{ mag arcsec}^{-2}$ within the observations of de Jong & van der Kruit. Finally, the problematic case of UGC 10445 for the OHP data can be explained by the relatively short exposure time for this object, including only one image, which affects the accuracy of the sky subtraction. Apart from these remarks, the overall picture is that there is good agreement with de Jong & van der Kruit (1994), which is in turn in agreement with several other works in the literature.

In Fig. 6, we show the internal consistency of the isophotal and integrated photometric parameters derived from the SB profiles by comparing the results obtained with the OHP and SDSS data sets. Shown are the PA, ellipticity, radius and integrated magnitude at

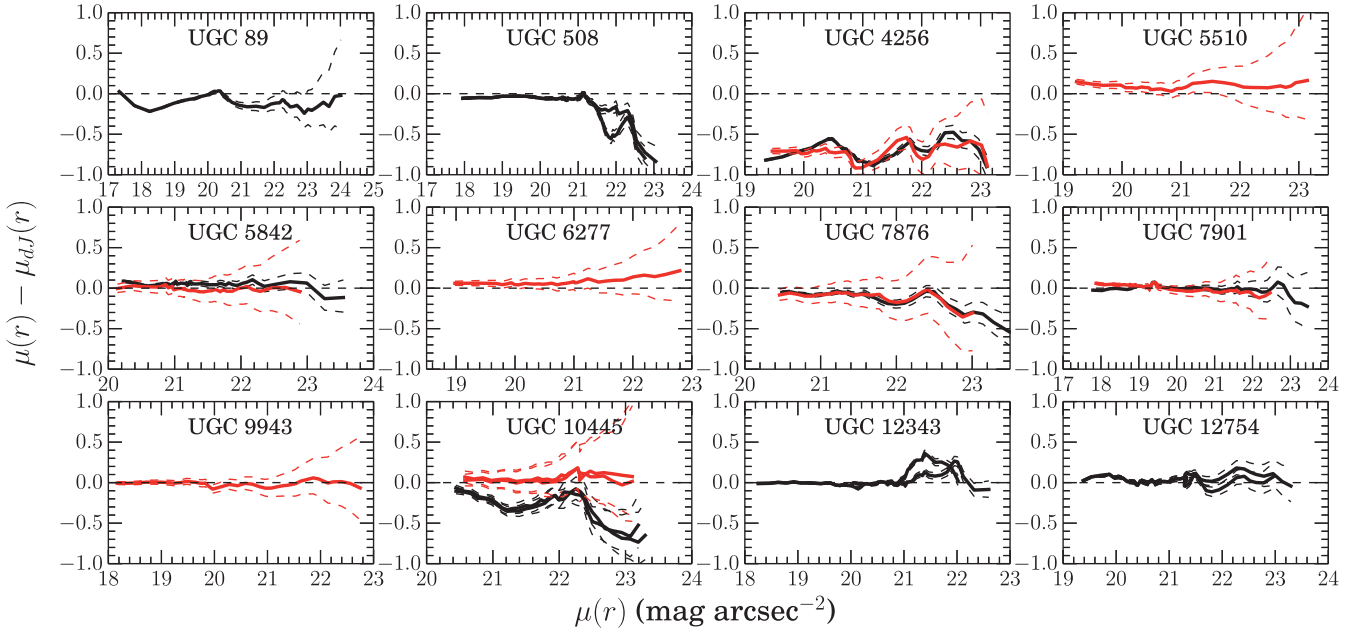


Figure 5. Differences in the SB as function of the isophotal level for 12 galaxy profiles in common with de Jong & van der Kruit (1994) in the R_c band. The solid black (red) lines are data from OHP (SDSS), while the dashed lines are the profile errors. Multiple profiles of a galaxy in de Jong & van der Kruit (1994) are shown in different lines. Dashed lines represent the errors in our profiles.

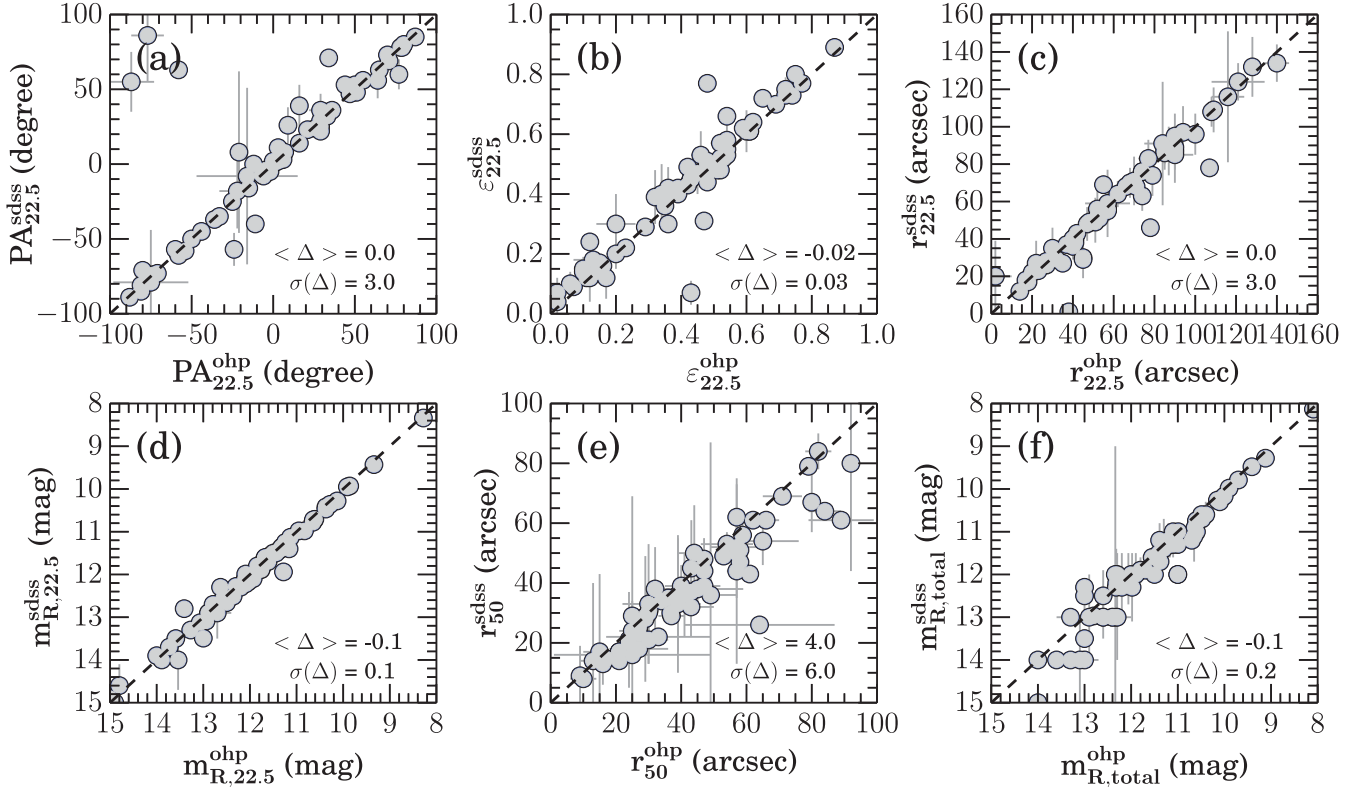


Figure 6. Comparison of photometric properties derived for the 66 galaxies in common between the OHP and SDSS data sets. The parameter Δ represents the difference between the parameters in the two data sets. Its mean value ($\langle \Delta \rangle$) and standard deviation [$\sigma(\Delta)$] are shown at the bottom of each panel. The parameters displayed are the following: (a) isophotal PA, (b) isophotal ellipticity, (c) isophotal radius, (d) isophotal apparent magnitude, (e) effective radius and (f) total apparent magnitude. The horizontal and vertical axes display the results for the OHP and SDSS data sets respectively, and the dashed line represents the line of equality.

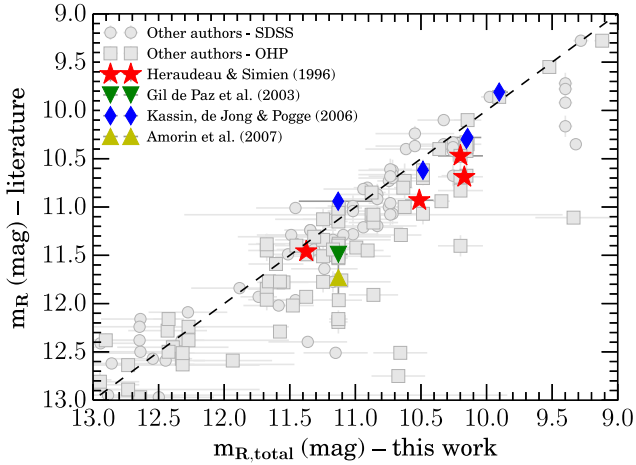


Figure 7. Comparison of total apparent magnitudes with the literature. Coloured symbols indicate the comparisons with data in the R_c band, for Heraudeau & Simien (1996), Gil de Paz, Madore & Pevunova (2003), Kassin, de Jong & Pogge (2006a) and Amorín et al. (2007). Grey symbols indicate comparisons with magnitudes in pass bands similar to R_c with our magnitudes both for the SDSS (circles) and OHP (squares) samples. This latter data include magnitudes from Hickson, Kindl & Auman (1989), Tully et al. (1996), James et al. (2004), Cabrera-Lavers & Garzón (2004), Taylor et al. (2005), Doyle et al. (2005), Hernández-Toledo et al. (2007), Noordermeer & van der Hulst (2007), Thomas et al. (2008), Hernández-Toledo & Ortega-Esbrí (2008), Matthews & Uson (2008) and Kriwattanawong et al. (2011). The dashed line represents equality between measurements.

the isophote of $22.5 \text{ mag arcsec}^{-2}$ and also the effective radius and total magnitude. We also display the mean residual difference ($\langle \Delta \rangle$) and its standard deviation $[\sigma(\Delta)]$ for each parameter. There are compatible measurements for both data sets within one standard deviation.

In Fig. 7, we compare our total magnitudes with data in the literature. There are just a few works in the literature for which total magnitudes are measured for the R_c band, so we also include in the figure measurements with similar filters in the literature without any additional correction or extrapolation, which are displayed as grey symbols: Tully et al. (1996), James et al. (2004), Cabrera-Lavers & Garzón (2004), Taylor et al. (2005), Doyle et al. (2005), Hernández-Toledo et al. (2007), Thomas et al. (2008), Hernández-Toledo & Ortega-Esbrí (2008), Matthews & Uson (2008) and Kriwattanawong et al. (2011). However, especially relevant is the comparison with proper R_c magnitudes, which we highlight in Fig. 7 using coloured symbols for the works of Heraudeau & Simien (1996), Gil de Paz, Madore & Pevunova (2003), Kassin, de Jong & Pogge (2006a) and Amorín et al. (2007). The number of overlapping galaxies with R_c -band data is scarce, only 12 galaxies, but those are in good agreement with most previous works, especially with the more recent survey of Kassin et al. (2006a).

In the top panel of Fig. 8, we compare our isophotal radius with the results of James et al. (2004). As the reference isophotal levels are different, there is a systematic offset in the isophotal radius in the sense that results from our work are systematically smaller than those from James et al., but still there is a good correspondence between the two data sets. In the bottom panel of Fig. 8, we show that the ellipticities are also well correlated, as expected, because at both reference isophotal levels the disc is the dominant component in the light of the galaxy, and has a simple geometry that does not vary drastically between these pass bands. Finally, in Fig. 9, we compare the isophotal PAs and inclinations with the results from

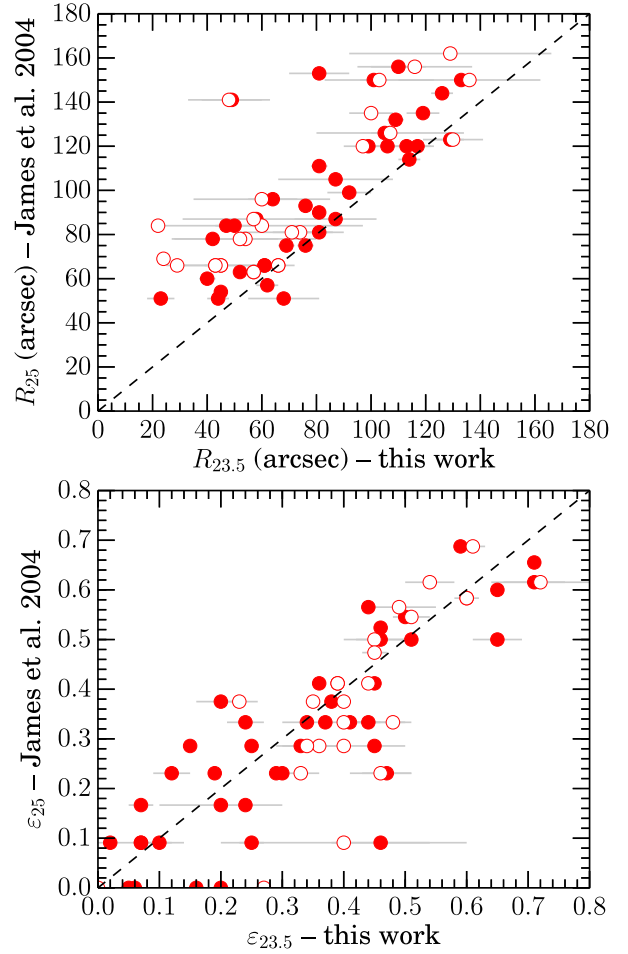


Figure 8. Comparison of our isophotal radius (above) and ellipticity (below) with those derived by James et al. (2004). Filled (hollow) points represent data from OHP (SDSS), and the dashed lines represent the equality between measurements.

the $H\alpha$ map analysis of Epinat et al. (2008), which demonstrates that our analysis produces results that are similar even to other tracers of galaxy shape.

6 SCALING RELATIONS

Scaling relations contain important information about the physical processes of galaxy formation and evolution, and impose important constraints on models that attempt to describe such objects (Courteau et al. 2007). In this section, we derive the most significant scaling relation involving luminosity, size and rotation curve velocity for each of the two most basic structural components of a galaxy, the bulge and the disc, and also for the whole galaxy. In section 6.1, we show how we correct the sizes and luminosities for the effects of distance, inclination and dust attenuation, and in section 6.2 we show how we estimate the scaling relations. In section 6.3 we present the main results and in section 6.4 we explore the Tully-Fisher relation in greater detail.

6.1 Correction for the effects of inclination and distance

We use all the galaxies in Table 4 with a bulge component according to our classification for the decomposition. Disc apparent

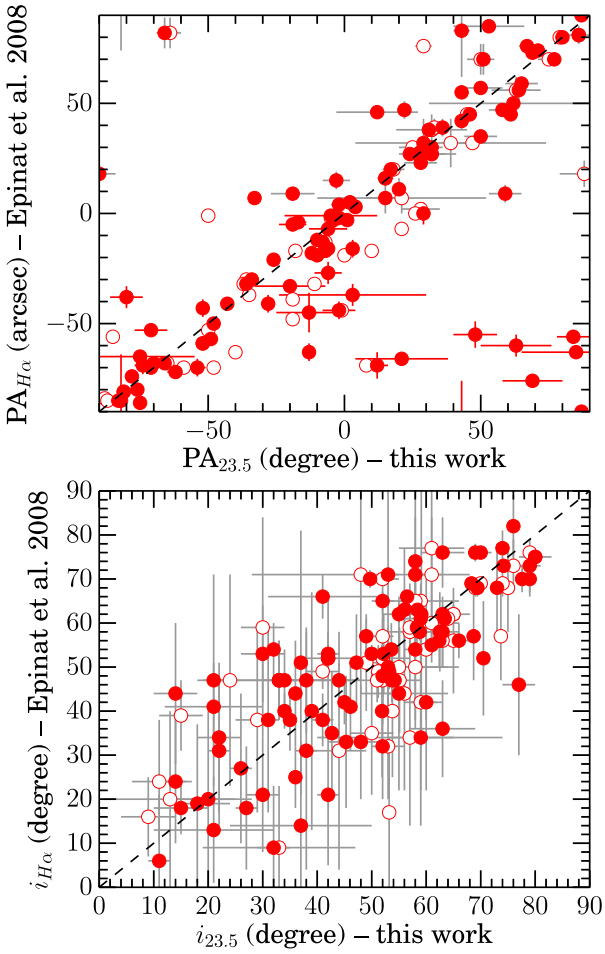


Figure 9. Comparison of our isophotal PAs (above) and inclinations (below) with those derived from the $H\alpha$ velocity fields of Epinat et al. (2008). Filled (hollow) points represent data from OHP (SDSS), and the dashed line represents the equality between measurements.

magnitudes (m_{disc}) are calculated using equation (5) or by numerical integration for broken profiles for the discs, while bulge luminosities (m_{bulge}) are calculated using equation (8). The absolute magnitudes of these components are then obtained using the equations

$$M_{\text{disc}} = m_{\text{disc}} - d_1 - d_2(1 - \cos i)^{d_3} - 5 \log D - 25, \quad (10)$$

$$M_{\text{bulge}} = m_{\text{bulge}} - b_1 - b_2(1 - \cos i)^{b_3} - 5 \log D - 25, \quad (11)$$

where the internal extinction coefficients $b_1 = 0.60$, $b_2 = 1.33$, $b_3 = 1.75$, $d_1 = 0.15$, $d_2 = 1.09$ and $d_3 = 2.82$ are obtained by linear interpolation from table 1 of Driver et al. (2008) for the R_c band ($\lambda = 647$ nm). D is the distance in megaparsecs according to Epinat et al. (2008), and the inclination i is taken from the gas velocity field analysis in Epinat et al. (2008), if available, or from the isophotal analysis otherwise. Individual distance errors are rarely available, and we adopt a value of 25 per cent for all objects.

The total luminosity of each galaxy is estimated by its total magnitude according to the analysis of the growth curve of the SB profiles (see Section 4.2). In this case, we obtain the absolute magnitude of the galaxies ($M_{R, \text{total}}$) from the apparent total magnitudes ($m_{R, \text{total}}$) using the expression

$$M_{R, \text{total}} = m_{R, \text{total}} - A_i(R) - 5 \log D - 25, \quad (12)$$

where $A_i(R)$ is the internal extinction correction given by Tully et al. (1998):

$$A_i(R) = \log(b/a) \times \{1.15 + 1.88(\log 2V_{\text{max}} - 2.5)\}. \quad (13)$$

Here b/a is again the minor-to-major axis ratio and V_{max} is the maximum velocity of the $H\alpha$ rotation curve derived from the velocity field analysis from Epinat et al. (2008).

We compare these luminosities with the physical sizes of each component, using the scale length of discs (h), or the inner disc length for broken discs, the effective radius of the bulge (r_e) and the effective radius of the galaxy (r_{50}). We do not attempt to correct the sizes of the components for extinction; we only correct the distances. Finally, we use V_{max} as in Epinat et al. (2008) as our dynamical tracer, excluding galaxies for which the flat part of the rotation curve was not reached in the velocity field analysis of the $H\alpha$ observations.

6.2 Fitting method

We assessed the statistical significance of pairs of luminosities, sizes and velocities using the Spearman's rank correlation coefficient r , which is a measurement of the strength of the correlation of two variables, and the associated p value, which indicates the probability of obtaining a result at least as extreme as the one obtained from a random distribution, both indicated in the boxes at the top of each panel in Fig. 10. For 18 cases, we obtain statistical significance above 3σ , considering a normal distribution as the reference. For these cases, we calculate the scaling law for the direct and inverse relations, displayed in the form of dashed lines in Fig. 10, using the following method. We consider a linear relation in the form of

$$y_i = \alpha x_i + \beta, \quad (14)$$

where each galaxy is represented by the index i , α is the slope of the relation and β is the zero-point. We then performed a χ^2 minimization considering the measurement uncertainties in both variables, considering also an intrinsic scatter, ε_0 , for the relation (see Tremaine et al. 2002), using the relation

$$\chi_\nu^2 = \frac{1}{N-2} \sum_{i=1}^N \frac{(y_i - \beta - \alpha x_i)^2}{\varepsilon_{y_i}^2 + \alpha^2 \varepsilon_{x_i}^2 + \varepsilon_0^2}, \quad (15)$$

where N is the number of galaxies in the sample, $\nu = N - 2$ is the number of degrees of freedom, and ε_{x_i} and ε_{y_i} are the parameter uncertainties. The presence of the variables in both the numerator and in the denominator of relation (15) makes the equation non-linear, and most common methods of minimization, such as the Levenberg–Marquardt algorithm (Press et al. 1992), may have problems in obtaining convergence. To obtain stable solutions, we used the interactive method described by Bedregal, Aragón-Salamanca & Merrifield (2006), which consists in solving equation (15) for a fixed value of ε_0 , and then updating ε_0 by multiplying by χ_ν^2 to a power of $2/3$, until $\chi_\nu^2 = 1$. The uncertainties for the coefficients are estimated using the bootstrapping method.

6.3 Results

Fig. 10 shows the resulting relations among luminosities, sizes and velocities for 89 galaxies selected in the previous section. To observe scaling relations in the form of power laws, we plot all quantities in logarithmic units. We adopt different colouring for the panels above and below the diagonal according to the strength of the bar and the morphological classification, respectively. However, we could not

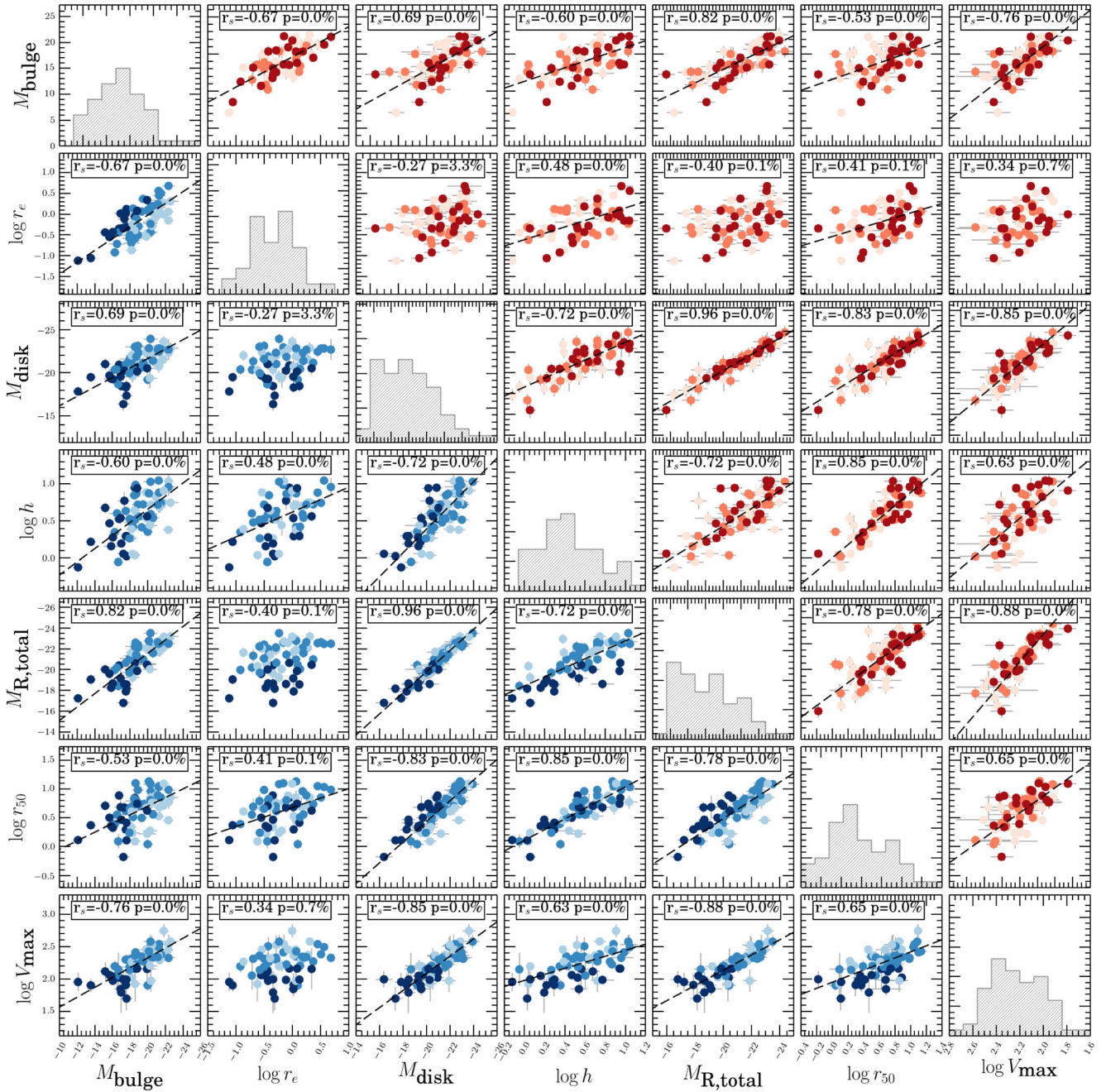


Figure 10. R_c -band correlations between luminosities and sizes for bulges (M_{bulge} , $\log r_e$) and discs (M_{disc} , $\log h$), and also the galaxy luminosities ($M_{R,\text{total}}$), sizes (r_{50}) and maximum velocities of the rotation curve (V_{max}). For the galaxies in the panels above the diagonal, the colour is according to the colour map in the bottom right of the figure, which divides galaxies according to the presence of bars following the morphological classification. For the galaxies in the panels below the diagonal, the colour is according to the colour map in the bottom left of the figure, classifying galaxies according to their numerical type in de Vaucouleurs’s classification. The Spearman’s rank correlation coefficient (r) and the p value for the relation are presented in the box at the top of each panel. For relations with significance greater than 3σ , we include a dashed black line to indicate the best-fitting linear regression, whose coefficients are presented in Table 5. The panels on the diagonal display the distribution of parameters as histograms.

study these correlations in subsamples due to the low statistics after dividing the data into those classes, and our quantitative results are all for the complete photometric sample. A summary of the scaling laws is shown in Table 5, where we sort the relations by decreasing Spearman’s coefficient.

All equations in Table 5 can be used to obtain approximate physical parameters for one given measurement as well as for constrain-

ing models of galaxy formation at the current cosmic time. Out of the 21 pairs of parameters, we observe that only three combinations have relatively low correlation coefficients. This indicates that most of the spiral galaxy properties are somehow linked. Although there are many properties that may shape galaxies, such as mass and angular momentum, and despite secular evolution effects, such as those which may form bars, there is still a great similarity among spirals

Table 5. Scaling relations with statistical significance above 3σ for the luminosities, sizes and velocities of the galaxies and two basic subcomponents, bulges and discs, ranked by decreasing Spearman’s rank coefficients. The first column indicates the identification of the relation. The second column indicates the variables involved in the relation, as well as the correlation coefficients and their p values. The third column indicates the direct and inverse relations. The fourth column shows the intrinsic scatter of the relation.

ID (1)	Parameters (2)	Relation (3)	ε_0 (4)
(a)	$M_{R,\text{total}}-M_{\text{disk}}$ $ r = 0.96, p = 3 \cdot 10^{-34}$	$M_{\text{disk}} = (0.98 \pm 0.03)M_{R,\text{total}} + (-0.6 \pm 0.7)$ $M_{R,\text{total}} = (1.02 \pm 0.04)M_{\text{disk}} + (0.6 \pm 0.8)$	– –
(b)	$\log V_{\text{max}}-M_{R,\text{total}}$ $ r = 0.88, p = 6 \cdot 10^{-21}$	$M_{R,\text{total}} = (-8.0 \pm 0.7) \log V_{\text{max}} + (-3 \pm 1)$ $\log V_{\text{max}} = (-0.12 \pm 0.01)M_{R,\text{total}} + (-0.2 \pm 0.2)$	0.37 ± 0.05 0.04 ± 0.01
(c)	$\log V_{\text{max}}-M_{\text{disk}}$ $ r = 0.85, p = 2 \cdot 10^{-18}$	$M_{\text{disk}} = (-7.1 \pm 0.8) \log V_{\text{max}} + (-5 \pm 2)$ $\log V_{\text{max}} = (-0.13 \pm 0.01)M_{\text{disk}} + (-0.6 \pm 0.3)$	0.31 ± 0.07 0.04 ± 0.01
(d)	$\log r_{50}-\log h$ $ r = 0.85, p = 4 \cdot 10^{-18}$	$\log h = (0.88 \pm 0.07) \log r_{50} + (0.00 \pm 0.04)$ $\log r_{50} = (0.93 \pm 0.06) \log h + (0.11 \pm 0.03)$	0.132 ± 0.003 0.135 ± 0.004
(e)	$\log r_{50}-M_{\text{disk}}$ $ r = 0.83, p = 9 \cdot 10^{-17}$	$M_{\text{disk}} = (-4.7 \pm 0.3) \log r_{50} + (-18.1 \pm 0.2)$ $\log r_{50} = (-0.18 \pm 0.02)M_{\text{disk}} + (-3.2 \pm 0.3)$	0.61 ± 0.03 0.12 ± 0.01
(f)	$M_{R,\text{total}}-M_{\text{bulge}}$ $ r = 0.82, p = 2 \cdot 10^{-16}$	$M_{\text{bulge}} = (1.1 \pm 0.1)M_{R,\text{total}} + (5 \pm 3)$ $M_{R,\text{total}} = (0.65 \pm 0.06)M_{\text{bulge}} + (-9 \pm 1)$	1.11 ± 0.02 0.84 ± 0.02
(g)	$\log r_{50}-M_{R,\text{total}}$ $ r = 0.78, p = 9 \cdot 10^{-14}$	$M_{R,\text{total}} = (-4.4 \pm 0.5) \log r_{50} + (-18.1 \pm 0.3)$ $\log r_{50} = (-0.16 \pm 0.02)M_{R,\text{total}} + (-2.7 \pm 0.3)$	0.88 ± 0.02 0.167 ± 0.005
(h)	$\log V_{\text{max}}-M_{\text{bulge}}$ $ r = 0.76, p = 7 \cdot 10^{-13}$	$M_{\text{bulge}} = (-9 \pm 1) \log V_{\text{max}} + (2 \pm 2)$ $\log V_{\text{max}} = (-0.08 \pm 0.01)M_{\text{bulge}} + (0.8 \pm 0.2)$	1.17 ± 0.07 0.107 ± 0.007
(i)	$\log h-M_{\text{disk}}$ $ r = 0.72, p = 3 \cdot 10^{-11}$	$M_{\text{disk}} = (-4.3 \pm 0.4) \log h + (-18.6 \pm 0.2)$ $\log h = (-0.16 \pm 0.02)M_{\text{disk}} + (-2.8 \pm 0.4)$	0.86 ± 0.02 0.165 ± 0.006
(j)	$M_{R,\text{total}}-\log h$ $ r = 0.72, p = 5 \cdot 10^{-11}$	$\log h = (-0.15 \pm 0.02)M_{R,\text{total}} + (-2.5 \pm 0.3)$ $M_{R,\text{total}} = (-4.3 \pm 0.6) \log h + (-18.4 \pm 0.3)$	0.181 ± 0.004 0.98 ± 0.01
(k)	$M_{\text{disk}}-M_{\text{bulge}}$ $ r = 0.69, p = 4 \cdot 10^{-10}$	$M_{\text{bulge}} = (1.0 \pm 0.1)M_{\text{disk}} + (3.0 \pm 3.0)$ $M_{\text{disk}} = (0.55 \pm 0.09)M_{\text{bulge}} + (-11.0 \pm 2.0)$	1.42 ± 0.03 1.03 ± 0.02
(l)	$\log r_e-M_{\text{bulge}}$ $ r = 0.67, p = 3 \cdot 10^{-09}$	$M_{\text{bulge}} = (-4.1 \pm 0.6) \log r_e + (-19.6 \pm 0.1)$ $\log r_e = (-0.14 \pm 0.02)M_{\text{bulge}} + (-2.9 \pm 0.3)$	1.41 ± 0.02 0.262 ± 0.004
(m)	$\log V_{\text{max}}-\log r_{50}$ $ r = 0.65, p = 1 \cdot 10^{-08}$	$\log r_{50} = (1.1 \pm 0.2) \log V_{\text{max}} + (-1.8 \pm 0.4)$ $\log V_{\text{max}} = (0.5 \pm 0.1) \log r_{50} + (1.95 \pm 0.06)$	0.204 ± 0.007 0.134 ± 0.005
(n)	$\log V_{\text{max}}-\log h$ $ r = 0.63, p = 3 \cdot 10^{-08}$	$\log h = (1.0 \pm 0.1) \log V_{\text{max}} + (-1.7 \pm 0.3)$ $\log V_{\text{max}} = (0.46 \pm 0.06) \log h + (1.98 \pm 0.04)$	0.205 ± 0.008 0.141 ± 0.004
(o)	$\log h-M_{\text{bulge}}$ $ r = 0.60, p = 3 \cdot 10^{-07}$	$M_{\text{bulge}} = (-4.6 \pm 0.8) \log h + (-16.3 \pm 0.4)$ $\log h = (-0.09 \pm 0.01)M_{\text{bulge}} + (-1.1 \pm 0.3)$	1.66 ± 0.02 0.231 ± 0.002
(p)	$\log r_{50}-M_{\text{bulge}}$ $ r = 0.53, p = 1 \cdot 10^{-05}$	$M_{\text{bulge}} = (-3.7 \pm 0.8) \log r_{50} + (-16.6 \pm 0.5)$ $\log r_{50} = (-0.08 \pm 0.02)M_{\text{bulge}} + (-0.8 \pm 0.4)$	1.83 ± 0.02 0.260 ± 0.004
(q)	$\log h-\log r_e$ $ r = 0.48, p = 9 \cdot 10^{-05}$	$\log r_e = (0.8 \pm 0.3) \log h + (-0.6 \pm 0.2)$ $\log h = (0.3 \pm 0.2) \log r_e + (0.62 \pm 0.03)$	0.41 ± 0.01 0.28 ± 0.01
(r)	$\log r_{50}-\log r_e$ $ r = 0.41, p = 1 \cdot 10^{-03}$	$\log r_e = (0.6 \pm 0.2) \log r_{50} + (-0.5 \pm 0.1)$ $\log r_{50} = (0.3 \pm 0.1) \log r_e + (0.68 \pm 0.02)$	0.362 ± 0.002 0.275 ± 0.003

that is still to be explained. Also, this large number of correlations restricts the interpretation of the correlations individually, and certainly a comprehensible interpretation will be possible only with a more complete model of galaxy evolution (see Shen et al. 2010). Nevertheless, we are going to discuss briefly a few of the scaling laws that have been observed here and previously in the literature, with the exception of the TF relation (Tully & Fisher 1977), which we address in greater detail in Section 6.4.

The relation (q) between the sizes of bulges and discs was obtained previously by other authors (Courteau, de Jong & Broeils 1996; Aguerri et al. 2005) and may give important clues for galaxy formation scenarios. Courteau et al. (1996) argue that discs should form earlier than bulges and, therefore, the properties of the bulges

are linked to their host discs. Due to the relatively low Sérsic indices of the bulges, these are indeed likely to be pseudo-bulges (Fisher & Drory 2008), which are formed by secular evolution of the discs and, therefore, correlations among these parameters naturally arise in a scenario of secular evolution, disfavoring scenarios of decoupled size relation, such as bulges formed by mergers. We have found that the median value of r_e/h is 0.14 considering all galaxies, which is in agreement with the values in the literature (for instance, Laurikainen et al. 2010).

The luminosity of a bulge is also important in understanding its origin. Bulge luminosities and sizes are expected to correlate, as already indicated in equation (9), $L_{\text{bulge}} \propto r_e^2$, and indeed there is a strong correlation as shown in equation (l). Moreover, bulge

luminosity is correlated to all other measured properties of the discs, to the whole galaxy and also to the rotational velocity. Therefore, the properties of the bulges we observe in late-type galaxies of the local Universe are probably the result of secular evolution. Interestingly, bulge luminosity is also correlated with supermassive black hole mass (Kormendy & Richstone 1995), illustrating the important role of the bulges in understanding galaxy formation, which is yet to be fully understood.

The luminosity of the galaxy correlates strongly with all parameters with the exception of the size of the bulge, and occupy five of the first ten equations, as shown in relations (a), (b), (f), (g), and (j). The importance of the total luminosity, also observed by Courteau et al. (2007), may indicate that the baryonic portion of a galaxy has a pivotal role in its appearance: it is connected with the gravitational potential through the velocity, but has a more direct link with the size (or shape) of the galaxy.

Other photometric relations that are well documented in the literature include the relation (k) between bulge and disc luminosities (Laurikainen et al. 2010) and (f) which relates bulge and total luminosities (Carollo et al. 2007). The rotational velocity of galaxies is usually studied in comparison with integrated photometry, such as in relation (b), the TF relation, and the size–velocity relation (m), also studied by Courteau et al. (2007). However, here we show that the rotational velocity also strongly scales with the luminosity and size of the disc component, as shown in relations (c) and (n), which is expected because the disc is responsible for the majority of the light of the galaxy. Interestingly, however, the luminosity of a bulge also correlates with the rotational velocity, as shown in relation (h), indicating that bulge properties have a dynamical link with the galaxy that hosts it.

6.4 Tully–Fisher relation

The TF relation (Tully & Fisher 1977) is the most important scaling relation for disc galaxies. It has been used for several purposes, including distance determinations and, historically, as a way of measuring the Hubble constant. The TF relation links the maximum velocity of the rotation curve V_{\max} with the total magnitude of the galaxies in the form of a power law. The TF relation was measured for the GHASP sample by Torres-Flores et al. (2011) in the near-infrared bands H and K , so here we add to those results the optical R_c band. We adopt the following parametrization:

$$M_\lambda = \alpha_\lambda \log (V_{\max} [\text{km s}^{-1}]) + \beta_\lambda, \quad (16)$$

where M_λ is the absolute total magnitude in the pass band λ , V_{\max} is the maximum velocity of the rotation curve, and α_λ and β_λ are the slope and zero-point of the TF relation. Both the slope and the zero-point of the TF relation are of importance because they may be used either as constraints or as tests for models of galaxy formation and evolution.

To produce a suitable sample for this specific relation, we select the galaxies according to the following criteria. We remove galaxies with inclinations greater than 75° due to their high internal extinction, and also galaxies with inclinations smaller than 20° because of the higher uncertainty in the determination of the rotation curve velocity. We also exclude galaxies with recession velocities lower than 3000 km s^{-1} due to possible peculiar velocities affecting the Hubble flow, except for the cases where more accurate distance indicators were used, such as Cepheids and red-giant branch distances. Finally, as we are only dealing with $H\alpha$ velocity fields, we use the analysis of Epinat et al. (2008) to exclude from the sample galaxies for which the maximum rotational velocity is not achieved accord-

ing to their classification of the maps. We use our two absolute magnitude estimators, the asymptotic ($M_{R, \text{total}}$) and the isophotal ($M_{R, 23.5}$), as the probes of galaxy luminosity, resulting in samples with 80 and 72 galaxies, respectively. Most galaxies in the GHASP sample are not in clusters of galaxies, so we consider that our TF relation is basically probing the field environment, although the expected difference in the TF relation for different environments is mild (De Rijcke et al. 2007; Mocz et al. 2012).

The TF relation in the R_c band is shown in Fig. 11. To calculate the regression coefficients, we used the χ^2 minimization of equation (15) as described in Section 6.3. The so-called inverse TF relation (Schechter 1980) coefficients are calculated as follows. We calculated the coefficients α' and β' by interchanging the variables $x_i \rightleftharpoons y_i$ in equation (14), and then calculated the inverse TF relation using the relations $\alpha = 1/\alpha'$ and $\beta = -\beta'/\alpha'$. A summary of the results for the TF relation and the inverse TF relations is presented in Table 6.

The TF relation is not just an important tool for measuring distances of galaxies, but it is also crucial in highlighting processes of galaxy evolution, for instance, by comparing the TF relation of different morphological types. Spiral galaxies have a single TF relation, but lenticular and elliptical galaxies have TF relations that run approximately parallel compared to spirals (Bedregal et al. 2006; De Rijcke et al. 2007). We observe that the TF relation for spirals in the R_c band is well defined for almost all galaxies, with only two exceptions that are worth discussing. NGC 12276, marked in Fig. 11 with a yellow halo, does not seem to have any special feature to offset it from the TF relation, so one possibility to explain its position is that the distance to the galaxy is not accurate. We used the value of 78.8 Mpc from Epinat et al. (2008) for consistency with previous works, which is the expected value according to the systematic velocity using the Hubble flow. However, Pedreros & Madore (1981) estimated the distance to this galaxy as 40 Mpc using the ring size, which implies a difference of ≈ 1.5 mag, which is enough to bring the galaxy much closer to the TF relation. The galaxy with a red halo in Fig. 11, NGC 4256, has a peculiar morphology of a single arm and an asymmetric rotation curve, which may be why the galaxy is off the TF relation defined for relatively more relaxed spirals. In this case, star formation may have been triggered recently as a response to a gravitational field, resulting in a relatively luminous object compared to the TF relation.

The slope and the zero-point of the R_c -band TF relation in our work are in agreement with those previously derived in the literature. Tully & Pierce (2000), for instance, determined the slope and zero-point for a sample of 115 galaxies in four nearby clusters with velocities derived from HI line widths, and by not considering errors in either variable nor the intrinsic scatter of the relation, they found $\alpha_R = -7.65$ and $\beta_R = -4.3$, which is consistent with our results within 2σ . On the other hand, Verheijen (2001) derived the TF relation for the Ursa Major cluster using the inverse relation without intrinsic scatter, and fixing the uncertainties as 0.05 mag for the magnitudes and 5 per cent for the velocities. In this framework, they found slopes ranging from -7.1 to -9 , and zero-points ranging from -3.15 to 2.81 for their various samples, which is similar to our inverse TF relation parameters.

The TF relation in the infrared pass bands is important because these wavelengths are reliable tracers of stellar mass. Torres-Flores et al. (2011) used the GHASP sample to derive the TF relation in the H and K bands using 2MASS survey data (Skrutskie et al. 2006) as well as stellar and baryonic TF relations. Using a method similar to ours, they obtained slopes of $\alpha_H = -10.84 \pm 0.61$ and $\alpha_K = -11.07 \pm 0.63$ and zero-points of $\beta_H = 1.97 \pm 1.36$ and

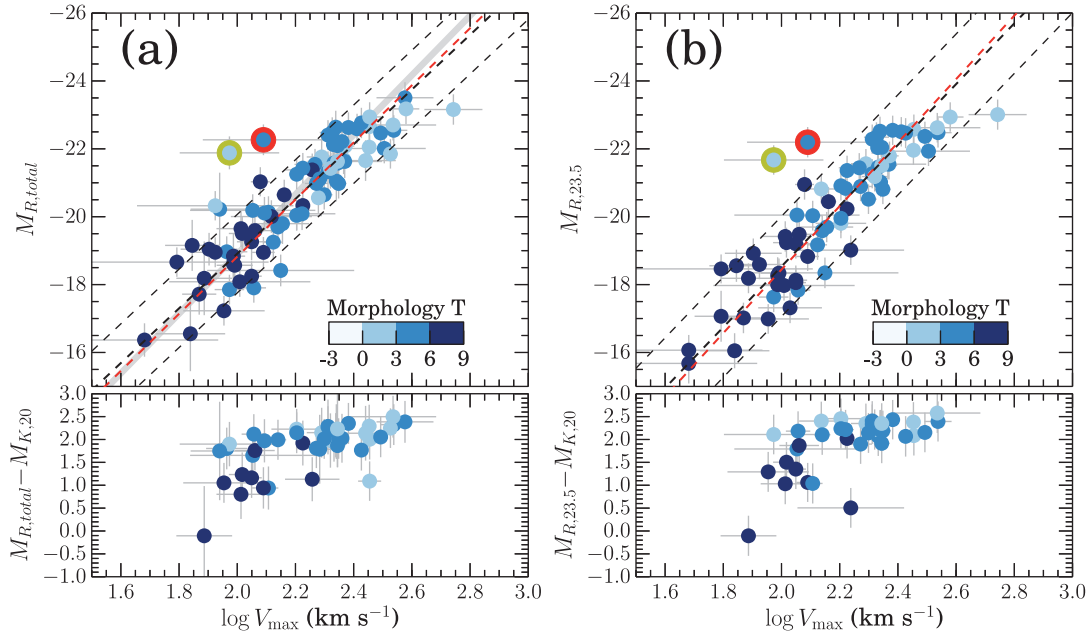


Figure 11. TF relation for the R_c band for GHASP galaxies considering (a) the total asymptotic magnitude, $M_{R, \text{total}}$, and (b) the isophotal total magnitude inside the isophote of $23.5 \text{ mag arcsec}^{-2}$. The grey line in panel (a) indicates the results from Sakai et al. (2000). In the top panel of each figure, the black dashed line indicates the direct TF relation results and the best-fitting $\pm 1\sigma_\beta$, while the red dashed line indicates the inverse TF relation results. The bottom panels indicate the colour of the galaxies using the K band total magnitudes used for the TF relation in Torres-Flores et al. (2011) inside the isophote of $20 \text{ mag arcsec}^{-2}$. The colour of each galaxy corresponds to the colour scale in the upper panels, which separates objects according to their numerical morphology. The two objects highlighted with a halo are NGC 12276 (yellow) and NGC 4256 (red), which for different reasons are offset to the TF relation (see text for details).

Table 6. Regression coefficients for the R_c -band TF relation using the total asymptotic magnitude and the total isophotal magnitude including 80 and 72 galaxies, respectively.

Relation	α_R	β_R	ϵ_0
Total asymptotic magnitude			
TF	-8.1 ± 0.5	-3.0 ± 1.0	0.28 ± 0.07
Inverse TF	-8.4 ± 0.7	-2.0 ± 2.0	0.28 ± 0.08
Total isophotal magnitude			
TF	-8.9 ± 0.6	-1.0 ± 1.0	0.33 ± 0.06
Inverse TF	-9.3 ± 0.7	0.0 ± 2.0	0.34 ± 0.08

$\beta_K = 2.27 \pm 1.39$ for the H and K bands, respectively. As expected, the R_c -band slope is greater than the slope in the near-infrared band (e.g. Verheijen 2001). However, one important feature observed in the infrared is a break in the TF relation for galaxies with $\log V_{\text{max}} \lesssim 2.2$, in the sense that galaxies below this velocity are under luminous based on the expected TF relation for bright galaxies. This break in the TF relation is not noticed in the R_c band. This difference in the shapes of the near-infrared and optical TF relations for the low-mass regime can be understood if one inspects the bottom panels of Fig. 11, which show the optical to near-infrared colours of the galaxies as a function of the maximum rotational velocities. These panels show a flat colour distribution except for the galaxies with $V_{\text{max}} \lesssim 125 \text{ km s}^{-1}$, indicating the different mass-to-light ratios of these galaxies. These low-mass systems are bluer than more massive galaxies, indicating that they are younger objects that may have been forming stars recently, and this effect fortuitously compensates for the difference in the stellar mass-to-light ratios, causing the differences in the shapes of the near-infrared and optical TF relations at low masses.

7 SUMMARY AND CONCLUSION

This study provided photometrically calibrated SB profiles of GHASP galaxies, with 170 profiles in the R_c band and 108 in the SDSS bands u , g , r , i and z . From these data, we derived R_c -band integrated photometric parameters, presented in Table 3, which are consistent with other works in the literature. All these results are public and will be available in digital format at the Fabry–Perot repository in <http://cesam.lam.fr/fabryperot>.

We perform multi-component structural decompositions in the R_c band, presented in Table 4, with the goal of separating the disc component from bulges, bars, lenses and nuclear sources, as preparation for our forthcoming paper on the kinematic decomposition of GHASP velocity fields, which will be compared with the photometric work.

Finally, we applied new photometric data to observe bulges and discs and to derive global scaling relations for the luminosities, sizes and velocities in the R_c band. We derived expressions for 18 scaling relations, which may be used to constrain models of galaxy formation and evolution. In particular, we studied the TF relation using velocities derived solely from $H\alpha$ maps from GHASP. We obtained slopes and zero-points that are consistent with previous findings in the literature for the R_c band for cluster galaxies, reinforcing the idea that the TF relation is basically a relation between the total stellar content and the gravitational potential, which is barely affected by the environment and the presence of photometric substructures.

ACKNOWLEDGEMENTS

We thank the OHP technical team, who helped this project in several ways, from support at the telescope to acquiring observational data. In particular, we would like to thank Didier Gravalon, Jacky

Taupenas and Jean-Claude M evolhon, who made several observation runs. We also wish to thank the several undergraduate students who had their first observing run during the completion of this project under the supervision of DR and CA. We thank the anonymous referee for constructive comments, which helped to improve this paper. CEB and CMdO are grateful to FAPESP (grants 2009/11236-0, 2011/21325-0 and 2006/56213-9) for financial support. PA, DR, BE, VP, CA and MM thank the Program National Cosmologie et Galaxies for funding this project. CMdO and PA thank USP-COFECUB for funding collaborative work between IAG and LAM. This research made use of the NASA/IPAC Extragalactic Database, which is operated by the Jet Propulsion Laboratory, California Institute of Technology, under contract with the National Aeronautics and Space Administration. We acknowledge use of the HyperLeda data base (<http://leda.univ-lyon1.fr>).

REFERENCES

- Abazjany K. N. et al., 2009, *ApJS*, 182, 543
Aguerri J. A. L., Elias-Rosa N., Corsini E. M., Mu oz-Tu n C., 2005, *A&A*, 434, 109
Amor n R. O., Mu oz-Tu n C., Aguerri J. A. L., Cair s L. M., Caon N., 2007, *A&A*, 467, 541
Balcells M., Graham A. W., Dom nguez-Palmero L., Peletier R. F., 2003, *ApJ*, 582, L79
Bedregal A. G., Arag n-Salamanca A., Merrifield M. R., 2006, *MNRAS*, 373, 1125
Bernardi M., Hyde J. B., Sheth R. K., Miller C. J., Nichol R. C., 2007, *AJ*, 133, 1741B
Bertin E., Arnouts S., 1996, *A&AS*, 117, 393
Cabrera-Lavers A., Garz n F., 2004, *AJ*, 127, 1386
Cair s L. M., Caon N., V lchez J. M., Gonz lez-P rez J. N., Mu oz-Tu n C., 2001, *ApJS*, 136, 393
Carollo C. M., Scarlata C., Stiavelli M., Wyse R. F. G., Mayer L., 2007, *ApJ*, 658, 960
Chevalier C., Ilovaisky S. A., 1991, *A&AS*, 90, 225
Ciotti L., 1991, *A&A*, 249, 99
Courteau S., 1996, *ApJS*, 103, 363
Courteau S., de Jong R. S., Broeils A. H., 1996, *ApJ*, 457, L73
Courteau S., Dutton A. A., van den Bosch F. C., MacArthur L. A., Dekel A., McIntosh D. H., Dale D. A., 2007, *ApJ*, 671, 203
de Jong R. S., van der Kruit P. C., 1994, *A&AS*, 106, 451
De Rijcke S., Zeilinger W. W., Hau G. K. T., Prugniel P., Dejonghe H., 2007, *ApJ*, 659, 1172
de Vaucouleurs G., 1948, *Annales d'Astrophysique*, 11, 247
de Vaucouleurs G., 1958, *ApJ*, 128, 465
Doyle M. T. et al., 2005, *MNRAS*, 361, 34
Driver S. P. et al., 2008, *ApJ*, 678, L101
Dutton A. A., Courteau S., de Jong R., Carignan C., 2005, *ApJ*, 619, 218
Epinat B. et al., 2008, *MNRAS*, 388, 500E
Epinat B., Amram P., Marcelin M., 2008, *MNRAS*, 390, 466E
Epinat B., Amram P., Balkowski C., Marcelin M., 2010, *MNRAS*, 401, 2113
Erwin P., Beckman J. E., Pohlen M., 2005, *ApJ*, 626, L81
Erwin P., Pohlen M., Beckman J. E., 2008, *AJ*, 135, 20
Fisher D. B., Drory N., 2008, *AJ*, 136, 773
Fisher D. B., Drory N., 2010, *ApJ*, 716, 942
Freeman K. C., 1970, *ApJ*, 160, 811
Gadotti D. A., 2011, *MNRAS*, 415, 3308
Garrido O., Marcelin M., Amram P., Boulesteix J., 2002, *A&A*, 387, 821
Garrido O., Marcelin M., Amram P., Boissin O., 2003, *A&A*, 399, 51
Garrido O., Marcelin M., Amram P., 2004, *MNRAS*, 349, 225
Garrido O., Marcelin M., Amram P., Balkowski C., Gach J. L., Boulesteix J., 2005, *MNRAS*, 362, 127
Gil de Paz A., Madore B. F., Pevunova O., 2003, *ApJS*, 147, 29
Haynes M. P., Giovanelli R., 1984, *AJ*, 89, 758
Heraudeau P., Simien F., 1996, *A&AS*, 118, 111
Hern andez-Toledo H. M., Ortega-Esbr  S., 2008, *A&A*, 487, 485
Hern andez-Toledo H. M., Zendejas-Dom nguez J., Avila-Reese V., 2007, *AJ*, 134, 2286
Hickson P., Kindl E., Auman J. R., 1989, *ApJS*, 70, 687
James P. A. et al., 2004, *A&A*, 414, 23
Jedrzejewski R. I., 1987, *MNRAS*, 226, 747
Jester S. et al., 2005, *AJ*, 130, 873
Kassin S. A., de Jong R. S., Pogge R. W., 2006a, *ApJS*, 162, 80
Kassin S. A., de Jong R. S., Weiner B. J., 2006b, *ApJ*, 643, 804
Kent S. M., 1984, *ApJS*, 56, 105
Kent S. M., 1986, *AJ*, 91, 1301
Kormendy J., Richstone D., 1995, *ARA&A*, 33, 581
Kriwattanawong W., Moss C., James P. A., Carter D., 2011, *A&A*, 527, A101
Landolt A. U., 1992, *AJ*, 104, L340
Lauer T. R. et al., 2007, *ApJ*, 662, L808
Laurikainen E., Salo H., Buta R., Knapen J. H., Comer n S., 2010, *MNRAS*, 405, 1089
Lisker T., Grebel E. K., Binggeli B., Glatt K., 2007, *ApJ*, 660, L1186
MacArthur L. A., Courteau S., Holtzman J. A., 2003, *ApJ*, 582, 689
Mart n-Navarro I. et al., 2012, *MNRAS*, 427, 110
Matthews L. D., Uson J. M., 2008, *AJ*, 135, 291
McDonald M., Courteau S., Tully R. B., 2009, *MNRAS*, 394, 2022
Mocz P., Green A., Malacari M., Glazebrook K., 2012, *MNRAS*, 425, 296
Moffat A. F. J., 1969, *A&A*, 3, 455
Noordermeer E., van der Hulst J. M., 2007, *MNRAS*, 376, 1480
Patterson F. S., 1940, *Harvard College Obser. Bull.*, 914, 9
Pedreros M., Madore B. F., 1981, *ApJS*, 45, 541
Pohlen M., Trujillo I., 2006, *A&A*, 454, 759
Press W. H., Teukolsky S. A., Vetterling W. T., Flannery B. P., 1992, *Cambridge Univ. Press, Cambridge*
Rubin V. C., Thonnard N., Ford W. K., Jr, 1978, *ApJ*, 225, L107
Sakai S., Mould J. R., Hughes S. M. G. et al., 2000, *ApJ*, 529, 698
Schechter P. L., 1980, *AJ*, 85, 801
Schlegel D. J., Finkbeiner D. P., Davis M., 1998, *ApJ*, 500, 525
S rsic J. L., 1968, *Atlas de galaxies australes. Observatorio Astronomico, Cordoba, Argentina*
Shen J., Rich R. M., Kormendy J., Howard C. D., De Propriis R., Kunder A., 2010, *ApJ*, 720, L72
Skrutskie M. F. et al., 2006, *AJ*, 131, 1163
Spano M., Marcelin M., Amram P., Carignan C., Epinat B., Hernandez O., 2008, *MNRAS*, 383, 297
Stoughton C. et al., 2002, *AJ*, 123, 485
Taylor V. A., Jansen R. A., Windhorst R. A., Odewahn S. C., Hibbard J. E., 2005, *ApJ*, 630, 784
Thomas C. F., Moss C., James P. A., Bennett S. M., Arag n-Salamanca A., Whittle M., 2008, *A&A*, 486, 755
Torres-Flores S., Epinat B., Amram P., Plana H., Mendes de Oliveira C., 2011, *MNRAS*, 416, 1936
Tremaine S. et al., 2002, *ApJ*, 574, 740
Trujillo I., Aguerri J. A. L., Cepa J., Guti rrez C. M., 2001, *MNRAS*, 328, 977
Tully R. B., Fisher J. R., 1977, *A&A*, 54, 661
Tully R. B., Fisher J. R., 1988, *Catalog of Nearby Galaxies. Cambridge Univ. Press, Cambridge*
Tully R. B., Pierce M. J., 2000, *ApJ*, 533, 744
Tully R. B., Verheijen M. A. W., Pierce M. J., Huang J.-S., Wainscoat R. J., 1996, *AJ*, 112, 2471
Tully R. B., Pierce M. J., Huang J.-S., Saunders W., Verheijen M. A. W., Witchalls P. L., 1998, *AJ*, 115, 2264
van Albada T. S., Sancisi R., 1986, *Royal Society of London Philosophical Transactions Series A*, 320, 447
van Albada T. S., Bahcall J. N., Begeman K., Sancisi R., 1985, *ApJ*, 295, 305
van der Hulst J. M., van Albada T. S., Sancisi R., 2001, *ASP Conf. Ser.*, 240, 451

van der Kruit P. C., Searle L., 1982, A&A, 110, 61
Verheijen M. A. W., 2001, ApJ, 563, 694
Zwicky F., 1937, ApJ, 86, 217

SUPPORTING INFORMATION

Additional Supporting Information may be found in the online version of this article. This includes full copies of the following tables in the printed version:

Table 1. Photometric sample of the GHASP survey.

Table 3. Isophotal and integrated photometric parameters for the R_c band.

Table 4. Decomposition parameters for the GHASP sample in the R_c band obtained at the OHP observatory. (<http://mnras.oxfordjournals.org/lookup/suppl/doi:10.1093/mnras/stv1685/-/DC>).

Please note: Oxford University Press are not responsible for the content or functionality of any supporting materials supplied by the authors. Any queries (other than missing material) should be directed to the corresponding author for the paper.

This paper has been typeset from a $\text{\TeX}/\text{\LaTeX}$ file prepared by the author.